Katedra anorganické chemie

Přírodovědecká fakulta

Univerzita Palackého v Olomouci

Přírodovědecká fakulta

Katedra anorganické chemie

DISERTAČNÍ PRÁCE

Experimentální a teoretické studium magnetické výměnné interakce a anizotropie v jednojaderných a polyjaderných koordinačních sloučeninách přechodných kovů

Experimental and Theoretical Study of Magnetic Exchange Interactions and Anisotropy in Mononuclear and Polynuclear Coordination Compounds of Transition Metals.

Mgr. Kamil Kotrle

Studijní obor: Anorganická chemie

Školitel: Doc. Ing. Radovan Herchel, PhD.

Olomouc 2023

Prohlašuji, že jsem závěrečnou práci vypracoval samostatně pod vedením školitele doc. Ing. Radovana Herchela, PhD. Veškerou literaturu a další zdroje, z nichž jsem při zpracování čerpal, uvádím v seznamu použité literatury a zdrojů.

Mgr. Kamil Kotrle

Bibliografická identifikace

Autor: Mgr. Kamil Kotrle

Téma: Experimentální a teoretické studium magnetické výměnné interakce a anizotropie v jednojaderných a polyjaderných koordinačních sloučeninách přechodných kovů

Typ práce: Disertační

Katedra: Katedra anorganické chemie

Školitel: Doc. Ing. Radovan Herchel, PhD.

Rok: 2023

Klíčová slova: Jedno-molekulový magnetismus, vícejaderné komplexy, magnetické výměnné interakce, spin-fononová interakce, CASSCF

Počet stran: 170

Jazyk: Čeština

Bibliographical identification

Author: Mgr. Kamil Kotrle

Topic: Experimental and Theoretical Study of Magnetic Exchange Interactions and Anisotropy in Mononuclear and Polynuclear Coordination Compounds of Transition Metals.

Type of thesis: Dissertation

Department: Department of Inorganic Chemistry

Supervisor: Doc. Ing. Radovan Herchel, PhD.

Year: 2023

Keywords: Single-molecule magnetism, polynuclear complexes, magnetic exchange interactions, spin-phonon coupling, CASSCF

Number of pages: 170

Language: Czech

Poděkování

Na tomto místě vyjadřuji poděkování kolegům za jejich odbornou pomoc a asistenci při vypracování této práce. Poděkování patří celému kolektivu Katedry anorganické chemie Přírodovědecké fakulty Univerzity Palackého.

Jmenovitě bych chtěl poděkovat:

Školiteli doc. Ing. Radovanu Herchelovi, Ph.D., za jeho cenné rady a pomoc při tvorbě disertační práce,

Ing. Ivanu Nemcovi, Ph.D. za rady a připomínky a rentgenové strukturní analýzy,

prof. Ing. Jánu Moncoľovi, DrSc. za rentgenové strukturní analýzy,

Mgr. Peterovi Antalovi, Ph.D. za měření práškové difrakce,

Pavle Richterové za měření CHNS elementární analýzy,

Mgr. Kamile Petrželové, Ph.D. za měření atomové absorpční spektroskopie,

Doc. RNDr. Eriku Čižmárovi, Ph.D. za provedení magnetických měření a elektronové paramagnetické rezonance,

Mgr. Radce Křikavové, Ph.D. za pomoc s korekcí disertační práce,

Prof. Dr. Mihailu Atanasovi a Prof. Dr. Frankovi Neesemu za pomoc a ochotu během zahraniční stáže na Max-Planck-Institut für Kohlenforschung.

Děkuji také ze možnost zapojit se do vědeckých projektů: projekt Doktorské studentské grantové soutěže DSGC-2021-0032 (*Towards Zero-Field Co(II) Single Ion Magnets)*, projekt Grantové agentury České republiky 23-07175S (*Semikoordinace: cesta k chemicky stabilním molekulárním nanomagnetům)*, projekt Podpora mobility na UP II., a projektů studentské grantové soutěže UP IGA_PrF_2018_011, IGA_PrF_2019_009, IGA_PrF_2020_016, IGA_PrF_2021_009, IGA_PrF_2022_006 (*Komplexy přechodných kovů pro medicinské a materiálové aplikace, Studium koordinačních sloučenin vybraných přechodných a vnitřně přechodných kovů I-IV).*

Obsah

Seznam použitých zkratek a symbolů

4OH-benz - 4-hydroxybenzoát
A_{dir} – parametr využívaný k popisu přímé relaxace (Rovnice 18)
AcimOx - acetylmethylimidazol-oximát
AcPyOx - acetylmethylpyridin-oximát
B – indukce magnetického pole
B_q^k – koeficient Stevensova operátoru
C_{Ram} - parametr využívaný k popisu Ramanovy relaxace (Rovnice 19)
C_k – Spin phonon coupling pro k-tý fonon
Chdc - 6,6'-{cyclohexan-1,3,5-diyltris[nitrilo(*E*)methylyliden]}dipyridin-3-karboxamid
COT – cyklooktatetraen
COT'' – 1,4-bis(trimethylsilyl)cyklooktatetraen
Cp* - 1,2,3,4,5-pentamethylcyklopentadienylový anion
Cp^{iPr4} – 1,2,3,4-tetraisopropylcyklopentadienylový anion
Cp^{iPr4Me} – 1-methyl-2,3,4,5-tetraisopropylcyklopentadienylový anion
Cp^{iPr4Et} – 1-ethyl-2,3,4,5-tetraisopropylcyklopentadienylový anion
Cp^{iPr5} – 1,2,3,4,5-pentaisopropylcyklopentadienylový anion
Cp^{ttt} – 1,2,4-tri*terc*butylcyklopentadienylový anion
Cp^{Me4} – 1,2,3,4-tetramethylcyklopentadienylový anion
C_4B^{tPhP} – 1-piperidin-2,3,4,5-tetrafenylborolylový dianion
$\overrightarrow{d_{12}}$ – vektor antisymetrické magnetické výměny
D – axiální parametr štěpení v nulovém magnetickém poli
$\overrightarrow{\overrightarrow{D_{12}}}$ – tenzor anizotropní magnetické výměny
Dtp – 2,5-di-*t*-butyl-3,4-dimethylfosfolylový anion
E – rombický parametr štěpení v nulovém magnetickém poli
E_{dip} – energie dipólové magnetické výměny
g – gyromagnetický faktor
g_J – Landého gyromagnetický faktor
g_L –gyromagnetický faktor pro orbitální moment hybnosti
g_S – gyromagnetický faktor pro spinový moment hybnosti
$g_{x/y/z}$ – složka gyromagnetického faktoru v daném směru
h – Planckova konstanta
ħ – redukovaná Planckova konstanta
hpy - tris(2,2'-bipyrid-6-yl)methanol
H_2hpmp = *R*-4-brom-2-((2-hydroxy-1-fenylethylimino)methyl)fenol
k – Boltzmannova konstanta
J – celkový moment hybnosti
J^{ex} – interakční matice magnetické výměny
J^{iso} – interakční konstanta isotropní magnetické výměny (Rovnice 16)
L – orbitální moment hybnosti
m_k – redukovaná hmotnost pro k-tý fonon
Mn12ac –$[Mn_{12}O_{12}(CH_3COO)_{16}(H_2O)_4)]\cdot 2CH_3COOH\cdot 4H_2O$
Mn30 –$[Mn_{30}O_{24}(OH)_8(O_2CCH_2But)_{32}(H_2O)_2(MeNO_2)_4]$
M_S – projekce spinu
M_{sat} – saturační magnetizace
n – exponent využívaný v popisu Ramanovy relaxace
n_α – populovanost fononu α
N_a – Avogadrovo číslo
$\overrightarrow{n_{12}}$ – vektor spojnice paramagnetických center
neo - neokuproin
$\hat{O}_q^k$ – Stevensův operátor
Pc – ftalocyanin
piv - pivalát
Pn - [1,4-bis(trisisopropylsilyl)pentalen]
PzOx - pyrazoloximát
r – poloměr mezi magnetickými centry
S – spinový moment hybnosti
t – relaxační čas
t_{QTM} – relaxační čas kvantového tunelování
t_{dir} – relaxační čas přímé relaxace
t_{Orb} – relaxační čas Orbachovy relaxace
t_0 – preexponenciální parametr Orbachovy relaxace
T - teplota
T_B – blokovací teplota
THF – tetrahydrofuran
tppm - 6,6',6''-(methoxymethantriyl)tris(2-(1H-pyrazol-1-yl)pyridin)
U/U_{eff} – označení pro energetickou bariéru magnetické anizotropie
V_α – spin-fononová interakce pro fonon α
v_k – vlnočet k-tého fononu
Q_k – normálová souřadnice pro k-tý fonon
W_{ba} – Maticový element rychlosti přechodu mezi hladinami a a b pro výpočet relaxačního času
χ' – reálná složka magnetické susceptibility (Rovnice 37)
χ'' – imaginární složka magnetické susceptibility (Rovnice 38)
χ_T – izotermická magnetické susceptibilita (Rovnice 37 a 38)
χ_S – adiabatická magnetické susceptibilita (Rovnice 37 a 38)
Δ_α – šířka spektrální čáry fononu α
δ – Diracova delta funkce
μ_B – Bohrův magneton
μ_{eff} – efektivní magnetický moment
$\overrightarrow{\mu_1}$- vektor magnetického momentu
λ – spin-orbitální konstanta
σ – orbitální redukce
τ – čas
ω_α – úhlová rychlost fononu α
ω – úhlová rychlost
ρ_j – hustota stavů
γ – maticové elementy pro výpočet rychlosti relaxace magnetizace

Seznam obrázků a tabulek

Seznam publikací a konferenčních příspěvků

Publikace v odborných časopisech:

1 **Kotrle, K.**; Herchel, R. Are Inorganic Single-Molecule Magnets a Possibility? A Theoretical Insight into Dysprosium Double-Deckers with Inorganic Ring Systems. *Inorg. Chem.* **2019**, *58* (20), 14046–14057. https://doi.org/10.1021/acs.inorgchem.9b02039. Článek je citován v 19 publikacích (Web of Science, ke dni 29. 11. 2023).

2 **Kotrle, K.**; Atanasov, M.; Neese, F.; Herchel, R. Theoretical Magnetic Relaxation and Spin–Phonon Coupling Study in a Series of Molecular Engineering Designed Bridged Dysprosocenium Analogues. *Inorg. Chem.* **2023**, *62* (42), 17499–17509. https://doi.org/10.1021/acs.inorgchem.3c02916. Článek dosud nebyl citován (Web of Science, ke dni 29. 11. 2023).

3 **Kotrle, K.**; Nemec, I.; Moncol, J.; Čižmár, E.; Herchel, R. 3d–4f Magnetic Exchange Interactions and Anisotropy in a Series of Heterobimetallic Vanadium(IV)–Lanthanide(III) Schiff Base Complexes. *Dalton Trans.* **2021**, *50* (39), 13883–13893. https://doi.org/10.1039/D1DT01944A. Článek je citován v 6 publikacích (Web of Science, ke dni 29. 11. 2023)

4 **Kotrle, K.**; Nemec, I.; Antal, P.; Petrželová, K.; Čižmár, E.; Herchel, R. 2-Formylphenoxyacetic Acid Schiff Bases: A Promising Ligand Scaffold for Readily Available Trigonal Prismatic Co(II) Single-Ion Magnets. *Inorg. Chem. Front.* **2023**, *10* (24), 7319–7332. https://doi.org/10.1039/D3QI01691A. Článek dosud nebyl citován (Web of Science, ke dni 29. 11. 2023).

5 Bhanja, A.; Smythe, L.; **Kotrle, K.**; Ortu, F.; Herchel, R.; Murrie, M.; Ray, D. Synthesis of Heptanuclear Ni4Dy3 Coordination Aggregate Using Tridentate Ligand: X-Ray Structure, Magnetism and Theoretical Studies. *Inorganica Chim. Acta* **2021**, *526*, 120524. https://doi.org/10.1016/j.ica.2021.120524. Článek dosud nebyl citován (Web of Science, ke dni 29. 11. 2023).

6 Dutta, B.; Guizouarn, T.; Pointillart, F.; **Kotrle, K.**; Herchel, R.; Ray, D. Lanthanoid Coordination Prompts Unusually Distorted Pseudo-Octahedral Ni^{II} Coordination in Heterodinuclear Ni–Ln Complexes: Synthesis, Structure and Understanding of Magnetic Behaviour through Experiment and Computation. *Dalton Trans.* **2023**, *52* (30), 10402–10414. https://doi.org/10.1039/D3DT01387A. Článek je citován v 1 publikaci (Web of Science, ke dni 29. 11. 2023).

Příspěvky na konferencích:

1. **Kotrle, K.**; Herchel, R. Theoretical Insight Into Single-Molecule Magnets With Inorganic Rings. In: Luptáková, I. D.; Beňo, M. The 7th International Scientific Conference Applied Natural Sciences 2019 Book of Abstracts. University of SS. Cyril and Methodius in Trnava. 1st edition, 2019, 113. ISBN: 978-80-572-0011-6
2. **Kotrle, K.**; Herchel, R.; Atanasov, M. Theoretical Predictions of single-molecule magnetism in rigid lanthanide organometallics. (poster) The Joint European Magnetic Symposia 2020.

3. **Kotrle, K.**; Nemec, I.; Moncol, J.; Čižmár, E.; Herchel, R. Exchange interactions and anisotropy in V(IV)-Ln(III) complexes (poster), ECMM 2022 - 8th European Conference on Molecular Magnetism
4. **Kotrle, K.**; Nemec, I.; Čižmár, I.; Antal, P.; Herchel, R. Kobaltnaté komplexy ve tvaru trigonální prizmy: Cesta k lepší magnetické anizotropii? In: Vyskočil, V. Czech Chemical Society Symposiums Series 20 (4), 74. sjezd českých a slovenských chemických společností, 2022, 211, ISSN 2336-7202
5. **Kotrle, K.**; Nemec, I.; Herchel, R. Studium magnetických výměnných interakcí a anizotropie u heterobimetalických komplexů lanthanoidů. In: Pinkas, J. Czech Chemical Society Symposiums Series 21 (3), 4. konference Pokroky anorganické chemie PANCH 2023, 141, ISSN 2336-7210

Zahraniční stáž:

09/2020-02/2021 – Max-Planck-Institut für Kohlenforschung, Molecular Theory and Spectroscopy group (prof. Dr. Frank Neese), Mülheim an der Ruhr, Německo

Zapojení do projektů:

Projekt Doktorské studentské grantové soutěže DSGC-2021-0032, 1. 1. 2022 – 31. 12. 2022, *Towards Zero-Field Co(II) Single Ion Magnets*, člen řešitelského týmu

Projekt Podpora mobility na UP II. CZ.02.2.69/0.0/0.0/18_053/0016919, 1. 9. 2020 – 31. 8. 2021

Projekt GAČR 23-07175S, 1. 1. 2023 – 31. 12. 2025, *Semikoordinace: cesta k chemicky stabilním molekulárním nanomagnetům:* člen řešitelského týmu

Projekty studentské grantové soutěže UP:

IGA_PrF_2018_011 – 1.3. 2018 – 28.2. 2019, *Komplexy přechodných kovů pro medicinské a materiálové aplikace:* člen řešitelského týmu

IGA_PrF_2019_009 - 1.3. 2019 – 28.2. 2020, *Studium koordinačních sloučenin vybraných přechodných a vnitřně přechodných kovů:* člen řešitelského týmu

IGA_PrF_2020_016 - 1.3. 2020 – 28.2. 2021, *Studium koordinačních sloučenin vybraných přechodných a vnitřně přechodných kovů II:* člen řešitelského týmu

IGA_PrF_2021_009 - 1.3. 2021 – 28.2. 2022, *Studium koordinačních sloučenin vybraných přechodných a vnitřně přechodných kovů III:* člen řešitelského týmu

IGA_PrF_2022_006 - 1.3. 2022 – 28.2. 2023, *Studium koordinačních sloučenin vybraných přechodných a vnitřně přechodných kovů IV:* člen řešitelského týmu

Abstract

The central theme of this dissertation thesis is single-molecule magnetism, an effect that induces the slow relaxation of molecules. This phenomenon is not rooted in magnetic exchange interactions but rather in a molecular property known as magnetic anisotropy. The primary focus of the field of single-molecular magnetism is to retain this ability at elevated temperatures. Various approaches have been employed to develop new single-molecule magnets and gain further insights into their properties and behaviour in order to create ones that are more efficient.

A significant portion of the dissertation is devoted to the theoretical investigation of dysprosium double-decker complexes, emphasizing their energetic structure and vibrational properties. The examination includes the quantification of spin-phonon coupling. Two series of complexes were studied: the first involving inorganic analogues of cyclopentadienyl, and the second incorporating cyclopentadienyl ligands connected with butylene linkers. In both series, the objective was to identify crucial vibrations that facilitate the transfer of energy for magnetization relaxation. The findings highlight the possibilities for improving single-molecule magnets through structural modifications.

Another segment focuses on exploring magnetic exchange interactions in 3d-4f systems and demonstrating how these interactions influence magnetic anisotropy. The investigation assesses whether controlling the exchange interactions in salen-type ligand 3d-4f systems can lead to the development of better single-molecule magnets. Our contribution to the field involves the synthesis and characterization of a series of V^{IV}-Ln^{III} complexes, scrutinized through both theoretical and experimental methods.

Part of this dissertation thesis is dedicated to manipulating the coordination environment geometry of Co^{II}, targeting the preparation of a trigonal prismatic shape. A series of complexes with this shape was synthetized, revealing intriguing magnetic properties. Notably, one complex exhibited single-molecule magnet behavior even in a zero magnetic field.

The thesis also encompasses collaborations on theoretical characterizations in two articles related to 3d-4f systems. The first article discusses a large Ni4Dy3 cluster, while the second focuses on a series of Ni-Ln complexes with Schiff base ligands.

1. Úvod a cíle práce

Tato disertační práce je věnována tématice jedno-molekulového magnetismu, tedy jevu, kdy molekuly vykazují schopnost pomalé magnetické relaxace. Technologické možnosti, které by lidstvu dalo ovládnutí tohoto jevu, jsou velké. Dalo by se očekávat velké zlepšení kapacity magnetických paměťových médií, další možnosti miniaturizace elektroniky nebo například i rozvoj v oblasti spintroniky a kvantových počítačů. Největší překážky na této cestě představují příliš nízké blokovací teploty a nevhodné chemické vlastnosti (například nízká stabilita) u potenciálně zajímavých materiálů. Přestože v posledních letech došlo k poměrně dynamickému rozvoji tohoto oboru, je zde ještě mnoho otázek, které čekají na zodpovězení.

Celkovým jednotícím tématem disertační práce je výzkum možností, jak lze zlepšit jedno-molekulové magnety pomocí manipulace jejich struktury. Tento problém řeší z mnoha pohledů, v práci je zahrnuta syntetická práce v laboratoři, provádění experimentů pomocí fyzikálně-chemických technik a jejich následné vyhodnocování a také výpočetní a teoretické studium připravených nebo i designovaných molekul. Podobně je z mnoha úhlů pohlíženo i na možnosti, jakými je možné vlastnosti studovaných látek ovlivňovat, zkoumán byl systematický vliv strukturních modifikací, záměny donorových atomů nebo změny funkčních skupin s cílem ovlivňovat deformaci výsledného komplexu nebo sledovat vliv magnetických výměnných interakcí na vlastnosti látek.

Cílem této práce bylo rozšířit poznatky o vztahu struktury a magnetických vlastností a připravit nebo případně ukázat cestu k potenciálně lepším jedno-molekulovým magnetům co se týče jejich energetických bariér, blokovacích teplot nebo relaxačních časů. Konkrétně je práce zaměřená na jedno-molekulové magnety z oblasti jednojaderných 3d a 4f a vícejaderných 3d-4f komplexů, zejména na komplexy obsahující kobalt, dysprosium, terbium a erbium jako paramagnetická centra s významnou magnetickou anizotropií. Teoretická část práce si tedy klade za cíl představit a popsat základy jedno-molekulového magnetismu a metod jeho studia v rozsahu, který odpovídá zaměření a obsahu tématiky prováděného výzkumu. Provedená literární rešerše se zaměřila na porovnání již známých systémů příbuzných těm, které byly v disertační práci studovány. Praktická část práce shrnuje nově dosažené poznatky. Formou komentáře jsou stručně představeny výsledky dosažené při řešení tématu, které byly publikovány v impaktovaných odborných časopisech. Jednotlivé časopisecké publikace jsou následně uvedeny v kompletní podobě jako přílohy k disertační práci.

2. Teoretická část

2.1 Úvod do jedno-molekulového magnetismu

Jedno-molekulový magnetismus je jev, který byl poprvé pozorován v roce 1991 u komplexu $[Mn_{12}O_{12}(CH_3COO)_{16}(H_2O)_4)]\cdot 2CH_3COOH\cdot 4H_2O$ označovaného zkratkou *Mn12ac*.[1] (Obrázek 1) U tohoto komplexu byly při měření magnetické susceptibility ve střídavém poli pozorovány vlastnosti, jako pomalá relaxace magnetizace a magnetická hystereze, které jsou obvykle typické pro makroskopické magnetické materiály. Komplex *Mn12ac* se ukázal jako mimořádný právě tím, že tyto vlastnosti mají čistě molekulový původ a nejsou důsledkem kooperativních jevů paramagnetických center.[2]

Jako základní parametry, pomocí kterých lze jedno-molekulové magnety charakterizovat, se běžně uvádí anizotropní energetická bariéra (U_{eff}), což je energie, nutná k tomu, aby systém změnil orientaci magnetického momentu, což odpovídá přechodu z magnetického stavu $M_S = +S$ do stavu $M_S = -S$ nebo naopak. Další významnou charakteristikou je pak blokovací teplota (T_B), která má několik možností definice, ale u jedno-molekulových magnetů je blokovací teplota nejčastěji definována jako teplota, při které je relaxační čas systému rovný 100 s.[3]

Ačkoliv je *Mn12ac* poměrně velký systém, brzy bylo objeveno, že klíčovou vlastností jedno-molekulového magnetu není celkový spin systému, ale jeho magnetická anizotropie,[4] neboť bylo připraveno množství dalších velkých vícejaderných systémů manganu, jako například *Mn30*[5] ($[Mn_{30}O_{24}(OH)_8(O_2CCH_2But)_{32}(H_2O)_2(MeNO_2)_4]$), které ale nedosahovaly lepších vlastností než *Mn12ac*. Toto vedlo ke studiu takzvaných jedno-iontových magnetů, tedy jednojaderných systémů, které mají ale velmi silnou anizotropii, která jim umožňuje dosahovat velmi dobrých vlastností. Jedním z prvních významných zástupců byl komplex $[TbPc_2]^-$, který také poukázal na vlastnosti lanthanoidů, které v mnoha důležitých aspektech předčily komplexy d-prvků.[6]

Po tomto objevu se začal výzkum jedno-molekulových magnetů soustředit mnohem více na sloučeniny lanthanoidů, zejména terbia a dysprosia, které se ukázaly jako prvky s největším potenciálem. Zatímco doposud byly všechny zmiňované a v té době známé jedno-molekulové magnety s blokovacími teploty nižšími než 10 K, v roce 2011 byl objeven dimerní komplex $\{[(Me_3Si)_2N]_2(THF)Tb\}_2(\mu\text{-}\eta^2\text{:}\eta^2\text{-}N_2)^-$, který nejen že byl velmi zajímavý z chemického hlediska,

neboť se jedná o vícejaderný komplex můstkovaný pomocí radikálu, ale také dosáhl blokovací teploty 14 K.[7]

Tato blokovací teplota byla po poměrně dlouhou dobu nepřekonaná. Podařilo se ji překonat až s rozvojem teoretických základů jedno-molekulového magnetismu, kdy bylo předpovězeno, že specificky u komplexů dysprosia je možné dosáhnout vysokých energetických bariér v geometriích, které mají axiální charakter.[8] Na základě tohoto pravidla bylo vyvinuto několik komplexů ve tvaru pentagonální bipyramidy dosahujících rekordních energetických bariér, které překonaly hranici 1000 K, a jejichž blokovací teploty dosahovaly až ke 20 K.[9]

Podobná myšlenka byla na počátku další, zatím poslední významné a úspěšné skupiny jedno-molekulových magnetů, organokovových sendvičových komplexů dysprosia $[Dy(Cp^{ttt})_2]^+$ (Obrázek 1) a $[Dy(Cp^{iPr5})(Cp^*)]^+$. [10] Tyto komplexy mají energetické bariéry srovnatelné s výše zmiňovanými pentagonálními bipyramidami, avšak jejich blokovací teploty jsou mnohem vyšší – dosahují až 80 K, což už je nad bodem varu dusíku, a jedná se tedy o velký krok směrem k možným praktickým aplikacím. Problémem těchto látek je ovšem jejich citlivost na vzduch a vodu.

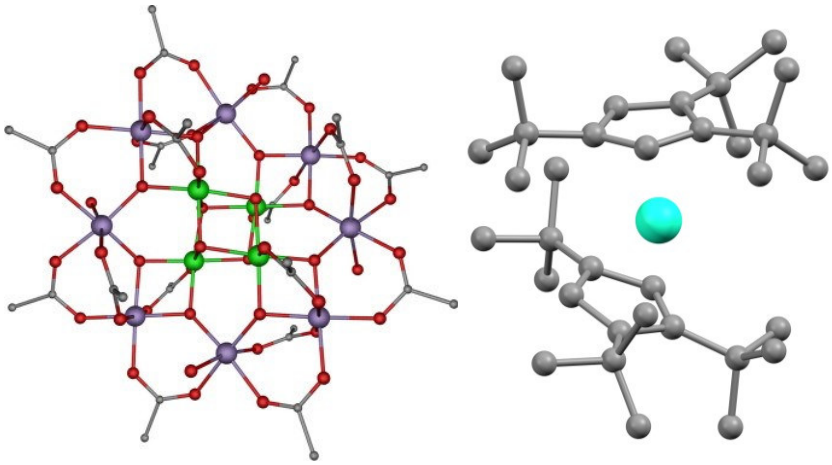

Obrázek 1: Struktura komplexu Mn12ac, vodíkové atomy a solventy nejsou zobrazeny, atomy Mn jsou označeny fialovou (Mn^{III}) a zelenou (Mn^{IV}) barvou (vlevo).[11] Struktura komplexu $[Dy(Cp^{ttt})_2][B(C_6F_5)_4]$ (vpravo)[10]

Získávání nových poznatků při výzkumu jedno-molekulových magnetů je jednak realizováno pomocí popisu vlastností nově připravených systémů. Neméně důležité je ovšem také teoretické studium relaxačních dějů, které nám umožňuje odpovědět na otázky, jestli lze najít

ještě výhodnější molekulové struktury nebo jak přesně spolu souvisí blokovací teplota a energetická bariéra.

2.2 Elektronová struktura kovových iontů a její vztah k magnetismu

Z chemického pohledu jsou jedno-molekulové magnety většinou komplexy kovů patřících mezi d- a f- prvky, nejčastěji jde o Co, Dy a Tb vzhledem k jejich vhodné elektronové konfiguraci v běžných oxidačních stavech. Přestože je zřejmé, že ligandy a celková struktura komplexů má na jejich magnetické vlastnosti velký vliv, tento vztah je natolik komplexní, že ještě stále nejsou známy zcela uspokojivé magneto-strukturní korelace.

Co se týče 3d-prvků, jejich elektronovou strukturu lze popsat jednodušeji, než u těžších d-prvků a f-prvků, a tudíž jsou jejich vlastnosti lépe probádané. Obecně je za štěpení elektronových hladin odpovědná elektron-elektronová repulze, štěpení v ligandovém poli a spin-orbitální interakce (Obrázek 3). U 3d prvků je v mnoha případech možné díky jejich nízkému příspěvku spin-orbitální interakce, který je obvykle menší než působení ligandového pole a elektronové repulze, použít model spinového hamiltoniánu využívajícího projekce spinu (S, M_S), který je ve většině případů aproximací s přijatelnou shodou s realitou.

Teoretickou hodnotu magnetického momentu je možné pro 3d-prvky vypočítat pomocí následujícího vztahu:

$$\frac{\mu_{\mathrm{eff}}}{\mu_{\mathrm{B}}} = g\sqrt{S(S+1)} \qquad (1)$$

Kde g je g-faktor, který je obecně blízký hodnotě elektronu, tedy přibližně $g = 2$, ale může nabývat i jiných hodnot v důsledku jevů, jako jsou například spin-orbitální interakce nebo Jahn-Tellerův efekt.

Pro jedno-molekulový magnetismus je jeho zásadní složkou kromě vlivu ligandového pole zejména štěpení v nulovém magnetickém poli (zero-field splitting), což je jev, kdy dochází ke štěpení energetických hladin vlivem vzájemné interakce více nepárových elektronů v iontu. Toto štěpení je přítomné pouze u iontů, které mají celkový spinový moment větší než $S = 1/2$. V jeho zjednodušené formě lze štěpení v nulovém magnetickém poli zapsat pomocí tohoto hamiltoniánu:[12]

$$\hat{H} = \hat{S} \cdot \overline{\overline{D}} \cdot \hat{S} + \mu_{\mathrm{B}} g B S \qquad (2)$$

který se skládá ze dvou členů, první z nich popisuje štěpení energetických hladin v nulovém magnetickém poli (zero-field splitting), druhý pak štěpení v magnetickém poli (Zeemanův jev). V praxi se obvykle používá zjednodušené formy tohoto operátoru:[13]

$$\widehat{H} = D\left(\hat{S}_z^2 - \frac{1}{3}\hat{S}^2\right) + E\left(\hat{S}_x^2 - \hat{S}_y^2\right) + \mu_B g B S \tag{3}$$

V tomto tvaru hamiltoniánu se pak vyskytují parametry *D* a *E* označované jako axiální a rombický parametr. Při působení tímto operátorem následně získáme rozložení hladin (± *S*, ± (*S*-1), …, až po hladinu *S* = 0 pro ionty s celočíselným spinem a *S* = ±1/2 pro ionty s neceločíselným spinem), kde energetické rozdíly mezi hladinami budou ve vztahu k parametrům *D* a *E* (Obrázek 2). Tím, jak štěpení v nulovém magnetickém poli ovlivňuje energetické hladiny (pro ionty s poločíselným spinem nazývané Kramersovy dublety), je axiální parametr *D* v přímém vztahu s anizotropní energetickou bariérou:

$$U_{\text{eff}} = |D|S^2 \tag{4}$$

$$U_{\text{eff}} = |D|S^2 - 1/4 \tag{5}$$

kde vztah (4) platí pro ionty s celočíselným spinem a (5) pro ionty s poločíselným spinem.

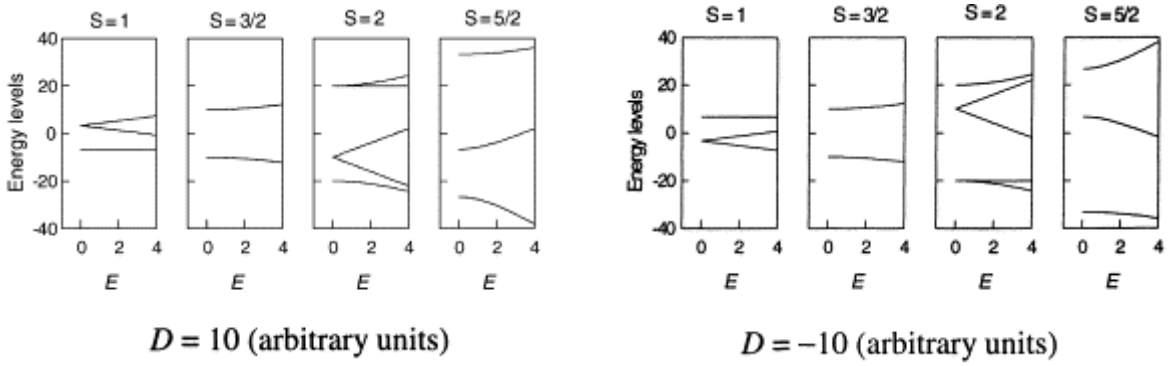

Obrázek 2: Efekt štěpení v nulovém magnetickém poli na energetické hladiny iontů s různým spinem[14]

Parametry *D* a *E* jsou ve velké míře závislé na štěpení v ligandovém poli a silně je ovlivňuje tvar koordinačního polyedru.

U těžších d-prvků a lanthanoidů je situace komplikovaná tím, že jejich spin-orbitální interakce jsou větší než efekt štěpení v ligandovém poli. Na popis tohoto jevu existují dva modely, které se liší tím, jaký prvek interakce v kovovém iontu je dominantní (Obrázek 3). Pokud je to elektronová repulze, používáme LS model, pokud je dominantní spin-orbitální interakce, je vhodnější použít JM model.[15]

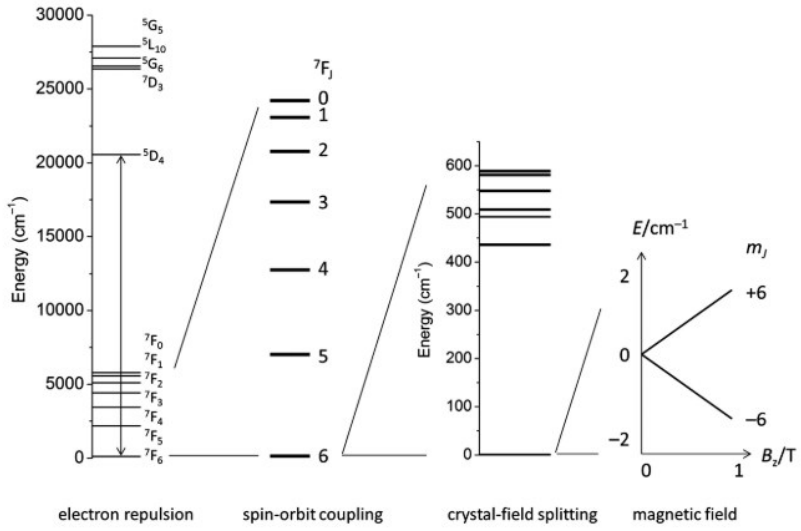

Obrázek 3: Elektronové interakce v atomu Tb^{III} s vyznačenými jednotlivými interakcemi, jejichž vlivem dochází ke štěpení hladin, jako ilustrace pro řádovou velikost energetických rozdílů mezi hladinami.[16]

U JM modelu se spin-orbitální interakce vkládá do modelu pomocí sloučení orbitálního momentu hybnosti *L* a spinového momentu hybnosti *S* do celkového momentu hybnosti *J*. Maximální hodnota celkového momentu hybnosti *J* je definována jako:[17]

$$J = L + S$$

J může nabývat hodnot (*J*, *J*-1,…,-*J*). Základní stav iontu je určen na základě obsazení jeho f-orbitalů. U iontů s obsazením nižším než polovičním je základní stav definován jako $J = |L\text{-}S|$, u iontů s nadpolovičním obsazením jako $J = L+S$. U iontů s polovičním obsazením, například Gd^{3+}, je příspěvek spin-orbitální interakce zanedbatelný, neboť jejich orbitální moment *L* je pro jejich základní term roven 0, a popisují se pouze pomocí spinového momentu hybnosti.

Pro výpočet hodnoty magnetického momentu pomocí celkového momentu hybnosti *J* je definován Landého *g*-faktor jako konstanta:

$$g_J = \frac{3}{2}\frac{S(S+1)-L(L+1)}{2J(J+1)} \quad (6)$$

LS model používá při popisu iontu orbitální moment *L* a spinový model *S* a k popisu spin orbitální interakce využívá zvláštní člen ve spinovém hamiltoniánu:[18]

$$\hat{H}^{\mathrm{SOC}} = \sum_{j=1}^{2S} \lambda_j \left(\sigma \vec{L}\vec{S}\right)^j \quad (7)$$

Kde λ je spin-orbitální konstanta *j*-tého řádu a σ je parametr orbitální redukce.

Pro tento model se jako *g*-faktory většinou v praxi používají $g_L = 1$ a $g_S = 2$.

Při výpočtu teoretických magnetických momentů pro lanthanoidy se většinou užívá pro tyto účely jednoduššího JM modelu, kde platí následující vztah: [19]

$$\frac{\mu_{\text{eff}}}{\mu_{\text{B}}} = g_j\sqrt{J(J+1)} \tag{8}$$

Ale je odvozen i vztah pro LS model:[20]

$$\frac{\mu_{\text{eff}}}{\mu_{\text{B}}} = \sqrt{g_L^2 L(L+1) + g_S^2 S(S+1)} \tag{9}$$

Protože mají lanthanoidy oproti spin-orbitálním interakcím jen malou energii štěpení v ligandovém poli, je jejich limitní hodnota magnetického momentu prakticky nezávislá na koordinační sféře, a tedy z jeho hodnoty, na rozdíl od d-prvků, není možné získat prakticky žádné informace například o tvaru koordinační sféry.

Analogicky jako pro d-prvky je pak pro lanthanoidy platný Curieho zákon v následující formě:

$$\chi = \frac{N_a \mu_B^2 g_J^2}{3kT} J(J+1) \tag{10}$$

2.3 Štěpení v ligandovém poli

Jako štěpení v ligandovém poli se nazývá interakce mezi náboji elektronových párů ligandu a elektronů v orbitalech centrálního atomu, jejímž vlivem je odstraněna degenerace d- nebo f-orbitalu (Obrázek 4). Je běžně uplatňována u d-prvků, kde v případě 3d-prvků tvoří dominantní interakci, která způsobuje štěpení základního termu, vzhledem k nízké síle spin-orbitálních interakcí. Pro d-orbital je popsáno, jak se d-orbitaly štěpí v běžných symetriích, kterých geometrie chromoforu dosahuje. Dále je popsáno, jaký vliv mají různé ligandy na štěpení ligandového pole a jak jsou na základě toho rozděleny komplexy na vysokospinové (high spin) a nízkospinové (low spin), podle uspořádání jejich elektronů závislém na energetickém rozložení d-orbitalů.

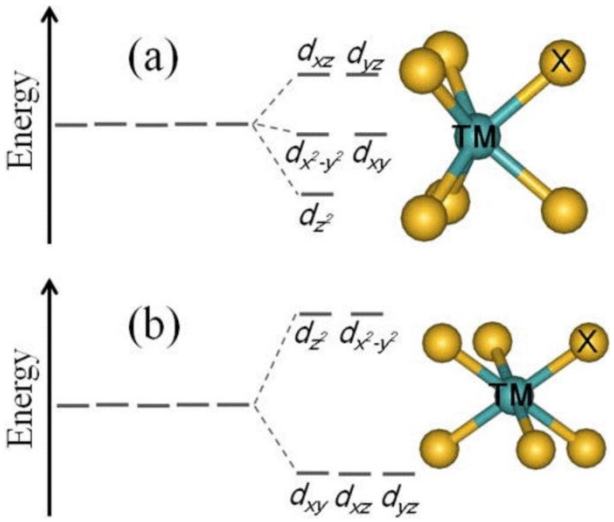

Obrázek 4: Ukázka štěpení d-orbitalů pro trigonální prizma (a) a oktaedr (b).[21]

Situace je komplikovanější v případě f-orbitalů, kde je vliv štěpení v ligandovém poli malý oproti spin-orbitální interakci, a modely používané pro 3d kovy zde nejsou užitečné. Přesto je potřeba vliv ligandového pole popsat, neboť je to druh štěpení, který je na rozdíl od spin-orbitální interakce a elektronové repulze vyvolaný okolím kovového iontu. Pro tento účel se používá člen hamiltoniánu, který se vyjadřuje ve formě Stevensových operátorů:[22]

$$\hat{H} = \sum_{k=2,4,6} \sum_{q=-k}^{k} B_k^q \hat{O}_k^q \tag{11}$$

kde se tyto operátory značí jako $\hat{O}$, *B* pak je koeficient, který může nabývat různých hodnot v závislosti na studovaném systému. Pod označením *k* a *q* jsou řády operátoru, *k* nabývá hodnot kladných sudých čísel, často se používá do řádu 6, ale někdy i do vyšších řádů. Řád *q* pak nabývá hodnot od *-k* do *+k*.

Přestože jsou Stevensovy operátory popisovány jako nástroj k popisu štěpení v krystalovém poli, mají mimo jiné také úzký vztah s parametry štěpení v nulovém magnetickém poli:

$$D = 3B_2^0 \tag{12}$$

$$E = B_2^2 \tag{13}$$

čehož lze využít například při analýze magnetických dat.

2.4 Vícejaderné komplexy

V případě, že se více paramagnetických center nachází dostatečně blízko u sebe, dochází u nich k vzájemné interakci, která se projevuje dalším štěpením magnetických hladin. Této interakci se říká magnetická výměnná interakce. Skládá se ze dvou částí; první z nich je dipól-dipólová interakce, která se šíří skrz prostor mezi centry. Lze ji kvantifikovat pomocí následujícího vztahu:[23]

$$E_{\mathrm{dip}} = \frac{\mu_{\mathrm{B}}^2}{r^3}[\vec{\mu}_1 \cdot \vec{\mu}_2 - 3 \cdot (\vec{\mu}_1 \cdot \vec{n}_{12}) \cdot (\vec{\mu}_2 \cdot \vec{n}_{12})] \tag{14}$$

kde μ jsou vektory magnetických momentů, *n* vektor jejich spojnice a *r* jejich vzdálenost.

Druhou složkou výměnné interakce pak je takzvaná supervýměna, která je způsobena orientací spinové hustoty ve vazebných orbitalech a přenáší se prostřednictvím chemických vazeb, například na ligandech.

Efekt štěpení hladin prostřednictvím výměnných interakcí se popisuje pomocí členu ve spinovém hamiltoniánu:

$$\hat{H}_{\mathrm{ex}} = \hat{S}_1 \cdot J_{12}^{\mathrm{ex}} \cdot \hat{S}_2 \tag{15}$$

který obecně popisuje interakci v mnohojaderném systému mezi každým párem paramagnetických center, kde je interakce vyjádřena pomocí tenzoru J^{ex}. Po úpravě lze vztah vyjádřit takto: [3]

$$\hat{H}_{\mathrm{ex}} = -J_{12}^{\mathbf{iso}} \cdot S_1 \cdot S_2 + S_1 \cdot \overline{\overline{D}}_{12} \cdot S_2 + \vec{d}_{12} \cdot (S_1 \times S_2) \tag{16}$$

kde první člen je izotropní výměna, která dává informaci o tom, o jaký typ výměny se jedná. V nejjednodušším případě, kdy máme dvoujaderný systém, kde obě centra mají $S_1 = S_2 = ½$, pak dojde k tomu, že celkový spin systému bude mít dva možné stavy – $S = S_1+S_2 = 1$ a $S = S_1-S_2 = 0$. Energetický rozdíl mezi těmito stavy pak bude roven interakční konstantě J^{iso}, pokud bude základní stav $S = 1$ (když J^{iso} bude kladné), mluvíme o feromagnetické výměnné interakci, pokud bude $S = 0$ (záporné J^{iso}), jedná se o antiferomagnetickou výměnnou interakci. (Obrázek 5).

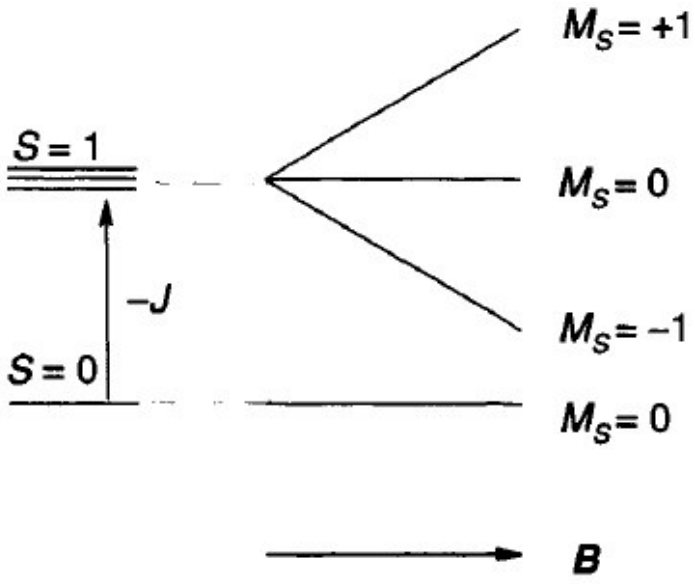

Obrázek 5: Ilustrace energetických hladin u systému $S_1 = S_2 = ½$, které jsou štěpeny výměnnou interakcí J^{iso}, ve vyobrazeném případě je J^{iso} záporná a výměnná interakce antiferomagnetická.[24]

Druhý člen je takzvaná anizotropní výměna a je definován tenzorem $\overline{\overline{D}}_{12}$, který rozhoduje o orientaci výsledného magnetického momentu páru v prostoru. Třetí člen je pak antisymetrická výměna, jejíž působení se sčítá s izotropní výměnou a může způsobit vychýlení magnetických momentů od ideálně paralelních směrů.

U magnetické výměnné interakce se často uplatňuje přístup, kdy se ostatní členy mimo izotropní výměnu zanedbávají. Tento jednoduchý a přitom většinou dostačující způsob popisu výměnné interakce je výhodný například i pro větší systémy, kde exponenciálně narůstá počet energetických hladin s vyšším počtem magnetických center.

Výše uvedené modely magnetické výměnné interakce používají jako charakteristiku paramagnetických center spin. Toto je ovšem problémem u lanthanoidů, jak už bylo zmíněno v předchozích kapitolách, protože jejich silná spin-orbitální interakce způsobuje velkou odchylku od čistě spinového modelu a lepší metody popisu magnetické výměnné interakce zatím nejsou pro lanthanoidy uspokojivě vyvinuty. Pro tyto účely se u lanthanoidů používá Linesův model.[25] Tento model využívá pro každý Kramersův dublet nahrazení *J* za pseudospin *S* = ½, který se vynásobí příslušným koeficientem, aby dosáhl magnetického momentu

v souladu s teorií. Jako korekci na příspěvek vyšších hladin v důsledku její teplotní populace má každý dublet přiřazen teplotně závislý ekvivalent *g*-faktoru.

2.5 Relaxační procesy

Jako magnetická relaxace se obecně označuje přechod materiálu do rovnovážného stavu, obvykle ze stavu orientovaného vlivem magnetického pole do rovnovážného stavu v nulovém poli. Čas, během kterého je této rovnováhy dosaženo, se označuje jako relaxační čas a je jednou z nejdůležitějších charakteristik u jedno-molekulových magnetů. Z mikroskopického hlediska relaxace magnetizace úzce souvisí s energetickou bariérou, neboť ona je tím, co spontánní relaxaci brání. K jejímu překonání může dojít několika způsoby.

První z relaxačních mechanismů je zajímavý tím, že nevyžaduje žádný přenos energie. Je jím kvantové tunelování magnetizace, tedy jev, který má svůj původ v kvantové povaze atomů. Je zajímavé, že jedno-molekulové magnety jsou fyzikálními systémy, kde je možné kvantové jevy poměrně snadno pozorovat. Jsou patrné například na hysterezních křivkách některých jedno-molekulových magnetů, kde tvoří „schody“ (Obrázek 6).[26]

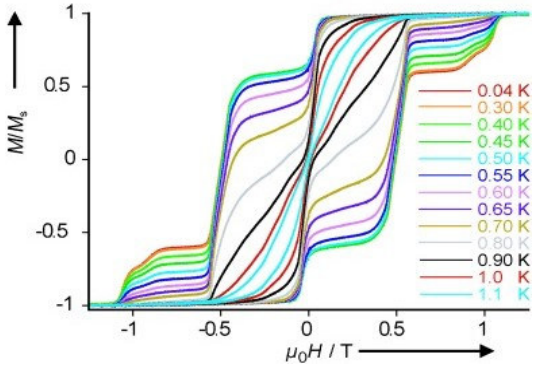

Obrázek 6: Hysterezní křivky jedno-molekulového magnetu $Na_6(C_4H_{12}N)_4[Fe_4(H_2O)_2(FeW_9O_{34})_2] \cdot 45\ H_2O$ s patrnou přítomností kvantového tunelování magnetizace v podobě průběhu křivky ve tvaru „schodů“.

Problematika tunelování je poměrně komplikovaná. Je známo, že je nutné, aby stavy, mezi kterými k tunelování dochází, byly téměř degenerované. Tento předpoklad je spojen také s metodou, jakou je tunelování běžně potlačováno při provádění experimentů, tedy měřením v magnetickém poli, které degeneraci odstraní prostřednictvím Zeemanova jevu (Obrázek 7). Tímto způsobem se magnety dělí na „zero-field“ magnety, tedy ty, které vykazují pomalou relaxaci i bez magnetického pole, a „field-induced“, které bez magnetického pole relaxují

rychle prostřednictvím tunelování v základním stavu, avšak při zapnutém magnetickém poli se u nich relaxace objevuje.

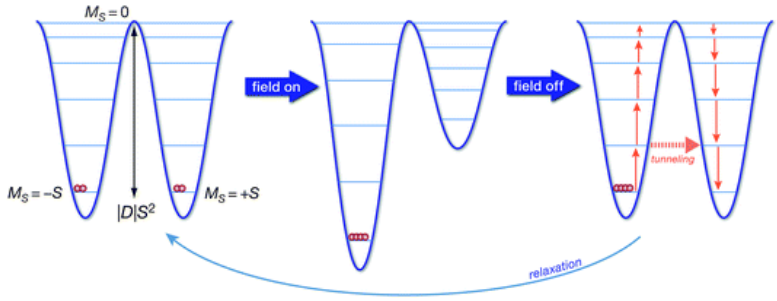

Obrázek 7: Ilustrace kvantového tunelování magnetizace v anizotropní energetické bariéře[27]

Na druhou stranu ovšem, oproti této zažité představě, je situace komplikovaná v tom, že pokud by dvě hladiny ležící na opačných stranách bariéry byly opravdu degenerované, k tunelování by docházet nemohlo.[28] Ovšem v reálných systémech hladiny nejsou degenerované kvůli Zeemanovu efektu z velmi malého, ale pro účely teorie prakticky všudypřítomného magnetického pole, které se dá přičíst například molekulovému poli ze sousedních molekul. Pro takový případ pak byl odvozen následující vztah, který umožňuje predikce kvantového tunelování z velikosti složek *g*-tenzoru:

$$t_{\mathrm{QTM}}^{-1} = \frac{\mu_{\mathrm{B}} B}{h} \frac{(g_x^2+g_y^2)}{2\sqrt{(g_x^2+g_y^2)+g_z^2}} \tag{17}$$

kde *B* je velikost indukce? magnetického pole. Z tohoto vztahu byly úspěšně předpovězeny velikosti energetických bariér pro jedno-molekulové magnety za předpokladu, že se vychází z velikosti složek *g*-faktoru pro každý Kramersův dublet zvlášť.

Na závěr je nutné zmínit, že tunelování neprobíhá pouze v základním stavu, ale v každém z Kramersových dubletů a v každém různou rychlostí. Někdy se proto také odděluje jako různé relaxační děje tunelování v základním stavu a termicky asistované tunelování, tedy relaxace po excitaci do vyššího Kramersova dubletu. Co se týče designu molekul pro potlačení tunelování, z výše uvedeného vztahu je zřejmé, že záleží na velikosti *g*-tenzoru. Konkrétně tunelování často koreluje s velikostí rombických složek g_{xy}, je tedy nutné připravovat systémy s co největší axiální anizotropií pro potlačení kvantového tunelování.

Všechny ostatní základní relaxační mechanismy pak vyžadují přenos energie, který je v pevných látkách přenášen pomocí takzvaných fononů, což jsou vibrace krystalové mřížky,

kterým je pro přenos energie mezi atomy přiřazena fiktivní pseudočástice. Existují dva druhy vibrací mřížky, kterým se říká akustické a optické fonony. První vibrují pomocí zkracování a prodlužování vzdáleností mezi molekulami, a tím připomínají zvukové vlny. Optické fonony jsou podobné molekulovým vibracím, které se šíří skrz celý krystal (Obrázek 8).

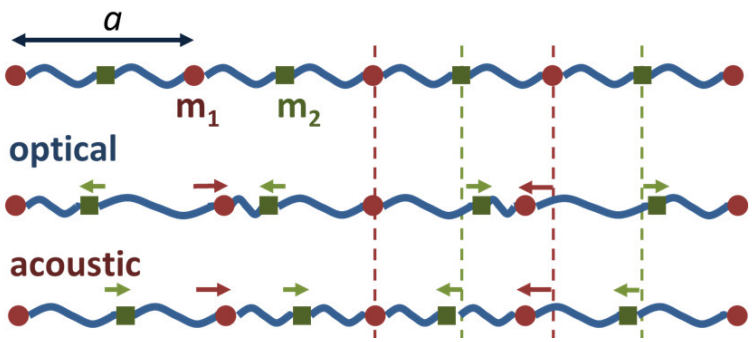

Obrázek 8: Zjednodušené znázornění akustických a optických fononů s vlnovou délkou označenou jako a[29]

Relaxační mechanismy u jedno-molekulových magnetů se dále dělí na jedno-fononové a dvou-fononové děje podle počtu fonony přenášených excitací, ze kterých se dané děje skládají.[30] Jediným dějem, který se řadí mezi jedno-fononové děje, je takzvaná přímá relaxace, což je děj, vyžadující přítomnost magnetického pole, kdy dojde vlivem Zeemanova efektu k přechodu mezi dvěma stavy, které se dostanou do rezonance s energií fononu. Případná další energie může být dodána jako tepelná excitace, proto je děj závislý i na teplotě. Jeho popis při analýze experimentálních dat je obvykle prováděn pomocí následující rovnice:[31]

$$t_{\mathrm{dir}}^{-1} = A_{\mathrm{dir}} B^4 T \tag{18}$$

Kde *t* je rychlost relaxace, *A* je parametr, *B* je indukce magnetického pole a *T* teplota. Tato rovnice ale platí pouze pro Kramersovy ionty, pro ne-Kramersovy ionty je namísto B^4 používáno pouze B^2.[32]

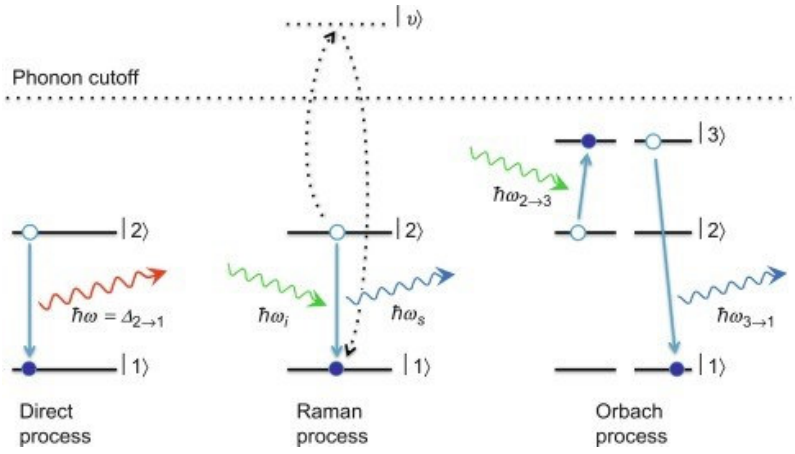

Obrázek 9: Znázornění relaxačních dějů (přímý, Ramanův a Orbachův) zprostředkovaných fonony.[33] Jako „phonon cutoff" je označena hranice energie, nad kterou fonony neinteragují s Kramersovými dublety.

Jedním ze dvou dvou-fononových dějů je Ramanův proces (Obrázek 9). Dochází při něm k pohlcení a vyzáření fotonu, přičemž mezistupněm je tzv. virtuální hladina, do které se systém excituje a ze které následně dochází k deexcitaci, což provází pohlcení, případně vyzáření fononu. Je tedy nutné, aby byly v systému dostupné fonony v rezonanci s energiemi potřebnými pro přechody. Tento jev probíhá kompetitivně s Orbachovým jevem a může být aktivní i v oblasti teplot, kde systém nemá dost energie na překročení energetické bariéry. Ramanova relaxace pak snižuje blokovací teplotu, je tedy naším zájmem ji co nejvíce potlačit.[34]

Co se týče teoretických popisů a možností predikce Ramanovy relaxace, je zatím bohužel asi tím nejméně popsaným relaxačním mechanismem. Již bylo prokázáno, že je důvodem toho, že komplexy s vysokými experimentálně zjištěnými energetickými bariérami U_{eff} mohou mít relativně nízké blokovací teploty. Snaha o potlačení Ramanovy relaxace by tak mohla přinést zlepšení v této skupině jedno-molekulových magnetů.[35] Jediný zatím navržený spolehlivý způsob je ovšem omezení fononů na nižších energiích, aby jimi nemohla být přenášena energie[36], což je ovšem zatím úkol, jehož dosažení je v praxi velmi obtížné.

Při vyhodnocování experimentálních dat je Ramanův děj obvykle popisován pomocí následující rovnice:

$$t_{\text{Ram}}^{-1} = C_{\text{Ram}} T^n \tag{19}$$

Kde *C* je parametr, a *n* by mělo pro ideální případy být blízké 9 pro Kramersovy ionty, 7 pro ne-Kramersovy ionty, 5 při přítomnosti nízko ležících stavů blízkých základnímu stavu a 2 pro vysoké teploty.[37]

Druhým mechanismem, který se řadí mezi dvou-fononové mechanismy je Orbachův mechanismus, což je děj, kdy dochází k excitaci do vyšších stavů, a tedy k překonání energetické bariéry U_{eff}, aby mohlo dojít ke změně směru magnetizace. V reálných systémech sice většinou nejde o excitaci do nejvyššího dubletu. Obvykle stačí přechod do vyššího stavu, kde je tunelování silnější než v základním stavu (Obrázek 10).[38] Tento děj je v teorii někdy ztotožňován s takzvaným tepelně asistovaným tunelováním (Obrázek 10), tedy excitací do vyššího stavu pomocí přímého mechanismu, a poté kvantovým tunelováním. Prakticky ovšem není možné tyto mechanismy odlišit.[39]

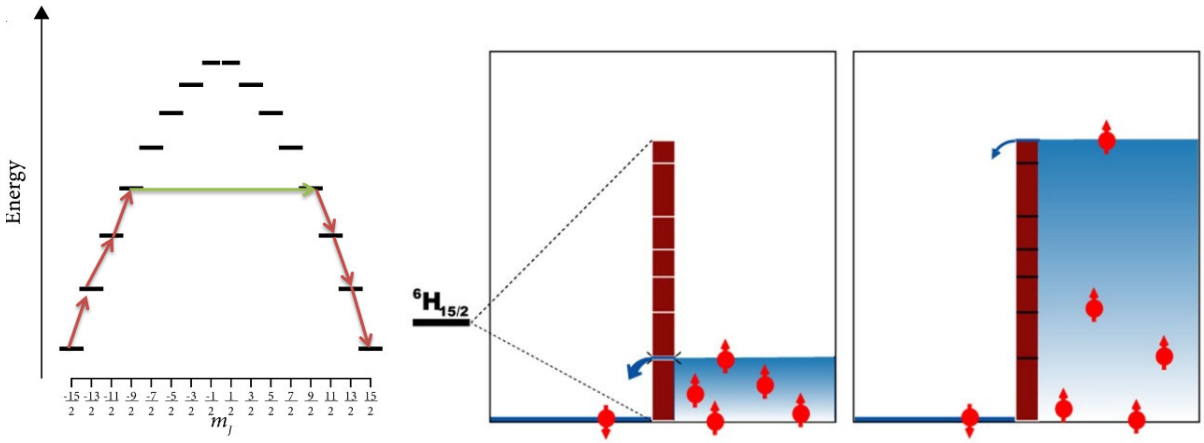

Obrázek 10: Ilustrace tepelně asistovaného tunelování (vlevo)[39] a zobrazení energetické bariéry jako „přehrady", kde ke změně směru magnetizace dojde v prvním stavu, který to tunelováním umožňuje (uprostřed), nebo ideálně až na vrcholu bariéry (vpravo)[38]

Tyto připomínky jsou ovšem pouze formální. Fakticky je Orbachův mechanismus relaxace z hlediska jedno-molekulových magnetů tím nejvýhodnějším pro jejich design, neboť úzce souvisí s energetickou bariérou, jejíž velikost jsme s dnešním stavem poznání schopní do jisté míry kontrolovat a designovat molekuly pro její maximální velikost. Pro popis Orbachova jevu se většinou používá upravená verze Arrheniovy rovnice:

$$t_{\mathrm{Orb}}^{-1} = t_0^{-1}\exp(-\frac{U_{\mathrm{eff}}}{kT}) \qquad (20)$$

kde t_0 je parametr, U_{eff} energetická bariéra, k Boltzmannova konstanta a T je teplota.

Bylo již prokázáno, že v případě komplexů s výhradně Orbachovou relaxací nebo v případě zanedbání Ramanovy relaxace spolu velmi dobře koreluje velikost energetické bariéry a blokovací teploty. Tento vztah lze velmi jednoduše napsat jako:[36]

$$T_{\mathrm{B\ Orb}} = -\frac{U_{\mathrm{eff}}}{\ln(\frac{t_0}{t_{\mathrm{ref}}})} \approx -\frac{U_{\mathrm{eff}}}{28} \tag{21}$$

kde 28 je aproximovaná hodnota, kterou dostaneme při dosazení t_{ref} = 100 s (což vychází z blokovací teploty), a za t_0 se dosadí hodnota odpovídající rozsahu 10^{-11} až 10^{-12}, což odpovídá konstantě t_0 u jedno-molekulových magnetů typu dysprosocenia. Jak je vidět z extrapolace, je i přes jistou úroveň aproximace vidět jasnou korelaci mezi odhadovanou hodnotou blokovací teploty pro Orbachův jev a velikostí energetické bariéry (Obrázek 11).

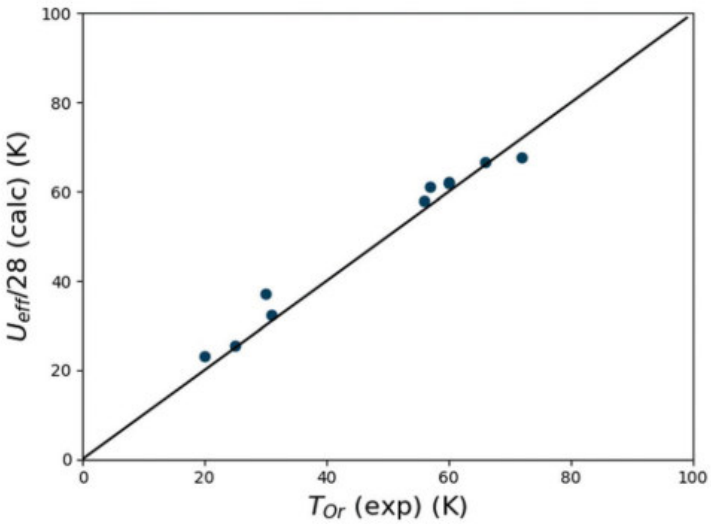

Obrázek 11: Korelace mezi velikostí U_{eff} a blokovací teplotou pro Orbachův jev[36]

2.6 Interakce fononů se spinovým momentem hybnosti

Již bylo v minulé kapitole popsáno, že se energie při magnetické relaxaci přenáší za pomoci takzvaných fononů neboli vibrací krystalové mřížky. Ovšem ne každá vibrace interaguje s magnetickým momentem stejně. Relaxace magnetizace je často spojena s populací konkrétní vibrace. Pro popis této interakce byla zavedena veličina označovaná jako „spin-phonon coupling“, která popisuje propojení mezi spinem a fonony s využitím teoretických metod. Fonony se při takových výpočtech obvykle redukují na molekulové vibrace, což je aproximace, která ale umožňuje využít jednodušší výpočetní metody bez periodického DFT nebo jiné korekce na okolní prostředí. Spin-fononová interakce se poté zjišťuje pomocí výpočtu určité veličiny spojené s magnetismem v rovnovážné struktuře a poté ve struktuře deformované vibracemi. Definice této veličiny se prozatím v literatuře v různých zdrojích může lehce odlišovat.

$$C_k = \frac{\hbar}{4\pi}\left(\frac{\partial^2 g_z}{\partial {Q_k}^2}\right)\frac{1}{m_k v_k} \tag{22}$$

V tomto případě je spin-fononová interakce definována jako druhá derivace složky *g*-faktoru ve směru z podle normálové souřadnice vibrace (Obrázek 12).[40] Dále pak ve vztahu vystupuje m_k jako redukovaná hmotnost a v_k jako frekvence vibrace.

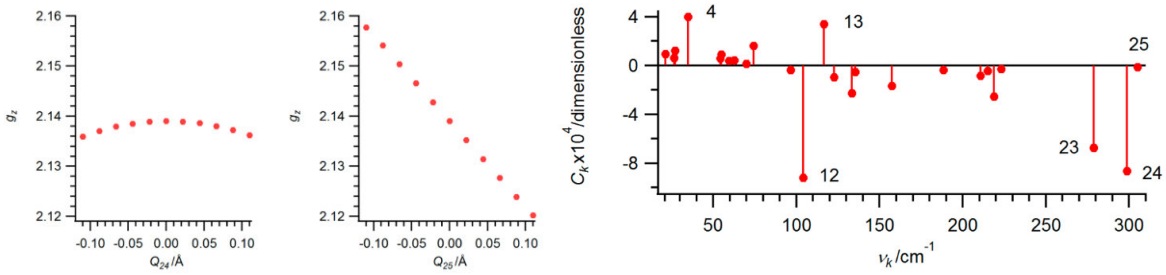

Obrázek 12: Průběh závislosti g_z na normálové souřadnici pro dvě vybrané vibrace (vlevo) a spin-fononové spektrum pro studovaný komplex $[Cu(C_4S_2N_2)_2]$[40]

V tomto případě Escalera-Moreno *et al.* studovali komplex Cu^{II} z pohledu molekuly potenciálně použitelné pro kvantové počítače, nicméně princip je stejný i u jedno-molekulových magnetů. Podařilo se opravdu potvrdit, že jsou určité vibrace, které silně interagují se spinem a způsobují přenos energie (nebo u qubitů kvantovou dekoherenci), zatímco ostatní mají poměrně malý vliv.

Existují pak i jiné přístupy, kdy je namísto *g*-faktoru v derivaci použito například *D*-parametru nebo koeficientů Stevensonových operátorů.[41]

V nedávné době se objevily i přístupy, které jdou ještě o krok dále a pokouší se dosáhnout kompletní teoretické předpovědi pro relaxační čas u všech relaxačních procesů, pro kterou by právě spin-fononová interakce měla být klíčovým parametrem. Pokud víme, jak daná vibrace ovlivňuje magnetickou relaxaci, je možné následně z její populovanosti při dané teplotě a hustotě stavů, které budou v rezonanci s energií přechodu mezi energetickými hladinami spin-orbitální interakce, předpovědět relaxační čas pro všechny děje, při kterých dochází k přenosu energie pomocí fononů.

Jako první byla spin-fononová interakce využita pro charakteristiku magnetických vlastností pro komplex $[Co(C(SiMe_2ONaph)_3)_2]$, kde ovšem nebyla použita teoretická předpověď, ale koeficienty spin-phonon coupling byly získány z experimentálních dat.[42] Pro analýzu dat bylo použito následujícího vztahu:

$$t^{-1} = {t_{\text{tun}}}^{-1} + \sum_{\alpha}\left(\frac{{V_\alpha}^2}{\hbar}\frac{\Delta_\alpha(2n_\alpha+1)}{({\Delta_\alpha}^2+(\hbar\omega_\alpha)^2)}\right) + {t_0}^{-1}\exp\left(-\frac{U}{kT}\right) \quad (23)$$

Kde mimo již zmiňovaných členů popisujících kvantové tunelování magnetizace a Orbachovu relaxaci vystupuje prostřední člen, který popisuje přímou relaxaci na základě spin-fononové interakce. Jako α jsou označeny jednotlivé vibrace. Pro každou z nich pak jsou v rovnici specifické hodnoty *V* (spin-fononová interakce), *Δ* (šířka spektrální čáry), *n* (populace vibrace) a *ω* (úhlová rychlost). Protože fonony jsou bosony, populace se obvykle počítá pomocí Bose-Einsteinova rozdělení:

$$n_\alpha = \frac{1}{e^{\frac{\hbar\omega_\alpha}{kT}}-1} \quad (24)$$

U spektrální šířky fononu se definice liší, v případě této publikace byl použit následující vztah:

$$\Delta_\alpha^2 = \frac{(\hbar\omega_\alpha)^2\cdot e^{\frac{\hbar\omega_\alpha}{kT}}}{(e^{\frac{\hbar\omega_\alpha}{kT}}-1)^2} \quad (25)$$

Ale v jiných případech se šířka spektrální čáry pro zjednodušení zafixuje na konstantní hodnotu. [41b]

Ve výsledku pak byla v případě práce autorů Reta *et al.*[41b] analyzována křivka závislosti relaxačního času na teplotě a bylo dosaženo shody na základě dosazení za parametry t_{tun}, V_α, t_0 a *U* (Obrázek 13).

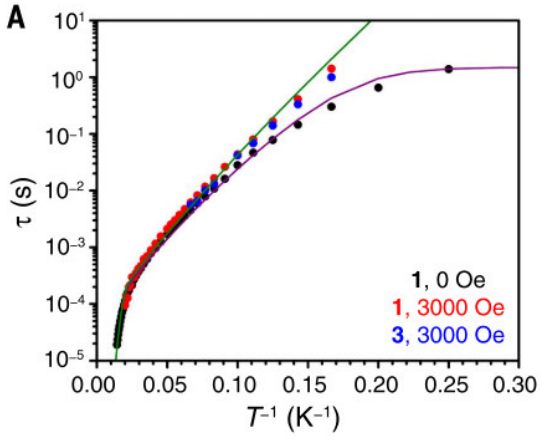

*Obrázek 13: Analýza relaxačního času pro komplexy [Co(C(SiMe$_2$ONaph)$_3$)$_2$] (**1**) a [Co$_{0.02}$Zn$_{98.8}$(C(SiMe$_2$ONaph)$_3$)$_2$] (**3**)*

V nedávné době byly ale publikovány dva různé, ale přesto ve své podstatě podobné postupy, jak lze relaxační čas získat s využitím výhradně *ab-initio* výpočtů. Obě metody jsou založeny na výpočtu matice, která obsahuje maticový element pro každou excitaci mezi každými dvěma

kombinacemi přechodů mezi energetickými hladinami Kramersových dubletů. Tyto maticové elementy jsou definovány následovně:[41b]

$$\gamma_{fi} = \sum_j^{3N-6} \frac{2\pi}{\hbar} \left| \left\langle f \left| \widehat{H}_{\mathrm{SP}_J} \right| i \right\rangle \right|^2 \left\langle n_j - 1 \left| Q_j \right| n_j \right\rangle^2 \rho_j(\left| E_f - E_i \right|) \tag{26}$$

Pro $E_f > E_i$; pokud platí, že $E_f < E_i$, vypadá vztah následovně:

$$\gamma_{fi} = \sum_j^{3N-6} \frac{2\pi}{\hbar} \left| \left\langle f \left| \widehat{H}_{\mathrm{SP}_J} \right| i \right\rangle \right|^2 \left\langle n_j + 1 \left| Q_j \right| n_j \right\rangle^2 \rho_j(\left| E_f - E_i \right|) \tag{27}$$

kde *f* a *i* jsou dvě energetické hladiny a *j* je fonon. Definice spin-fononového hamiltoniánu vychází ze Stevensových operátorů:

$$\widehat{H}_{\mathrm{SP}_J} = Q_j \sum_{k=2,4,6} \sum_{q=-k}^{k} \theta_k \left(\frac{\partial B_k^q}{\partial Q_j} \right) \widehat{O_k^q} \tag{28}$$

kde *Q* je dislokace pro danou vibraci, *a k*, *q*, *Θ*, *B*, *O* vychází z definice pro Stevensovy operátory.

Populace fononu *n* vychází z Bose-Einsteinova rozdělení, *ρ* je hustota stavů pro daný rozdíl energetických hladin.

$$\rho_j(\Delta E) = \frac{1}{\Delta\sqrt{2\pi}} e^{-\frac{(\Delta E - \hbar\omega_j)^2}{2\Delta^2}} \tag{29}$$

kde *Δ* je šířka spektrální čáry, která zde byla definována jako konstantní pro všechny fonony nezávisle na teplotě a frekvenci. Výsledná matice nám pak umožňuje získat převrácené hodnoty relaxačních časů pro jednotlivé přechody jako vlastní čísla matice *γ*, z nich je poté možné předpovědět relaxační dynamiku na základě výběru přechodů s nejkratšími relaxačními časy.

Tento přístup byl použit k simulaci relaxačních časů pro několik reálných nebo teoretických komplexů, odvozených na základě dysprosocenia. Uváděný rozptyl by měl být v oblasti jednoho desetinného řádu, což je, vzhledem k nutnosti zavádění různých aproximací, poměrně přijatelná hodnota odchylky (Obrázek 14).

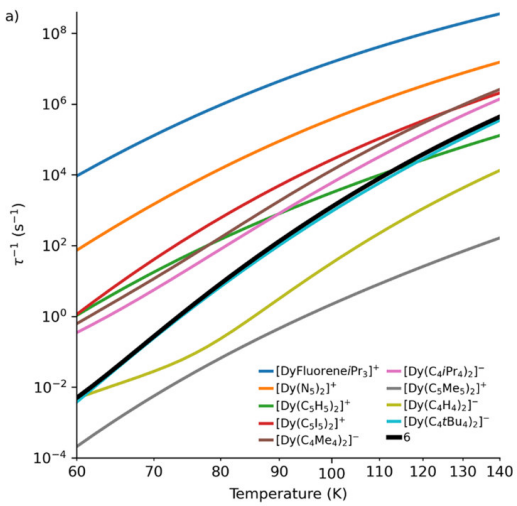

*Obrázek 14: Simulované relaxační časy pro různé analogy dysprosocenia, **6** je pro strukturu [Dy(Cp^{iPr5})(Cp*)]$^+$*

Výše uvedený postup umožňuje teoreticky vypočítat relaxační časy pro Orbachovu relaxaci. Kromě něj byl publikovaný i druhý přístup, který kromě Orbachova jevu zohledňuje i Ramanovu relaxaci (byť pojmy uvedené v článku jsou vzhledem k počtu fononů ne zcela odpovídající definici uvedené v předchozí kapitole):[43]

$$W_{ba}^{1-\mathrm{ph}} = \frac{2\pi}{\hbar^2}\sum_\alpha \left|\langle b|\hat{V}_\alpha|a\rangle\right|^2 G^{1-\mathrm{ph}}(\omega_{ba},\omega_\alpha) \tag{30}$$

Takto je definována rychlost relaxace mezi hladinami *a* a *b*, *α* jsou fonony, *V* je spin-fononová interakce, *G* pak je hustota stavů, která je definována následovně:

$$G^{1-\mathrm{ph}}(\omega_{ba},\omega_\alpha) = \delta(\omega_{ba}-\omega_\alpha)\bar{n}_\alpha + \delta(\omega_{ba}+\omega_\alpha)(\bar{n}_\alpha+1) \tag{31}$$

Kde ω_{ba} je úhlová rychlost energetického rozdílu mezi energetickými hladinami, ω_α je úhlová rychlost fononu, *n* je populace fononu podle Bose-Einsteinova rozdělení a *δ* je Diracova delta:

$$\delta(\omega_{ba},\omega_\alpha) = \lim_{\Delta\to 0}\frac{1}{\Delta\sqrt{\pi}}e^{-\frac{(\omega_{ba}\pm\omega_\alpha)^2}{\Delta^2}} \tag{32}$$

kde *Δ* je šířka spektrální čáry definovaná podobně jako v předchozím případě.

Pro Ramanovu relaxaci pak je použit následující vzorec:

$$W_{ba}^{2-\mathrm{ph}} = \frac{2\pi}{\hbar^2}\sum_{\alpha\beta}\left|\sum_c \frac{\langle b|\hat{V}_\alpha|c\rangle\langle c|\hat{V}_\beta|a\rangle}{E_c-E_a\pm\hbar\omega_\beta}\right|^2 G_\pm{}^{2-\mathrm{ph}}(\omega_{ba},\omega_\alpha,\omega_\beta) \tag{33}$$

kde *α* a *β* jsou fonony, *E* jsou energie hladin *a*, *b* nebo *c* a *G* je hustota stavů:

$$G_{+}^{2-\mathrm{ph}} = \delta(\omega_{ba} - \omega_a + \omega_b)\bar{n}_\alpha\left(\bar{n}_\beta + 1\right) + \delta(\omega_{ba} + \omega_a + \omega_b)(\bar{n}_\alpha + 1)(\bar{n}_\beta + 1) \quad (34)$$

$$G_{+}^{2-\mathrm{ph}} = \delta(\omega_{ba} + \omega_a - \omega_b)(\bar{n}_\alpha + 1)\bar{n}_\beta + \delta(\omega_{ba} - \omega_a - \omega_b)\bar{n}_\alpha\bar{n}_\beta \quad (35)$$

Výpočet relaxačního času se poté provádí, stejně jako v předchozím případě, pomocí vlastních čísel z matic *W*, které obsahují všechny možné přechody mezi všemi hladinami.

Tato metoda byla použita na popis relaxace komplexu $[Dy(acac)_3(H_2O)_2]$ (Obrázek 15), a dosahuje poměrně dobré shody s experimentem s odchylkou v podobných řádech jako první popsaná metoda.

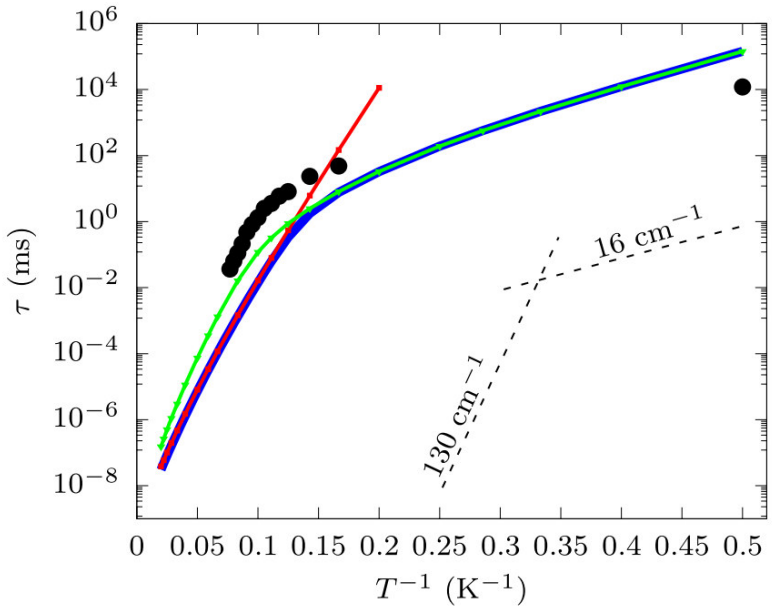

Obrázek 15: Porovnání vypočítané a experimentální relaxace pro $[Dy(acac)_3(H_2O)_2]$, černé tečky jsou experimentální hodnoty, červená čára relaxace z vzorce pro $W^{1\text{-ph}}$ (Orbachova relaxace), zelená z $W^{2\text{-ph}}$ (Ramanova relaxace), modrá pak jejich součet.

2.7 Experimentální techniky studia jedno-molekulových magnetů

Co se týče studia jedno-molekulových magnetů, obecně se využívá zejména magnetochemických, ale v mnoha případech také spektrálních metod, které mohou magnetické metody velmi dobře doplňovat, protože pro magnetismus je klíčová struktura energetických hladin ve stavbě atomu kovu. Cílem těchto metod je objevovat vztahy mezi strukturou molekul, jejich vnitřní elektronovou strukturou a jejich magnetickými vlastnostmi.

Základní magnetochemickou metodou je magnetometrie, tedy metoda měření magnetického momentu vzorku. Používá se několik způsobů, jak tuto metodu používat a různé konfigurace

přístrojů. Obecně jsou nejvíce používané dvě konfigurace, VSM (vibrating sample magnetometer) a SQUID (superconducting quantum interference device).

VSM využívá periodického vibračního pohybu vzorku ve vzorkové komoře, který je realizovaný pomocí motoru, který zajišťuje stálou periodu a rychlost pohybu. Pohyb vzorku pak probíhá mezi detekčními cívkami, ve kterých se pohybem vzorku s nenulovým magnetickým momentem indukuje elektrický proud, který se následně detekuje (Obrázek 16). Celý experiment probíhá v magnetickém poli, které je vytvářeno elektromagnetem.[44]

SQUID magnetometr je pojmenovaný podle detektoru, který využívá principu Josephsonova jevu,[45] kdy dochází k tunelování elektrického proudu v supravodivé smyčce přes tenkou vrstvu izolantu, kterým je přerušená (Obrázek 16) v důsledku shlukování elektronů do tzv. Cooperových párů. Elektrický proud ale může přes bariéru proniknout v důsledku kvantového tunelování. V důsledku toho je pak oscilace proudu v supravodivé smyčce velice citlivá na změny v magnetickém toku, čehož se využívá při provádění magnetických měření.[3]

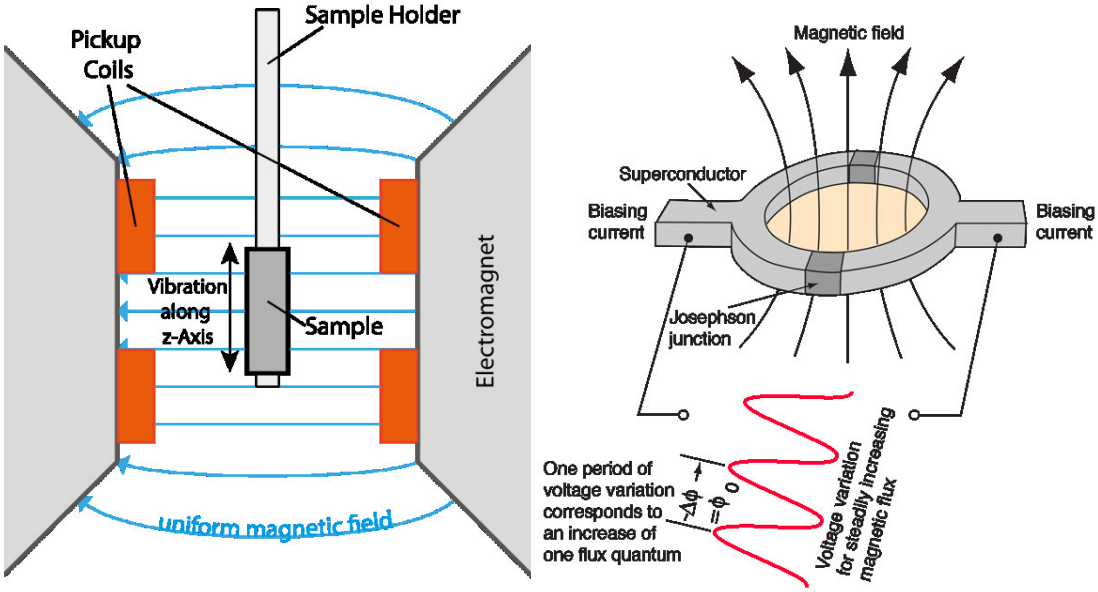

Obrázek 16: Schématické nákresy magnetometrů typu VSM (vlevo)[46] a SQUID (vpravo)[47]

Experimenty s touto metodou se dělí na metody ve stálém a ve střídavém poli. Z metod ve stálém poli jsou při studiu jedno-molekulových magnetů nejčastěji prováděny dva typy měření – měření závislé na poli a na teplotě.

Měření závislosti magnetických veličin na poli se obvykle uvádí jako závislost magnetizace na velikosti magnetického pole, a tato data pak vypovídají o struktuře energetických hladin

v systému. V případě jednoduchého měření závislosti magnetizace na magnetickém poli má křivka u iontů, které jsou isotropní, tvar takzvané Brillouinovy křivky, která popisuje ideální paramagnetikum. Ovšem u iontů, které vykazují anizotropii nebo kooperativní jevy, pak dochází deformaci, kterou již nelze pomocí Brillouinovy křivky popsat bez zahrnutí těchto jevů. S rostoucí teplotou se tvar křivky u paramagnetických materiálů mění na přímku. Saturační hodnota magnetizace je dána následujícím vztahem:[12]

$$M_{\mathrm{sat}} = N_A \mu_B g S \tag{36}$$

V běžně používaném zápise, kdy magnetizaci udáváme vydělenou Bohrovým magnetonem a vztaženou na jednu molekulu, pak bude saturační hodnota rovná *gS*.

Typickým měřením prováděným v tomto režimu je magnetická hystereze. Zde se měří smyčka, kde se od nulové hodnoty magnetického pole jeho hodnota zvyšuje. Z maximální hodnoty +*H* se pak velikost postupně snižuje zpět na nulu a následně se toto opakuje v opačném směru do velikosti pole –*H* a tato smyčka se opakuje.

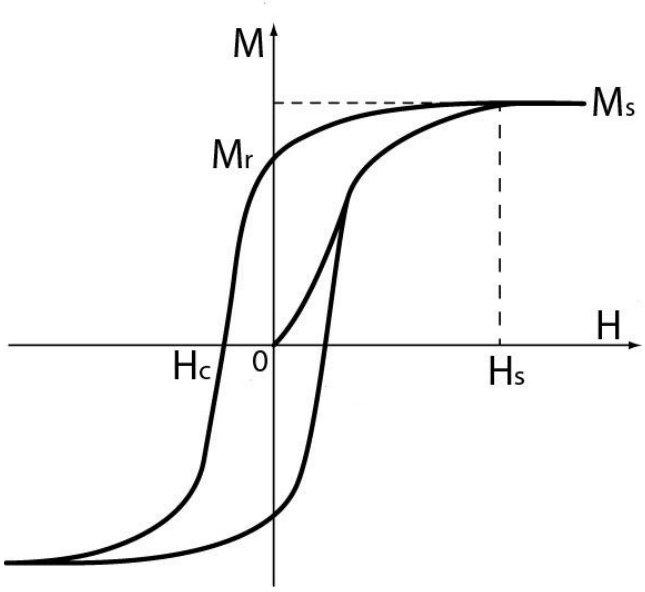

Obrázek 17: Schéma hysterezní křivky[48] s označením významných bodů, M_S je saturační magnetizace, H_S saturační pole, M_r je remanentní magnetizace a H_c je koercivní pole.

Magnetizace je v počátku nulová a se zvýšením pole postupně saturuje. Při změně směru pole se u materiálů, které nevykazují magnetickou hysterezi, křivka opět protne s nulou. U materiálů, které jsou hysterezní v nulovém poli, zůstává takzvaná remanentní magnetizace M_r a magnetizace se dostane na nulovou hodnotu až při aplikaci koercivního pole H_c (Obrázek 17). Šířka hysterezní smyčky rozděluje magnetické materiály na takzvaně tvrdé a měkké.

U měření teplotní závislosti se většinou vyhodnocuje závislost magnetického momentu a magnetické susceptibility na teplotě. Tato metoda se doplňuje spolu s měřením závislosti magnetizace na magnetickém poli a vyhodnocuje se analogicky za použití spinového hamiltoniánu.

Kromě této metody je na místě zmínit také další typ měření závislosti magnetizace na teplotě, a tím je „zero-field cooled magnetisation/field cooled magnetization“ (ZFCM/FCM). Toto měření spočívá v tom, že se vzorek ochladí v nulovém magnetickém poli a následně zahřívá v magnetickém poli. Při zvyšování teploty dojde k nárůstu magnetizace v důsledku orientace magnetických momentů ve směru pole a následně k jejímu poklesu vlivem entropie. V další fázi se pak vzorek v přítomnosti magnetického pole ochlazuje. Z dat této závislosti můžeme odečíst maximum křivky ZFCM, kde se nachází blokovací teplota. Dalším důležitým údajem je bod, kde se rozdělují křivky ZFCM a FCM, kterému se říká ireverzibilní teplota. Rozdíl mezi blokovací a ireverzibilní teplotou je pak ukazatelem distribuce relaxačních časů ve studovaném materiálu. Někdy se také po měření FCM měří ještě remanentní magnetizace (RM), tedy následné ochlazení s vypnutým magnetickým polem (Obrázek 18). Tato metoda je velmi užitečná zejména při studiu kooperativních jevů a často se využívá zejména u studia nanočástic.

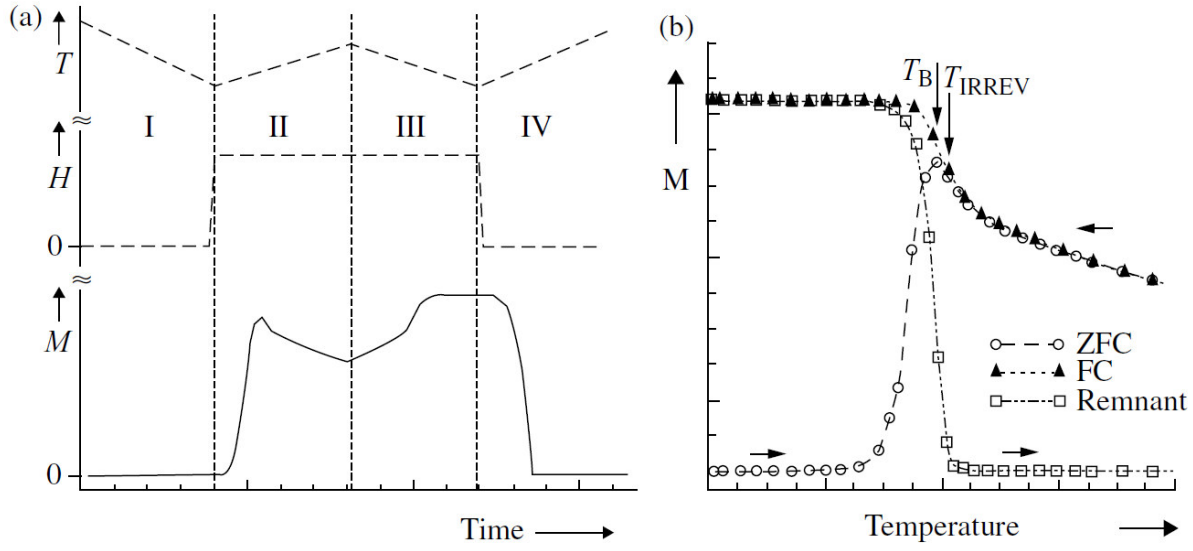

Obrázek 18: Schématické znázornění metody ZFCM/FCM a vývoje teploty, indukce vnějšího magnetického pole a magnetizace na teplotě v jednotlivých fázích (a), (I – příprava, II – ZFCM, III – FCM, IV – RM). Výsledné křivky závislosti magnetizace na čase (b) s označenou blokovací a ireverzibilní teplotou.[3]

Při studiu komplexů se často využívá pouze jednoduchých měření závislosti magnetického momentu nebo magnetické susceptibility na teplotě ve stálém poli. Z tohoto měření lze jednoduše poznat přítomnost ferromagnetické výměny podle nárůstu magnetického momentu se snižující se teplotou, který začíná bodem zvaným Curieova teplota, což je bod přechodu feromagnetu v paramagnet. Naopak antiferomagnetická výměna se projevuje poklesem magnetického momentu od bodu přechodu, kterému se zde říká Néelova teplota. Opačně je to pak s trendy u magnetické susceptibility. Jednoznačně lze poznat přítomnost feromagnetické interakce podle maxima na křivce závislosti magnetického momentu na teplotě. Pokles magnetického momentu lze vysvětlit i jinými faktory, než je antiferomagnetická výměna, například depopulací vyšších hladin základního termu. Proto určení přítomnosti této výměny vyžaduje analýzu magnetických dat podle příslušného spinového hamiltoniánu (Obrázek 19).

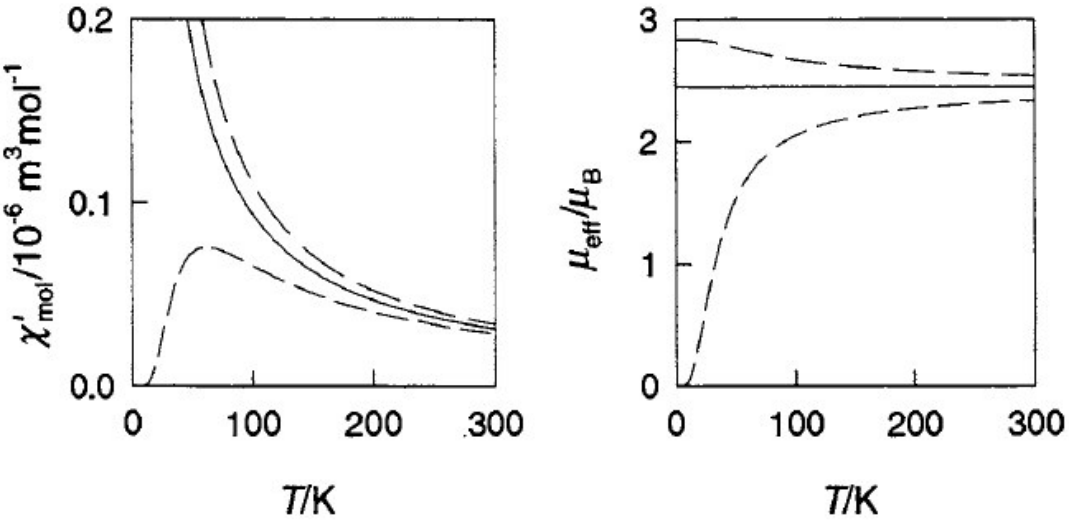

Obrázek 19: Ukázka závislosti magnetické susceptibility a magnetického momentu na teplotě u dimeru $S_1 = S_2 = ½$, kde J^{iso} = 100 K (delší přerušované čáry), J^{iso} = 0 K (nepřerušovaná čára) a J^{iso} = -100 K (kratší přerušované čáry)[24]

Druhou kategorií jsou magnetická měření ve střídavém magnetickém poli, která umožňují zjišťovat dynamické jevy, jako například přechod mezi magnetickými fázemi. U jedno-molekulových magnetů je tato technika často používaná na určování relaxačního času. Principem je, že při pomalé relaxaci magnetizace se fáze naměřené střídavé susceptibility zpožďuje za fází vnějšího střídavého magnetického pole. Naměřenou susceptibilitu poté můžeme vyjádřit pomocí dvou složek, reálné (fázové) a imaginární (mimofázové):

$$\chi' = \frac{\chi_T - \chi_S}{1+\omega^2\tau^2} \tag{37}$$

$$\chi'' = \frac{(\chi_T - \chi_S)\omega\tau}{1+\omega^2\tau^2} \tag{38}$$

Kde χ_T a χ_S je izotermická a adiabatická složka magnetické susceptibility, ω úhlová rychlost a τ čas. Z těchto měření je možné získat údaje o relaxačním času, který lze získat z průběhu křivky imaginární složky susceptibility, která má v závislosti na frekvenci magnetického pole maximum v bodě, kde frekvence odpovídá relaxačnímu času. (Obrázek 20)

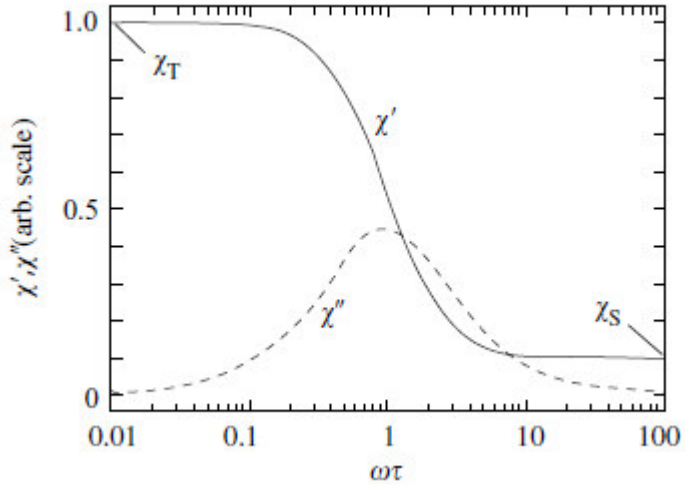

Obrázek 20: Znázornění průběhu křivek reálné a imaginární susceptibility pro měření střídavé magnetické susceptibility[3]

Z těchto údajů poté můžeme získat informace o magnetické relaxaci, pokud změříme střídavou susceptibilitu při různých teplotách. Výsledkem bude závislost relaxačního času na teplotě, která se analyzuje pomocí modelů relaxačního času (rovnice 17-20).

Další metodou studia magnetických materiálů, která je použita i v této práci, je EPR spektroskopie. Tato metoda je založená na štěpení magnetických hladin pomocí magnetického pole a následným pohlcením radiofrekvenčního záření, což dává informace o míře štěpení hladin. Štěpení hladin lze popsat pomocí spinového hamiltoniánu a jeho parametry lze technikou EPR spektroskopie určit.

Obecně, v nejjednodušším případě u spinového systému S = ½, je energie přechodu rovna energii štěpení Zeemanových hladin a pro absorpci radiofrekvenčního záření je možno použít tento vztah:

$$h\nu = \mu_B g B$$

V praxi se běžně EPR spektra zobrazují jako derivace absorpce v závislosti na magnetickém poli. Ze záznamu jde v takovém případě rozlišit podle tvaru absorpční křivky, jestli je *g*-faktor, izotropní, nebo anizotropní. (Obrázek 21)

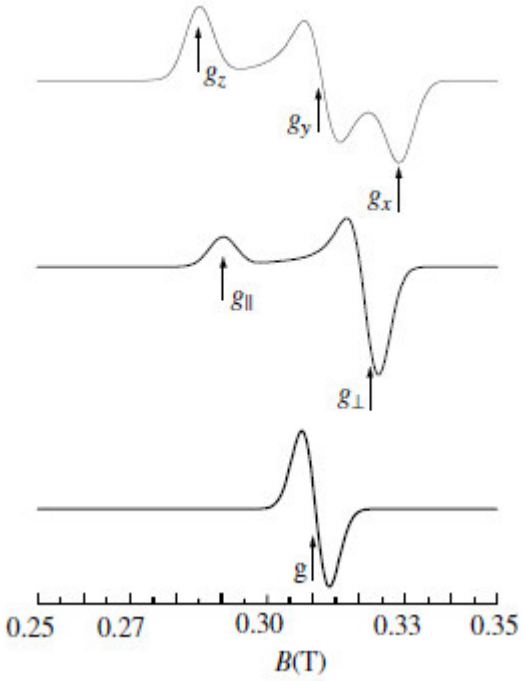

Obrázek 21: Ilustrace EPR spektra pro rozdílné g_x, g_y a g_z (nahoře), pro $g_x = g_y$, (uprostřed), a pro izotropní g-faktor (dole).[3]

Obecně, jakmile v systému narůstá počet hladin, systém se velmi komplikuje a v EPR spektru můžeme vidět nejen vliv štěpení v nulovém magnetickém poli, ale i magnetické výměnné interakce nebo hyperjemné interakce. Z EPR spekter tedy jde extrahovat informace o všech těchto jevech a například z hyperjemné interakce také o struktuře této látky.

2.8 Teoretické metody studia jedno-molekulových magnetů

Výpočetní metody se dnes využívají snad ve všech oblastech chemie, a je proto zřejmé, že se dnes používají a pro charakterizaci komplexů využívaných jako jedno-molekulové magnety. Pro tyto účely se využívají zejména metody DFT a multireferenční metody založené na CASSCF a případně dalších metodách zahrnujících dynamickou korelaci.

Metoda teorie funkcionálu hustoty (DFT) je velmi rozšířenou metodou kvantové chemie založenou nikoli na řešení Schrodingerovy rovnice pro elektrony, ale na nalezení elektronové hustoty, což je výpočetně méně náročné. Problémovou částí tohoto postupu je přepočet elektronové hustoty na energii, který není exaktně vyřešen, a jako jeho náhrada jsou takzvané funkcionály, tedy aproximované metody výpočtu energie.[49] Těchto funkcionálů existuje

poměrně široké spektrum a liší se mezi sebou ve způsobu výpočtu energie, přesnosti i výpočetní náročnosti.

Výhodou metody DFT je zejména její nízká výpočetní náročnost, která při studiu paramagnetických koordinačních sloučenin umožňuje snadno provádět například optimalizace struktur a výpočty vibračních frekvencí. Bohužel není vhodná pro výpočty týkající se podrobnějšího studia elektronové struktury kovů, zejména těch s vyšším protonovým číslem. DFT totiž není schopná popsat systém, kde se nachází nízko ležící excitované stavy, které jsou populované a silně ovlivňují základní stav systému. Pro takovéto případy se používají takzvané multireferenční metody.

Asi nejčastěji používanou multireferenční metodou ve studiu jedno-molekulových magnetů je metoda je „Complete Active Space Self-Consistent Field“ (CASSCF). Existují různé další metody, které popisují systém, který vyžaduje zahrnutí excitací, jako například metody konfigurační interakce (CI) nebo metoda vázaných klastrů (CC), avšak oproti CASSCF jsou tyto metody poměrně dost výpočetně náročné. Výhodou CASSCF je, že nezahrnuje excitace ve všech dostupných orbitalech, ale pouze ve zvolených aktivních orbitalech, což znatelně snižuje výpočetní náročnost. (Obrázek 22)

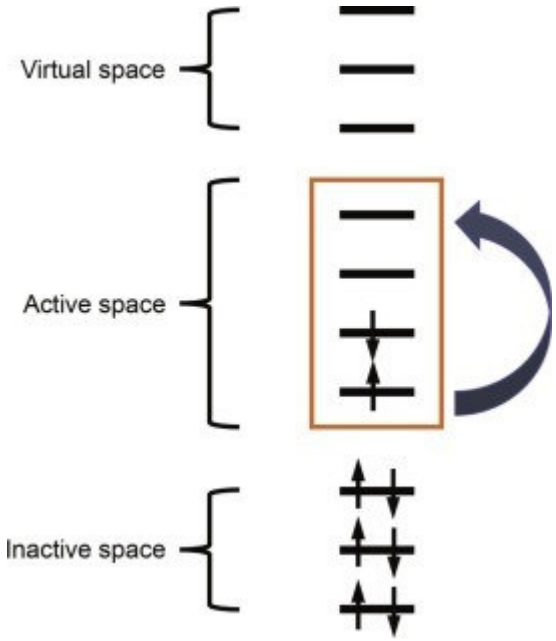

Obrázek 22: Ilustrace aktivního prostoru v CASSCF výpočtu[50]

Problémem ve výpočtu CASSCF metody je takzvaná dynamická korelace, která ve výpočtu není zahrnuta, což je ve zkratce korekce na výměnnou energii elektronů při pohybu. Tento problém

se řeší s využitím pokročilých metod využívajících poruchovou teorii, jako například „N-electron valence perturbation theory“ (NEVPT2) nebo „Complete active space perturbation theory“ (CASPT2). Tyto metody jsou sice výpočetně náročnější a nejsou vhodné pro systémy, které zahrnují příliš velké množství stavů v aktivním prostoru, ale u komplexů 3d kovů je možné je běžně využívat.

Výhodou těchto metod je, že dokážou určit energii elektronových stavů v atomu kovu po štěpení v ligandovém poli, což je užitečná věc u studia jedno-molekulových magnetů nebo sloučenin s křížením spinových stavů, případně pak i další vlastnosti, jako jsou například hladiny po spin-orbitální interakci, *g*-faktory nebo parametry štěpení v nulovém magnetickém poli.

3. Současný stav problematiky

3.1 Sendvičové komplexy lanthanoidů s ligandy typu cyklopentadienylu

Tato oblast chemie je poměrně intenzivně rozvíjena od roku 2016, kdy byl připraven a studován komplex $[Dy(Cp^{ttt})_2][B(C_6F_5)_4]$ s blokovací teplotou 60 K a následně pak také komplex $[Dy(Cp^{iPr5})(Cp^*)][B(C_6F_5)_4]$, který má blokovací teplotu až 80 K.[10] Mimo tyto dva známé komplexy ale v poslední době bylo připraveno poměrně mnoho dalších podobných látek, využívajících zajímavé magnetické vlastnosti těchto systémů.

Tabulka 1: Jedno-molekulové magnety typu sendvičových komplexů s lanthanoidy jako centrálními atomy

Složení	U_{eff}	T_B	**Ref**
$[Dy^{III}(Cp^{ttt})_2]^+$	1760	60	10a
$[Dy^{III}(Cp^{iPr5})(Cp^*)]^+$	2215	80	10b
$[Dy^{III}(Cp^{iPr4})_2]^+$	1849	17	51
$[Dy^{III}(Cp^{iPr4Me})_2]^+$	2112	62	51
$[Dy^{III}(Cp^{iPr4Et})_2]^+$	1986	59	51
$[Dy^{III}(Cp^{iPr5})_2]^+$	1919	56	51
$[Dy^{III}(Cp^*)(\eta^8\text{-Pn})]$	270	2.4	52
$[Dy^{III}(C_4B^{tPhP})_2]^-$	2302	66	53
$[Tb^{III}(Cp^{ttt})_2]^+$	42		54
$[Tb^{II}(Cp^{iPr5})_2]$	1734	52	55

$[Dy^{III}(Dtp)_2]$	1760	23	[56]
$[(TbCp^{Me4}{}_2)_2(\mu{-}N_2)]^-$	276	20	[57]
$[(DyCp^{Me4}{}_2)_2(\mu{-}N_2)]^-$	108.1	6.6	[57]
$[Dy(Cp^{iPr5})(Cp^{PEt4})]^+$	1410	70	[58]
$[Dy(BC_4Ph_5)_2]^-$	1500	66	[59]
$[Dy_2(Cp^{iPr5})_2I_3]$	1631	72	[60]
$[Er(COT)(Cp^{ttt})]$	228		[61]
$[Er^{III}(COT'')_2]^-$	187	8	[62]
$[Er_2^{III}(COT'')_3]$	323	12.5	[63]
$[Er_2^{III}(COT)_4]^{2-}$	187	12.9	[63]
$[Er(C_9H_9)(COT)]$	361	10	[64]

V těchto látkách se vyskytují jako ligandy buďto deriváty cyklopentadienylu a od něj odvozených heterocyklů nebo větší aromatické cykly, jako je cyklooktatetraen, případně $(C_9H_9)^-$. Z kovů jsou zastoupeny hlavně Tb a Dy, které vytváří velmi dobré jedno-molekulové magnety s pětičlennými kruhy, zatímco s většími ligandy se ukazují jako dobré hlavně komplexy Er. Nicméně, v porovnání s komplexy Dy a Tb mají komplexy Er poměrně nízké blokovací teploty, protože komplexy sendvičového typu s pětičlennými ligandy dosahují poměrně běžně blokovacích teplot nad 60 K. Jejich problémem je ovšem nízká stabilita kvůli nízkému koordinačnímu číslu, kterého je dosaženo volbou ligandů s velkou sterickou zábranou, které také umožňují dosáhnout většího úhlu mezi centrálním atomem a středy aromatických kruhů, což napomáhá axiální anizotropii. V poslední době bylo vedeno mnoho pokusů, jak se přiblížit k rekordní blokovací teplotě 80 K například pomocí substituce heteroatomy, ale zatím neúspěšně.

3.2 Teoretické studie

Studium jedno-molekulových magnetů je kromě experimentálních metod realizováno i výpočetními metodami a některé z prací, které byly publikovány, pomohly velkou mírou vysvětlit chování komplexů jedno-molekulových magnetů, případně pomoci najít správné zaměření pro syntetické chemiky.

Důležitým nástrojem pro teoretické studium jedno-molekulových magnetů se stal software Single_Aniso a Poly_Aniso.[65] Tento software umožňuje pomocí výpočtů zjistit hladiny Kramersových dubletů a pravděpodobnosti přechodů mezi nimi na základě maticových elementů magnetického momentu, vypočítat operátory krystalového pole nebo například *g*-faktory pro Kramersovy dublety na základě CASSCF výpočtů. V současné době je tento program velmi rozšířený a stal se jednou ze základních metod teoretické charakterizace jedno-molekulových magnetů.

Je používaný i v čistě teoretických pracích. Například jedna velmi významná od samotných autorů programu se věnuje diskuzi o ideálním tvaru koordinačního polyedru komplexů lanthanoidů, zejména Dy^{III}, pomocí studia ideálního teoretického komplexu $[DyO]^{+}$ a pomocí různých tvarů pro komplexy $[DyF_n]^{3-n}$.[66] Tato studie ukázala význam axiálního uspořádání ligandů u komplexů dysprosia, které vede k velké axiální anizotropii a k velkým energetickým bariérám (Obrázek 23). Tento objev vedl k vysvětlení velmi vysokých bariér U_{eff} u komplexů ve tvaru pentagonálních bipyramid, u kterých je axialita dosažena nerovnoměrnou distribucí elektronegativity u donorových ligandů, kde jsou elektronegativní a nabité atomy v axiálních polohách a v ekvatoriálních jsou často slabší ligandy s nulovým nábojem. Později bylo podobných vlastností dosaženo také s dysprosoceniem, což je další typ komplexů s axiální symetrií.

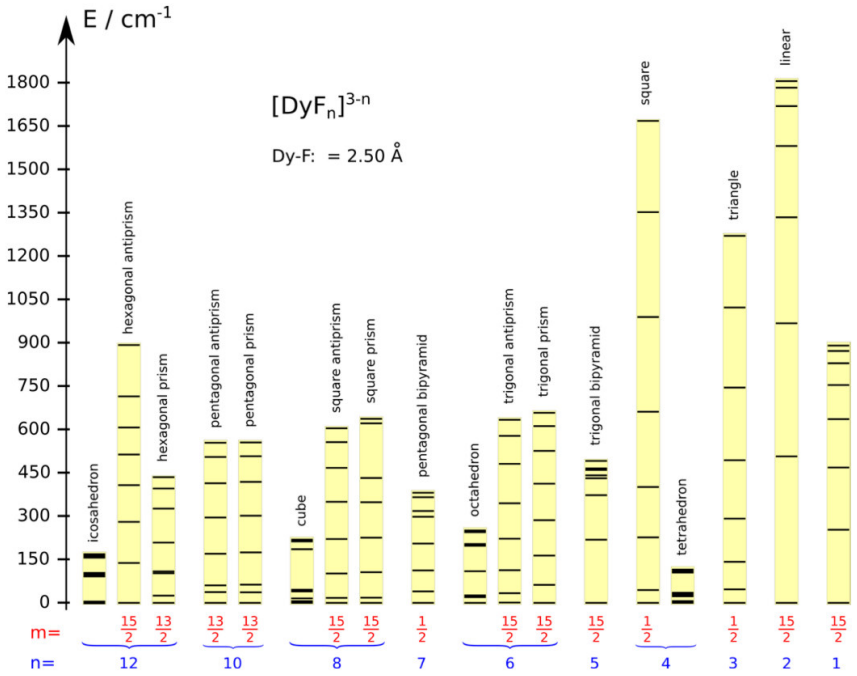

Obrázek 23: Odhadovaná velikost energetické bariéry pro komplexy $[DyF_n]^{3-n}$ v různých tvarech koordinačního polyedru.[66]

V této souvislosti je možné zmínit techniku nazvanou „molecular engineering“, kde jsou výpočetně charakterizovány *ab initio* optimalizované komplexy, obvykle z důvodu nemožnosti studia reálných komplexů kvůli komplikované přípravě. Cílem těchto studií je obvykle nalézt strukturní korelace a najít vhodné cíle pro syntetické chemiky. Mezi příklady takových studií patří například zajímavý článek studující vliv magnetických výměnných interakcí u mnohojaderných komplexů složených z jednotek $[Mo^{III}(CN)_7]^{4-}$ a V^{II}, kde bylo zjištěno, že energetická bariéra je silně závislá na struktuře těchto komplexů a při jejich spojování vhodným způsobem může být díky vlivu magnetických výměnných interakcí zvětšována (Obrázek 24).[67]

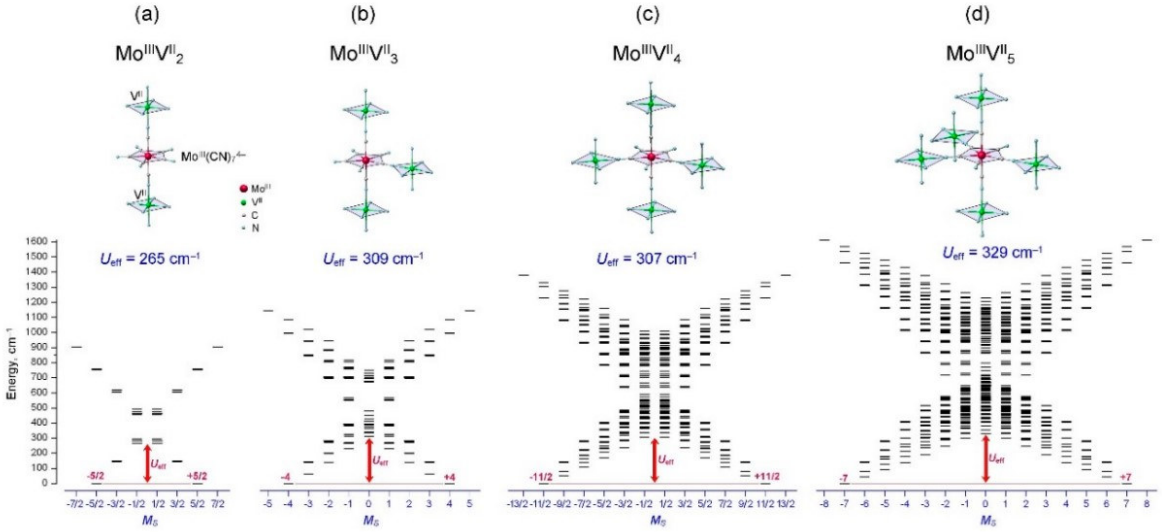

Obrázek 24: Příklad struktur vícejaderných $Mo^{III}V^{II}$ komplexů a vliv jejich struktury na jejich U_{eff}.[67]

Metoda „molecular engineering“ se často využívá například i při studiu derivátů dysprosocenia kvůli jejich velmi komplikované přípravě a jejím účelem je najít strukturní korelace a trendy, které pomohou najít zaměření pro přípravu komplexů s vysokými blokovacími teplotami. Vzhledem k moderním poznatkům se často také studují magnetické vlastnosti s molekulovými vibracemi nebo spin-fononovou interakcí. Jednoduchým indikátorem je například překryv energetických přechodů Kramersových dubletů s molekulovými vibracemi, který by měl být ukazatelem ohledně relaxační dynamiky. Tímto způsobem byly studovány například analogy dysprosocenia s 1,2,3,4,5-pentaisopropylcyklopentadienylem, 1,2,3,4,5-pentajodcyklopentadienylem nebo 3,6,9-triisopropylfluorenem.[68]

Kromě CASSCF výpočtů je v této části možné zmínit také modely, kterými se dříve tyto výpočty nahrazovaly kvůli velké výpočetní náročnosti. Asi nejvýznamnější z nich jsou REC (radial

effective charge) a LPEC (lone pair effective charge).[69] Oba dva jsou zaměřené na výpočet elektronových hladin kovových iontů nikoli na základě kvantově chemických výpočtů, ale na základě hamiltoniánu krystalového pole (Stevensových operátorů), které jsou vytvořené z bodových nábojů reprezentujících ligandy. Rozdíl mezi modely je ten, že REC model používá reprezentaci elektronového páru na spojnici jader, a je tedy vhodný pro jednoduché ligandy, LPEC model uvažuje i korekci na vychýlení elektronového páru ze spojnice jader kvůli rigiditě ligandu, například heterocyklu. Existují programy[70] a studie[71], kde tento model je používán, avšak jednoduchost modelu je velmi limitující vzhledem k jeho přesnosti, a vzhledem k růstu výkonu počítačů dnes hraje vedle CASSCF metod jen podružnou roli.

Mimo zde zmíněné ještě existuje celá řada teoretických studií, která se zabývá relaxační dynamikou, objasněním relaxačních mechanismů nebo spin-fononovou interakcí, ale vzhledem k tomu, že jsou těmto poznatkům věnovány části 2.5. a 2.6. v Teoretické části, zde tyto práce již znovu uvedeny nebudou.

3.3 Komplexy lanthanoidů a 3d kovů v systémech typu salenu jako jedno-molekulové magnety

Komplexy lanthanoidů a 3d kovů jsou z pohledu molekulového magnetismu velmi zajímavé a intenzivně studované systémy. U lanthanoidů je pro potřeby molekulového magnetismu vhodné volit takové ionty, které mají velkou anizotropii a celkový úhlový moment *J*, nejčastěji jsou tedy používány Dy^{III}, Tb^{III}, nebo Er^{III}. Další kov zajímavý z pohledu magnetismu pak je Gd^{III}, neboť má konfiguraci $4f^7$, jeho základní term je ^8S a tento term je izotropní a má nulový orbitální moment a jediný příspěvek spin-orbitální interakce je z vyšších excitovaných hladin. Kvůli tomu je spin-orbitální interakce u Gd^{III} nízká a lze jej dobře popsat pomocí aproximace analogicky jako 3d kovy, kde je možné použít pouze spinový moment hybnosti. Proto je u Gd^{III} komplexů snazší studovat magnetické výměnné interakce, neboť mezi spinovými momenty je magnetická výměna obecně lépe definovaná.

Při syntéze jedno-molekulových magnetů je pak anizotropní lanthanoid doplněn vhodným 3d kovem. Tyto kovy mohou být diamagnetické nebo paramagnetické. Heterodimetalické komplexy s diamagnetickými kovy jsou poměrně časté a budou v této kapitole zmíněny, avšak na magnetismus působí obvykle pouze změnou elektronové hustoty na donorových atomech

vlivem náboje, případně způsobují sterické pnutí, ale lze je považovat za metaloligandy, které přímo nepřispívají k magnetismu systému. Oproti tomu paramagnetické kovy přispívají k celkovému spinu molekuly a na rozdíl od lanthanoidů mají 3d kovy tendenci tvořit silné magnetické výměnné interakce, protože jejich nepárové elektrony v d-orbitalech jsou stíněny méně, než u f-orbitalů v lanthanoidech. Tyto vlastnosti se pak doplňují s vlastnostmi f-prvků, neboť výměnné interakce s f-prvky mají vliv na kvantové tunelování magnetizace[72] a obecně mohou ovlivňovat magnetickou anizotropii.[73]

Systémy s ligandy typu salenu (Obrázek 15) jsou jedním z intenzivně studovaných systémů, který tvoří heterometalické 3d-4f systémy, a to zřejmě kvůli jeho velké variabilitě, kdy je možné provádět změny na různých částech, například v řetězci mezi iminovými skupinami nebo v substituentech na poloze R_1 a R_2, kde obvykle jsou skupiny obsahující kyslík. Na tento ligand se také poměrně snadno váže mnoho 3d kovů a komplexy s 4f-prvky tvoří značná část z nich poměrně snadno. 3d kov se váže do kavity tvořené atomy dusíku a kyslíku z hydroxylových skupin (Obrázek 25: Obecný vzorec ligandu typu salenu a obecné syntetické principy k přípravě komplexů s tímto ligandem.) v koordinačním okolí většinou tvaru buďto čtverce nebo oktaedru s dalšími dvěma ligandy. Lanthanoid se pak váže do kavity tvořené kyslíkovými atomy a z druhé strany se na něj navazují další ligandy. Existují i heterotrimetalické systémy založené na těchto ligandech, které jsou tvořeny pomocí můstkujícího ambidentátního ligandu, často jde o připojení kyanometalátových stavebních bloků.

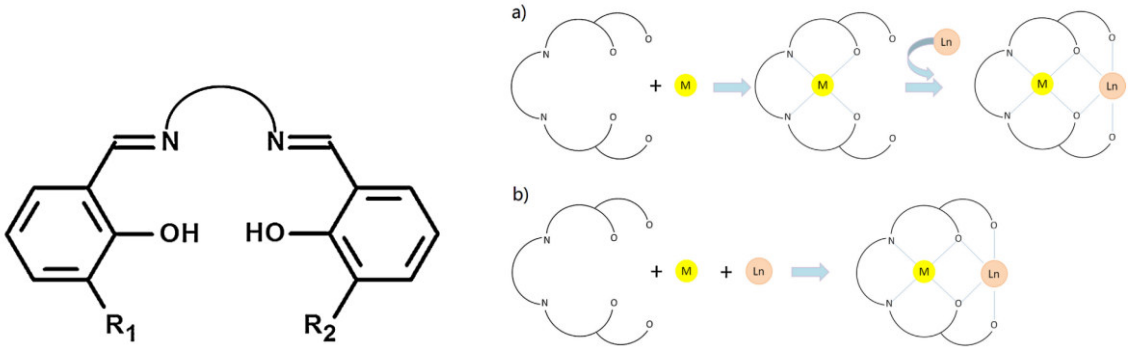

Obrázek 25: Obecný vzorec ligandu typu salenu a obecné syntetické principy k přípravě komplexů s tímto ligandem.[74]

Mezi d-prvky, které se v tomto systému objevují, jsou významné hlavně komplexy s mědí, vanadem, zinkem a niklem. První zmiňované jsou většinou systémy Cu^{II} a V^{IV}, oboje tedy s ionty paramagnetickými se spinem S = ½. Komplexy zinku a většinou i niklu jsou nejčastěji

diamagnetické, nikl se v těchto systémech totiž většinou objevuje ve čtvercové geometrii. Vzhledem k tomu, že součástí této práce je publikace na téma komplexů V^{IV} a lanthanoidů, rešerše byla zaměřena zejména na komplexy V^{IV} a analogicky také na komplexy Cu^{II}. Rešerše je součástí této publikace (Kapitola 4.3.), je zaměřená zejména na magnetické výměnné interakce, případně magnetickou anizotropii, pokud u těchto komplexů byla zjištěna.

Komplexů vanadu a lanthanoidů popsaného složení není známo příliš mnoho. U komplexů obsahujících vanad nebyly dosud známy žádné jedno-molekulové magnety (první byly publikovány v této práci – příloha č. 3). Komplexy mědi a lanthanoidů jsou studované více a také jsou lépe prozkoumané z hlediska jejich vlastností jako jedno-molekulových magnetů (Tabulka 2:Rešerše 3d-4f komplexů V^{IV} a Cu^{II} a lanthanoidů Gd^{III}, Tb^{III}, Dy^{III}, Ho^{III} a Er^{III} s ligandy typu salenu, a jejich vybrané parametry související s magnetickými výměnnými interakcemi a anizotropií). Nejvyšší zjištěná bariéra U_{eff} mezi nimi je 42.3 K u komplexu $[CuTb(L3)(NO_3)_3(CH_3COCH_3)]$[92]. Obecně se vlastnosti jednomolekulových magnetů v těchto 3d-4f systémech vyskytují zřejmě výhradně v komplexech obsahujících Dy^{III} a Tb^{III}.

Co se týče magnetických výměnných interakcí, je mezi těmito sloučeninami vidět zajímavý trend. U všech komplexů obsahujících Cu^{II} byla zjištěna přítomnost ferromagnetické výměnné interakce, zatímco u komplexů V^{IV} jsou zastoupeny oba druhy výměny. Přestože tyto kovy mají oba $S = 1/2$, rozložení elektronů v orbitalech je jiné a konkrétně u mědi toto může vysvětlit, proč je ve všech studovaných případech výměna ferromagnetická.

Tabulka 2:Rešerše 3d-4f komplexů V^{IV} a Cu^{II} a lanthanoidů Gd^{III}, Tb^{III}, Dy^{III}, Ho^{III} a Er^{III} s ligandy typu salenu, a jejich vybrané parametry související s magnetickými výměnnými interakcemi a anizotropií. Ligandy L1 – L23 jsou vyobrazeny na Obrázku 26.

Komplex	J (cm^{-1})	τ_0 (s^{-1})	U_{eff} (K)	Ref
[(VO)Gd(L1)]NO_3·*n*(H_2O)]	−1.6			75
[(VO)Gd(L2)(NO_3)$_3$(H_2O)]	1.5			76
[(VO)Gd(L3)(NO_3)$_3$(CH_3COCH_3)]	−2.6			76
[(VO)Tb(L3)(NO_3)$_3$(CH_3COCH_3)]	0.06(1)			77
[(VO)Dy(L3)(NO_3)$_3$(CH_3COCH_3)]	0.28(1)			77
[(VO)Ho(L3)(NO_3)$_3$(CH_3COCH_3)]	−0.19(1)			77
[(VO)Er(L3)(NO_3)$_3$(CH_3COCH_3)]	−0.02(1)			77
[Cu2Tb2(L4)$_2$(NO_3)$_4$]	> 0	$1.7\cdot10^{-10}$	32	78
[Cu_2Dy_2(L4)$_2$(NO_3)$_4$]	> 0			78
[CuGd(L5)(NO_3)$_3$]	4.38/6.59			79
[DyCuL5(CH_3COO)$_2$(NO_3)]	> 0			80
[CuGd(L6)Cl_3(CH_3OH)$_2$]	7.78			81
[CuGd(S,S-L7)(NO_3)$_3$(CH_3OH)]$_n$	12.57			82
[CuGd(R,R-L7)(NO_3)$_3$(CH_3OH)]$_n$	14.816			82
[CuGd(L8)(CF_3SO_3)$_3$(H_2O)$_2$]	8.0(2)			83
[CuGd(L7)(CF_3SO_3)$_2$(H_2O)$_2$](CF_3SO_3)·H_2O·CH_3COCH_3	8.6(2)			83
[CuGd(L9)(NO_3)$_2$]$_2$	6.94			84
[CuGd(L4)(NO_3)$_2$]$_2$	7.26			84
[CuGd(L10)(NO_3)$_2$]$_2$	3.94			84
[CuGd(L11)(NO_3)$_2$(H_2O)]$_2$	2.80			84
[CuGd(L12)(NO_3)$_2$(H_2O)]$_2$	4.16			84
[CuGd(L13)(NO_3)$_2$(H_2O)]$_2$	5.89			84
[CuGd(L13)($C_7H_6NO_2$)$_2$]$_2$	2.56			84
[CuGd(L7)(NO_3)$_3$(H_2O)]	12.6			85
[CuGd(L14)(NO_3)$_3$]	10.8			85
[CuGd(L15)(NO_3)$_3$]	8.08			86
[CuGd(L16)(NO_3)$_{2.5}$(OH)$_{0.5}$(H_2O)]·0.5 H_2O	3.3			87
[CuGd(L17)(NO_3)$_3$]	1.3			87
[CuGd(L18)(CF_3COO)$_3$(CH_3OH)$_2$]	4.42(1)			88
[CuGd(L19)(NO_3)$_3$(CH_3COCH_3)]	5.6			89
[CuGd(L3)(Cl)$_2$(H_2O)$_4$]Cl·$2H_2O$	10.1			90
[CuGd(L3)(Cl)$_3$(H_2O)$_6$]	8.8(4)			90
[CuGd(L2)(N_3C_2)$_3$(H_2O)	7.8(1)			90
[CuGd(L2)(CF_3COO)$_3$(H_2O)	6.3(1)			90
[CuGd(L20)(NO_3)(H_2O)$_3$]	11.4			91
[CuGd(L3)(NO_3)$_3$(CH_3COCH_3)]	6.9			92
[CuTb(L3)(NO_3)$_3$(CH_3COCH_3)]	>3.3	$7.1(9)\cdot10^{-10}$	42.3(4)	92
[CuDy(L3)(NO_3)$_3$(CH_3COCH_3)]	1.63(1)	$4(2)\cdot10^{-10}$	11.5(10)	92
[CuHo(L3)(NO_3)$_3$(CH_3COCH_3)]	1.09(2)			92
[CuEr(L3)(NO_3)$_3$(CH_3COCH_3)]	0.24(1)			92
[CuGd(L3)(CH_3)$_3$(CH_3COCH_3)]	5.2			93
[CuGd(L6)(CH_3COO)($CF_3COCH_2COCF_3$)$_2$]	5.2			94
[CuTb(L3)(MeOH)(NO_3)$_2$(sal)]	4.2(2)	$3.0(8)\cdot10^{-8}$	32.9(4)	95
[CuDy(L3)(MeOH)(NO_3)$_2$(sal)]	2.0(2)	$1.02(11)\cdot10^{-5}$	26.0(5)	95
[CuHo(L3)(MeOH)(NO_3)$_2$(sal)]	1.3(1)			95
[CuGd(L21)(NCS)$_3$(H_2O)(CH_3COCH_3)]	9.20			96
[CuGd(L22)(NCS)$_3$(H_2O)]·2(CH_3COCH_3)	5.5			96
[CuGd(L23)(NO_3)$_2$(H_2O)$_3$]NO_3	5.08			97
[CuTb(L23)(NO_3)$_3$(MeOH)]		$2.1\cdot10^{-8}$	24.6	97

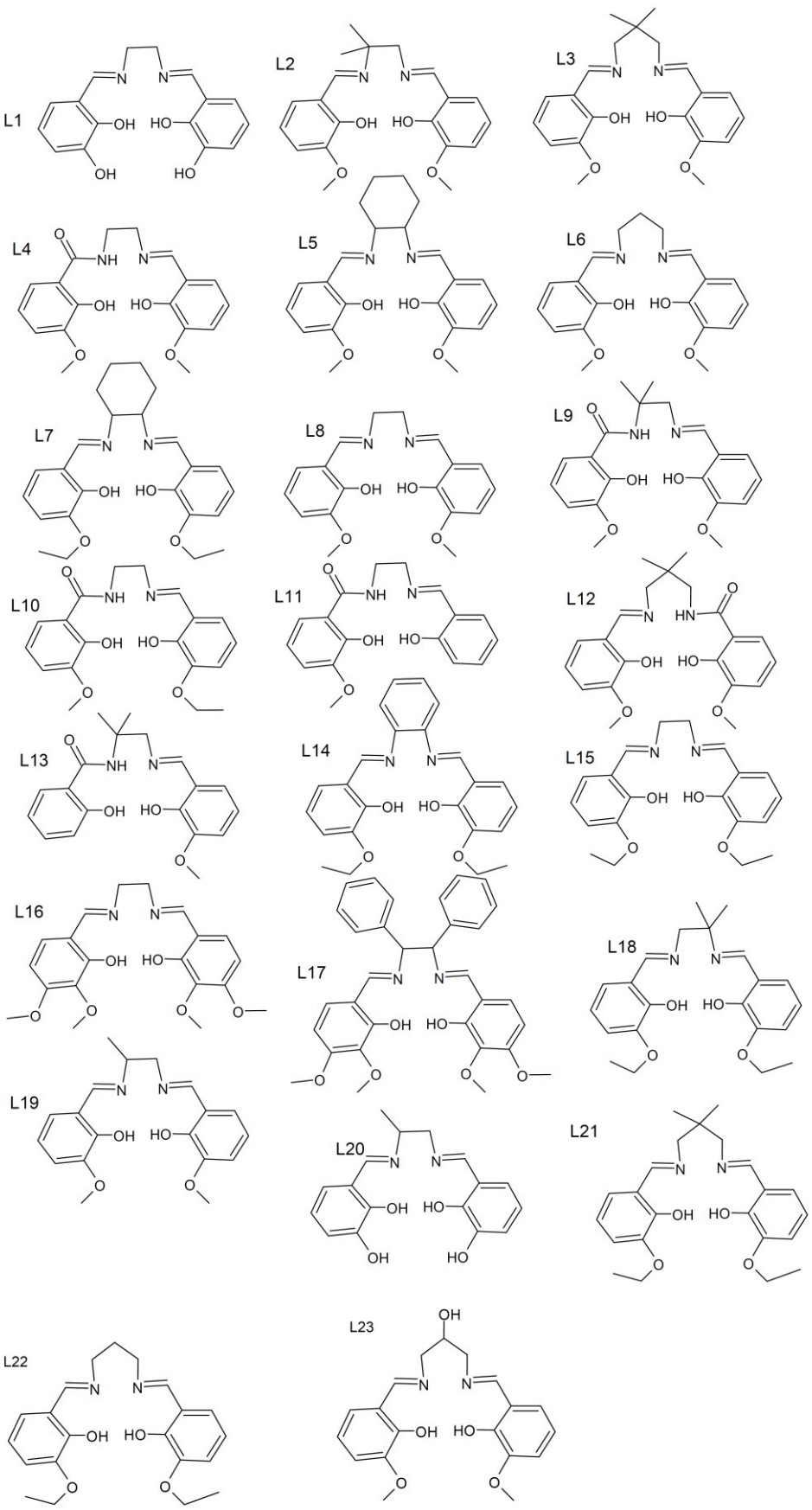

Obrázek 26: Ligandy využité při tvorbě komplexů uvedených v Tabulce 2 spolu s jejich označením.

3.4 Komplexy kobaltu ve tvaru trigonálního prizmatu

Trigonální prizma je tvar koordinačního polyedru, který je vhodný pro jedno-molekulové magnety kobaltu kvůli svému štěpení v ligandovém poli (Obrázek 4: Ukázka štěpení d-orbitalů pro trigonální prizma (a) a oktaedr (b). V tomto typu symetrie (D_{3h}) je základním termem pro konfiguraci $3d^7$ (tedy Co^{II}) ^4E. Pro tyto komplexy je běžné, že mají velký a záporný *D*-parametr.[98] Toto se ukazuje i v praxi, kde mnoho komplexů Co^{II} ve tvaru trigonálního prizmatu má vlastnosti jedno-molekulových magnetů i v nulovém magnetickém poli.

Tabulka 3: Vybrané komplexy Co^{II} ve tvaru trigonálního prizmatu spolu s jejich magnetickými parametry a CSM (continuous shape measurements)[99] popisujícími odchylku od ideálního tvaru těchto komplexů

Komplex	*D* (cm^{-1})	*E* (cm^{-1})	U_{eff} (cm^{-1})	τ_0 (s)	*B* (T)	CSM TP	CSM OH	Ref.
$[Co(tppm)][BPh_4]_2$	-97.2(2)	$9.3(1)\cdot10^{-3}$	192	$2.6(2)\cdot10^{-12}$	0	0.554	15.893	[100]
$[Co(hpy)][BPh_4]_2\cdot3CH_2Cl_2$	−107.5(4)	3.5(3)	20	$1.2(1)\cdot10^{-3}$	0	2.471	8.237	[100]
$[Co(PzOx)_3(BC_6H_5)]Cl\cdot CHCl_3$	-82	0.246	152	$2.07\cdot10^{-9}$	0	0.828	16.272	[101]
$[Co(AcimOx)_3(BC_6H_5)]ClO_4$	-102.5		101	$2.56\cdot10^{-6}$	0	0.905	13.462	[102]
$[Co(AcPyOx)_3BC_6H_5]ClO_4$	-86		194.6	$3.55x10^{-10}$	0	2.006	10.042	[103]
{Na[(Chdc)Co]}(BPh4)3	-75.8	$9.1\cdot10^{-4}$	52.6		0.1	1.793	9.293	[104]
$[Co(tppm)][ClO_4]_2\cdot2CH_3CN\cdot H_2O$	-80.7	0.6	39.2	$1.7\cdot10^{-4}$	0	0.588	14.920	[105]
$(HNEt_3)[Co^{II}Co^{III}_3(hpmp)_6]$	-115	2.8	76.3	$1\cdot10^{-7}$	0	2.341	9.284	[106]
$[Co(neo)(CH_3COO)_2]$			26.3	$1.361\cdot10^{-7}$	0.1	3.761	11.893	[107]
$[Co(neo)(piv)_2]$			13.2	$6.2\cdot10^{-6}$	0.1	9.801	7.650	[107]
$[Co(neo)(4OH\text{-}benz)_2]\cdot2CH_3OH$			12.2	$1.04\cdot10^{-6}$	0.1	10.110	6.352	[107]

Výše uvedené komplexy dosahují energetických bariér až 200 cm^{-1}, což je sice málo v porovnání s lanthanoidy, ale mezi d-prvky jde o velmi dobré výsledky. Roli hraje i to, že u lanthanoidů relaxace může probíhat mezi vyššími Kramersovými dublety, u kobaltu jsou tyto dublety pouze dva.

Mezi komplexy uvedenými v tabulce 3 si můžeme všimnout, že je jejich geometrie dosahováno pomocí tří syntetických postupů. Prvním z nich je navázání tří bidentátních heterocyklických ramen tak, aby rigidně držely tvar, například na jeden atom boru nebo v polohách 1,3,5 na cyklohexan.[100-105] Druhou metodou, využitou u komplexu $[Co^{II}Co^{III}_3(hpmp)_6]^+$, je Co^{II} obklopený třemi částicemi $\{Co^{III}(hpmp)_2\}$, kde hpmp je šestivazný $[N_2O_4]$ ligand. Tyto částice slouží jako metaloligandy, každá z nich se váže dvěma kyslíky na Co^{II} a díky sterickým faktorům drží jeho koordinační sféru ve tvaru trigonálního prizmatu.[106] Příbuzná je pak třetí metoda, kde se používá sterického vlivu přímo ligandů, jak je vidět například u komplexu $[Co(neo)(CH_3COO)_2]$, kde je příčinou této geometrie pravděpodobně sterický vliv methylových skupin na neokuproinu, díky kterým komplex zaujímá tvar blízký trigonálnímu prizmatu, avšak u více

objemných ligandů pivalátu a 4-hydroxybenzoátu už dochází k silné deformaci, kde není výsledný tvar blízký ani oktaedru, ani trigonálnímu prizmatu.[107]

4. Výsledky a diskuse

Tato část je věnovaná výsledkům dosažených během řešení disertační práce, které byly publikovány v impaktovaných časopisech. Celkem bylo během řešení této disertační práce publikováno 6 článků v odborných časopisech, které jsou zde následně krátce popsány a pak jsou kompletně uvedeny jako přílohy k disertační práci. Jedná se o následující články:

1. **Kotrle, K.**; Herchel, R. Are Inorganic Single-Molecule Magnets a Possibility? A Theoretical Insight into Dysprosium Double-Deckers with Inorganic Ring Systems. *Inorg. Chem.* **2019**, *58* (20), 14046–14057. https://doi.org/10.1021/acs.inorgchem.9b02039. – Příloha 1, komentář ke článku a jeho závěrům je popsán v kapitole 4.1.

2. **Kotrle, K.**; Atanasov, M.; Neese, F.; Herchel, R. Theoretical Magnetic Relaxation and Spin–Phonon Coupling Study in a Series of Molecular Engineering Designed Bridged Dysprosocenium Analogues. *Inorg. Chem.* **2023**, *62* (42), 17499–17509. https://doi.org/10.1021/acs.inorgchem.3c02916. – Příloha 2, komentář ke článku a jeho závěrům je popsán v kapitole 4.2.

3. **Kotrle, K.**; Nemec, I.; Moncol, J.; Čižmár, E.; Herchel, R. 3d–4f Magnetic Exchange Interactions and Anisotropy in a Series of Heterobimetallic Vanadium(IV)–Lanthanide(III) Schiff Base Complexes. *Dalton Trans.* **2021**, *50* (39), 13883–13893. https://doi.org/10.1039/D1DT01944A. – Příloha 3, komentář ke článku a jeho závěrům je popsán v kapitole 4.3.

4. **Kotrle, K.**; Nemec, I.; Antal, P.; Petrželová, K.; Čižmár, E.; Herchel, R. 2-Formylphenoxyacetic Acid Schiff Bases: A Promising Ligand Scaffold for Readily Available Trigonal Prismatic Co(II) Single-Ion Magnets. *Inorg. Chem. Front.* **2023**, *10* (24), 7319–7332. https://doi.org/10.1039/D3QI01691A. – Příloha 4, komentář ke článku a jeho závěrům je popsán v kapitole 4.4.

5. Bhanja, A.; Smythe, L.; **Kotrle, K.**; Ortu, F.; Herchel, R.; Murrie, M.; Ray, D. Synthesis of Heptanuclear Ni4Dy3 Coordination Aggregate Using Tridentate Ligand: X-Ray

Structure, Magnetism and Theoretical Studies. *Inorganica Chim. Acta* **2021**, *526*, 120524. https://doi.org/10.1016/j.ica.2021.120524. - Příloha 5, komentář ke článku a jeho závěrům je popsán v kapitole 4.5.

6. Dutta, B.; Guizouarn, T.; Pointillart, F.; **Kotrle, K.**; Herchel, R.; Ray, D. Lanthanoid Coordination Prompts Unusually Distorted Pseudo-Octahedral Ni^{II} Coordination in Heterodinuclear Ni–Ln Complexes: Synthesis, Structure and Understanding of Magnetic Behaviour through Experiment and Computation. *Dalton Trans.* **2023**, *52* (30), 10402–10414. https://doi.org/10.1039/D3DT01387A. - Příloha 6, komentář ke článku a jeho závěrům je popsán v kapitole 4.6.

4.1 Teoretická studie anorganických sendvičových komplexů dysprosia jako analogů cyklopentadienylových komplexů

V rámci této části práce byly pomocí teoretických metod studovány vlastnosti 5 komplexů dysprosia ($[Dy(N_5)_2]^+$, $[Dy(P_5)_2]^+$, $[Dy(B_3N_3)_2]^{3+}$, $[Dy(B_3P_3)_2]^{3+}$, $[Dy(B_3S_3)_2]^{3+}$. Studie byla zaměřena na jejich elektronovou strukturu a na magnetickou anizotropii, a to jak z pohledu statického, tak z hlediska dynamických vlastností, které se týkají interakce molekulových vibrací s magnetickými vlastnostmi (spin-fononová interakce). Cílem pak bylo na základě této analýzy evaluovat potenciální využitelnost těchto komplexů jako jedno-molekulových magnetů. Zaměřili jsme se také na vliv substituce uhlíkových atomů v organometalických komplexech dysprosia na magnetické vlastnosti látek, zejména spin-fononovou interakci, s cílem případně určit, zda by tato substituce mohla být potenciálně využitelný směr pro design jedno-molekulových magnetů.

Na začátku bylo nutné optimalizovat struktury těchto látek (Obrázek 27), což bylo provedeno pomocí metod DFT (detaily o provedení výpočtů jsou v Příloze 1). Při optimalizaci byly zároveň vypočítány frekvence molekulových vibrací a ověřeno, že žádná z nich není imaginární, a tedy optimalizovaná struktura opravdu odpovídá energetickému minimu. Dále pak bylo ověřeno, zda jsou ligandy aromatické, pro což byl použit Shannonův index, vycházející z informační entropie elektronové hustoty v kritických bodech vazeb, které jsou definovány v teorii atomů v molekulách (QT-AIM). Po tomto ověření byly porovnány základní geometrické parametry, bylo zjištěno, že jsou tyto kruhy o něco více deformované v tom, že úhel mezi středy kruhů a centrálním atomem je menší než ideálních 180°, a že tato deformace je u těchto komplexů

větší než u porovnávaných známých cyklopentadienylových komplexů, a to pravděpodobně z důvodu substituce, která tvoří sterickou zábranu (Příloha 1 Tabulka 1)

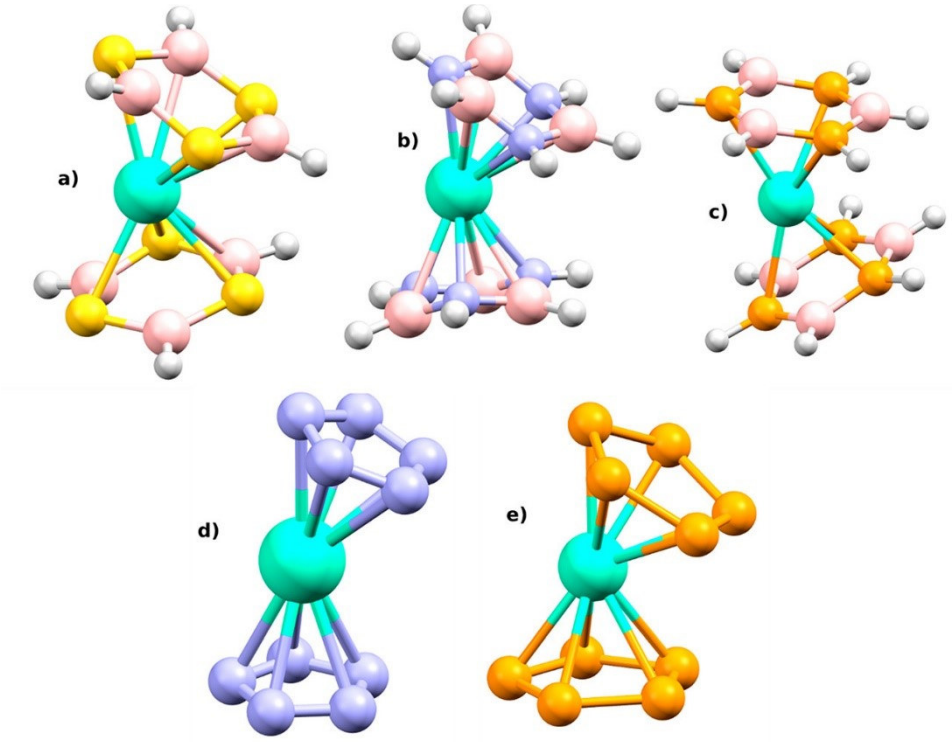

Obrázek 27: Optimalizované struktury komplexů $[Dy(B_3S_3)_2]^{3+}$, $[Dy(B_3N_3)_2]^{3+}$, $[Dy(B_3P_3)_2]^{3+}$, $[Dy(N_5)_2]^{+}$, $[Dy(P_5)_2]^{+}$ (a-e).

Dále pak byly prozkoumány magnetické vlastnosti a elektronová struktura pomocí metod CASSCF a také metod zahrnujících dynamickou korelaci NEVPT2 a DCD-CAS(2). Pomocí těchto metod byly získány informace o elektronové struktuře, například energie f-orbitalů (Příloha 1 Obrázek 2) nebo energetická struktura Kramersových dubletů. U ní bylo provedeno porovnání metod a zjištěno, že zahrnutí dynamické korelace způsobuje zvýšení energií Kramersových dubletů oproti běžné CASSCF metodě, více patrné je to u metody DCD-CAS(2). Porovnání metod CASSCF z programu ORCA s využitím ZORA relativistické korekce a z programu MOLCAS s DKH korekcí dává očekávatelně poměrně podobné výsledky. Metoda ZORA však vypočítává hladiny Kramersových dubletů lehce vyšší. Co se týče energetických hladin komplexů, ukazuje se, že nejvyšší štěpení, a tím pádem i nejvyšší anizotropii mají komplexy $[Dy(N_5)_2]^{+}$, $[Dy(P_5)_2]^{+}$ a $[Dy(B_3N_3)_2]^{3+}$. Z těchto výsledků vyplývá, že mezi studovanými komplexy mají větší energetické štěpení komplexy s aniontovými ligandy oproti neutrálním ligandům, a pak také to, že štěpení roste s rostoucí elektronegativitou atomů v ligandech (Obrázek 28).

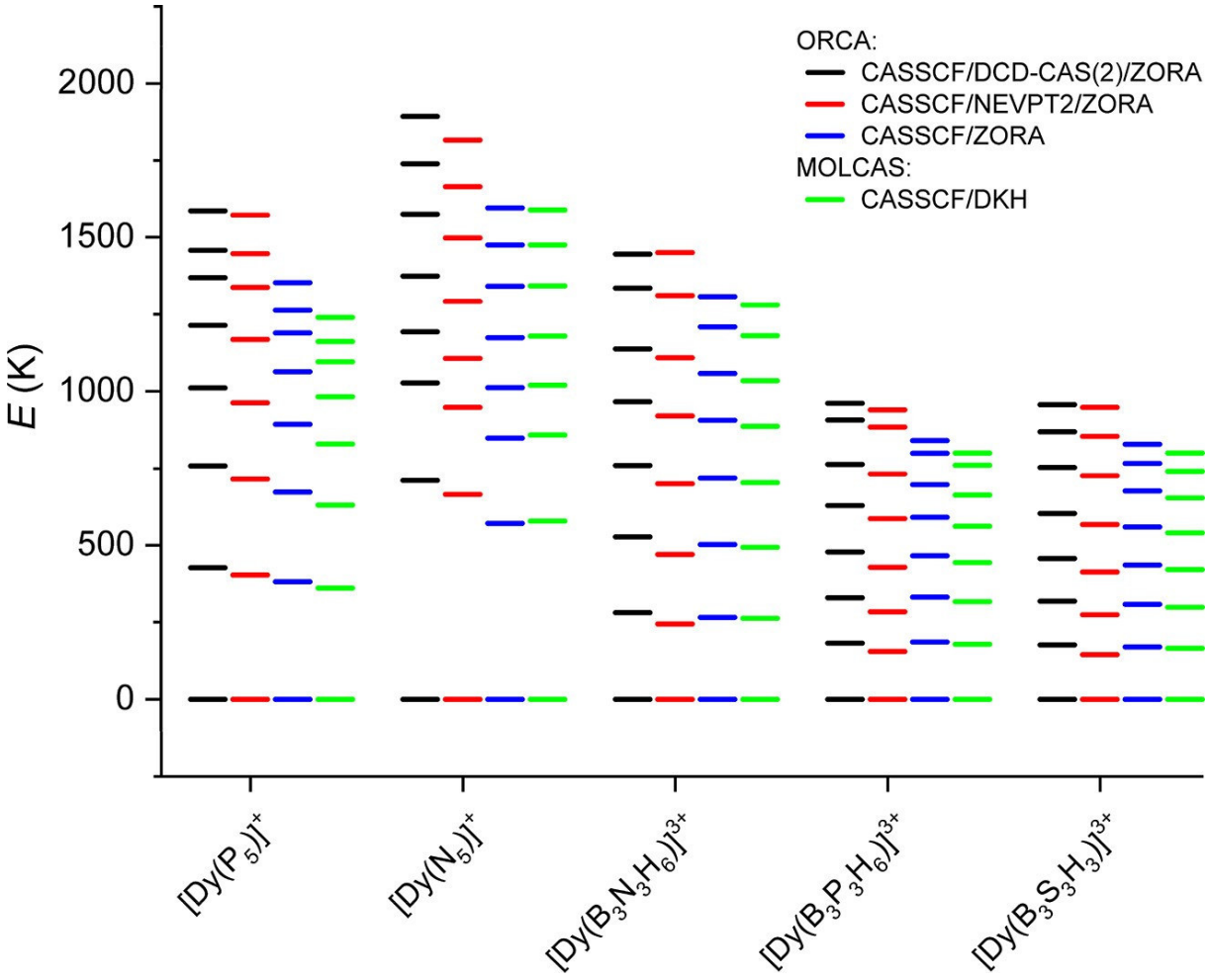

Obrázek 28: Porovnání energie Kramersových dubletů vypočítaných pomocí různých metod pro studované komplexy.

Kromě výpočtu energií byla dále provedena analýza relaxace magnetizace pomocí softwaru Single_aniso, který umožňuje vypočítat maticové elementy magnetického momentu mezi hladinami Kramersových dubletů, což by mělo odpovídat pravděpodobnostem přechodu mezi těmito hladinami. Z hladin pravděpodobností přechodů lze následně odhadnout, přes které hladiny může směřovat nejpravděpodobnější cesta relaxace magnetizace. Ideální stav je, pokud cesta relaxace dosahuje k energeticky vysokým hladinám Kramersových dubletů, protože to teoreticky vede k vysokým energetickým bariérám U_{eff} (Obrázek 29).

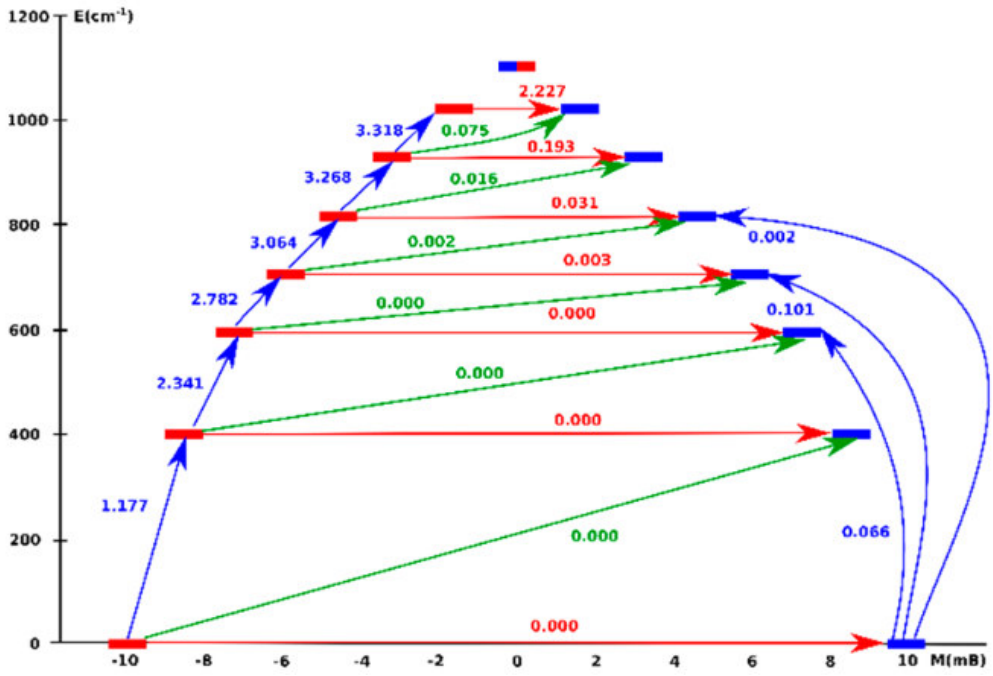

Obrázek 29: Znázornění Kramersových dubletů a pravděpodobností přechodů mezi nimi pro komplex $[Dy(N_5)_2]^+$

I podle tohoto kritéria se ukázala jako nejlepší varianta ze studovaných komplexů látka $[Dy(N_5)_2]^+$ kvůli nízkému kvantovému tunelování magnetizace, kde podle modelu Single_aniso je možné očekávat silné tunelování až od šestého dubletu výše, zatímco u ostatních sloučenin je tunelování vyšší a často patrné už v nižších dubletech. U látky $[Dy(B_3S_3)_2]^{3+}$ je navíc očekávatelné, že v druhém dubletu dojde k velké změně orientace magnetizace oproti základnímu stavu, což je pro jedno-molekulový magnet v praktickém použití nežádoucí.

Kromě analýzy jednotlivých stavů byla v práci použita i metoda předpovídání velikosti energetické bariéry (Příloha 1, rovnice 3 a 4). I z této metody se ukazuje komplex $[Dy(N_5)_2]^+$ jako nejvíce zajímavý, kde by jeho energetická bariéra U_{eff} měla dosahovat velikosti 1475 K, což je s relativně velkým odstupem i od ostatních sledovaných komplexů, kde druhý $[Dy(P_5)_2]^+$ má předpovězenou velikost energetické bariéry 1127 K, poté $[Dy(B_3N_3)_2]^{3+}$ s 1009 K. Ostatní komplexy s deriváty borazinu mají předpovězenou velikost energetických bariér nižší než 1000 K (734 K pro $[Dy(B_3P_3)_2]^{3+}$ a 650 K pro $[Dy(B_3S_3)_2]^{3+}$). Tyto hodnoty jsou sice nižší, než u nejlepších známých jedno-molekulových magnetů, avšak i tak by byl alespoň komplex $[Dy(N_5)_2]^+$ zajímavou možností, jak připravit potenciálně velmi dobrý jedno-molekulový magnet.

Mimo statických vlastností byly v této práci zkoumány i dynamické vlastnosti elektronové struktury a magnetické anizotropie, tedy interakce s fonony reprezentovanými molekulovými

vibracemi (spin-fononová interakce). Pro ten byly zvoleny dvě varianty výpočtu, pomocí derivace g_z nebo maticových elementů magnetických momentů z programu Single_aniso (k_{QT}), podle deformace způsobené vibračními módy (Příloha 1 rovnice 5).

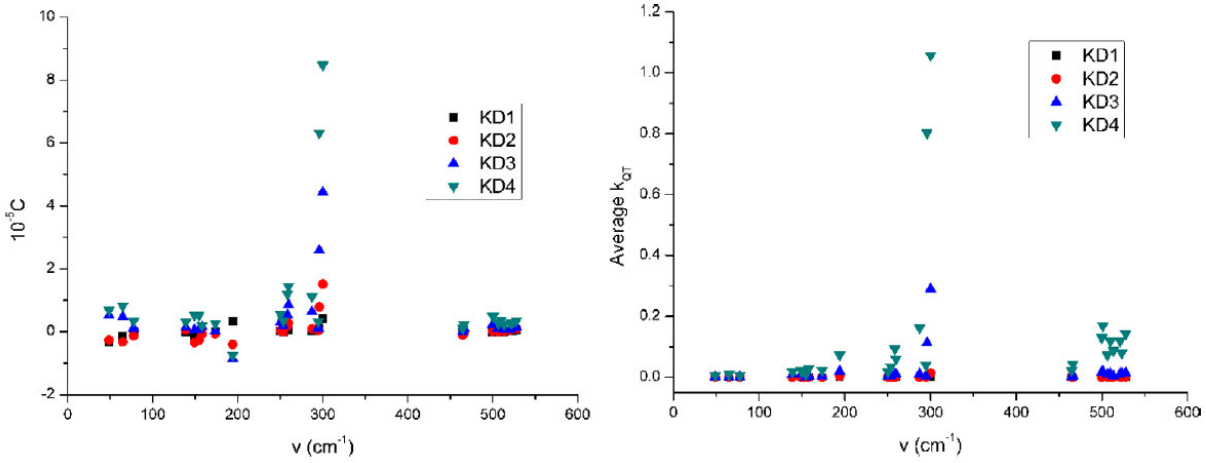

Obrázek 30: Analýza spin-fononové interakce na základě g_z (vlevo) a maticových prvků magnetického momentu (vpravo) pro $[Dy(P_5)_2]^+$

Tato analýza umožňuje určit aktivní vibrace, jejichž deformace koordinačního okolí centrálního atomu nejvíce narušuje magnetickou anizotropii, a tím pádem usnadňuje magnetickou relaxaci. U obou studovaných metod byla často nalezena poměrně dobrá shoda, stejně jako vyobrazení vybraných nejvíce aktivních vibrací. Co se týče porovnání všech studovaných komplexů na základě velikosti koeficientů, ukazují se jako nejvýhodnější opět komplexy $[Dy(N_5)_2]^+$, případně $[Dy(P_5)_2]^+$ (Obrázek 30).

Závěrem, v této práci bylo rozvinuto využití výpočtů U_{eff} pomocí metody využívající vypočítané hodnoty energií Kramersových dubletů, což je plánováno rozvíjet dále jako zajímavý ukazatel, který lze získat pouze z teoretických výpočtů. Dále také tato práce přispěla k rozvoji metod využívajících spin-fononovou interakci a její závěry byly pak dále rozvinuty. Mimo jiné byla citována i při syntéze sloučenin podobných dysprosoceniu, obsahujících heteroatomy v aromatických kruzích.[56] Stejně tak se o predikovaných sloučeninách studovaných v této publikaci diskutovalo i v rámci rozvoje teoretických metod směrem k *ab initio* výpočtům relaxačních časů, kde byly využity jako modelové systémy.[41b]

4.2 Teoretická studie sendvičových komplexů dysprosia s alkylovými spojkami jako analogů dysprosocenia

Tato práce navazuje na závěry zpracované v předchozí kapitole. Na rozdíl od anorganických ligandů byly v této práci zvoleny ligandy typu cyklopentadienylu, které jsou používané i u reálných komplexů tohoto typu. Byly tedy studovány komplexy s cyklopentadienylovými kruhy propojenými pomocí butylenových spojovacích článků, které byly k těmto ligandům připojeny v různých počtech (**1-5**, komplexy jsou označeny podle jejich počtu) a různých polohách (komplexy **2a** a **2b** – 1,2 a 1,3 izomery, a komplexy **3a** a **3b** – 1,2,3 a 1,2,4 izomery) (Obrázek 31). Cílem této práce bylo optimalizovat struktury těchto komplexů a následně analyzovat jejich magnetickou anizotropii prostřednictvím teoretických metod studujících štěpení energetických hladin. Dále pak byly studovány také interakce těchto systémů s molekulovými vibracemi se snahou kvantifikovat spin-fononovou interakci.

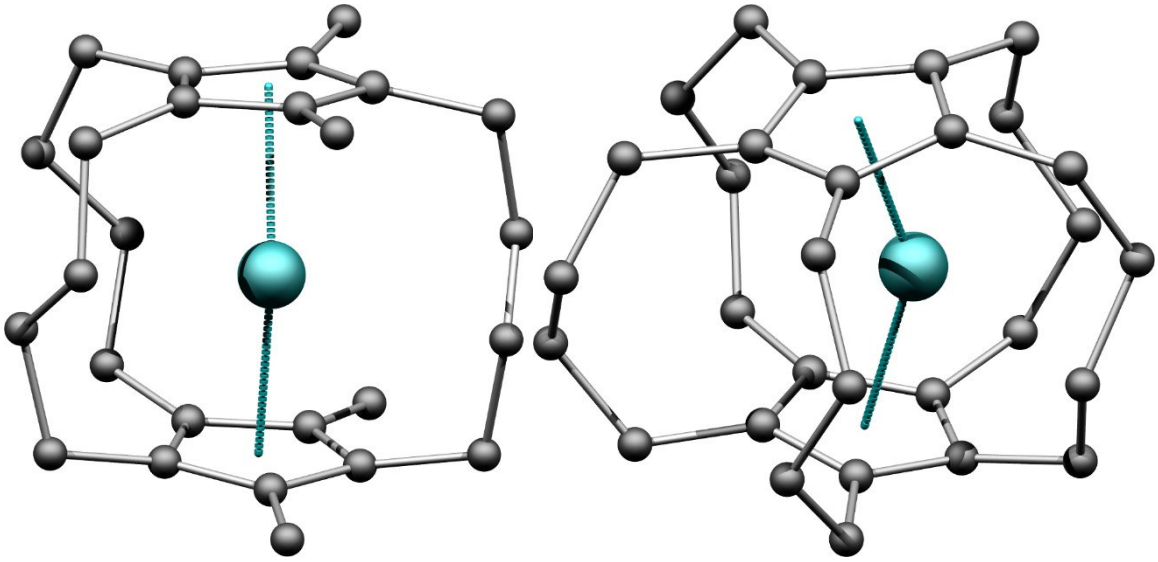

*Obrázek 31: Optimalizované struktury komplexů **3b** a **5***

Pomocí metody DFT byly optimalizovány geometrie sedmi studovaných komplexů s různým počtem a polohou linkerů (Příloha 2, Tabulka 1 a Schéma 1). Geometrické parametry u optimalizovaných komplexů byly porovnány s geometrickými parametry u podobných sloučenin, u kterých jsou známy struktury, konkrétně s $[Dy(Cp^{iPr5})(Cp^{Me5})]^+$ (**6**) a $[Dy(Cp^{tBu3})_2]^+$ (**7**)[10a,b]. Porovnání (Příloha 2 Tabulka 2) ukázalo, že u optimalizovaných struktur dochází ke zkracování vzdálenosti mezi cyklopentadienylovým kruhem a centrálním atomem. Tento vliv je zřetelnější u látek s větším počtem spojovacích ramen pravděpodobně kvůli sterickému vlivu. Podobný trend je vidět také u snižování úhlu mezi středy cyklopentadienylových kruhů

a centrálním atomem, kde se opět tento úhel s počtem spojovacích ramen zmenšuje. Výjimkou je komplex **3b**, tedy komplex se třemi rameny v polohách 1,2,4-, u kterého je tento úhel 168°, tedy více, než u ostatních studovaných komplexů a i porovnávaných molekulových struktur známých komplexů.

U těchto komplexů byly také vypočítány frekvence molekulových vibrací (Obrázek 32), aby bylo zjištěno, že struktura odpovídá skutečnému energetickému minimu, tedy že žádné z frekvencí nejsou imaginární. Kromě sedmi studovaných komplexů, označených jako **1, 2a, 2b, 3a, 3b, 4, 5**, byla vypočítaná spektra porovnána i s optimalizovanými strukturami komplexů **6** a **7**.

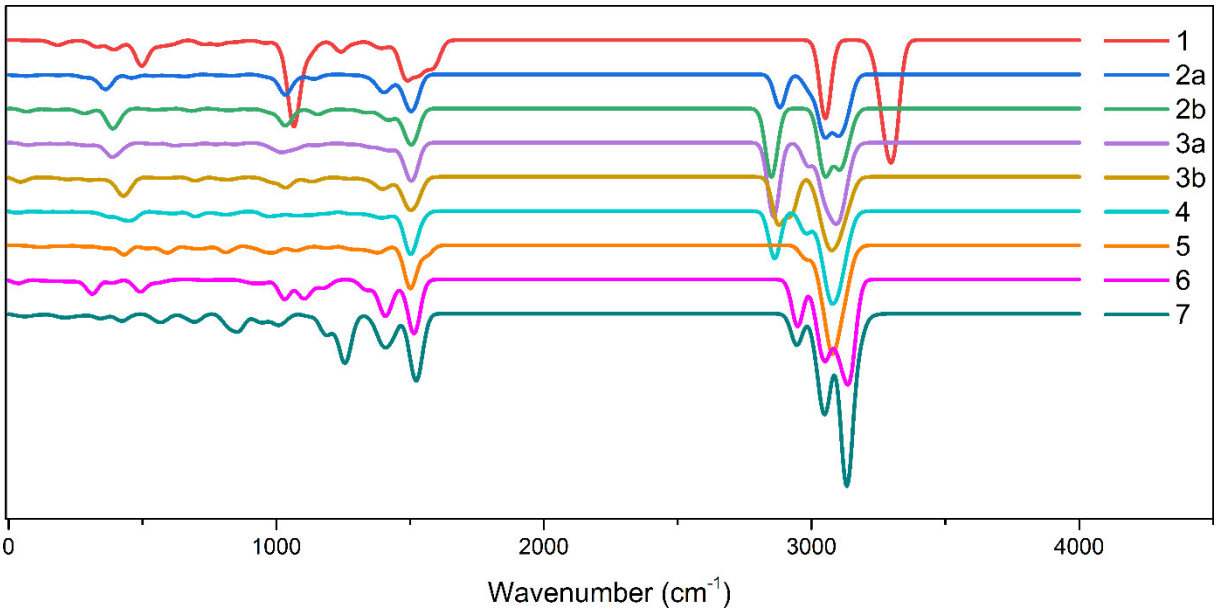

*Obrázek 32: Simulovaná infračervená spektra pro komplexy **1-7***

Kromě toho byla provedena také analýza rigidity těchto komplexů založená na dvou metodách. První metoda analyzuje velikost délky pohybu atomu dysprosia a atomů uhlíku v cyklopentadienylových kruzích způsobenou vibracemi, kdy by teoreticky komplex s nejmenšími pohyby měl být nejvíce rigidní. Tato metoda analýzy ukázala trend, že s narůstajícím počtem spojovacích ramen rigidita roste, zároveň jsou ale studované komplexy **1-5** méně rigidní než komplexy **6** a **7**. Druhá metoda analýzy rigidity se zabývala počtem nízko ležících molekulových vibrací s myšlenkou, že čím energeticky výše se vibrace u komplexu nachází, tím více je tento komplex rigidní. Podle této analýzy naopak vyšly komplexy **6** a **7** jako nejméně rigidní a jako nejvíce rigidní se ukázaly komplexy **1** a **5** (Obrázek 33).

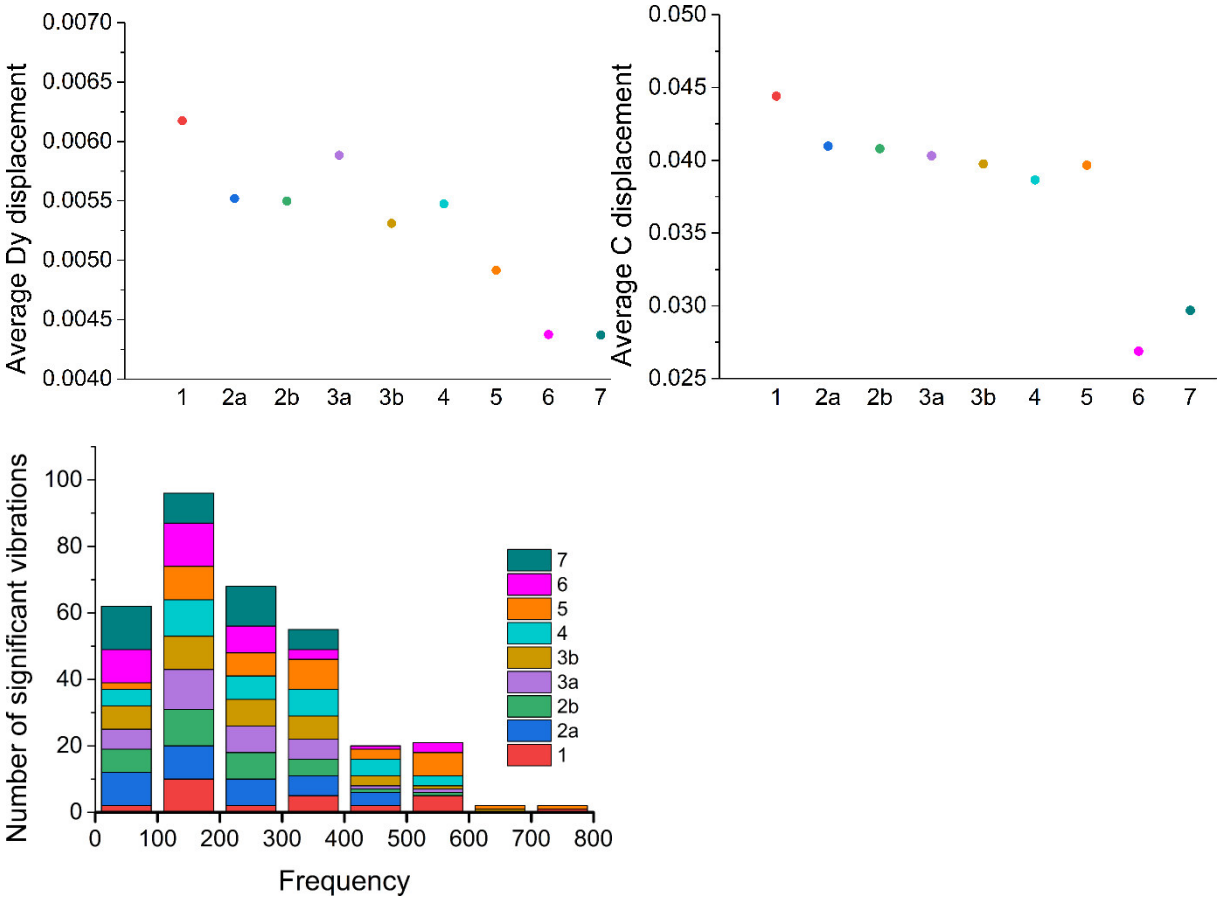

Obrázek 33: Výsledky analýzy rigidity na základě pohybu atomů v důsledku molekulových vibrací a počtu vibrací na nízkých frekvencích

V další fázi byla studována struktura energetických hladin u studovaných komplexů pomocí metody CASSCF. Pomocí této metody byl zjištěn rozsah energetického štěpení Kramersových dubletů, kde bylo zjištěno, že štěpení je největší u látky **3b**, která je srovnatelná a potenciálně i lepší, než porovnávané známé komplexy $[Dy(Cp^{iPr5})(Cp^{Me5})]^+$ (**6**) a $[Dy(Cp^{tBu3})_2]^+$ (**7**). Tato vlastnost byla dále porovnána s velikostí úhlu mezi centroidy a centrálním atomem, kde byla nalezena zřejmá korelace mezi velikostí úhlu a štěpením mezi základním a prvním excitovaným Kramersovým dubletem (Obrázek 34).

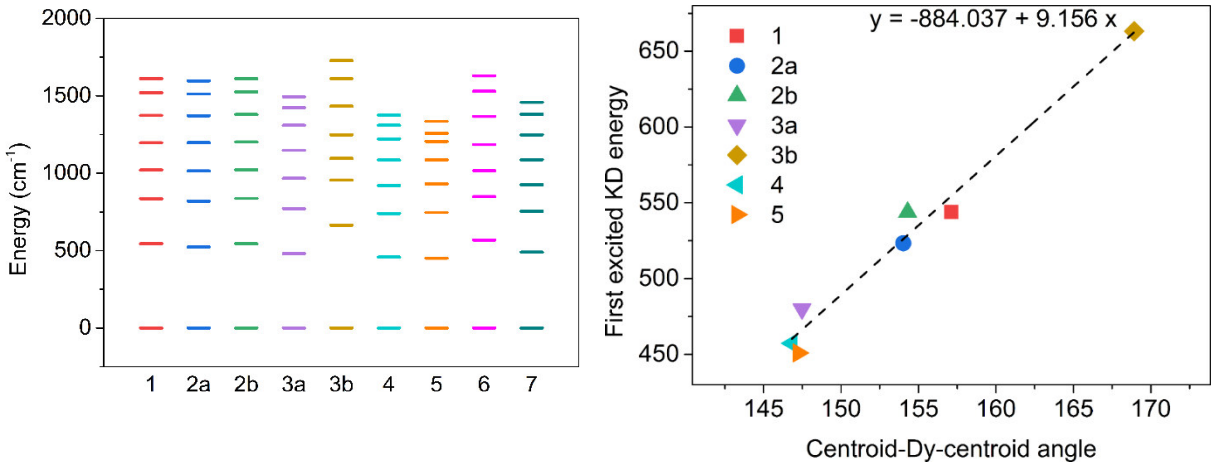

*Obrázek 34: Energie Kramersových dubletů (vlevo) a korelace energie prvního excitovaného dubletu s úhlem mezi středy ligandů (vpravo) pro komplexy **1-7**, respektive **1-5**.*

Následně byly Kramersovy dublety analyzovány pomocí programu Single_Aniso, který umožňuje kvantifikovat pravděpodobnost přechodů mezi magnetickými hladinami. Z těchto dat vychází, že signifikantní kvantové tunelování magnetizace je přítomné až ve vyšších hladinách, u většiny komplexů od pátého Kramersova dubletu, u komplexu **3b** například až u šestého (Příloha 2, Obrázek 5). Z těchto dat byla následně vypočítána velikost energetické bariéry (Příloha 1 Rovnice 1-3), a pomocí ní byly odhadnuty velikosti blokovacích teplot pro Orbachův jev.

Tabulka 4: Vypočítané velikosti energetických bariér pro 300 K, odhady blokovacích teplot a energetické bariéry nezávislé na teplotě (Příloha 2, rovnice 1-3)

Komplex	**1**	**2a**	**2b**	**3a**	**3b**	**4**	**5**	**6**	**7**
U_{eff}/K	2069	2072	1991	1888	2306	1777	1749	2233	2023
T_B/K	73.9	74	71.1	67.4	82.3	63.4	62.5	79.8	72.3
$U_{\mathrm{eff}}^{\mathrm{TI}}/K$	2239	2228	2221	2057	2423	1880	1805	2315	2069

Z těchto výsledků se opět ukazuje, že co se týče vlastností plynoucích z distribuce energetických hladin, nejlepším komplexem ze série by měl být komplex **3b**, zřejmě kvůli jeho struktuře, která je více lineární, než u ostatních komplexů. Lze také čekat, že by mohl dosahovat podobných vlastností, jako známé komplexy **6** a **7**, tedy nejlepší v současnosti známé jedno-molekulové magnety. Navíc je vidět u komplexů **6** a **7** poměrně dobrá shoda s experimentálními hodnotami (2219 K pro **6** a 1761 K pro **7**).

Jako další rozšíření možností jak studovat vlastnosti těchto látek byl sledován vliv molekulových vibrací na magnetickou anizotropii připravených látek. Pro tyto účely byla v této práci vyvinuta nová metoda, která spoléhá na výpočet energetické bariéry U_{eff} pro struktury deformované molekulovými vibracemi (Příloha 2 Rovnice 4) (Obrázek 35), která byla následně porovnána s metodou využívající parametry krystalového pole (Příloha 2 Rovnice 6) (Obrázek 36). Výhodou nové metody je, že používá veličinu přímo spjatou s relaxací magnetizace a započítává do vlivu vibrací jak změny energetických hladin, tak i přechodové magnetické momenty mezi hladinami úměrné rychlosti tunelování mezi dublety.

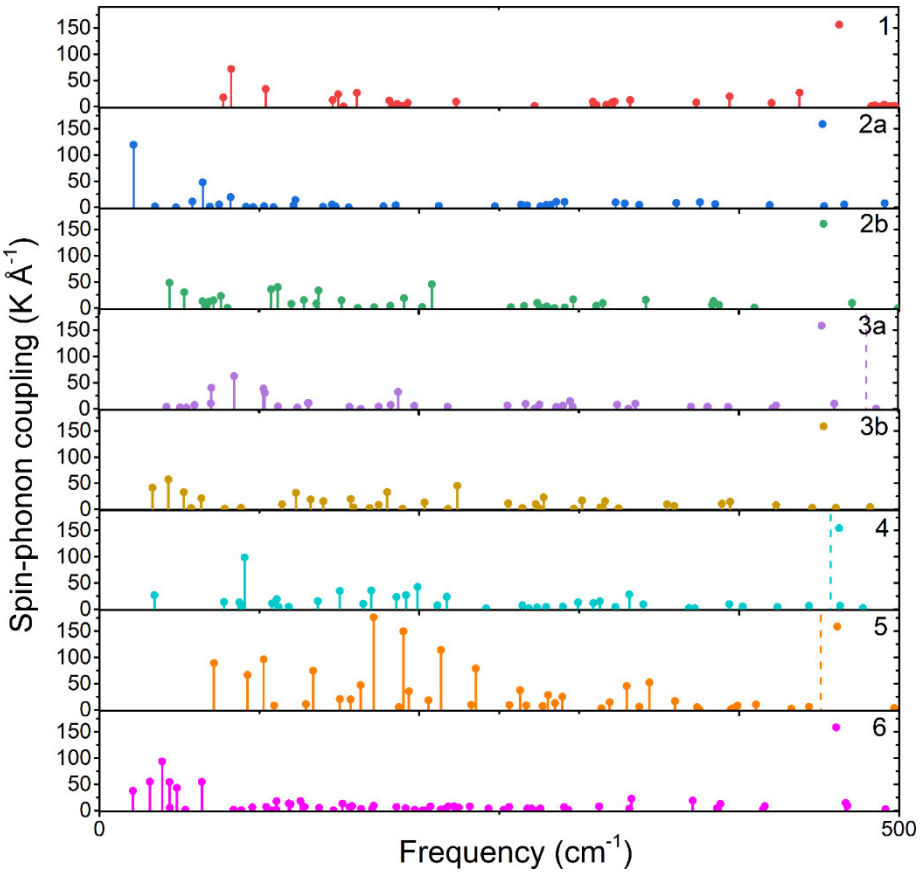

*Obrázek 35: Porovnání spin-fononové interakce vypočítané metodou $|\partial U_{eff}^{TI}/\partial q_{\alpha}|$ v komplexech **1-6***

Pomocí této metody je možné určit signifikantní molekulové vibrace, které budou zodpovědné za přenos energie při magnetické relaxaci. Důležitým parametrem je pak kromě velikosti spin-fononové interakce také jejich energetická dostupnost, která je nejvýhodnější u komplexů **1** a **5**, kde jsou první vibrace energeticky výše než u ostatních komplexů. Dalším důležitým faktorem je pak překryv vibrací s energiemi přechodů mezi Kramersovými dublety. Tento překryv je malý zejména u komplexu **3b**, který má energie Kramersových dubletů výše než ostatní studované komplexy.

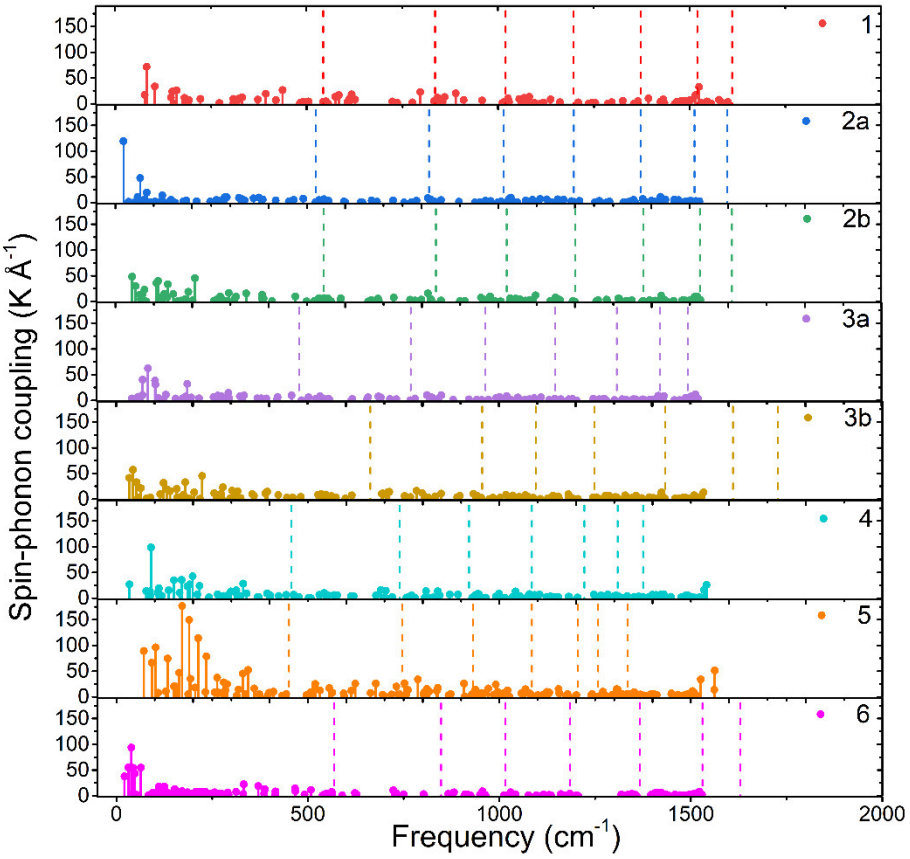

*Obrázek 36: Porovnání spin-fononové interakce vypočítané metodou $|\partial B_m^l/\partial q_\alpha|$ v komplexech **1-6***

Závěrem, v tomto článku byl teoreticky studován nový a potenciálně velmi zajímavý přístup k přípravě nových jedno-molekulových magnetů pomocí spojování cyklopentadienylových ligandů, který by mohl vést ke komplexům s velmi vysokými energetickými bariérami. Kromě jejich charakterizace běžnými teoretickými metodami byla studie doplněna o poměrně nové metody *ab initio* výpočtu energetické bariéry U_{eff} a její využití pro výpočet spin-fononové interakce jako alternativu k současným metodám. Celkově se jako nejlepší komplex ze série ukázal **3b**, který vyniká hlavně vysokou energetickou bariérou a odlišuje se od ostatních komplexů v geometrických parametrech.

4.3 Výměnné interakce a magnetická anizotropie v komplexech V^{IV}-Ln^{III} s Schiffovou bází typu salenu jako ligandem

Tato část práce je věnovaná přípravě a charakterizaci série dimerních komplexů vanadylu s lanthanoidy (Gd (**1**), Tb (**2**), Dy (**3**), Er (**4**)). V systémech obsahujících tyto kovy byly pomocí experimentálních a teoretických metod studovány jejich magnetické vlastnosti se zaměřením na magnetické výměnné interakce a vlastnosti jedno-molekulových magnetů. Existuje poměrně velké množství podobných systémů obsahujících Cu^{II}, avšak komplexy vanadu jsou

v této oblasti poměrně málo prozkoumané, a cílem této práce bylo tuto oblast výzkumu rozvinout. Dále pak tyto komplexy mohou být potenciálně použitelné jako stavební bloky pro konstrukci heterotrimetalických komplexů.[108]

V této části byla připravena série čtyř komplexů. Syntéza byla provedena v několika krocích. Nejprve byl připraven volný ligand (L) Schiffovou kondenzací *o*-vanilinu a propylendiaminu. Z tohoto prekurzoru byl následně reakcí s $[VO(acac)_2]$ připraven komplex [VO(L)], který však nebyl izolován a byl rovnou použit do reakce s příslušným dusičnanem lanthanoidu (Obrázek 37). Výsledný zelený roztok byl zfiltrován a ponechán volně krystalizovat za laboratorní teploty. Produkt se během několika dní vyloučil ve formě zelených krystalů.

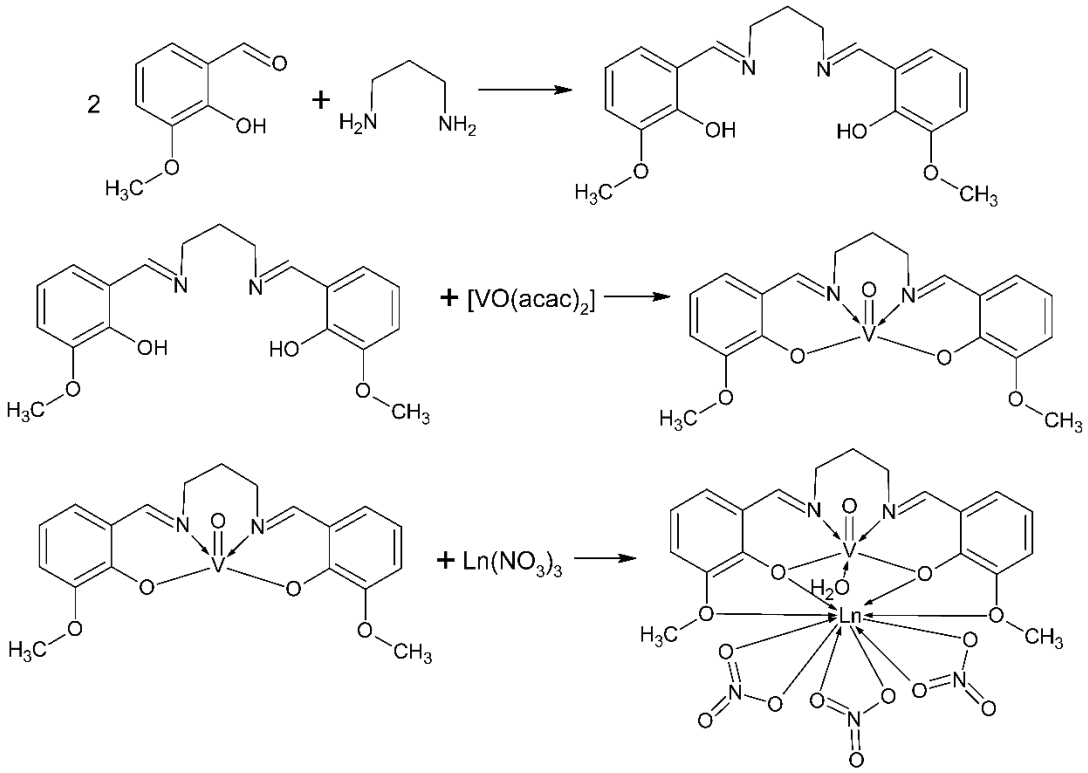

*Obrázek 37: Schéma přípravy komplexů **1-4.***

Složení a fázová čistota připravených vzorků byla následně potvrzena pomocí CHNS elementární analýzy, FTIR spektroskopie a RTG práškové difrakce. Molekulové struktury připravených látek byly vyřešeny pomocí monokrystalové rentgenové strukturní analýzy. Z této analýzy bylo zjištěno, že složení komplexů je $[Ln(VO)(L)(H_2O)(NO_3)_3]$ (**1-4**). Komplexy **1-3** se ukázaly být izostrukturní s koordinačním číslem lanthanoidu 10. Komplex **4** se liší ve způsobu vázání nitrato-ligandů k erbiu a jeho koordinační číslo je pouze 9. To je způsobeno tím, že jeden z nitrato ligandů je vázán pouze jedním kyslíkem na rozdíl od ostatních, které

jsou vázány bidentátně (Obrázek 38). Tento jev je pravděpodobně způsoben klesajícím iontovým poloměrem v sérii vlivem lanthanoidové kontrakce. Koordinační číslo vanadu je ve všech komplexech 6. Tvary koordinačního polyedru byly popsány pomocí softwaru SHAPE[99] a pro lanthanoidy byly určeny jako tetradekaedr (komplexy **1**-**3**) a tvar muffinu (komplex **4**). U vanadu byla geometrie koordinačního polyedru ve všech případech blízká oktaedru.

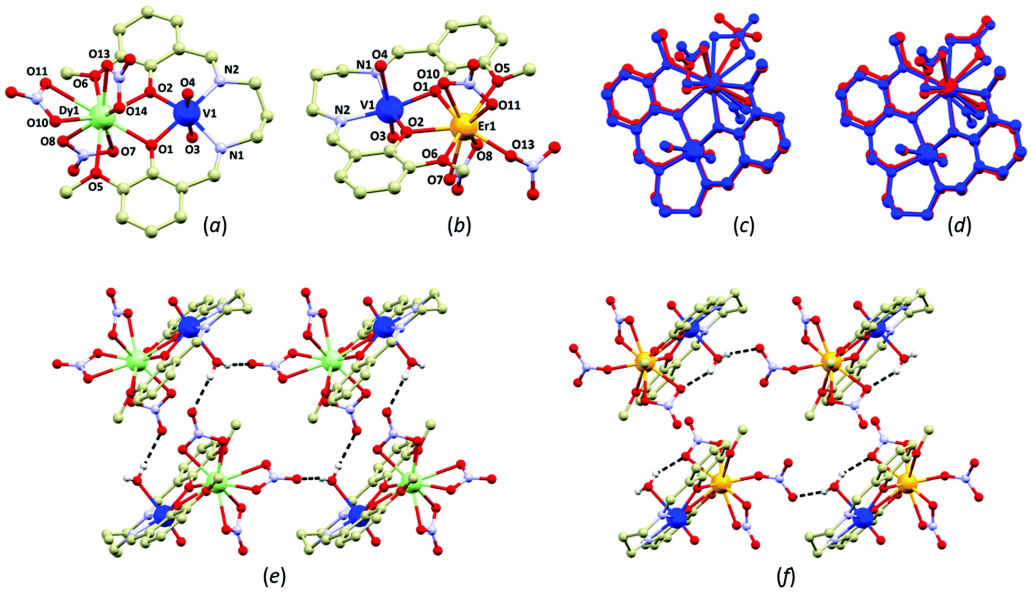

*Obrázek 38: Zobrazení molekulových struktur komplexů **1-3** (a) a **4** (b), Překryv struktur **3** s oběma variantami uspořádání ve struktuře **4** (c a d) a zobrazení mezimolekulových vodíkových vazeb u struktur **3** (e) a **4** (f)*

Následně byla provedena magnetická měření. V prvé řadě byla pozornost věnována DC magnetickým měřením, která byla využita pro analýzu magnetických výměnných interakcí. Z grafu závislosti magnetického momentu lze vypozorovat, že u komplexu **2** (obsahujícím Tb) je v oblasti nízké teploty vidět maximum (i když málo patrné). Toto maximum je znakem přítomnosti feromagnetické výměny. Ostatní komplexy jej nemají a pouhý pokles magnetického momentu s klesající teplotou, který vykazují, může být sice způsoben antiferomagnetickou výměnou, ale také dalšími faktory, které s výměnnými interakcemi nesouvisí, například s depopulací vyšších hladin základního termu (Obrázek 39).

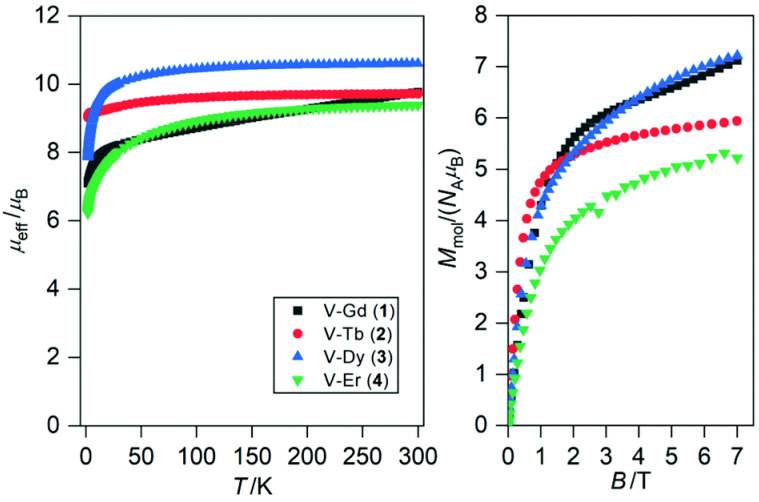

*Obrázek 39: Výsledky magnetických měření magnetického momentu na teplotě a magnetizace na magnetickém poli pro komplex **1-4**.*

Aby bylo možné spolehlivě popsat pozorované vlastnosti, bylo nutné provést analýzu magnetických dat pomocí teoretických modelů. Pro gadolinium se používají velmi jednoduché modely, stejné jako pro d-prvky, neboť Gd^{III} kvůli své elektronové konfiguraci vykazuje jen zanedbatelnou spin-orbitální interakci. Proto byl i v tomto případě použit zjednodušující spinový hamiltonián (Příloha 3 Rovnice 3), který ukázal na pravděpodobnou přítomnost antiferomagnetické výměny. Pro ostatní lanthanoidy tento přístup použít nejde kvůli tomu, že u nich spin-orbitální interakce velmi výrazně ovlivňuje elektronovou strukturu jejich základního stavu.

Byly pro ně zvoleny dva přístupy, které vychází z různých modelů jak lanthanoidy popisovat, konkrétně byly použity LS a JM modely (Příloha 3, Rovnice 4-5). Parametry *D* a *E* vycházejí ze Stevensových parametrů pro popis krystalového pole. Je to metoda, která byla poprvé vyzkoušena v tomto případě jako analogie spinového hamiltoniánu. Oproti plnému popisu pomocí Stevensových operátorů bylo cílem vytvořit model s nižším počtem parametrů, který lze použít bez využití výpočetních metod a zároveň není přeparametrizovaný. Pomocí tohoto modelu pak byla provedena analýza dat a byly stanoveny předpokládané velikosti magnetických výměnných interakcí (Tabulka 5). Výsledky těchto metod mezi sebou nejsou dobře porovnatelné vzhledem k zásadním rozdílům mezi modely. U komplexu **2** model v obou případech ukázal na pravděpodobnou přítomnost feromagnetické výměny, u komplexů **3** a **4** se jako pravděpodobná ukazuje naopak antiferomagnetická výměna.

Dále byly tyto komplexy studovány pomocí AC magnetických měření, která dokáží prokázat přítomnost pomalé relaxace magnetizace jako nenulový signál mimofázové složky magnetické susceptibility χ''. Tento signál byl zjištěn u komplexů **3** a **4** při měření ve stálém magnetickém poli B = 0.4 (**3**) a 0.3 (**4**) T. Bohužel u těchto komplexů nebylo možné dále vyhodnotit parametry magnetické relaxace, pravděpodobně kvůli překryvu několika relaxačních dějů. I přes komplikovaný profil relaxace lze tyto komplexy zařadit mezi jedno-molekulové magnety. Jedná se o první komplexy V^{IV} – Ln^{III}, které tento jev vykazují (Obrázek 40).

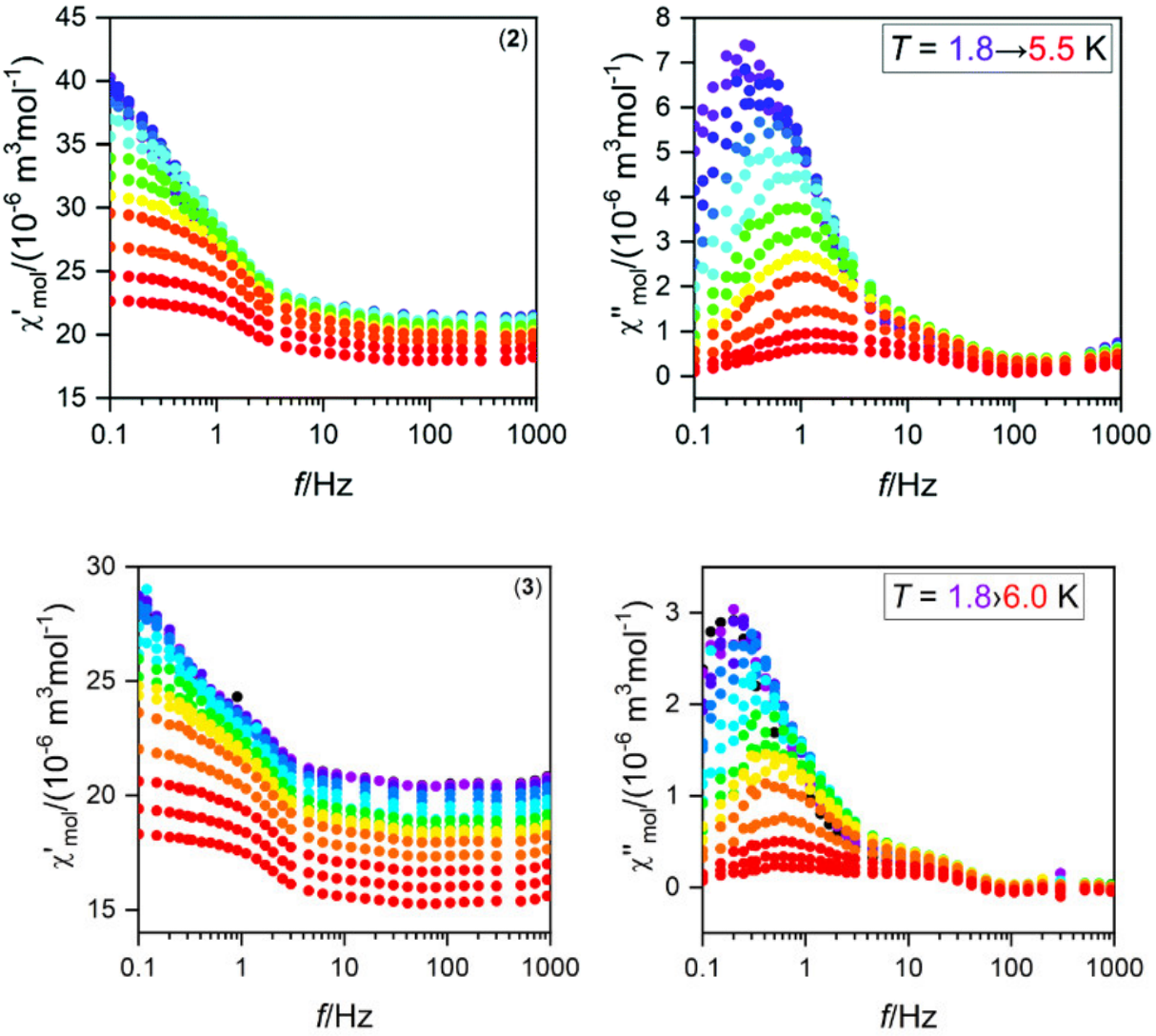

*Obrázek 40: Měření magnetické susceptibility ve střídavém poli pro komplexy **2** (nahoře) a **3** (dole).*

Kromě experimentálních metod byly pro charakterizaci připravených komplexů využity i teoretické výpočty. Byly využity postupy umožňující analýzu magnetické anizotropie a magnetických výměnných interakcí, a to jak pomocí metody BS-DFT, tak CASSCF. Co se týče analýzy magnetické anizotropie, ta byla studována pomocí softwaru Single_aniso a

Poly_aniso, který využívá metody CASSCF a mimo anizotropie umožňuje zjistit také velikost magnetických výměnných interakcí. Pomocí těchto programů je možné porovnat energetickou strukturu základního termu po štěpení vyvolaném spin-orbitální interakcí pouze u iontu lanthanoidu se zanedbáním vlivu dalšího paramagnetického centra se strukturou v heterospinovém systému. Nejenže dojde ke štěpení vlivem magnetické výměnné interakce, ale protože V^{IV} má spin S = ½, dojde ke změně parity spinu v celém systému, z Kramersových systémů se stanou non-Kramersovské a naopak.

Ve studovaných sloučeninách **2-4** bylo, co se týče magnetické anizotropie, sledováno hlavně kvantové tunelování magnetizace v základním stavu. Vyjadřuje se buď jako maticové elementy magnetického momentu (u Kramersových iontů), anebo jako „tunelovací štěpení“ (tunnelling splitting), které je u non-Kramersových iontů a jedná se o energetický rozdíl blízko ležících hladin, takzvaných pseudo-dubletů. Obecně platí, že čím blíže u sebe hladiny pseudodubletu jsou, tím silnější je anizotropie non-Kramersova systému. [109]

Výsledky výpočtů dobře korelují s experimenty. Ukazují, že komplexy **2** a **3** mají sice znatelné, ale ne příliš silné tunelování v základním stavu, což vysvětluje jejich chování jako polem-indukovaných jedno-molekulových magnetů. Naopak komplex **4** bude přecházet ze základního stavu do stavu s opačnou magnetizací, který vzniká ze základního stavu vlivem magnetických výměnných interakcí. To vysvětluje, proč u tohoto komplexu nebyla experimentálně zaznamenána pomalá relaxace magnetizace (Obrázek 41).

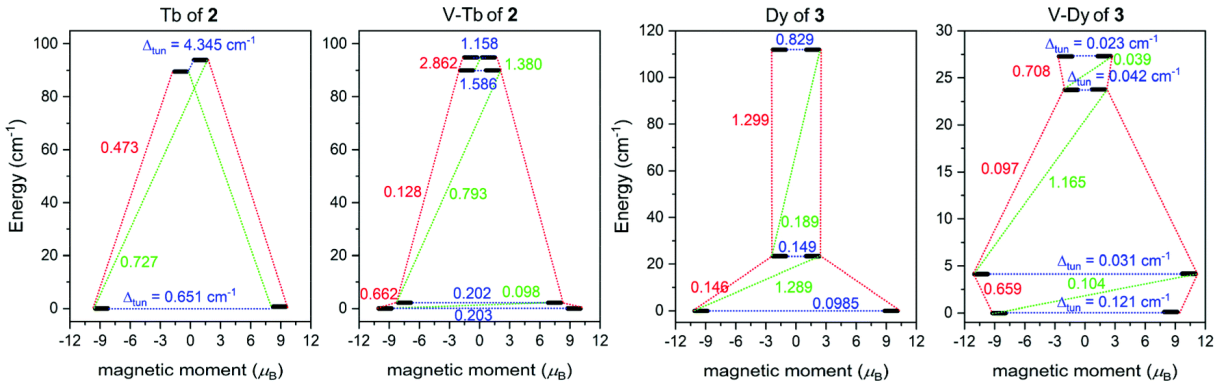

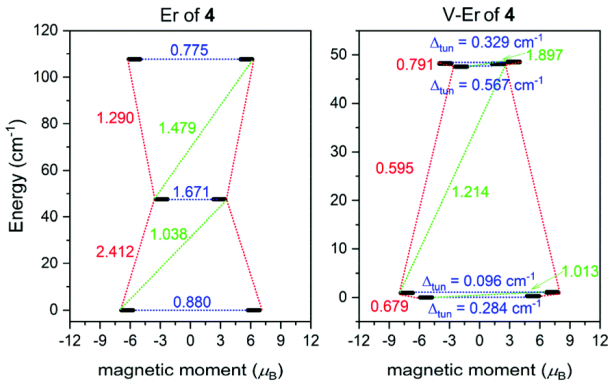

*Obrázek 41: Výsledky Single_Aniso a Poly_Aniso analýzy přechodů mezi Kramersovými dublety pro komplexy **2-4**.*

Pomocí metody Poly_aniso byly také vypočítány velikosti magnetických výměnných interakcí, kde bylo zjištěno, že výměna v komplexu **2** je feromagnetická (J^{ex} = +0.716 cm^{-1}), zatímco v komplexech **3** a **4** je antiferomagnetická (J^{ex} = -1.69 cm^{-1} a J^{ex} = -0.736 cm^{-1}).

Poté byly u studovaných komplexů vyhodnoceny magnetické výměnné interakce pomocí dalších dvou metod. Jednou z nich je metoda BS-DFT, která se u lanthanoidů mimo Gd^{III} příliš nepoužívá, avšak existují nějaké příklady[110], kdy byla použita, a jedním z cílů téhle práce bylo porovnat metody i vzájemně. BS-DFT metoda využívá pro výpočet magnetické výměnné interakce energetický rozdíl mezi high-spin a „broken symmetry“ stavem, které by měly reprezentovat stav s paralelní a antiparalelní orientací magnetických momentů u paramagnetických center. Analogicky k této metodě byl použit podobný postup u CASSCF metody vycházející z porovnání rozdílu mezi energiemi hladin základního stavu s multiplicitou (S_1+S_2) a (S_1-S_2). Teoreticky by měla být velikost interakční konstanty ve všech vypočítaných stavech přibližně stejná.[111]

*Tabulka 5: Magnetické interakční konstanty J^{ex} pro komplexy **1-4**, určené pomocí různých metod.*

Metoda určení J_{ex}	**1Gd**	**1Tb**	**1Dy**	**1Er**
$\|S\rangle_{Gd} - \|S\rangle_{V}$	-1.41 cm^{-1}	-	-	-
$\|JM\rangle_{Ln} - \|S\rangle_{V}$	-	0.245 cm^{-1}	−0.254 cm^{-1}	−0.140 cm^{-1}
$\|LS\rangle_{Ln} - \|S\rangle_{V}$	-	0.775 cm^{-1}	−0.698 cm^{-1}	−1.56 cm^{-1}
CASSCF/POLY_ANISO	-	0.716 cm^{-1}	−1.69 cm^{-1}	−0.736 cm^{-1}
BS-DFT (TPSSh) (Ruiz)	-1.59 cm^{-1}	0.00635 cm^{-1}	−0.819 cm^{-1}	−2.46 cm^{-1}

BS-DFT (TPSSh) (Yamaguchi)	-4.55 cm^{-1}	0.0166 cm^{-1}	−1.96 cm^{-1}	−4.93 cm^{-1}
CASSCF/MΓ andM−2Γ levels	-	1.07	1.25	1.65
NEVPT2/MΓ andM−2Γ levels	-	1.23	0.48	0.03

Protože každá z metod používá poněkud jiný model, je těžké tyto hodnoty vzájemně porovnat. Očekávatelně nejkonzistentnější výsledky jsou u metod, které při vyhodnocování využívají srovnání s experimentálními daty, tedy simulace pomocí spinových hamiltoniánů a Poly_aniso CASSCF výpočty. Výpočty BS-DFT ukazují shodu s experimentem ohledně znaménka magnetické interakční konstanty, avšak u komplexu **2** je jejich hodnota velmi malá, což ukazuje, že tato metoda pravděpodobně podhodnocuje energii „broken symmetry" stavu. Navíc, protože jde o metodu DFT, je závislá na volbě funkcionálu a pro širší využití této metody by bylo nutné provést širší benchmarking, nakolik je tato metoda opravdu spolehlivá. U metody porovnávání energetických hladin z CASSCF nebo NEVPT2 vycházejí všechny hodnoty výměnných interakcí jako feromagnetické, metoda tedy pravděpodobně podhodnocuje energie stavu s maximální multiplicitou spinu v systému. Je teoreticky možné použít pokročilejší multireferenční metodu, například MRCI nebo DDCI3. Tyto metody by mohly dosáhnout přesnějších výsledků, ale jsou velmi výpočetně náročné, tedy ne příliš vhodné pro lanthanoidy.

Tato práce přispěla k rozšíření znalostí 3d-4f systémů s ligandy typu salenu, kde byly objeveny první jedno-molekulové ligandy, které obsahují V^{IV} a lanthanoidy jako centrální atomy. Teoreticky je tyto komplexy možné použít jako stavební bloky a studovat vliv dalších paramagnetických center. Dále pak v této práci byly vyzkoušeny nové metody výpočtu magnetických výměnných interakcí pomocí simulace průběhu křivky magnetických veličin na spinový hamiltonián upravený pro potřeby lanthanoidů, a k tomu bylo otestováno poměrně široké spektrum metod na vyhodnocování velikosti magnetických výměnných interakcí. Po publikaci této práce byly tyto navrhované metody aplikovány i v jiných studiích na dalších systémech.[112,113]

4.4 Série komplexů kobaltu ve tvaru trigonálního prizmatu

V této části práce byla připravena série kobaltnatých komplexů jako jedno-molekulových magnetů s ligandem typu Schiffovy báze. (Obrázek 42). Tyto komplexy mají tvar blízký trigonálnímu prizmatu, které je blízké D_{3h} symetrii, od které je očekávatelná silná anizotropie a vysoké a záporné hodnoty *D* parametru štěpení v nulovém magnetickém poli. Existuje poměrně široká řada komplexů, které tuto symetrii využívají a dosahují parametrů jedno-molekulových magnetů i v nulovém magnetickém poli, což není pro kobaltnaté komplexy moc časté (Příloha 4 Tabulka 1).

Bylo připraveno a studováno 6 komplexů s různými Schiffovými bázemi jako ligandy. Cílem bylo měnit strukturu části ligandu pomocí záměny aminové části ligandu a sledovat vliv této substituce na strukturu a magnetické vlastnosti komplexu, které by teoreticky mohly vést k magneto-strukturním korelacím.

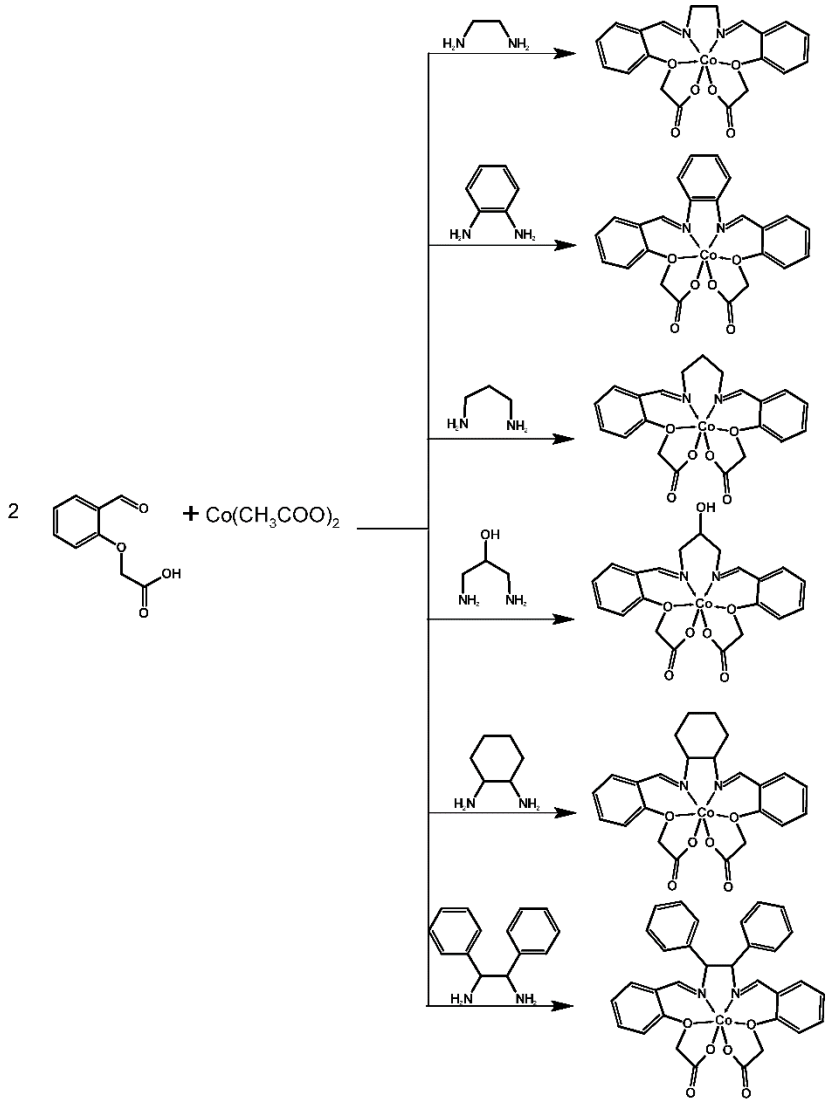

*Obrázek 42: Schémata reakcí vedoucím k přípravám studovaných komplexů **1-6**. (Příloha 1, Schéma 1)*

Syntéza byla provedena *in situ* smícháním kyseliny 2-formylfenoxyoctové a octanu kobaltnatého a k této směsi byl přidán příslušný amin (1,2-ethylendiamin pro **1**, 1,2-fenylendiamin pro **2**, 1,2-propylendiamin pro **3**, 2-hydroxy-1,2-propylendiamin pro **4**, 1,2-cyklohexylendiamin pro **5** a 1,2-difenyl-1,2-ethylendiamin pro **6**). Všechny komplexy kromě **2** byly dobře rozpustné v alkoholech, u komplexu **1** byly krystaly získány z methanolu, u **3-6** byly získány ze směsi propanol-methanol. Nerozpustný komplex **2** byl rekrystalizován z dimethylsulfoxidu. Komplex **4** bohužel nebylo možné připravit v množství dostatečném pro další studium v požadované čistotě a byl charakterizován pouze pomocí monokrystalové strukturní analýzy a teoretických metod.

Připravené komplexy byly charakterizovány pomocí CHNS elementární analýzy, FTIR spektroskopie, rentgenové práškové difrakce a rentgenové monokrystalové strukturní

analýzy. (Příloha 4 Tabulka 2) Všechny studované látky tvoří komplexy se složením [CoL], u komplexů **5** a **6** se v základní buňce objevují dvě symetricky neekvivalentní molekuly (Obrázek 43).

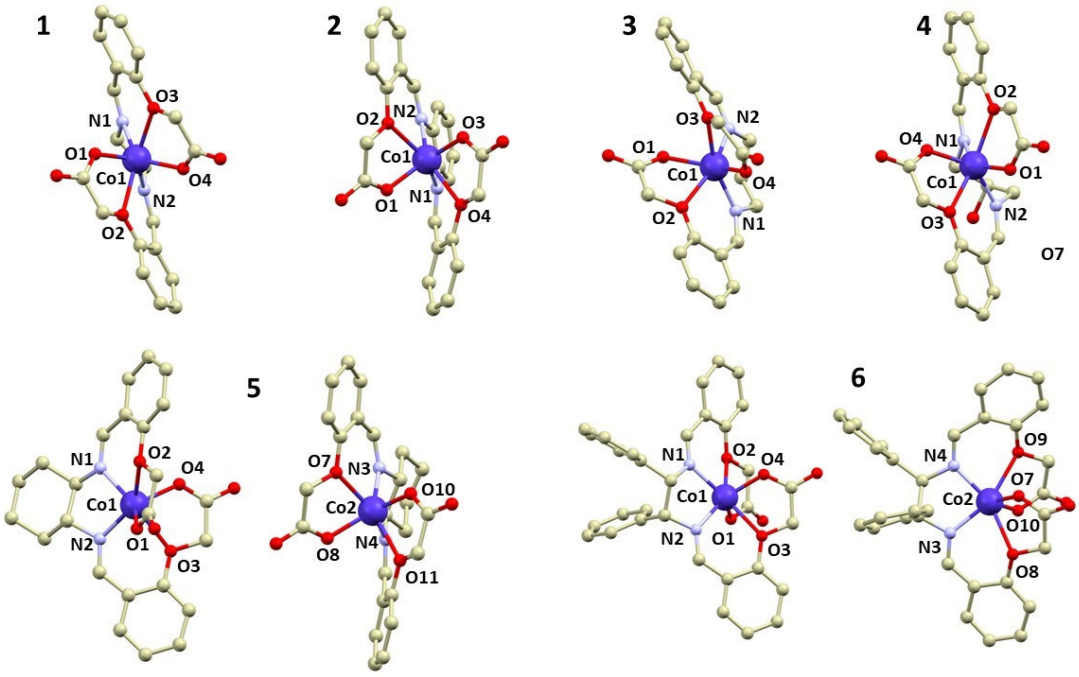

*Obrázek 43: Molekulové struktury komplexů **1-6** (Příloha 1. Obrázek 1)*

Tvar koordinačních polyedrů připravených komplexů byl studován pomocí softwaru SHAPE. Z výsledků bylo zjištěno, že geometrie koordinační sféry pro všechny komplexy odpovídá tvaru trigonálního prizmatu, jediná výjimka je komplex **3**, který je na pomezí mezi tvary oktaedru a trigonálního prizmatu.

Magnetická měření byla provedena pro komplexy **1-3** a **5-6**. Byla provedena měření závislosti magnetizace na teplotě a magnetickém poli (Obrázek 44) a dále také měření susceptibility ve střídavém magnetickém poli, aby byla v připravených komplexech potvrzena přítomnost pomalé relaxace magnetizace.

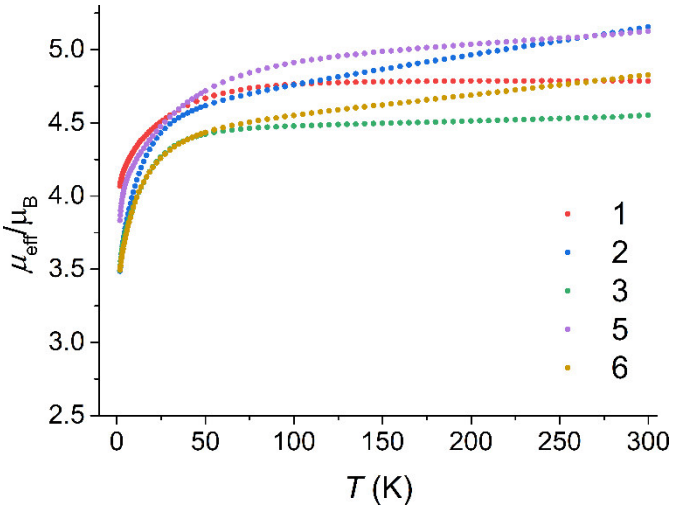

*Obrázek 44: Výsledky měření teplotní závislosti magnetického momentu pro komplexy **1-3** a **5-6** (Příloha 1, Obrázek 2)*

Měření ve stálém poli (DC) bylo vyhodnocováno hlavně se zaměřením na parametry štěpení v nulovém magnetickém poli u spinového hamiltoniánu:

$$\hat{H} = D\left(\hat{S}_z^2 - \hat{S}^2/3\right) + E\left(\hat{S}_x^2 - \hat{S}_y^2\right) + \mu_B B g \hat{S} \qquad (36)$$

Naměřené výsledky byly porovnány se simulovanými křivkami. V tomto směru se ukázaly jako nejlepší komplexy **1** a **3**, které mají oba parametr *D* blízký -30 cm^{-1}.

*Tabulka 6: Parametry spinového hamiltoniánu a korekce pro teplotně nezávislý paramagnetismus (TIP) pro komplexy **1-3** a **5-6** získané pomocí magnetometrie (Příloha 1, Tabulka 3)*

	$g^{\dagger}$	D (cm^{-1})	E/D	TIP (cm^3mol^{-1})
1	2.724; 2.299	-30.3	0.173	0
2	2.344	-13.2	0.281	$2.55 \cdot 10^{-3}$
3	2.357; 2.271	-17.0	0.195	$3.34 \cdot 10^{-4}$
5	2.641; 2.395	-30.49	0.207	$1.33 \cdot 10^{-3}$
6	2.148; 2.326	15.5	0.274	$1.67 \cdot 10^{-3}$

† zapsáno jako g_{iso}, nebo g_z; g_{xy}

Pro komplexy **5** a **6**, které obsahují více symetricky nezávislých molekul, od nichž lze čekat ne zcela stejné magnetické vlastnosti, byl tento fakt zanedbán. Nebylo by totiž možné spolehlivě určit větší množství parametrů nutných k popisu takového systému.

U AC měření byla zjištěna přítomnost pomalé relaxace při měření ve stálém poli. Měření byla následně vyhodnocena pro všechny komplexy kromě **6**, kde sice signál mimofázové složky susceptibility byl přítomný, ale jen v nízkém rozsahu teplot, který neumožňoval vyhodnocení.

Naměřená data pro ostatní komplexy byla vyhodnocena pomocí Havriliak-Negami modelu (Příloha 1, Rovnice 4 a 5), a výsledné relaxační časy vyhodnoceny pomocí následujícího vztahu:

$$\tau^{-1} = A_{\mathrm{dir}} T H^{n_{\mathrm{dir}}} + C_{\mathrm{Ram}} T^{n_{\mathrm{Ram}}} + \tau_0^{-1} e^{\frac{-U_{\mathrm{eff}}}{T}} \quad (37)$$

Většina z vyhodnocovaných ostatních komplexů, mimo **3**, vykazovala přítomnost dvou relaxačních dějů, avšak pouze u komplexu **5** byly tyto dva děje možné vyhodnotit díky dostatečnému rozsahu teplot, kde jsou oba děje zaznamenatelné.

*Tabulka 7: Výsledky vyhodnocení parametrů relaxačních procesů pro komplexy **1-3** a **5-6** (Příloha 1, Tabulka 4)*

Komplex	log τ_0^{-1} (s^{-1})	U_{eff} (K)	C ($s^{-1}K^{-5}$)	log A_{dir} ($s^{-1}K^{-1}T^{-4}$)
1	8.445	72.89	0.135	4.603
2	6.263	33.63	0	4.583
3	9.311	50.53	0	3.323
5s†	0	0	0.154	3.805
5f	0	0	78.277	5.886

† Pro **5** byly analyzovány dva procesy, označené jako pomalejší (s) a rychlejší (f)

Komplex	log τ_0^{-1} (s^{-1})	U_{eff} (K)	log A_{dir} ($s^{-1}K^{-1}T^{-4}$)	log B_1 (s^{-1})	log B_2 ($s^{-1}T^{-2}$)
1Zn	5.761	26.96	4.602	5.76	6.03

Kromě těchto měření bylo provedeno měření komplexu **1Zn** s magneticky ředěným vzorkem odvozeným od vzorku **1**, který obsahuje zhruba 3% Co^{II} a 97% Zn^{II}. Studium tohoto vzorku ukázalo, že tento komplex může relaxovat i v nulovém magnetickém poli.

Kromě magnetometrických metod byly závěry ověřeny také s využitím EPR spektroskopie. Tato metoda umožnila ověřit velikosti *g*-faktorů a také znaménka *D* parametru. Toto znaménko a stejně tak poměr parametrů *E/D* vychází v poměrně dobré shodě s magnetometrickými měřeními. Analýza *g*-faktorů také ukazuje na pravděpodobnou přítomnost silné axiální anizotropie ve studovaných komplexech mimo **6**.

Mimo tyto metody byly provedeny teoretické výpočty s cílem spolehlivěji vysvětlit vlastnosti připravených látek. Pomocí metody CASSCF/NEVPT2 byla analyzována elektronová struktura připravených komplexů a také bylo pomocí modulu AILFT studováno štěpení d-orbitalů v ligandovém poli (Obrázek 45).

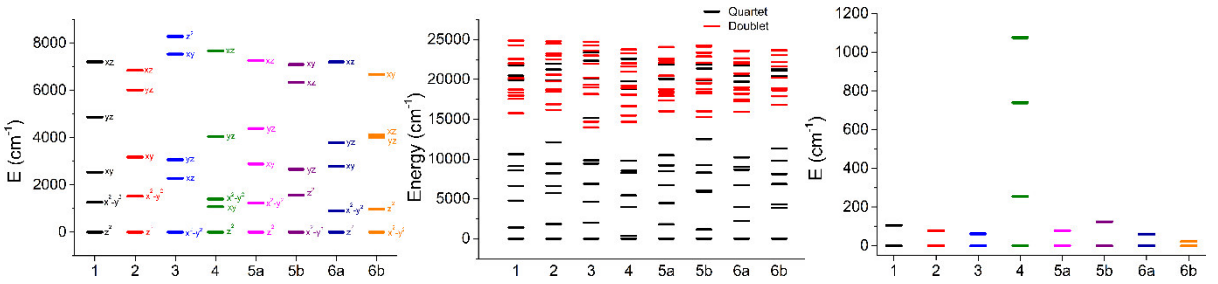

*Obrázek 45: Ab initio vypočítané štěpení d-orbitalů (vlevo), štěpení hladin atomových termů (uprostřed) a štěpení Kramersových dubletů (vpravo) pro komplexy **1-6**.*

U štěpení d-orbitalů bylo studováno, zda jejich štěpení v krystalovém poli odpovídá profilu očekávatelného v deformované trigonálně prizmatické geometrii. Ideální trigonální prizma má energeticky nejníže orbital d_{z^2}, poté jsou dva degenerované orbitaly d_{xy} a $d_{x^2-y^2}$, a nejvýše jsou degenerované orbitaly d_{xz} a d_{yz}. Podobnou strukturu štěpení orbitalů lze nalézt u všech studovaných komplexů kromě **3**, **5b** a **6b**. Mimo to bylo studováno štěpení atomových termů v ligandovém poli a dále štěpení hladin spin-orbitálních interakcí na Kramersovy dublety, kde se ukazuje, že největší štěpení, a tedy největší potenciální energetickou bariéru U_{eff}, mají komplexy **4**, **1** a **5b**. Navíc byly vypočítány i parametry spinového hamiltoniánu (Příloha 4 Tabulka 7).

Byl využit také software Single_aniso k detailnějšímu zkoumání energetické bariéry U_{eff} a ke kvantifikaci přechodových momentů mezi hladinami Kramersových dubletů. U většiny komplexů se ukázalo, že je u nich očekávatelné nezanedbatelné kvantové tunelování magnetizace v základním stavu, což vysvětluje nepřítomnost pomalé relaxace v experimentech bez použití vnějšího magnetického pole. Navíc je u komplexu **6b** naznačena pravděpodobná přítomnost profilu anizotropie typu lehké roviny, který pomalou relaxaci magnetizace neumožňuje, zatímco u komplexu **6a** by anizotropie měla být typu lehké osy. Toto chování, kdy jsou v krystalové struktuře komplexu dva typy molekulových struktur s opačnou anizotropií, vysvětlují některé jevy, jako například naměřený kladný *D* parametr u EPR spektroskopie a zároveň přítomnost pomalé relaxace magnetizace na AC magnetometrických měřeních (Obrázek 46).

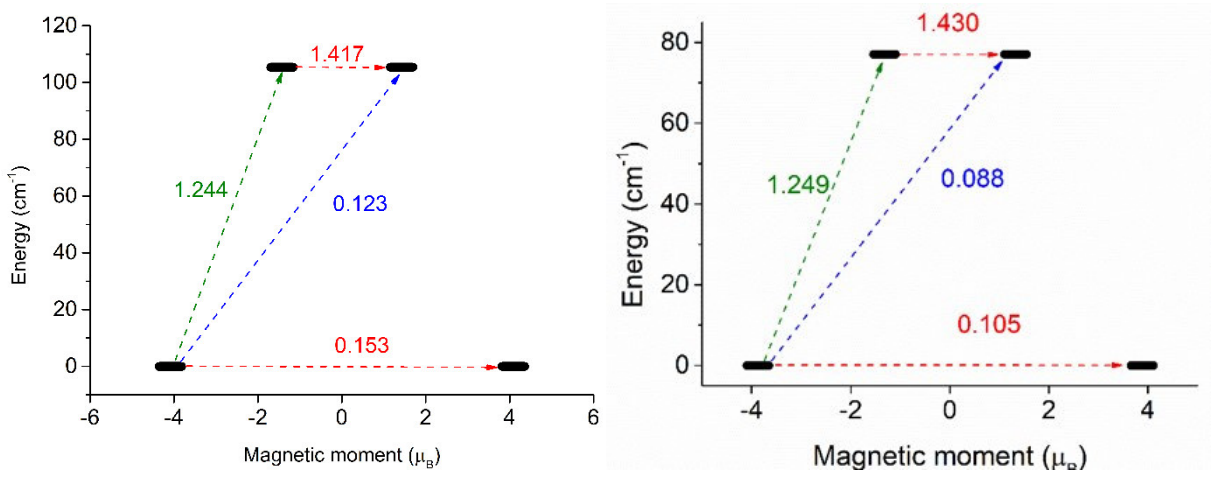

*Obrázek 46: Energetické hladiny Kramersových dubletů a přechodové momenty mezi nimi pro komplexy **1** (vlevo) a **2** (vpravo)*

V této práci byla připravena a dostupnými metodami široce charakterizována série zajímavých komplexů Co^{II} ve tvaru trigonálního prizmatu. Ukázalo se, že všechny tyto látky vykazují pomalou relaxaci magnetizace, což bylo dále studováno pomocí magnetometrických metod, EPR spektroskopie a výpočetních metod. Pomalá relaxace byla pozorována pouze v nulovém poli. U komplexu **1** byl pak připraven i magneticky ředěný vzorek, který vykazoval pomalou relaxaci i v nulovém poli. Kromě toho byly studovány i geometrické parametry a vliv deformace ideální geometrie na elektronovou strukturu centrálních atomů kobaltu.

4.5 Studium magnetických vlastností komplexu {Ni_4Dy_3}

Tato část práce byla zaměřena na teoretickou charakterizaci komplexu {Ni_4Dy_3}, který byl připraven a charakterizován pomocí experimentálních metod spoluautory. Jedná se o poměrně velký sedmijaderný systém, který je navíc poměrně málo symetrický, což je poměrně limitující při studiu jeho vlastností.

Komplex obsahuje ligand H_2L typu Schiffovy báze, který byl připraven reakcí salicylaldehydu a salicylaminu, celý komplex {Ni_4Dy_3} byl pak připraven *in situ* reakcí ligandu H_2L s dusičnanem dysprositým, chloridem nikelnatým, benzoanem sodným a triethylaminem (Obrázek 47). Z roztoku této směsi byly pak izolovány zelené krystaly připraveného komplexu.

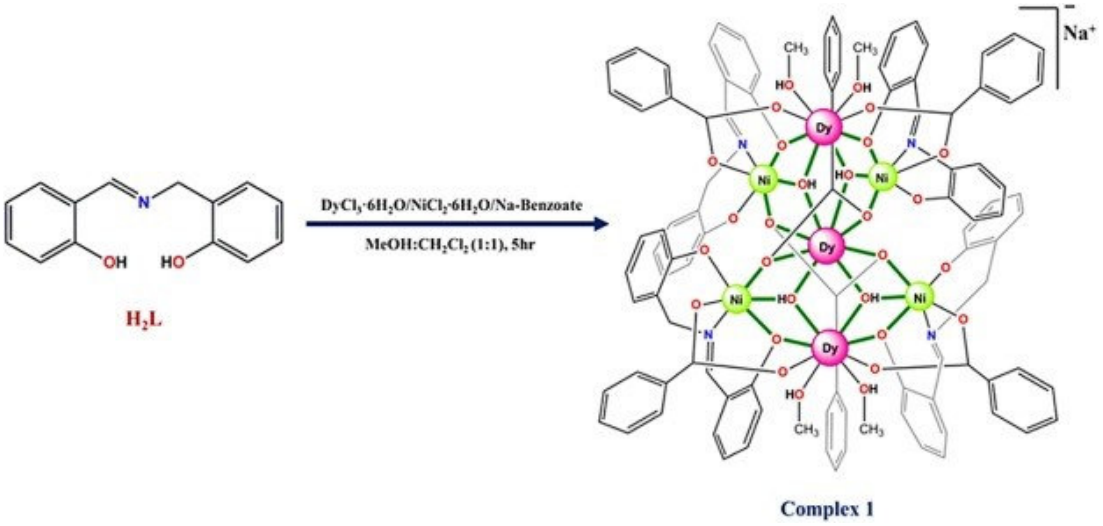

Obrázek 47: Schéma syntézy komplexu Ni_4Dy_3.

Komplex $Na[Ni_4Dy_3(L)_4(\mu_3\text{-}OH)_4(\mu_{1,1,3,3}\text{-}PhCO_2)_2(\mu_{1,3}\text{-}PhCO_2)_4(CH_3OH)_4]$ je tvořen dvěma jednotkami typu dikubanu $\{Ni_2Dy_2\}$, které jsou propojeny společným vrcholem, který je tvořen jedním z atomů Dy^{III}, a dohromady tvoří tvar „motýlka“ (Obrázek 48). Tyto jednotky jsou můstkované pomocí karboxylových skupin, hydroxidových skupin a také fenolických kyslíků z ligandů L^{2-}.

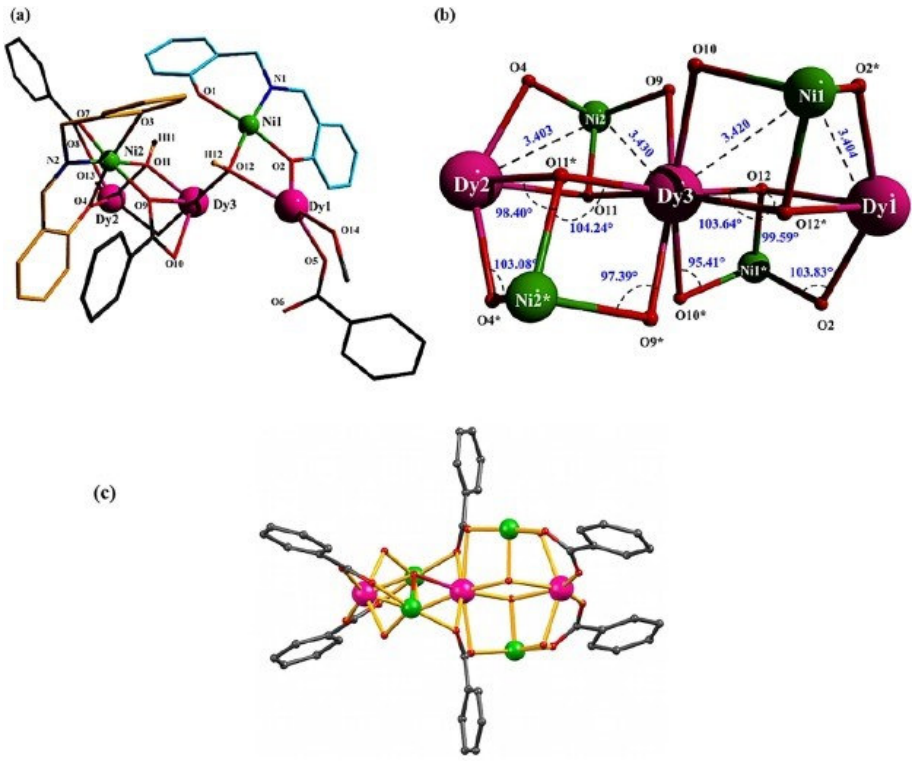

Obrázek 48: Schémata znázorňující strukturu komplexu Ni_4Dy_3.

Ačkoli se komplex zdá být symetrický podle centra inverze, a je tomu skutečně poměrně blízko, není to zcela přesné, neboť jsou obě dikubanové jednotky jinak deformované, což se projevuje zejména například na geometrii atomů Dy^{III}. Koordinační číslo je u všech atomů dysprosia 8, koordinační okolí atomů dysprosia, v příloze označené jako Dy1 a Dy2 (tedy „krajní“ atomy), mají tvar nejbližší k trigonálnímu dodekaedru a poměrně blízký také k tetragonálnímu antiprizmatu. Koordinační polyedr v okolí prostředního atomu Dy3 má tvar nejbližší ke krychli. Atomy niklu jsou symetricky ekvivalentní v každé z dikubánových částí (ale liší se od Ni^{II} center v druhé části) a všechny mají koordinační číslo 6 v koordinačním okolí tvaru oktaedru.

U magnetických měření byla u teplotní závislosti magnetického momentu na teplotě naměřena v limitě hodnota odpovídající čtyřem atomům Ni^{II} a třem atomům Dy^{III}, jak je očekávatelné ze struktury. Při poklesu teploty pak zhruba od 100 K dochází k poklesu magnetického momentu, což lze přisoudit depopulaci vyšších hladin základního termu nebo antiferomagnetickým výměnným interakcím. Při velmi nízké teplotě se oproti tomu objevuje maximum magnetického momentu typické pro feromagnetickou interakci (Obrázek 49). Vzhledem k tomu, že se jedná o sedmijaderný komplex, je reálná i možnost, že se v něm objevují oba typy výměnných interakcí mezi různými páry paramagnetických iontů. Bohužel další vyhodnocení na základě magnetických dat je prakticky nemožné právě kvůli počtu atomů, asymetrii komplexu a počtu možných interakcí a parametrů, které by na vyhodnocení mohly mít vliv.

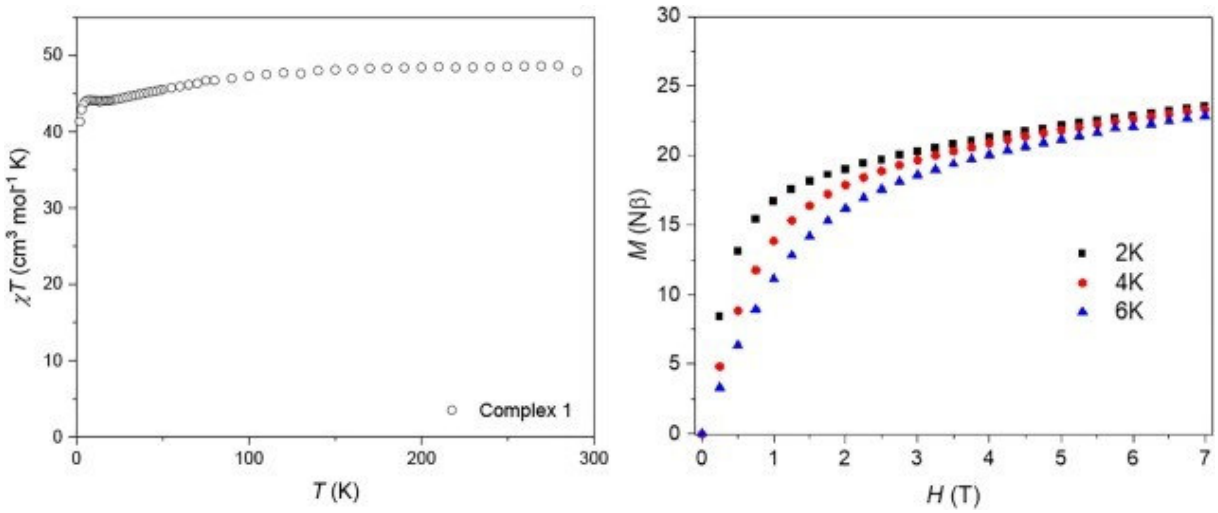

Obrázek 49: Výsledky magnetických měření závislosti χT na teplotě (vlevo) a magnetizace na magnetickém poli (vpravo) pro komplex Ni_4Dy_3.

Magnetická měření AC susceptibility pak ukázala, že v tomto komplexu není přítomná pomalá relaxace magnetizace ani v přítomnosti vnějšího magnetického pole a komplex tedy nepatří mezi jedno-molekulové magnety.

Pro další vysvětlení vlastností těchto látek byly použity teoretické metody, zejména metody CASSCF, pro atomy niklu pak byla použita metoda BS-DFT s cílem určit velikost magnetických výměnných interakcí. Pomocí metod CASSCF byly pro všechna paramagnetická centra určeny energie d- a f- orbitalů, energetické hladiny atomových termů a štěpení hladin po spin-orbitální interakci (Příloha 5 Obrázek 6). Z těchto dat bylo možné odečíst parametry spinového hamiltoniánu u atomů Ni^{II}, kde bylo zjištěno, že D = -13.9 cm^{-1} pro **1** a -12.9 cm^{-1} pro **2** a E/D = 0.265 pro **1** a 0.205 pro **2**. Kromě toho byly analyzovány jednotlivé Kramersovy dublety u atomů Dy^{III} a bylo zjištěno, že mají poměrně velké příspěvky g_{xy}, což naznačuje pravděpodobnou přítomnost kvantového tunelování magnetizace v základním stavu a může to vysvětlovat nepřítomnost pomalé relaxace magnetizace. Ukazuje se, že zvláště atom Dy3 s geometrií koordinační sféry ve tvaru krychle by měl vykazovat velké kvantové tunelování magnetizace. Pro potvrzení vlivu tvaru geometrie chromoforu byly provedeny výpočty pro ideální tvary, které ukazují, že ideální O_h symetrie kubické geometrie je opravdu z hlediska rozložení energetických hladin pro přípravu jedno-molekulových magnetů nevhodná a D_{2d} symetrie trigonálního dodekaedru je vhodnější (Příloha 6 Obrázek 7).

Poté byly analyzovány velikosti magnetických výměnných interakcí, kde vzhledem k počtu interakcí a magnetických stavů není možná úplná analýza. Pro atomy dysprosia bylo možné kvantifikovat velikost dipól-dipólové složky výměnné interakce, kde bylo vypočítáno, že tato složka má mezi všemi atomy dysprosia feromagnetický charakter. Poměrně silná je mezi atomy Dy1 a Dy2, což souvisí s jejich shodnou orientací magnetického momentu.

Kromě toho byly vypočítány velikosti interakční konstanty magnetické výměnné interakce pro interakci mezi atomy niklu Ni1 a Ni2* a Ni1* a Ni2 pomocí metody BS-DFT. Výpočty naznačují, že i mezi těmito atomy je očekávaná feromagnetická výměnná interakce. Bohužel ostatní interakce, zejména mezi atomy dysprosia a niklu, nebylo vzhledem ke komplikovanosti možné zjistit. Avšak i získané výsledky jsou v souladu s magnetickými měřeními, která indikují pravděpodobný výskyt feromagnetické výměny v komplexu.

4.6 Série komplexů $[NiLn(L)_2(NO_3)_3]$ s ligandem typu Schiffovy báze

V této části práce byla spoluautory připravena a charakterizována série komplexů obsahujících ionty Ni^{II} a Ln^{III} (Gd (**1**), Tb (**2**), Dy (**3**), Ho (**4**), Er (**5**), Yb (**6**), Y (**7**)). Cílem práce bylo charakterizovat tyto sloučeniny z hlediska jejich magnetických vlastností se zaměřením na jedno-molekulový magnetismus a magnetické výměnné interakce.

Ligand L je Schiffova báze, která byla připravena kondenzací *o*-vanilinu a 2-(methylthio)anilinu. Komplexy byly následně připraveny *in situ* reakcí ligandu s $Ni(NO_3)_2$, $Ln(NO_3)_3$ a triethyaminem jako bází (Obrázek 50). Touto reakcí vznikl zelenožlutý roztok, z něhož byly získány krystaly, vhodné pro rentgenovou strukturní analýzu.

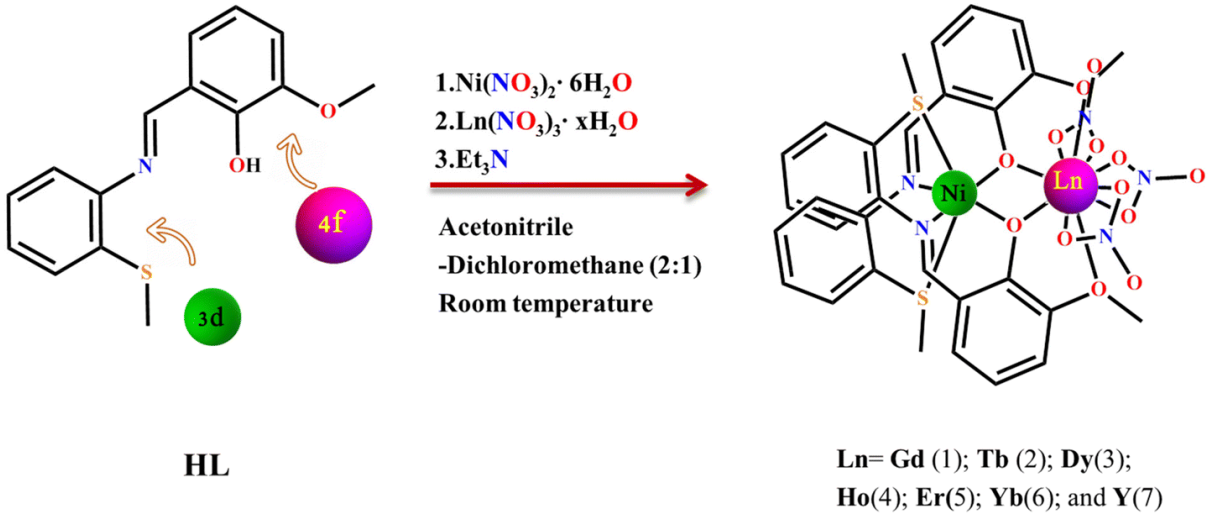

*Obrázek 50: Schéma syntézy komplexů **1-7***

Strukturní analýza ukázala, že všechny komplexy v sérii jsou izostrukturní. Nikl je vázán ligandy L v koordinačním prostředí $N_2O_2S_2$ a podle CSM analýzy pomocí programu SHAPE bylo prokázáno, že tvar jeho koordinační geometrie je oktaedr, avšak v důsledku deformace ligandů koordinací iontu lanthanoidu dochází ke znatelné deformaci oktaedrické symetrie. Ionty lanthanoidu jsou můstkované přes fenolické kyslíky a dále jsou vázané přes etherické kyslíky a nitrato ligandy. Koordinační číslo těchto atomů je 10 s tvarem koordinačního okolí nejbližšímu k dvojitě zastřešenému trigonálnímu prizmatu (Obrázek 51).

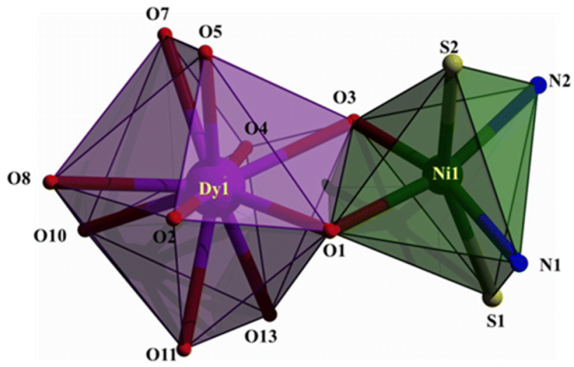

*Obrázek 51: Schéma geometrie koordinačního polyedru komplexu **3***

Pro všechny připravené komplexy byla provedena magnetická měření ve stálém magnetickém poli. (Příloha 6, Obrázek 5) Z měření teplotní závislosti magnetického momentu na teplotě jsou zřetelně vidět ferromagnetické interakce u komplexů **1** a **2**, které se projevují jako nárůst magnetického momentu při nízkých teplotách. U komplexů **3** a **5** je feromagnetická výměna pravděpodobně přítomná také, ale neprojevuje se tak zřetelně, jen jako zlom na křivce závislosti magnetického momentu na teplotě. U ostatních komplexů je na nízkých teplotách patrný pokles magnetického momentu, který není jasným znakem přítomnosti magnetické výměnné interakce.

Přítomnost pomalé relaxace magnetizace byla studována pomocí měření magnetické susceptibility ve střídavém magnetickém poli. Při těchto měřeních se ukázalo, že jediná z těchto látek, která vykazuje pomalou relaxaci, je komplex **5** a to pouze v přítomnosti stálého vnějšího magnetického pole (Obrázek 52).

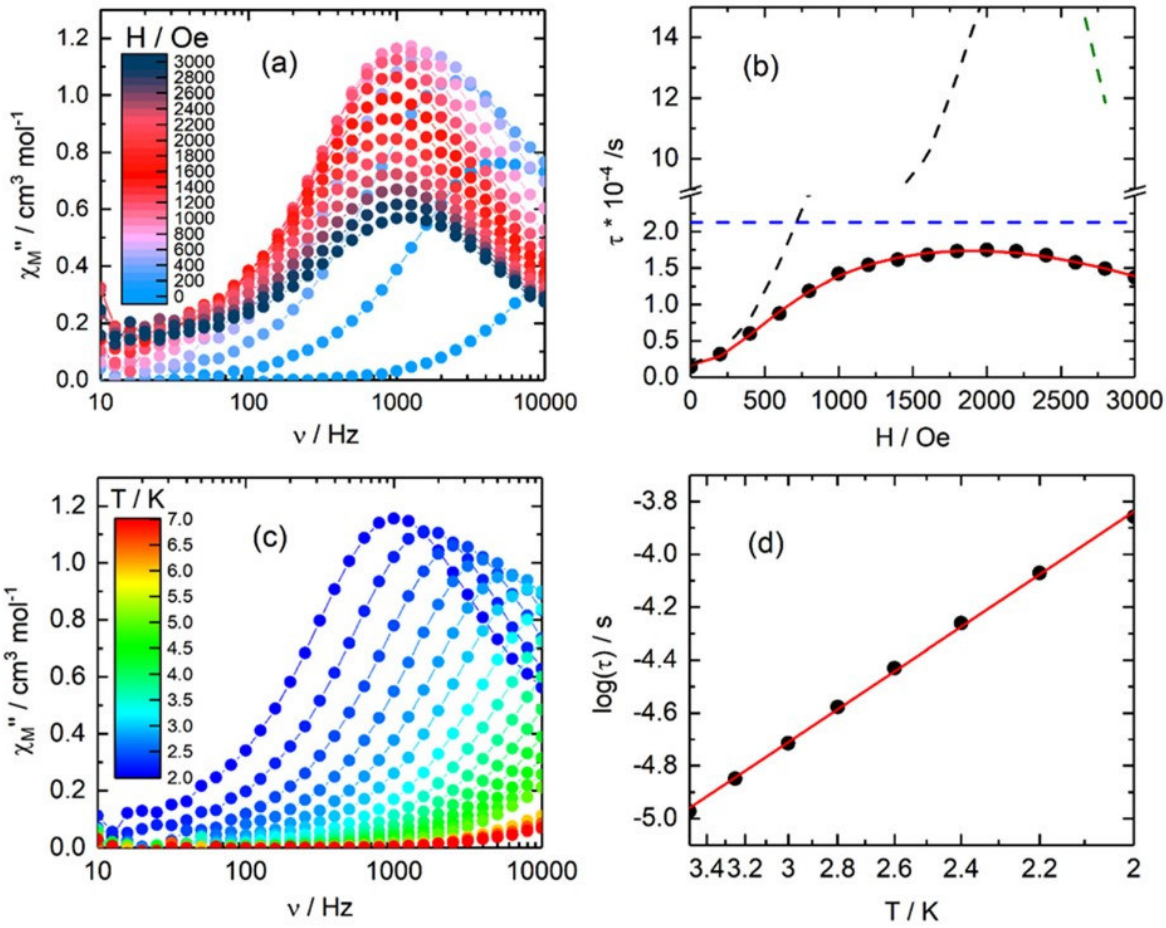

*Obrázek 52: Výsledky měření magnetické susceptibility ve střídavém magnetickém poli pro komplex **5***

Data závislosti reálné a imaginární magnetické susceptibility na frekvenci pro různé teploty a pole byla vyhodnocena podle rovnice, která obsahuje členy pro přímý, Ramanův, Orbachův mechanismus relaxace a kvantové tunelování magnetizace (Příloha 6, rovnice 3). Z analýzy dat pomocí tohoto vztahu bylo zjištěno, že energetická bariéra U_{eff} = 12.1 K a τ_0 = 3.49(2) 10^{-7} s.

Kvůli vysvětlení chování těchto komplexů hlavně z hlediska toho, proč u nich není zřetelná pomalá relaxace magnetizace, byly použity teoretické metody. K analýze magnetických vlastností bylo využito metody SA-CASSCF s využitím softwaru Single_Aniso. Pomocí CASSCF metody bylo zjištěno rozložení energetických hladin základního termu po spin-orbitální interakci. Největší štěpení mezi základní a první excitovanou hladinou bylo jednoznačně zjištěno u komplexu **5**, což souhlasí se závěry vyhodnocení experimentálních metod a vysvětluje, proč má tento komplex největší potenciál jako jedno-molekulový magnet (Obrázek 53).

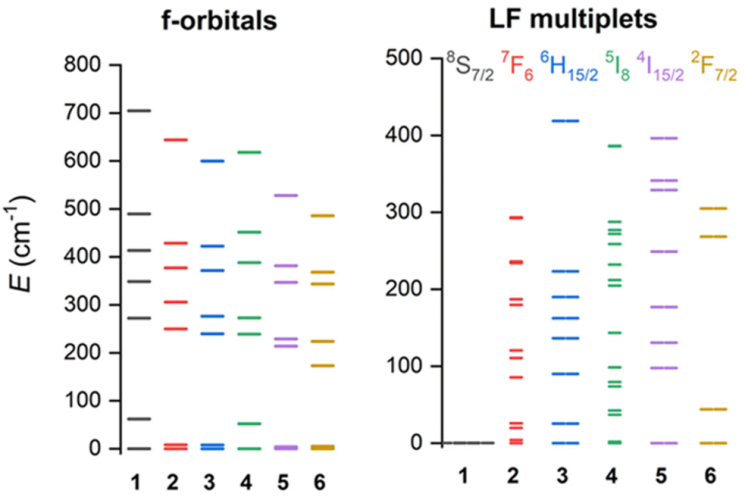

*Obrázek 53: Energetické hladiny f-orbitalů a multipletů ligandového pole pro komplexy **1-6**.*

Tyto závěry byly následně doplněny výsledky z programu Single_Aniso, kde byly analyzovány vlastnosti lanthanoidů v podmínkách simulujících připravené komplexy (atom Ni^{II} byl pro účely výpočtu nahrazen atomem Zn^{II}). Z nich plyne, že komplex obsahující Er^{III} má nejlepší vlastnosti i co se týče velikosti přechodového magnetického momentu mezi stavy základního Kramersova dubletu, který by měl být úměrný velikosti kvantového tunelování magnetizace, a tudíž je u tohoto komplexu očekávaná nejmenší míra tunelování z celé připravené série. Dále byl pak podobně analyzován celý systém **5** pomocí programu Poly_aniso (Obrázek 54). Tato analýza dále potvrzuje výsledky analýzy z programu Single_Aniso. Výsledky naznačují, že u komplexu **5** probíhá i v základním stavu nezanedbatelné tunelování, což vysvětluje, proč není přítomná relaxace v nulovém poli, ale v magnetickém poli je toto kvantové tunelování magnetizace potlačeno, a komplex se proto chová jako polem indukovaný magnet. Energetický rozdíl mezi vypočítanou základní a první excitovanou hladinou je 15.3 K, což je v dobré shodě s experimentálně zjištěnou bariérou U_{eff} = 12.1 K. Tento program umožňuje analyzovat i velikost magnetické výměnné interakce, která byla vypočítána jako feromagnetická interakce s interakční konstantou J = 1.65 cm^{-1}. Kromě této metody byla velikost magnetické výměnné interakce pro komplexy **1** a **5** určena také metodou BS-DFT, kde bylo vzájemně porovnáno několik DFT funkcionálů (Příloha 6 Tabulka 1), které ukázaly, že výměna je u obou komplexů feromagnetického charakteru.

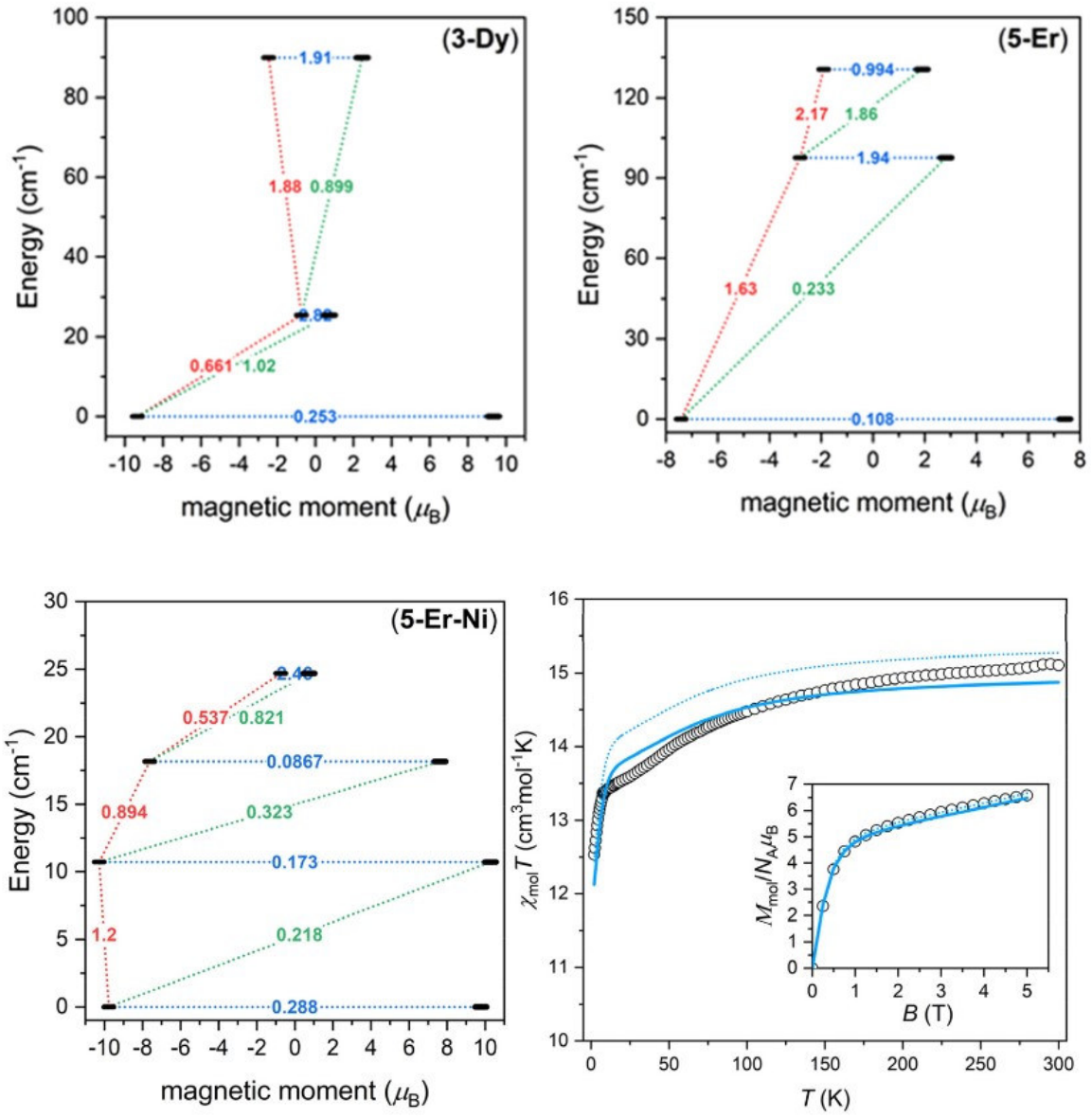

*Obrázek 54: Single_Aniso analýza pro ionty lanthanoidů v komplexech **3** a **5** (nahoře), Poly_Aniso analýza pro systém Er^{III} – Ni^{II} v komplexu **5** (dole vlevo) a porovnání simulovaných a experimentálních magnetických měření pro **5**.*

Závěrem lze shrnout, v tomto článku byla připravena a charakterizována série látek obsahujících Ni^{II} a lanthanoidy jako centrální atomy v dimerním systému s ligandem typu Schiffovy báze. Tato série byla následně charakterizována pomocí fyzikálně chemických metod a byla popsána struktura připravených látek. Komplexy byly dále studovány pomocí magnetochemických metod, na základě kterých bylo zjištěno, že jeden z komplexů, a to komplex **5**, se chová jako polem indukovaný magnet. Tyto vlastnosti a také to, proč ostatní komplexy jedno-molekulovými magnety nejsou, bylo vysvětleno na základě teoretických výpočtů, které ukázaly malý energetický rozdíl mezi Kramersovými dublety a nezanedbatelné kvantové tunelování magnetizace, které způsobuje rychlou magnetickou relaxaci u většiny

látek mimo **5**. Pomocí teoretických výpočtů byla také provedena kvantifikace magnetických výměnných interakcí u látek **1** a **5**, kde bylo vyhodnoceno, že interakce mezi magnetickými centry je u obou látek feromagnetická.

5. Závěr

Tato disertační práce byla řešena na základě pokynů pro vypracování a stanovených cílů disertační práce, které byly uvedeny v úvodu práce. Ke splnění stanovených cílů disertační práce se lze vyjádřit následovně:

Tato práce byla rozčleněna na teoretickou část, ve které jsou sepsány základní principy, na kterých je založen výzkum jedno-molekulového magnetismu a které byly vyhodnoceny jako relevantní vzhledem k tématům řešeným v dalších částech disertační práce. Následně byla provedena rešerše, která je členěná do čtyř částí a nachází se zde přehled komplexů typu dysprosocenia se zaměřením na jejich magnetické vlastnosti. Následně jsou uvedeny vybrané významné teoretické práce z oboru výpočetní chemie zabývající se jedno-molekulovým magnetismem a strukturními korelacemi v magneticky zajímavých komplexech. Další části rešerše poté byly věnovány komplexům salenu s Cu^{II} a V^{IV} se zaměřením na jejich magnetické výměnné interakce a anizotropii a také komplexům Co^{II} ve tvaru trigonálního prizmatu.

V rámci praktické části jsou shrnuty výsledky, které byly publikovány v celkem šesti publikacích. Dvě z těchto publikací jsou zaměřeny na analogy komplexů dysprosocenia, konkrétně jedna z nich na komplexy dysprosia s anorganickými cyklickými ligandy vázanými ve stejném módu jako cyklopentadienyl a druhá na komplexy dysprosia s ligandy typu cyklopentadienylu propojené alkylovými spojkami. Obě tyto práce jsou zaměřeny na studium energetické bariéry U_{eff} a spin-fononové interakce a jednoznačným přínosem je popis nového přístupu k metodám teoretických výpočtů těchto veličin. Navíc byly řešeny strukturní korelace ve studovaných sériích, které mají za úkol sloužit jako podklady pro budoucí práci syntetických chemiků.

Následně byla v rámci disertační práce připravena série dvojjaderných komplexů se Schiffovými bázemi, které obsahují trojmocné lanthanoidy (Gd, Tb, Dy, Er) a vanadylový kation. V této části práce byly studovány magnetické anizotropie a také magnetické výměnné interakce v těchto komplexech. Bylo zjištěno, že komplexy obsahující Tb a Dy vykazují pomalou

relaxaci magnetizace, a jde tedy o první jedno-molekulové magnety typu V^{IV} – Ln^{III}, a navíc byly poměrně detailně a několika různými metodami studovány magnetické výměnné interakce.

Další část práce byla věnována sérii komplexů Co^{II} s ligandy typu Schiffových bází, které jsou zajímavé jejich silnou tendencí k deformaci jejich geometrie do tvaru, který je blízký trigonálnímu prizmatu, což je typ koordinačního polyedru, který u kovů s obsazením d-orbitalů d^7 poskytuje potenciálně velmi zajímavé magnetické vlastnosti. Tato série byla charakterizována pomocí experimentálních a výpočetních metod se zaměřením na magnetismus a bylo zjištěno, že všechny studované komplexy jsou polem-indukované magnety, a u látky s nejvíce zajímavými vlastnostmi bylo provedeno magnetické zředění pomocí zinku, kde bylo následně zjištěno, že je poté tento komplex jedno-molekulovým magnetem i v nulovém magnetickém poli.

Nakonec jsou zde uvedeny dva články, kde má autor této disertační práce podíl jako spoluautor u charakterizace 3d-4f komplexů pomocí metod výpočetní chemie. V obou případech jde o komplexy lanthanoidů a niklu. V prvním případě jde o sedmijaderný komplex $\{Ni_4Dy_3\}$, kde byly teoreticky vyhodnocovány magnetické výměnné interakce a anizotropie na jednotlivých iontech dysprosia, avšak tento komplex bohužel nevykazoval příliš dobré vlastnosti, co se jedno-molekulového magnetismu týče, a je zajímavým spíše z pohledu syntetické chemie. Ve druhé z těchto prací byly charakterizovány komplexy niklu se sedmi různými trojmocnými kovy z oblasti lanthanoidů (Gd, Tb, Dy, Ho, Er, Yb) a yttriem. U těchto komplexů byly opět vyhodnocovány magnetické výměnné interakce a jejich elektronová struktura. Z této skupiny se ukázal být jako jediný komplex zajímavý z pohledu jedno-molekulového magnetismu komplex Er^{III}. Důvodem zjištěným na základě analýzy výpočetních metod je velké tunelování v základním stavu u ostatních komplexů a také malý rozdíl mezi energiemi Kramersových dubletů plynoucí pravděpodobně z vlivu geometrie koordinačního polyedru.

6. Použitá literatura

[1] Caneschi, A.; Gatteschi, D.; Sessoli, R.; Barra, A. L.; Brunel, L. C.; Guillot, M. Alternating Current Susceptibility, High Field Magnetization, and Millimeter Band EPR Evidence for a Ground S = 10 State in [Mn12O12(Ch3COO)16(H2O)4].2CH3COOH.4H2O. *J. Am. Chem. Soc.* **1991**, *113* (15), 5873–5874. https://doi.org/10.1021/ja00015a057.

[2] Cavallini, M.; Facchini, M.; Albonetti, C.; Biscarini, F. Single Molecule Magnets: From Thin Films to Nano-Patterns. *Phys. Chem. Chem. Phys.* **2008**, *10* (6), 784–793. https://doi.org/10.1039/b711677b.

[3] GATTESCHI, Dante, Roberta SESSOLI a Jacques VILLAIN. *Molecular nanomagnets*. Oxford: Oxford University Press, 2011. Mesoscopic physics and nanotechnology. ISBN 978-0-19-960226-1.

[4] Craig, G. A.; Murrie, M. 3d Single-Ion Magnets. *Chem. Soc. Rev.* **2015**, *44* (8), 2135–2147. https://doi.org/10.1039/C4CS00439F.

[5] Soler, M.; Wernsdorfer, W.; Folting, K.; Pink, M.; Christou, G. Single-Molecule Magnets: A Large Mn 30 Molecular Nanomagnet Exhibiting Quantum Tunneling of Magnetization. *J. Am. Chem. Soc.* **2004**, *126* (7), 2156–2165. https://doi.org/10.1021/ja0297638.

[6] Ishikawa, N.; Sugita, M.; Ishikawa, T.; Koshihara, S.; Kaizu, Y. Lanthanide Double-Decker Complexes Functioning as Magnets at the Single-Molecular Level. *J. Am. Chem. Soc.* **2003**, *125* (29), 8694–8695. https://doi.org/10.1021/ja029629n.

[7] Rinehart, J. D.; Fang, M.; Evans, W. J.; Long, J. R. A N 2 3– Radical-Bridged Terbium Complex Exhibiting Magnetic Hysteresis at 14 K. *J. Am. Chem. Soc.* **2011**, *133* (36), 14236–14239. https://doi.org/10.1021/ja206286h.

[8] Ungur, L.; Chibotaru, L. F. Strategies toward High-Temperature Lanthanide-Based Single-Molecule Magnets. *Inorg. Chem.* **2016**, *55* (20), 10043–10056. https://doi.org/10.1021/acs.inorgchem.6b01353.

[9] a) Chen, Y.-C.; Liu, J.-L.; Ungur, L.; Liu, J.; Li, Q.-W.; Wang, L.-F.; Ni, Z.-P.; Chibotaru, L. F.; Chen, X.-M.; Tong, M.-L. Symmetry-Supported Magnetic Blocking at 20 K in Pentagonal Bipyramidal Dy(III) Single-Ion Magnets. *J. Am. Chem. Soc.* **2016**, *138* (8), 2829–2837. https://doi.org/10.1021/jacs.5b13584. b) Liu, J.; Chen, Y.-C.; Liu, J.; Vieru, V.; Ungur, L.; Jia, J.; Chibotaru, L. F.; Lan, Y.; Wernsdorfer, W.; Gao, S.; Chen, X.-M.; Tong, M. A Stable Pentagonal Bipyramidal Dy(III) Single-Ion Magnet with a Record Magnetization Reversal Barrier over 1000 K. *J. Am. Chem. Soc.* **2016**, *138* (16), 5441–5450. https://doi.org/10.1021/jacs.6b02638. c) Ding, Y.-S.; Chilton, N. F.; Winpenny, R. E. P.; Zheng, Y.-Z. On Approaching the Limit of Molecular Magnetic Anisotropy: A Near-Perfect Pentagonal Bipyramidal Dysprosium(III) Single-Molecule Magnet. *Angew. Chemie Int. Ed.* **2016**, *55* (52), 16071–16074. https://doi.org/10.1002/anie.201609685.

[10] a) Goodwin, C. A. P.; Ortu, F.; Reta, D.; Chilton, N. F.; Mills, D. P. Molecular Magnetic Hysteresis at 60 Kelvin in Dysprosocenium. *Nature* **2017**, *548* (7668), 439–442. https://doi.org/10.1038/nature23447. b) Guo, F.; Day, B. M.; Chen, Y.; Tong, M.; Mansikkamäki, A.; Layfield, R. A. Magnetic Hysteresis up to 80 Kelvin in a Dysprosium Metallocene Single-Molecule Magnet. *Science (80-.).* **2018**, *362* (6421), 1400–1403. https://doi.org/10.1126/science.aav0652. c) Randall McClain, K.; Gould, C. A.; Chakarawet, K.; Teat, S. J.; Groshens, T. J.; Long, J. R.; Harvey, B. G. High-Temperature Magnetic Blocking and Magneto-Structural Correlations in a Series of Dysprosium(III) Metallocenium Single-Molecule Magnets. *Chem. Sci.* **2018**, *9* (45), 8492–8503. https://doi.org/10.1039/C8SC03907K.

[11] Zabala-Lekuona, A.; Seco, J. M.; Colacio, E. Single-Molecule Magnets: From Mn12-Ac to Dysprosium Metallocenes, a Travel in Time. *Coord. Chem. Rev.* **2021**, *441*, 213984. https://doi.org/10.1016/j.ccr.2021.213984.

[12] Kahn, O. (1993). *Molecular magnetism*. VCH.

[13] Feng, M.; Tong, M. L. Single Ion Magnets from 3d to 5f: Developments and Strategies. *Chem. - A Eur. J.* **2018**, *24* (30), 7574–7594. https://doi.org/10.1002/chem.201705761.

[14] Boča, R. Zero-Field Splitting in Metal Complexes. *Coord. Chem. Rev.* **2004**, *248* (9–10), 757–815. https://doi.org/10.1016/j.ccr.2004.03.001.

[15] Layfield, R., Murugesu, M. (2015). *Lanthanides and actinides in molecular magnetism*. Wiley-VCH.

[16] Liddle, S. T.; van Slageren, J. Improving F-Element Single Molecule Magnets. *Chem. Soc. Rev.* **2015**, *44* (19), 6655–6669. https://doi.org/10.1039/C5CS00222B.

[17] Chilton, N. F. *PHI User Manual v3*. https://www.molmag.manchester.ac.uk/software/phi_manual.pdf

[18] Benelli, C.; Gatteschi, D. (2015). Introduction to molecular magnetism: From transition metals to lanthanides. Wiley-VCH Verlag GmbH & Co. KGaA.

[19] Cotton, S. (2009). *Lanthanide and actinide chemistry*. John Wiley & Sons.

[20] Figgis, B.N.; Lewis, *J. (1960). "The Magnetochemistry of Complex Compounds".*
[21] Gong, C.; Zhang, H.; Wang, W.; Colombo, L.; Wallace, R. M.; Cho, K. Band Alignment of Two-Dimensional Transition Metal Dichalcogenides: Application in Tunnel Field Effect Transistors. *Appl. Phys. Lett.* **2013**, *103* (5). https://doi.org/10.1063/1.4817409/667647.
[22] Ryabov, I. D. On the Operator Equivalents and the Crystal-Field and Spin Hamiltonian Parameters. *Appl. Magn. Reson.* **2009**, *35* (3), 481–494. https://doi.org/10.1007/S00723-009-0179-Z/METRICS.
[23] 4.2.44. POLY_ANISO¶. 4.2.44. POLY_ANISO - Molcas Manual (version 23.06). (n.d.). https://molcas.gitlab.io/OpenMolcas/sphinx/users.guide/programs/poly_aniso.html
[24] Boča, R. (1999). *Theoretical Foundations of Molecular Magnetism*. Elsevier.
[25] Lines, M. E. Orbital Angular Momentum in the Theory of Paramagnetic Clusters. *J. Chem. Phys.* **1971**, *55* (6), 2977–2984. https://doi.org/10.1063/1.1676524.
[26] Compain, J.-D.; Mialane, P.; Dolbecq, A.; Mbomekallé, I. M.; Marrot, J.; Sécheresse, F.; Rivière, E.; Rogez, G.; Wernsdorfer, W. Iron Polyoxometalate Single-Molecule Magnets. *Angew. Chemie Int. Ed.* **2009**, *48* (17), 3077–3081. https://doi.org/10.1002/anie.200900117.
[27] Neese, F.; Pantazis, D. A. What Is Not Required to Make a Single Molecule Magnet. *Faraday Discuss.* **2011**, *148*, 229–238. https://doi.org/10.1039/C005256F.
[28] Yin, B.; Li, C.-C. A Method to Predict Both the Relaxation Time of Quantum Tunneling of Magnetization and the Effective Barrier of Magnetic Reversal for a Kramers Single-Ion Magnet. *Phys. Chem. Chem. Phys.* **2020**, *22* (18), 9923–9933. https://doi.org/10.1039/D0CP00933D.
[29] Phonon - Wikipedia. [online]. Dostupné z: https://en.wikipedia.org/wiki/Phonon [cit. 29. 03. 2022]
[30] Tarantul, A.; Tsukerblat, B. Direct and Two-Phonon Orbach-Aminov Type Spin-Lattice Relaxation in Molecular Magnet V 15. *J. Phys. Conf. Ser.* **2011**, *324* (1), 012007. https://doi.org/10.1088/1742-6596/324/1/012007.
[31] Aravena, D.; Ruiz, E. Spin Dynamics in Single-Molecule Magnets and Molecular Qubits. *Dalt. Trans.* **2020**, *49* (29), 9916–9928. https://doi.org/10.1039/D0DT01414A.
[32] Rajnák, C.; Boča, R. Reciprocating Thermal Behavior in the Family of Single Ion Magnets. *Coord. Chem. Rev.* **2021**, *436*, 213808. https://doi.org/10.1016/j.ccr.2021.213808.
[33] Bartolomé, E.; Arauzo, A.; Luzón, J.; Bartolomé, J.; Bartolomé, F. Magnetic Relaxation of Lanthanide-Based Molecular Magnets. In *Handbook of Magnetic Materials*; Elsevier, 2017; Vol. 26, pp 1–289. https://doi.org/10.1016/bs.hmm.2017.09.002.
[34] Chiesa, A.; Cugini, F.; Hussain, R.; Macaluso, E.; Allodi, G.; Garlatti, E.; Giansiracusa, M.; Goodwin, C. A. P.; Ortu, F.; Reta, D.; Skelton, J. M.; Guidi, T.; Santini, P.; Solzi, M.; De Renzi, R.; Mills, D. P.; Chilton, N. F.; Carretta, S. Understanding Magnetic Relaxation in Single-Ion Magnets with High Blocking Temperature. *Phys. Rev. B* **2020**, *101* (17), 174402. https://doi.org/10.1103/PhysRevB.101.174402.
[35] Giansiracusa, M. J.; Kostopoulos, A. K.; Collison, D.; Winpenny, R. E. P.; Chilton, N. F. Correlating Blocking Temperatures with Relaxation Mechanisms in Monometallic Single-Molecule Magnets with High Energy Barriers (: U Eff > 600 K). *Chem. Commun.* **2019**, *55* (49), 7025–7028. https://doi.org/10.1039/c9cc02421b.
[36] Castro-Alvarez, A.; Gil, Y.; Llanos, L.; Aravena, D. High Performance Single-Molecule Magnets, Orbach or Raman Relaxation Suppression? *Inorg. Chem. Front.* **2020**. https://doi.org/10.1039/d0qi00487a.
[37] Liddle, S. T.; van Slageren, J. Improving F-Element Single Molecule Magnets. *Chem. Soc. Rev.* **2015**, *44* (19), 6655–6669. https://doi.org/10.1039/C5CS00222B.
[38] Guo, Y. N.; Ungur, L.; Granroth, G. E.; Powell, A. K.; Wu, C.; Nagler, S. E.; Tang, J.; Chibotaru, L. F.; Cui, D. An NCN-Pincer Ligand Dysprosium Single-Ion Magnet Showing Magnetic Relaxation via the Second Excited State. *Sci. Reports 2014 41* **2014**, *4* (1), 1–7. https://doi.org/10.1038/srep05471.
[39] Manchester Molecular Magnetism Group [online]. Dostupné z: http://www.molmag.manchester.ac.uk/software/CHEM40111_2019_6.pdf [cit. 30.03.2022].
[40] Escalera-Moreno, L.; Suaud, N.; Gaita-Ariño, A.; Coronado, E. Determining Key Local Vibrations in the Relaxation of Molecular Spin Qubits and Single-Molecule Magnets. *J. Phys. Chem. Lett.* **2017**, *8* (7), 1695–1700. https://doi.org/10.1021/acs.jpclett.7b00479.
[41] a) Lunghi, A.; Totti, F.; Sessoli, R.; Sanvito, S. The Role of Anharmonic Phonons in Under-Barrier Spin Relaxation of Single Molecule Magnets. *Nat. Commun.* **2017**, *8* (1), 14620. https://doi.org/10.1038/ncomms14620. b) Reta, D.; Kragskow, J. G. C.; Chilton, N. F. Ab Initio Prediction of High-Temperature Magnetic Relaxation Rates in Single-Molecule Magnets. *J. Am. Chem. Soc.* **2021**, *143* (15), 5943–5950. https://doi.org/10.1021/jacs.1c01410.
[42] Bunting, P. C.; Atanasov, M.; Damgaard-Møller, E.; Perfetti, M.; Crassee, I.; Orlita, M.; Overgaard, J.; van Slageren, J.; Neese, F.; Long, J. R. A Linear Cobalt(II) Complex with Maximal Orbital Angular Momentum from a Non-Aufbau Ground State. *Science (80-.).* **2018**, *362* (6421), eaat7319. https://doi.org/10.1126/science.aat7319.
[43] Briganti, M.; Santanni, F.; Tesi, L.; Totti, F.; Sessoli, R.; Lunghi, A. A Complete Ab Initio View of Orbach and Raman Spin–Lattice Relaxation in a Dysprosium Coordination Compound. *J. Am. Chem. Soc.* **2021**, *143* (34),

13633–13645. https://doi.org/10.1021/jacs.1c05068.
[44] J. M. D. Coey (2009). *Magnetism and magnetic materials*. Cambridge Univ. Press.
[45] B. D. Josephson, *Phys. Lett.*, 1962, **1**, 251–253.
[46] Vibrating-sample magnetometer - Wikipedia. [online]. Dostupné z: https://en.wikipedia.org/wiki/Vibrating-sample_magnetometer
[47] SQUID Magnetometer - [online]. Dostupné z: http://hyperphysics.phy-astr.gsu.edu/hbase/Solids/Squid.html
[48] Arora, A. (2018). *Optical and electric field control of magnetism* [PhD dissertation]. Helmholtz-Zentrum Berlin.
[49] Harvey, J. (2018). *Computational Chemistry*. Oxford University Press.
[50] Townsend, J.; Kirkland, J. K.; Vogiatzis, K. D. Post-Hartree-Fock Methods: Configuration Interaction, Many-Body Perturbation Theory, Coupled-Cluster Theory. In *Mathematical Physics in Theoretical Chemistry*; Elsevier, 2019; pp 63–117. https://doi.org/10.1016/B978-0-12-813651-5.00003-6.
[51] Randall McClain, K.; Gould, C. A.; Chakarawet, K.; Teat, S. J.; Groshens, T. J.; Long, J. R.; Harvey, B. G. High-Temperature Magnetic Blocking and Magneto-Structural Correlations in a Series of Dysprosium(<scp>iii</Scp>) Metallocenium Single-Molecule Magnets. *Chem. Sci.* **2018**, *9* (45), 8492–8503. https://doi.org/10.1039/C8SC03907K.
[52] Kilpatrick, A. F. R.; Guo, F.-S.; Day, B. M.; Mansikkamäki, A.; Layfield, R. A.; Cloke, F. G. N. Single-Molecule Magnet Properties of a Monometallic Dysprosium Pentalene Complex. *Chem. Commun.* **2018**, *54* (51), 7085–7088. https://doi.org/10.1039/C8CC03516D.
[53] Vanjak, J. C.; Wilkins, B. O.; Vieru, V.; Bhuvanesh, N. S.; Reibenspies, J. H.; Martin, C. D.; Chibotaru, L. F.; Nippe, M. A High-Performance Single-Molecule Magnet Utilizing Dianionic Aminoborolide Ligands. *J. Am. Chem. Soc.* **2022**, *144* (39), 17743–17747. https://doi.org/10.1021/JACS.2C06698/ASSET/IMAGES/MEDIUM/JA2C06698_M003.GIF.
[54] Goodwin, C. A. P.; Reta, D.; Ortu, F.; Liu, J.; Chilton, N. F.; Mills, D. P. Terbocenium: Completing a Heavy Lanthanide Metallocenium Cation Family with an Alternative Anion Abstraction Strategy. *Chem. Commun.* **2018**, *54* (66), 9182–9185. https://doi.org/10.1039/C8CC05261A.
[55] Gould, C. A.; McClain, K. R.; Yu, J. M.; Groshens, T. J.; Furche, F.; Harvey, B. G.; Long, J. R. Synthesis and Magnetism of Neutral, Linear Metallocene Complexes of Terbium(II) and Dysprosium(II). *J. Am. Chem. Soc.* **2019**, *141* (33), 12967–12973. https://doi.org/10.1021/JACS.9B05816.
[56] Evans, P.; Reta, D.; Whitehead, G. F. S.; Chilton, N. F.; Mills, D. P. Bis-Monophospholyl Dysprosium Cation Showing Magnetic Hysteresis at 48 K. *J. Am. Chem. Soc.* **2019**, *141* (50), 19935–19940. https://doi.org/10.1021/jacs.9b11515.
[57] Demir, S.; Gonzalez, M. I.; Darago, L. E.; Evans, W. J.; Long, J. R. Giant Coercivity and High Magnetic Blocking Temperatures for N2 3− Radical-Bridged Dilanthanide Complexes upon Ligand Dissociation. *Nat. Commun. 2017 81* **2017**, *8* (1), 1–9. https://doi.org/10.1038/s41467-017-01553-w.
[58] Guo, F. S.; He, M.; Huang, G. Z.; Giblin, S. R.; Billington, D.; Heinemann, F. W.; Tong, M. L.; Mansikkamäki, A.; Layfield, R. A. Discovery of a Dysprosium Metallocene Single-Molecule Magnet with Two High-Temperature Orbach Processes. *Inorg. Chem.* **2022**, *61* (16), 6017–6025. https://doi.org/10.1021/ACS.INORGCHEM.1C03980/ASSET/IMAGES/LARGE/IC1C03980_0007.JPEG.
[59] Vincent, A. H.; Whyatt, Y. L.; Chilton, N. F.; Long, J. R. Strong Axiality in a Dysprosium(III) Bis(Borolide) Complex Leads to Magnetic Blocking at 65 K. *J. Am. Chem. Soc.* **2023**, *145* (3), 1572–1579. https://doi.org/10.1021/JACS.2C08568/ASSET/IMAGES/LARGE/JA2C08568_0004.JPEG.
[60] Gould, C. A.; McClain, K. R.; Reta, D.; Kragskow, J. G. C.; Marchiori, D. A.; Lachman, E.; Choi, E. S.; Analytis, J. G.; Britt, R. D.; Chilton, N. F.; Harvey, B. G.; Long, J. R. Ultrahard Magnetism from Mixed-Valence Dilanthanide Complexes with Metal-Metal Bonding. *Science (80-.).* **2022**, *375* (6577), 198–202. https://doi.org/10.1126/SCIENCE.ABL5470/SUPPL_FILE/SCIENCE.ABL5470_SM.V1.PDF.
[61] Korzyński, M. D.; Bernhardt, M.; Romankov, V.; Dreiser, J.; Matmon, G.; Pointillart, F.; Le Guennic, B.; Cador, O.; Copéret, C. Cyclooctatetraenide-Based Single-Ion Magnets Featuring Bulky Cyclopentadienyl Ligand. *Chem. Sci.* **2022**, *13* (35), 10574–10580. https://doi.org/10.1039/D2SC02560D.
[62] Le Roy, J. J.; Korobkov, I.; Murugesu, M. A Sandwich Complex with Axial Symmetry for Harnessing the Anisotropy in a Prolate Erbium(<scp>iii</Scp>) Ion. *Chem. Commun.* **2014**, *50* (13), 1602–1604. https://doi.org/10.1039/C3CC48557A.
[63] Le Roy, J. J.; Ungur, L.; Korobkov, I.; Chibotaru, L. F.; Murugesu, M. Coupling Strategies to Enhance Single-Molecule Magnet Properties of Erbium-Cyclooctatetraenyl Complexes. *J. Am. Chem. Soc.* **2014**, *136* (22), 8003–8010. https://doi.org/10.1021/JA5022552/SUPPL_FILE/JA5022552_SI_002.ZIP.
[64] Münzfeld, L.; Schoo, C.; Bestgen, S.; Moreno-Pineda, E.; Köppe, R.; Ruben, M.; Roesky, P. W. Synthesis, Structures and Magnetic Properties of [(H9-C9H9)Ln(H8-C8H8)] Super Sandwich Complexes. *Nat. Commun.* **2019**, *10* (1), 3135. https://doi.org/10.1038/s41467-019-10976-6.

[65] a) Ungur, L.; Van Den Heuvel, W.; Chibotaru, L. F. Ab Initio Investigation of the Non-Collinear Magnetic Structure and the Lowest Magnetic Excitations in Dysprosium Triangles. *New J. Chem.* **2009**, *33* (6), 1224–1230. https://doi.org/10.1039/b903126j. b) Chibotaru, L. F.; Ungur, L.; Soncini, A. The Origin of Nonmagnetic Kramers Doublets in the Ground State of Dysprosium Triangles: Evidence for a Toroidal Magnetic Moment. *Angew. Chemie Int. Ed.* **2008**, *47* (22), 4126–4129. https://doi.org/10.1002/anie.200800283. c) Ungur, L.; Thewissen, M.; Costes, J.-P.; Wernsdorfer, W.; Chibotaru, L. F. Interplay of Strongly Anisotropic Metal Ions in Magnetic Blocking of Complexes. *Inorg. Chem.* **2013**, *52* (11), 6328–6337. https://doi.org/10.1021/ic302568x. d) Chibotaru, L. F.; Ungur, L.; Aronica, C.; Elmoll, H.; Pilet, G.; Luneau, D. Structure, Magnetism, and Theoretical Study of a Mixed-Valence Co II3CoIII4 Heptanuclear Wheel: Lack of SMM Behavior despite Negative Magnetic Anisotropy. *J. Am. Chem. Soc.* **2008**, *130* (37), 12445–12455. https://doi.org/10.1021/ja8029416. e) Chibotaru, L. F.; Ungur, L.; Soncini, A. The Origin of Nonmagnetic Kramers Doublets in the Ground State of Dysprosium Triangles: Evidence for a Toroidal Magnetic Moment. *Angew. Chemie - Int. Ed.* **2008**, *47* (22), 4126–4129. https://doi.org/10.1002/anie.200800283.

[66] Ungur, L.; Chibotaru, L. F. Strategies toward High-Temperature Lanthanide-Based Single-Molecule Magnets. *Inorg. Chem.* **2016**, *55* (20), 10043–10056. https://doi.org/10.1021/acs.inorgchem.6b01353.

[67] Mironov, V. Molecular Engineering of High Energy Barrier in Single-Molecule Magnets Based on [MoIII(CN)7]4− and V(II) Complexes. *Inorganics* **2018**, *6* (2), 58. https://doi.org/10.3390/inorganics6020058.

[68] Ullah, A.; Cerdá, J.; Baldoví, J. J.; Varganov, S. A.; Aragó, J.; Gaita-Ariño, A. In Silico Molecular Engineering of Dysprosocenium-Based Complexes to Decouple Spin Energy Levels from Molecular Vibrations. *J. Phys. Chem. Lett.* **2019**, *10* (24), 7678–7683. https://doi.org/10.1021/acs.jpclett.9b02982.

[69] Baldoví, J. J.; Borrás-almenar, J. J.; Clemente-juan, J. M.; Coronado, E.; Gaita-ariño, A. Modeling the Properties of Lanthanoid Single-Ion Magnets Using an Effective Point-Charge Approach †. *Dalt. Trans.* **2012**, *41*, 13705–13710. https://doi.org/10.1039/c2dt31411h.

[70] Baldoví, J. J.; Cardona-Serra, S.; Clemente-Juan, J. M.; Coronado, E.; Gaita-Ariño, A.; Palii, A. SIMPRE: A Software Package to Calculate Crystal Field Parameters, Energy Levels, and Magnetic Properties on Mononuclear Lanthanoid Complexes Based on Charge Distributions. *J. Comput. Chem.* **2013**, *34* (22), 1961–1967. https://doi.org/10.1002/JCC.23341.

[71] Baldoví, J. J.; Clemente-Juan, J. M.; Coronado, E.; Gaita-Ariño, A. Two Pyrazolylborate Dysprosium(III) and Neodymium(III) Single Ion Magnets Modeled by a Radial Effective Charge Approach. *Polyhedron* **2013**, *66*, 39–42. https://doi.org/10.1016/j.poly.2013.01.034.

[72] Demir, S.; Jeon, I.-R.; Long, J. R.; Harris, T. D. Radical Ligand-Containing Single-Molecule Magnets. *Coord. Chem. Rev.* **2015**, *289–290* (1), 149–176. https://doi.org/10.1016/j.ccr.2014.10.012.

[73] Mironov, V. Molecular Engineering of High Energy Barrier in Single-Molecule Magnets Based on [MoIII(CN)7]4− and V(II) Complexes. *Inorganics* **2018**, *6* (2), 58. https://doi.org/10.3390/inorganics6020058.

[74] Liu, K.; Shi, W.; Cheng, P. Toward Heterometallic Single-Molecule Magnets: Synthetic Strategy, Structures and Properties of 3d-4f Discrete Complexes. *Coord. Chem. Rev.* **2015**, *289–290* (1), 74–122. https://doi.org/10.1016/j.ccr.2014.10.004.

[75] M. Sakamoto, T. Ishikawa, Y. Nishida, Y. Sadaoka, A. Matsumoto, Y. Fukuda, M. Sakai, M. Ohba, H. Sakiyama and H. Ōkawa, *J. Alloys Compd.*, 1996, **238**, 23–27.

[76] S. K. Singh and G. Rajaraman, *Dalt. Trans.*, 2013, **42**, 3623.

[77] T. Ishida, R. Watanabe, K. Fujiwara, A. Okazawa, N. Kojima, G. Tanaka, S. Yoshii and H. Nojiri, *Dalt. Trans.*, 2012, **41**, 13609.

[78] Y.-A. Liu, C.-Y. Wang, M. Zhang and X.-Q. Song, *Polyhedron*, 2017, **127**, 278–286.

[79] H.-R. Wen, J. Bao, S.-J. Liu, C.-M. Liu, C.-W. Zhang and Y.-Z. Tang, *Dalt. Trans.*, 2015, **44**, 11191–11201.

[80] P. Zhang, L. Zhang, S.-Y. Lin and J. Tang, *Inorg. Chem.*, 2013, **52**, 6595–6602.

[81] L. Xu, Q. Zhang, G. Hou, P. Chen, G. Li, D. M. Pajerowski and C. L. Dennis, *Polyhedron*, 2013, **52**, 91–95.

[82] Y. Sui, D.-S. Liu, R.-H. Hu and J.-G. Huang, *Inorganica Chim. Acta*, 2013, **395**, 225–229.

[83] J.-P. Costes, B. Donnadieu, R. Gheorghe, G. Novitchi, J.-P. Tuchagues and L. Vendier, *Eur. J. Inorg. Chem.*, 2008, **2008**, 5235–5244.

[84] J.-P. Costes, M. Auchel, F. Dahan, V. Peyrou, S. Shova and W. Wernsdorfer, *Inorg. Chem.*, 2006, **45**, 1924–1934.

[85] R. Koner, G.-H. Lee, Y. Wang, H.-H. Wei and S. Mohanta, *Eur. J. Inorg. Chem.*, 2005, **2005**, 1500–1505.

[86] R. Koner, H.-H. Lin, H.-H. Wei and S. Mohanta, *Inorg. Chem.*, 2005, **44**, 3524–3536..

[87] O. Margeat, P. G. Lacroix, J. P. Costes, B. Donnadieu, C. Lepetit and K. Nakatani, *Inorg. Chem.*, 2004, **43**, 4743–4750.

[88] G. Novitchi, S. Shova, A. Caneschi, J.-P. Costes, M. Gdaniec and N. Stanica, *Dalt. Trans.*, 2004, 1194–1200.

[89] H. Kara, Y. Elerman and K. Prout, *Zeitschrift für Naturforsch. B*, 2000, **55**, 1131–1136.

[90] J.-P. Costes, F. Dahan and A. Dupuis, *Inorg. Chem.*, 2000, **39**, 165–168.

[91] M. Sakamoto, M. Hashimura, K. Matsuki, N. Matsumoto, K. Inoue and H. Okawa, *Bull. Chem. Soc. Jpn.*, 1991, **64**, 3639–3641.
[92] T. Ishida, R. Watanabe, K. Fujiwara, A. Okazawa, N. Kojima, G. Tanaka, S. Yoshii and H. Nojiri, *Dalt. Trans.*, 2012, **41**, 13609.
[93] L. M. Lilley, K. Du, M. D. Krzyaniak, G. Parigi, C. Luchinat, T. D. Harris and T. J. Meade, *Inorg. Chem.*, 2018, **57**, 5810–5819..
[94] M. Towatari, K. Nishi, T. Fujinami, N. Matsumoto, Y. Sunatsuki, M. Kojima, N. Mochida, T. Ishida, N. Re and J. Mrozinski, *Inorg. Chem.*, 2013, **52**, 6160–6178.
[95] T. Kajiwara, M. Nakano, K. Takahashi, S. Takaishi and M. Yamashita, *Chem. - A Eur. J.*, 2011, **17**, 196–205.
[96] G. Novitchi, J.-P. Costes and B. Donnadieu, *Eur. J. Inorg. Chem.*, 2004, **2004**, 1808–1812.
[97] F. Z. Chiboub Fellah, S. Boulefred, A. Chiboub Fellah, B. El Rez, C. Duhayon and J.-P. Sutter, *Inorganica Chim. Acta*, 2016, **439**, 24–29.
[98] Sarkar, A.; Dey, S.; Rajaraman, G. Role of Coordination Number and Geometry in Controlling the Magnetic Anisotropy in FeII, CoII, and NiII Single-Ion Magnets. *Chem. – A Eur. J.* **2020**, 26 (62), 14036–14058.
[99] a) Alvarez, S. Polyhedra in (Inorganic) Chemistry. *Dalt. Trans.* **2005**, No. 13, 2209. https://doi.org/10.1039/b503582c. b) Casanova, D.; Alemany, P.; Bofill, J. M.; Alvarez, S. Shape and Symmetry of Heptacoordinate Transition-Metal Complexes: Structural Trends. *Chem. - A Eur. J.* **2003**, *9* (6), 1281–1295. https://doi.org/10.1002/chem.200390145. c) Ruiz-Martínez, A.; Casanova, D.; Alvarez, S. Polyhedral Structures with an Odd Number of Vertices: Nine-Atom Clusters and Supramolecular Architectures. *Dalt. Trans.* **2008**, No. 19, 2583. https://doi.org/10.1039/b718821h. d) Alvarez, S.; Alemany, P.; Casanova, D.; Cirera, J.; Llunell, M.; Avnir, D. Shape Maps and Polyhedral Interconversion Paths in Transition Metal Chemistry. *Coord. Chem. Rev.* **2005**, *249* (17-18 SPEC. ISS.), 1693–1708. https://doi.org/10.1016/j.ccr.2005.03.031.
[100] Yao, B.; Singh, M. K.; Deng, Y.-F.; Wang, Y.-N.; Dunbar, K. R.; Zhang, Y.-Z. Trigonal Prismatic Cobalt(II) Single-Ion Magnets: Manipulating the Magnetic Relaxation Through Symmetry Control. *Inorg. Chem.* 2020, ***59*** (12), 8505–8513. https://doi.org/10.1021/acs.inorgchem.0c00950.
[101] Novikov, V. V; Pavlov, A. A.; Nelyubina, Y. V; Boulon, M.-E.; Varzatskii, O. A.; Voloshin, Y. Z.; Winpenny, R. E. P. A Trigonal Prismatic Mononuclear Cobalt(II) Complex Showing Single-Molecule Magnet Behavior. *J. Am. Chem. Soc.* 2015, ***137*** (31), 9792–9795. https://doi.org/10.1021/jacs.5b05739.
[102] Pavlov, A. A.; Aleshin, D. Y.; Savkina, S. A.; Belov, A. S.; Efimov, N. N.; Nehrkorn, J.; Ozerov, M.; Voloshin, Y. Z.; Nelyubina, Y. V; Novikov, V. V. A Trigonal Prismatic Cobalt(II) Complex as a Single Molecule Magnet with a Reduced Contribution from Quantum Tunneling. *ChemPhysChem* 2019, ***20*** (8), 1001–1005. https://doi.org/10.1002/cphc.201900219.
[103] Pavlov, A. A.; Savkina, S. A.; Belov, A. S.; Nelyubina, Y. V; Efimov, N. N.; Voloshin, Y. Z.; Novikov, V. V. Trigonal Prismatic Tris-Pyridineoximate Transition Metal Complexes: A Cobalt(II) Compound with High Magnetic Anisotropy. *Inorg. Chem.* 2017, ***56*** (12), 6943–6951. https://doi.org/10.1021/acs.inorgchem.7b00447.
[104] Ozumerzifon, T. J.; Bhowmick, I.; Spaller, W. C.; Rappé, A. K.; Shores, M. P. Toward Steric Control of Guest Binding Modality: A Cationic Co(II) Complex Exhibiting Cation Binding and Zero-Field Relaxation. *Chem. Commun.* 2017, ***53*** (30), 4211–4214. https://doi.org/10.1039/C7CC01172E.
[105] Yao, B.; Deng, Y.-F.; Li, T.; Xiong, J.; Wang, B.-W.; Zheng, Z.; Zhang, Y.-Z. Construction and Magnetic Study of a Trigonal-Prismatic Cobalt(II) Single-Ion Magnet. *Inorg. Chem.* 2018, ***57*** (22), 14047–14051. https://doi.org/10.1021/acs.inorgchem.8b02692.
[106] Zhu, Y. Y.; Zhang, Y. Q.; Yin, T. T.; Gao, C.; Wang, B. W.; Gao, S. A Family of $Co^{II}Co^{III}_3$ Single-Ion Magnets with Zero-Field Slow Magnetic Relaxation: Fine Tuning of Energy Barrier by Remote Substituent and Counter Cation. *Inorg. Chem.* 2015, ***54*** (11), 5475–5486. https://doi.org/10.1021/ACS.INORGCHEM.5B00526
[107] Nemec, I.; Fellner, O. F.; Indruchová, B.; Herchel, R. Trigonally Distorted Hexacoordinate Co(II) Single-Ion Magnets. *Materials (Basel).* 2022, ***15*** (3), 1064. https://doi.org/10.3390/ma15031064.
[108] Andruh, M. Heterotrimetallic Complexes in Molecular Magnetism. *Chem. Commun.* **2018**, *54* (29), 3559–3577. https://doi.org/10.1039/c8cc00939b.
[109] J. Wang , J. J. Zakrzewski , M. Zychowicz , V. Vieru , L. F. Chibotaru , K. Nakabayashi , S. Chorazy and S.-I. Ohkoshi , *Chem. Sci.*, 2021, **12** , 730 —741
[110] M. Ferbinteanu , A. Stroppa , M. Scarrozza , I. Humelnicu , D. Maftei , B. Frecus and F. Cimpoesu , *Inorg. Chem.*, 2017, **56** , 9474 —9485
[111] F. Cimpoesu , F. Dahan , S. Ladeira , M. Ferbinteanu and J.-P. Costes , *Inorg. Chem.*, 2012, **51** , 11279 —11293
[112] I. Oyarzabal, A. Zabala-Lekuona, A. J. Mota, M. A. Palacios, A. Rodríguez-Diéguez, G. Lorusso, M. Evangelisti, C. Rodríguez-Esteban, E. K. Brechin, J. M. Seco and E. Colacio, *Dalt. Trans.*, 2022, **51**, 12954–12967.
[113] A. Panja, Z. Jagličić, R. Herchel, P. Brandão, K. Pramanik and N. C. Jana, *New J. Chem.*, 2022, **46**, 13546–13557.

7. Přílohy

Příloha 1: Kotrle, K.; Herchel, R. Are Inorganic Single-Molecule Magnets a Possibility? A Theoretical Insight into Dysprosium Double-Deckers with Inorganic Ring Systems. *Inorg. Chem.* 2019, *58* (20), 14046–14057. https://doi.org/10.1021/acs.inorgchem.9b02039.

Inorganic Chemistry
Article
Cite This: Inorg. Chem. 2019, 58, 14046−14057
pubs.acs.org/IC

Are Inorganic Single-Molecule Magnets a Possibility? A Theoretical Insight into Dysprosium Double-Deckers with Inorganic Ring Systems

Kamil Kotrle and Radovan Herchel*

Department of Inorganic Chemistry, Faculty of Science, Palacký University Olomouc, 17. listopadu 12, 771 46 Olomouc, Czech Republic

Supporting Information

ABSTRACT: Computational studies of sandwich dysprosium double-decker complexes $[Dy(L)_2]^{+/3+}$ as candidates for single-ion magnets with several inorganic aromatic ring systems (P_5^-, N_5^-, $B_3N_3H_6$, $B_3P_3H_6$, $B_3S_3H_3$) have been performed. The molecular structures were optimized with the TPSSh functional, and the ground state properties were investigated with the complete active space SCF method (CASSCF) complemented by the dynamic correlation dressed correction (DCD-CAS(2)) or NEVPT2. Besides the evaluation of the magnetic moment blocking barrier, the impact of the molecular vibration on the relaxation of magnetization was also inspected. We were able to make predictions about the performance of those molecules as single-molecule magnets, where estimated effective energy barrier, U_{eff}, values are as high as 1475 K in the case of $[Dy(N_5)_2]^-$, which is the most anisotropic complex from our choice of studied compounds, making them a potentially very effective carbon-free alternative to organometallic double-decker dysprosocenium high-temperature single-molecule magnets.

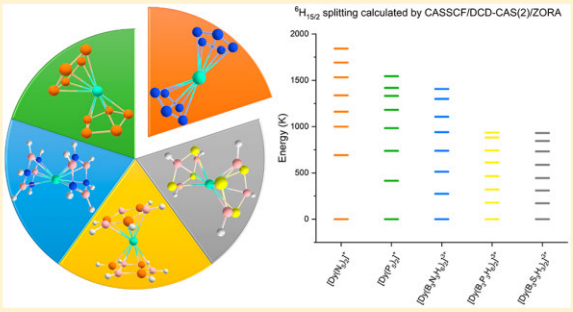

INTRODUCTION

In almost 30 years, progress in developing single-molecule magnets went from discovery of this phenomenon on the famous $Mn_{12}Ac$ complex,[1] through many major breakthroughs, such as the first lanthanide single-ion magnets,[2] to finally reaching the blocking temperature of 14 K with the terbium radical bridged dimer $[Tb_2(NSi_2C_6H_{18})_4(THF)_2(\mu-\eta^2:\eta^2-N_2)]$.[3] A few years later, based on structural correlation predictions, pentagonal bipyramidal complexes with highly electronegative ligands in axial positions were proven to be effective for developing single-molecule magnets with large blocking temperatures and energy barriers over 1800 K with $[Dy(O^tBu)_2(py)_5](BPh_4)$.[4] Axiality of the ligand field is characteristic also for the newest and most recent family of single-molecule magnets, organometallic double-deckers, which allowed for reaching blocking temperatures up to the boiling point of liquid nitrogen and were an inspiration for this theoretical study.

The first one among this family of "dysprosocenes" was $[Dy(Cp^{ttt})_2][B(C_6F_5)_4]$ (Cp^{ttt} = 1,2,4-tri-*terc*-butylcyclopentadienyl), whose preparation was not only a remarkable synthetic success but also has led to a complex with a blocking temperature 60 K, a value never seen before, and a reversal barrier of 1760 K.[5] Later on, $[Dy(Cp^{iPr5})(Cp^*)][B(C_6F_5)_4]$ (Cp^{iPr5} = pentaisopropylcyclopentadienyl) was prepared with a blocking temperature of 80 K and U_{eff} = 2217 K,[6] where both of those values are still unsurpassed today. In addition, a series of complexes $[Dy(Cp^{iPr4R})_2][B(C_6F_5)_4]$ have been recently prepared, where Cp^{iPr4R} is cyclopentadiene substituted by isopropyl in four positions and last one by hydrogen, methyl, ethyl, and isopropyl. Hysteresis temperatures and energy barriers have their lowest value for R = H, with T_B = 17 K and U_{eff} = 1848 K, and their highest value for R = Me, with T_B = 72 K and U_{eff} = 2112 K.[7] Also, many attempts on explaining the behavior of single-molecule magnets were performed by theoretical methods, aiming at insight into magnetic properties by the evaluation of the zero-field splitting energy levels. This can be achieved by employing ab initio multiconfigurational SCF calculations like CASSCF capable of describing the ground state properties of d- and f-metal ions.[8] This method led to the prediction of the anisotropic energy barrier as an energy difference between Kramers doublets and became one of the most frequent and efficient tools used for characterizing new single-molecule magnets, along with experimental methods.[9] In addition, general relationships applicable to all dysprosium-based single-molecule magnets taking into the account various structural motifs were elucidated with the help of the CASSCF method.[10] The main conclusions were that dysprosium's anisotropy rises with the axial coordination environment, which later led to the synthesis of pentagonal

Received: July 9, 2019
Published: October 9, 2019

DOI: 10.1021/acs.inorgchem.9b02039
Inorg. Chem. 2019, 58, 14046−14057

bipyramidal complexes and probably at least inspired recent development of dysprosocenium-like compounds.

From comparing values of the magnetic moment reversal energy barriers and hysteresis temperatures of dysprosocenium SMMs,[11] we can see that their dependence is not as clear as theory might suggest. This is where a deeper understanding of the relaxation mechanism comes into play. Apart from quantum tunneling of magnetization,[12] all other relaxation mechanisms are of the spin−lattice origin, and therefore, they are governed by phonon excitations. Phonons, in general, are vibrations, both intermolecular and intramolecular, and it has been suggested that their role in determining relaxation pathways is crucial.[13] One of the approaches consists of approximative assumption, where phonons can in some cases be reduced to molecular vibrations, and calculations of parameters important to relaxation, depending on structure deformation caused by vibrations, can lead to revealing of vibrational modes that are strongly coupled to the spin-vibrational relaxation.[14] However, this approach neglects the intermolecular vibrations; therefore, it can be used mainly on the well-isolated complexes with minimum noncovalent intermolecular interactions, such as $[Dy(Cp^{ttt})_2][B(C_6F_5)_4]$,[5] where it was also successfully employed.

The striking performance of these double-decker sandwich Dy^{III} complexes[5,6] in the realm of the single-molecule magnetism led us to investigate the answer to the question of whether complexes with other ring systems able to mimic axial ligand field found in cyclopentadienyl complexes can lead to novel SMMs. Thus, the goal of this article is to theoretically inspect the crucial properties of the dysprosium-based single-molecule magnets utilizing the inorganic aromatic rings as ligands in analogy to recently published record-breaker dysprosocenium compounds. For this purpose, we have chosen two penta-membered rings, P_5^- and N_5^-, as analogues of cyclopentadienyl and three neutral six-membered rings, $B_3N_3H_6$, $B_3P_3H_6$, and $B_3S_3H_3$, as examples from a wide number of inorganic rings,[15] which are on the edge between aromatic and nonaromatic systems, to explore the geometry, the electronic structure, the magnetic moment reversal barrier U_{eff}, and the influence of the molecular vibrations on the magnetic relaxation phenomenon for $[Dy^{III}L_2]^{+/3+}$ complexes. Although no complexes are known with those compounds coordinating on lanthanide ions, they are well-known in organometallic chemistry of other metals. The P_5^- serves as the η^5-ligand in many coordination compounds similar to metallocene, but there is only one example of homoleptic sandwich complex of Ti^0, $[Ti(P_5)_2]^{2-}$, reported so far.[16] On the contrary, there are many heteroleptic sandwich or half-sandwich compounds with a P_5^- ligand, mostly with central atoms like iron[17] or chromium.[18] Moreover, the ligand has the ability to act as a bridging ligand either in the η^5-fashion or in the η^1-fashion, thus making it a suitable ligand for the synthesis of polynuclear or polymeric coordination compounds, which can be demonstrated by recently published heterobimetallic Ru/Fe sandwich compounds[19] or by binuclear U^{IV} compound.[20] Pentazole (N_5^-) anion is deeply studied due to its utilization in the preparation of explosives; an advantageous synthetic route was recently published,[21] and there are only few complexes prepared comprised of 3d metals, in which pentazole is bound in the η^1-fashion.[22] However, the 3d-transition-metal metallocene analogs were already theoretically studied, and even a possible synthetic route was proposed.[23] The borazine derivatives coordinated in the η^6-fashion can be found in half-sandwich carbonyl complexes with chromium and manganese,[24] and η^1-$B_3N_3H_6$ with iron were also reported.[25] The derivative of 1,3,5,2,4,6-triphosphatriborinane, $B_3P_3R_6$, was utilized in the formation of a carbonyl half-sandwich complex of chromium.[26] Up to now, there are no known complexes of thioborazine ($B_3S_3H_3$).

Therefore, the geometries of $[Dy^{III}L_2]^{+/3+}$ complexes with L = P_5^-, N_5^-, $B_3N_3H_6$, $B_3P_3H_6$, and $B_3S_3H_3$ were optimized with the help of DFT method, and the aromaticity of these ligands was also assessed. Subsequently, the several up-to-date multireference theoretical approaches were applied to calculate the zero-field splitting of $^6H_{15/2}$ of Dy^{III} ions in these complexes, which enabled the analysis of the effective energy barrier U_{eff} based on the magnetic dipole transition moment and the Boltzmann population of the multiplets. Furthermore, the role of the molecular vibration modes on the magnetic anisotropy and the magnetization relaxation properties were inspected and discussed to better understand the advantages and the limitation of these proposed fully inorganic SMMs.

EXPERIMENTAL SECTION

Theoretical Methods. The DFT theoretical calculations were carried out with the ORCA 4.1. software,[27] using density functional theory for structure optimizations and numerical frequency calculations. DFT calculations were run with the hybrid meta-GGA TPSSh functional.[28] We have used basis sets utilized for ZORA relativistic approximation,[29] namely, quadruple-ζ basis SARC2-ZORA-QZV for Dy[30] and ZORA-def2-TZVP for all other atoms,[31] except for H atoms for which split valence ZORA-def2-SVP was used. The SARC/J Coulomb fitting basis set was utilized as an auxiliary basis set.[30] Chain-of-spheres (RIJCOSX) approximation to exact exchange was used[32] as implemented in ORCA for $[Dy(P_5)_2]^+$ and $[Dy(B_3N_3H_6)_2]^{3+}$, while RI-JK approximation[33] was applied for $[Dy(N_5)_2]^+$, $[Dy(B_3P_3H_6)_2]^{3+}$, and $[Dy(B_3S_3H_3)_2]^{3+}$. Increased integration grids (Grid6 and Gridx6 in ORCA convention) and tight SCF convergence criteria were used in all calculations. Analogously, geometries of $[Dy(Cp^{ttt})_2]^+$ and$[Dy(Cp^{iprs})(Cp^*)]^+$ were also optimized to verify the performance of TPSSh functional. However, the posterior multireference calculations were done on the experimental X-ray structures of these two complexes.

Subsequently, state average complete active space self-consistent field (SA-CASSCF)[34] wave function calculations complemented by the dynamic correlation dressed (DCD-CAS(2)) correction[35] or by N-electron valence second-order perturbation theory (NEVPT2)[36] were done. Active space was defined as 9 electrons in 7 f-orbitals resulting in 21 sextets, 224 quartets, and 490 doublets. The spin−orbit interactions were treated with an approximation to the Breit−Pauli form of the spin−orbit coupling operator (SOMF approximation).[37] The same basis sets as in DFT calculations were used. The calculations utilized the RIJCOSX approximation with the automatically generated auxiliary basis from ORCA's AutoAux implemented option.[38]

Calculations related to spin dynamics were done with the MOLCAS 8.0 program package[39] using the same active space CAS(9,7). The RASSCF method was employed in the CASSCF calculations with the following numbers of multiplets: 21 sextets, 224 quartets, and 490 doublets. The spin−orbit coupling based on atomic mean-field approximation (AMFI)[40] was taken into account using RASSI-SO with the following numbers of multiplets: 21 sextets, 128 quartets, and 130 doublets. The relativistic effects were treated with the Douglas−Kroll Hamiltonian.[41] The following basis sets were employed: ANO-RCC-VQZP for Dy and ANO-RCC-VTZP for all other atoms.[42] Then, the SINGLE_ANISO module[43] was used to calculate all relevant information and magnetic data.

DOI: 10.1021/acs.inorgchem.9b02039
Inorg. Chem. 2019, 58, 14046−14057

Table 1. Selected Distances and Angles between Ring Centroids and Central Atom for TPSSh Optimized Structures and Their Comparison with X-ray Data for Selected Published Dysprosium Sandwich Complexes

complex	Dy−Centr1 (Å)	Dy−Centr2 (Å)	Centr1−Dy−Centr2 (deg)
$[Dy(P_5)_2]^+$	2.379	2.389	141.7
$[Dy(N_5)_2]^+$	2.225	2.225	153.5
$[Dy(B_3N_3H_6)_2]^{3+}$	2.282	2.278	142.8
$[Dy(B_3P_3H_6)_2]^{3+}$	2.494	2.495	149.2
$[Dy(B_3S_3H_3)_2]^{3+}$	2.353	2.353	146.7
$[Dy(Cp^{ttt})_2]^{+a}$	2.318	2.314	152.6
$[Dy(Cp^{iprs})(Cp^*)]^{+a}$	2.296	2.284	162.5
$[Dy(Cp^{ttt})_2]^{+b}$	2.338	2.337	156.1
$[Dy(Cp^{iprs})(Cp^*)]^{+b}$	2.324	2.348	168.4

[a]The experimental X-ray structures. [b]The DFT optimized molecular structures.

RESULTS AND DISCUSSION

The theoretical calculations were done for dysprosocenium-like complexes $[Dy^{III}L_2]^{+/3+}$ comprising the inorganic aromatic ligands analogous to cyclopentadienyl, P_5^- and N_5^-, and neutral, six-membered rings $B_3N_3H_6$, $B_3P_3H_6$, and $B_3S_3H_3$. First, the results of the geometry optimization procedure are discussed. Next, several theoretical multireference approaches with and without dynamic correlation applied to $[Dy^{III}L_2]^{+/3+}$ complexes are compared. Subsequently, the effective energy barriers U_{eff} were estimated based on the respective CASSCF calculations. Furthermore, the impact of the molecular vibrations on the reduction of U_{eff} was also evaluated, so the crucial properties of the herein proposed candidates for SMMs are thoroughly discussed.

Geometry Optimizations. The TPSSh functional was used for the calculations of the molecular geometry of $[Dy^{III}L_2]^{+/3+}$ complexes, and it was also applied also to $[Dy(Cp^{ttt})_2]^+$ and $[Dy(Cp^{iprs})(Cp^*)]^+$ complexes. The comparison of the selected geometrical parameters in Table 1 proved its good performance. All optimized molecular structures adapt geometry similar to dysprosium cyclopentadienyl derivate complexes, with rings slightly distorted from the axial geometry (Figure 1). For $[Dy(N_5)_2]^+$ and $[Dy(P_5)_2]^+$, ligands adopt a near-eclipsed conformation, and the same holds for $[Dy(B_3S_3H_3)_2]^{3+}$; while for $[Dy(B_3N_3H_6)_2]^{3+}$, it seems to be closer to a staggered conformation. The complex $[Dy(B_3P_3H_6)_2]^{3+}$ is situated in between those two conformations. Coordinated ring systems are planar, with only $B_3N_3H_6$ and $B_3S_3H_3$ displaying small deformations from the ideal plane. Optimizations were verified by numerical frequencies calculation, which has shown no imaginary vibrational modes present (Table S1 and Figure S1).

The selected parameters of the optimized geometries are listed in Table 1. The distance between dysprosium ion and ring centroids varies between 2.22 and 2.49 Å, where the shortest is found for $[Dy(P_5)_2]^+$ and the longest for $[Dy(B_3P_3H_6)_2]^{3+}$, and these parameters are close to those found in $[Dy(Cp^{ttt})_2]^+$ and $[Dy(Cp^{iprs})(Cp^*)]^+$. The angle formed between the dysprosium ion and both centroids is in the range from 142° to 153°, where the largest angle was found for $[Dy(P_5)_2]^+$ with the value almost identical to $[Dy(Cp^{ttt})_2]^+$. Within the six-membered rings, the both the Dy−centroid distances and centroid−Dy−centroid angle are increasing in the order $[Dy(B_3N_3H_6)_2]^{3+}$ < $Dy(B_3S_3H_3)_2]^{3+}$ < $[Dy(B_3P_3H_6)_2]^{3+}$.

In case of the compounds studied here, both P_5^- and N_5^- are supposed to be aromatic,[44] while the aromaticity of borazine and its derivates, despite being called "inorganic benzene", is a bit unclear when considering different criteria.[45] As cyclopentadienyl-based sandwich complexes $[Dy(Cp^{ttt})_2]^+$ and $[Dy(Cp^{iPr5})(Cp^*)]^+$ provided record-breaking results, it is evident that aromatic rings can serve very well to provide an axial ligand field, which is the cardinal condition for the highest

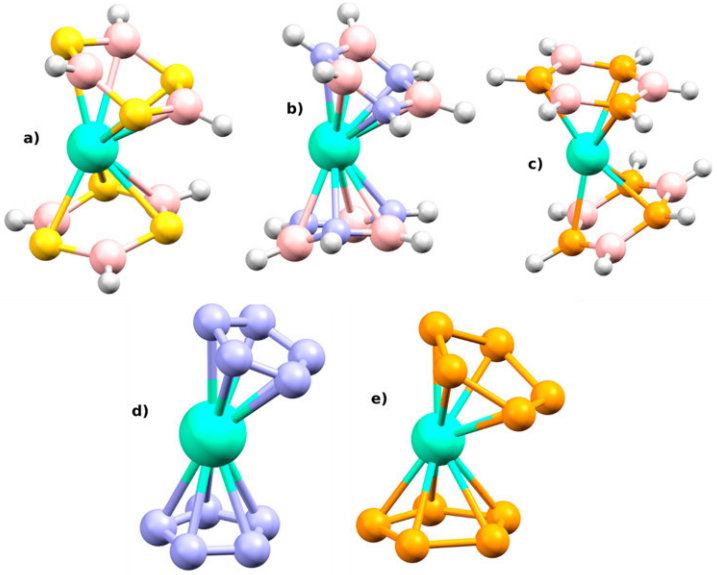

Figure 1. Optimized molecular structures of complexes $[Dy(B_3S_3H_3)_2]^{3+}$ (a), $[Dy(B_3N_3H_6)_2]^{3+}$ (b), $[Dy(B_3P_3H_6)_2]^{3+}$ (c), $[Dy(N_5)_2]^+$ (d), and $[Dy(P_5)_2]^+$ (e).

DOI: 10.1021/acs.inorgchem.9b02039
Inorg. Chem. 2019, 58, 14046−14057

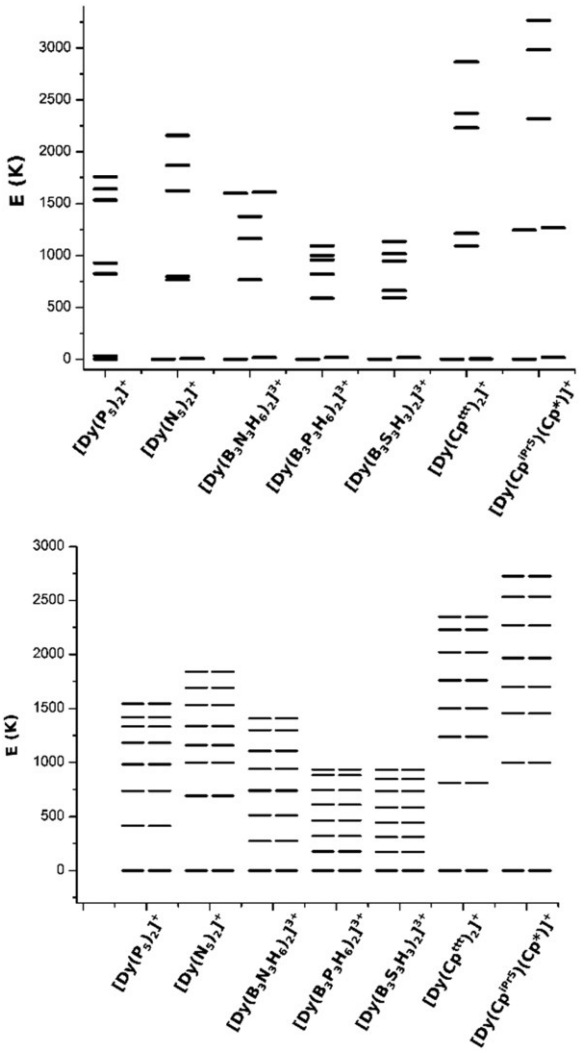

Figure 2. CASSCF/DCD-CAS(2) energy splitting of f-orbitals (top) and Kramers doublets of $^6H_{15/2}$ multiplet (bottom) in studied complexes compared to previously studied dysprosium cyclopentadienyl complexes.

U_{eff}, and such geometry is hard to achieve with monodentate ligands.[46] Therefore, we have decided to evaluate the aromaticity of the herein studied coordinated inorganic ring systems with the help of the Multiwfn program.[47] We have assigned bond critical points, as defined in atoms in molecules theory (AIM),[48] and determined the aromaticity as Shannon's entropy index as[49]

$$SA = \ln(N) - \sum_{i}^{N} (-p_i \ln p_i) \quad (1)$$

$$p_i = \frac{\rho(r_{BCPi})}{\sum_i^N \rho(r_{BCPi})} \quad (2)$$

where N is the number of bond critical points in the ring, r_{BCP} is the location of the bond critical point, and ρ is the electron density at this point. The smaller this index is, the more aromatic the system is, and it holds that SA equals 0.003−0.005 to constitute the borderline between the aromaticity and the antiaromaticity.[49] The calculated extremely low values of the Shannon aromaticity index listed in Table S2 suggest the presence of the aromaticity in all studied compounds.

Electronic Structures of Dysprosocenium-like Complexes. First, the ORCA 4.1 computational package was used to perform post-Hartree−Fock method calculations based on state-average complete active space self-consistent field (SA-CASSCF) approach to cope with the multiconfigurational character of Dy-based complexes under study. The active space was defined by 9 electrons in 7 f-orbitals, and the dynamic electronic correlation was treated with second-order dynamic correlation dressed CAS (DCD-CAS(2)). The ab initio ligand field theory (AILFT)[50] was employed in the analysis of CASSCF/DCD-CAS(2) calculations, and as a result, the energies of the f-orbitals are depicted in Figure 2 and listed in Table S3 (Supporting Information). All studied compounds have two almost degenerate low-lying f-orbitals, while the rest of f-orbitals are higher in energy by at least 600−800 K. In general, the lowest splitting of f-orbitals has been calculated for complexes with borazine derivates, especially $[Dy(B_3P_3H_6)_2]^{3+}$ and $[Dy(B_3S_3H_3)_2]^{3+}$, with the highest energy level at about 1200 K, while complex with borazine has its highest f-orbital energy level close to 1600 K. Both pentagonal ring ligands led to higher f-orbitals splitting with $[Dy(N_5)_2]^+$, showing splitting up to 2100 K. This trend can be associated with increasing electronegativity of donor atoms.

The ground state $^6H_{15/2}$ is split into eight Kramers doublets, and the lowest splitting was observed for complexes $[Dy(B_3P_3H_6)_2]^{3+}$ and $[Dy(B_3S_3H_3)_2]^{3+}$; both of these complexes have almost identical energy levels with the highest level approximately at 1000 K (Figure 2). A slightly higher expected energy barrier is observed for $[Dy(B_3N_3H_6)_2]^{3+}$ and $[Dy(P_5)_2]^+$, which both have the highest level at about 1500 K. Of all studied complexes, the largest splitting was observed for $[Dy(N_5)_2]^+$, which is, with the highest state slightly below 2000 K, comparable to previously published $[Dy(Cp^{ttt})_2]^+$. All Kramers doublets energies are listed in Table S4.

Furthermore, the contemporary multireference approaches were tested to estimate the possible variation of the energy splitting, because it is the decisive factor for the U_{eff} estimation of $[Dy^{III}L_2]^{+/3+}$ complexes. Therefore, the well-established dynamic electronic correlation method NEVPT2 (N-electron valence second-order perturbation theory) was also applied, and the energy comparison is depicted in Figure 3. It is evident that both methods, DCD-CAS(2) and NEVPT2, provided very similar energy splitting diagrams, but utilization of NEVPT2 resulted in a slightly lower energy splitting. Next, we compared also the standalone calculations based on CASSCF without any dynamic correlation included. Results are displayed for the calculation done in ORCA with ZORA and the respective relativistic version of Ahlrichs basis set (ZORA-def2-TZVP) and the segmented all-electron relativistically contracted basis set for Dy and for the calculation done in MOLCAS with DKH and the respective ANO-RCC basis set based on atomic natural orbitals (ANO), see Figure 3. Both calculations based only on the static electronic correlation resulted in lower energy splitting of $^6H_{15/2}$ providing analogous results, see Figure 3. To summarize, all four tested methods resulted in similar energy schemes, but variation of the overall energy splitting between CASSCF/DKH method done in MOLCAS and the CASSCF/DCD-CAS(2)/ZORA method done in

DOI: 10.1021/acs.inorgchem.9b02039
Inorg. Chem. 2019, 58, 14046−14057

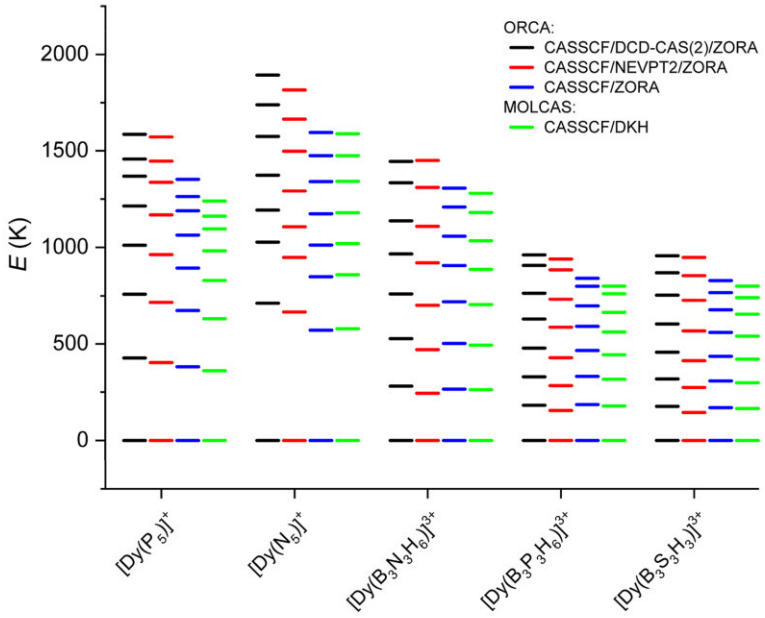

Figure 3. Comparison of Kramers doublets energy levels resulting from the zero-field splitting of $^6H_{15/2}$ of $[Dy^{III}L_2]^{+/3+}$ complexes calculated by CASSCF in ORCA with ZORA and SARC2/def2 basis sets complemented by DCD-CAS(2) or NEVPT2 and by CASSCF in MOLCAS with DKH and ANO-RCC basis sets.

Table 2. CASSCF/DKH/ANO-RCC Energy Levels and the Transition Magnetic Dipole Moments (k_{QT}) of KDs Calculated with MOLCAS and SINGLE_ANISO Module along with the Evaluated Effective Energetic Barriers U_{eff}

	$[Dy(P_5)_2]^+$		$[Dy(N_5)_2]^+$		$[Dy(B_3N_3H_6)_2]^{3+}$		$[Dy(B_3P_3H_6)_2]^{3+}$		$[Dy(B_3S_3H_3)_2]^{3+}$	
	E (K)	k_{QT}	E (K)	k_{QT}	E (K)	k_{QT}	E (K)	k_{QT}	E (K)	k_{QT}
KD1	0	0.000	0	0.000	0	0.000	0	0.000	0	0.000
KD2	361	0.000	579	0.000	263	0.001	178	0.000	165	0.002
KD3	630	0.002	859	0.000	493	0.013	317	0.002	298	0.008
KD4	829	0.007	1020	0.003	703	0.061	443	0.020	421	0.135
KD5	982	0.291	1179	0.031	887	0.285	562	0.098	540	0.717
KD6	1096	0.292	1343	0.193	1035	1.896	664	2.171	654	2.046
KD7	1162	2.919	1475	2.227	1181	0.613	761	1.960	741	1.222
KD8	1240	0.224	1590	0.845	1281	0.335	800	3.546	801	1.081
U_{eff} (K)	1127		1475		1009		734		650	

ORCA was up to ca. 20%, which is important information regarding our further evaluation of the U_{eff} value.

The Effective Energy Barrier, U_{eff}. For the more detailed prediction of SMMs properties of $[Dy^{III}L_2]^{+/3+}$ complexes, the overall splitting of $^6H_{15/2}$ multiplet is not sufficient information, because very often the magnetic anisotropy of the respective Kramers doublets (KD) induces quantum tunneling of the magnetization either in the ground state or through excited KDs, and the observed effective energy barrier are less than the maximal splitting of eight KDs ($U_{eff} \ll U_{max}$). Therefore, it is inevitable that the properties of each individual KD need to be inspected and that the magnetic dipole transition moments between various states that allow us to assess various relaxation mechanisms (quantum tunneling, thermal relaxation, thermally assisted tunneling) need to be assessed. Such analysis is implemented in the SINGLE_ANISO module of MOLCAS, and therefore, further investigation of SMMs properties is based on CASSCF/DKH calculations with ANO-RCC basis set. The respective energy levels and calculated transition probabilities are listed in Table 2, and the g-tensor values quantifying the magnetic anisotropy of these KDs for all compounds are listed in Table S5 with the respective Cartesian coordinates in Table S6.

Qualitative analysis of these results is done through respective diagrams showing the magnetic moment reversal energy barriers, which are depicted in Figure 4 for $[Dy(N_5)_2]^+$ and $[Dy(P_5)_2]^+$ complexes, whereas Figures S2−S4 show the situation for $[Dy(B_3N_3H_6)_2]^{3+}$, $[Dy(B_3P_3H_6)_2]^{3+}$, and $[Dy(B_3S_3H_3)_2]^{3+}$ complexes. The values displayed on each arrow are the mean absolute values for the corresponding matrix elements of the transition magnetic moment between selected KD states, and for values larger than 0.1, an efficient relaxation mechanism is expected.[51]

According to Figure 4 and Table 2, the complex $[Dy(N_5)_2]^+$ looks like the most promising candidate for high U_{eff} SMM due to the largest splitting of $^6H_{15/2}$ manifold and also due to the fact that the transition magnetic dipole moment related to the quantum tunneling is minute for the lowest Kramers doublets. These transition magnetic dipole moments are negligible up to sixth KD, and even there, the preferred pathway should be kept

DOI: 10.1021/acs.inorgchem.9b02039
Inorg. Chem. 2019, 58, 14046−14057

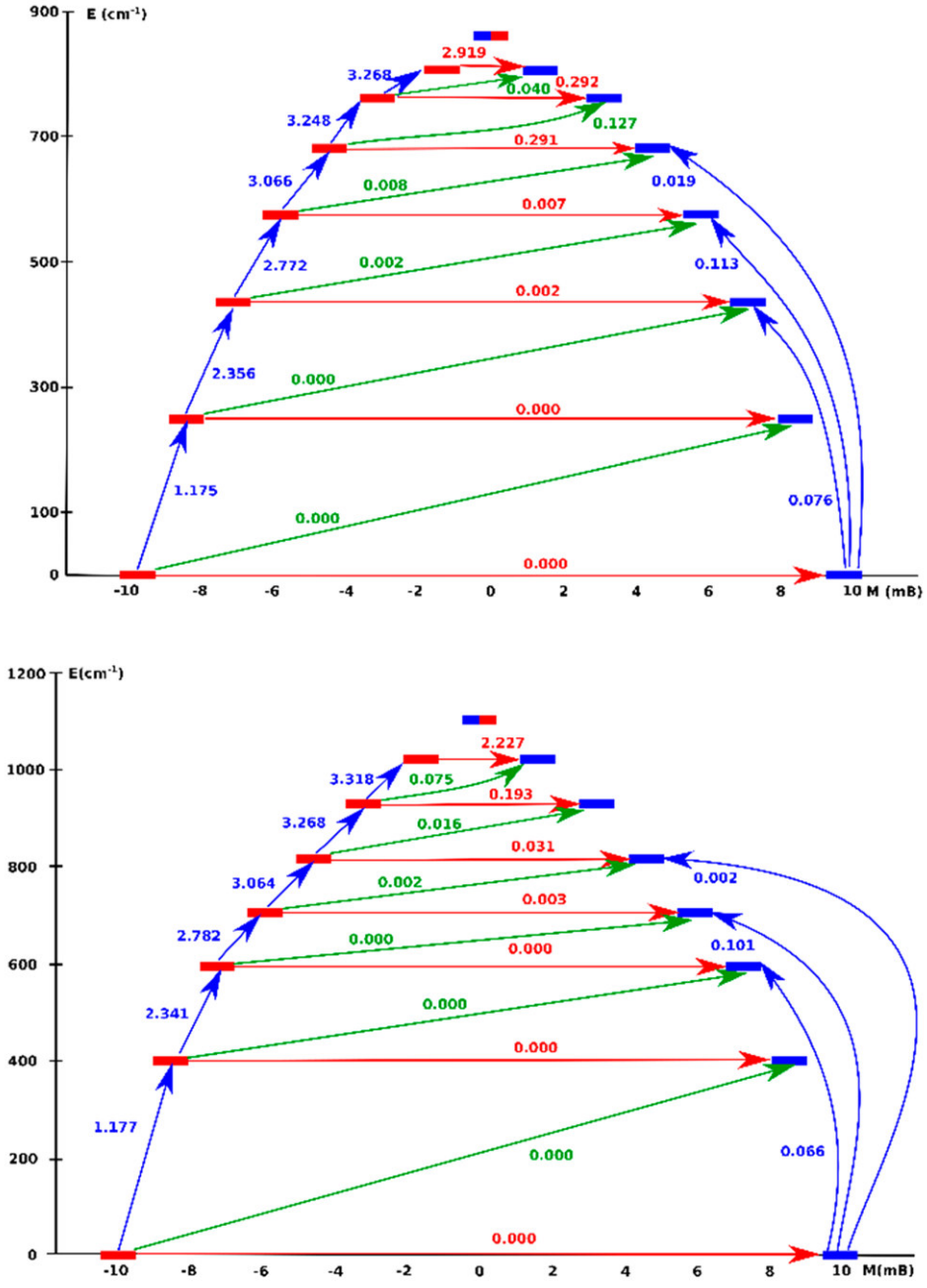

Figure 4. Kramers doublets energies and transition moments for studied compounds $[Dy(P_5)_2]^+$ (top) and $[Dy(N_5)_2]^+$ (bottom). Arrows depict direct relaxation (blue), QTM (red), and thermally assisted QTM (green) relaxation processes.

without flipping the magnetization direction even to the seventh doublet, making this complex possible of reaching an energy barrier of ca. 1000 cm^{-1} (1439 K). The complex $[Dy(P_5)_2]^+$ has its Kramers doublets structure similar to the previous complex, but its energy gaps between KDs are smaller and the transition magnetic dipole moment related to quantum tunneling grows significantly already for the fifth and sixth doublet, thus weakening the energy barrier. In case of borazine derivates (Figures S2−S4), the analogous computations show that the highest splitting between Kramers doublets occurs in $[Dy(B_3N_3H_6)_2]^{3+}$ in the comparison to complexes $[Dy(B_3P_3H_6)_2]^{3+}$ and $[Dy(B_3S_3H_3)_2]^{3+}$. However, the relaxation path prediction suggests that in $[Dy(B_3S_3H_3)_2]^{3+}$ the magnetization moment flips into the opposite direction during the transition from the ground state into the second KD; therefore, its reversal anisotropy energy barrier should not overcome this energy separation. On the contrary, both relaxation paths for $[Dy(B_3N_3H_6)_2]^{3+}$ and $[Dy(B_3P_3H_6)_2]^{3+}$ are more similar, having very low the transition magnetic dipole moments up to the fourth KD which makes temperature-assisted quantum

DOI: 10.1021/acs.inorgchem.9b02039
Inorg. Chem. 2019, 58, 14046−14057

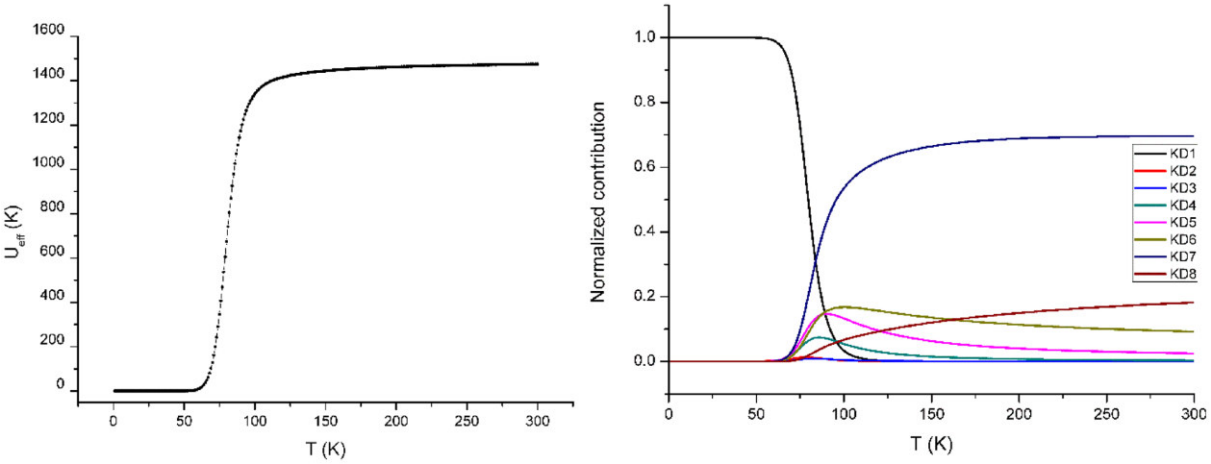

Figure 5. Dependence of effective energy barrier of Orbach mechanism on temperature (left) and temperature-dependent relative contribution of each Kramers doublets to the relaxation calculated as $k_i(T)/N_k$ (right) for $[Dy(N_5)_2]^+$ based on eqs 3 and 4.

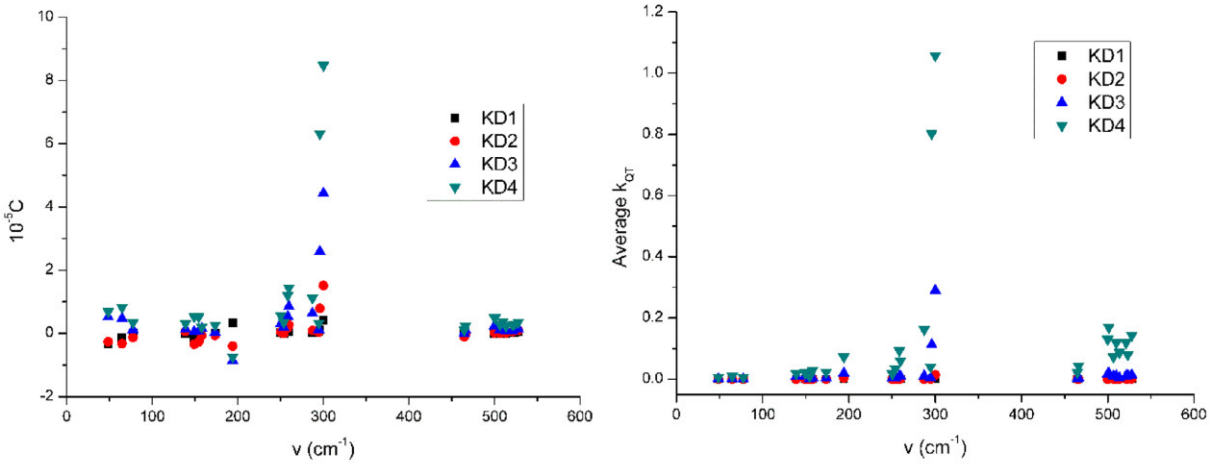

Figure 6. Spin-vibrational coupling coefficient C (left) and average transition magnetic dipole moments k_{QT} (right) for vibrational modes of $[Dy(P_5)_2]^+$.

tunneling probable in the fifth KD. Due to the change of the orientation of the magnetic moment for the sixth Kramers doublets for both complexes $[Dy(B_3N_3H_6)_2]^{3+}$ and $[Dy(B_3P_3H_6)_2]^{3+}$, the effective barrier should not exceed these energies.

Next, the effective energy demagnetization barriers U_{eff} for Orbach relaxation mechanism were computed by a previously published method[52] utilizing energies of Kramers doublets and the transition magnetic dipole moment related to the quantum tunneling between them resulting from CASSCF calculations:

$$U_{eff}(T) = \sum_{i=1}^{M} \frac{k_i(T)}{N_k} E_i \tag{3}$$

where M is the number of KDs, k_i values are the demagnetization rates for the respective doublets with E_i energies, and N_k is the normalization factor for k_i ($N_k = \Sigma k_i(T)$). The demagnetization rate k_i is defined as

$$k_i(T) = \frac{\exp\left(-\frac{E_i}{k_B T}\right)}{Z} k_{QT,i} \tag{4}$$

where k_B is the Boltzmann constant, T is the temperature, Z is the partition function, and $k_{QT,i}$ values are the transition magnetic dipole moment related to the quantum tunneling for KDs, calculated from CASSCF, along with energy levels E_i, see Table 2. These calculations provided the estimation of U_{eff} in the range from 650 to 1475 K for $[Dy^{III}L_2]^{+/3+}$ complexes, see Figure 5 and Figures S5−S8.

It is obvious from results in Table 2 that $[Dy(N_5)_2]^+$ seems to be the most promising candidate among studied complexes. Its predicted barrier (Figure 5) reaches the seventh Kramers doublet up to 1475 K, which is a value comparable with the best currently known single-molecule magnets. Other complexes surpassing the 1000 K border are $[Dy(P_5)_2]^+$ with 1127 K and $[Dy(B_3N_3H_6)_2]^{3+}$ with 1009 K; in both cases, those values are close to the sixth Kramers doublet, and slight differences are the result of contributions from relaxation through upper or lower KDs. The barrier for $[Dy(B_3P_3H_6)_2]^{3+}$

DOI: 10.1021/acs.inorgchem.9b02039
Inorg. Chem. 2019, 58, 14046−14057

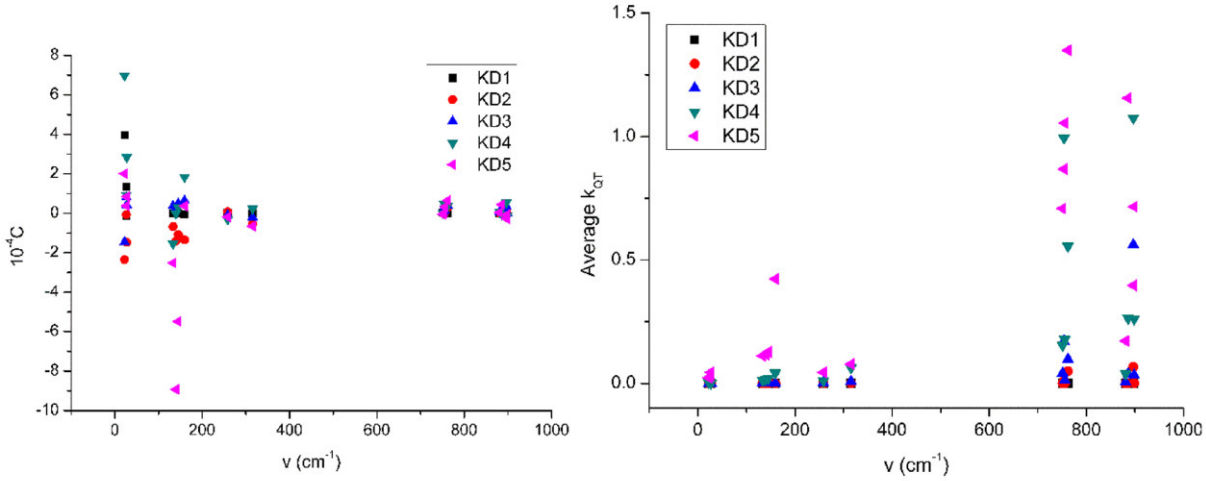

Figure 7. Spin-vibrational coupling coefficient C (left) and average transition magnetic dipole moments k_{QT} (right) for vibrational modes of $[Dy(N_5)_2]^+$.

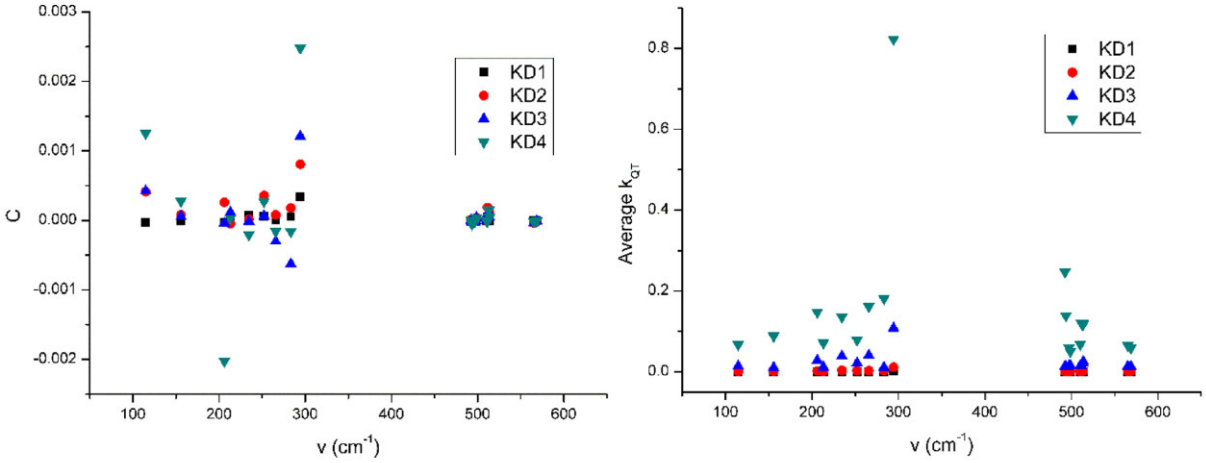

Figure 8. Spin-vibrational coupling coefficient C (left) and average transition magnetic dipole moments k_{QT} (right) for vibrational modes of $[Dy(B_3N_3H_6)_2]^{3+}$.

was predicted as 734 K, which is surprisingly slightly above the sixth doublet with high transition magnetic dipole moment, which can be explained by the contribution from relaxation through seventh doublet. Similarly, $[Dy(B_3S_3H_3)_2]^{3+}$ has a barrier of 650 K, reaching slightly below the sixth doublet because of increased transition magnetic dipole moment in the fifth doublet.

Spin-Vibration Coupling Analysis. The performance of high-temperature SMMs is also affected by the phonons, hence the lattice vibrations in the solid state, and therefore, it is also important to assess the impact of the vibrations on the SMMs properties.[13] In some cases, the spin dynamics of SMMs were explored by the theoretical approach in which the phonons can be reduced only to molecular vibrations. Such an approach was used in a case of $[Dy(Cp^{ttt})_2]^+$,[5] where authors have proven this presumption by measuring relaxation dynamics in crystals and amorphous frozen solution with the same results. Although we do not have opportunity to do this for the herein studied $[Dy^{III}L_2]^{+/3+}$ complexes, we assume that this tactic can also be used under the condition that suitable counterions would be incorporated into the final compounds for minimizing noncovalent contacts in solid state. Therefore, we have used an already published method with intentions to make a complementary analysis, which can point out how structure changes caused by molecular vibration affects g-factors and the transition magnetic dipole moments related to the quantum tunneling of Kramers doublets as this can lead to reducing the U_{eff}. This method is able to show where those systems' "weak spots" are, thus making us able to predict which parts of the molecule are affected by the vibrational modes that cause major changes in the g-factor, and this information can be valuable for the future design of better systems.

In this analysis, only vibrational modes with an energy lower than estimated effective energy barrier U_{eff} for a given complex were considered. Within this analysis, it is necessary to perform CASSCF-based calculations for all modified geometries induced by the selected vibrational modes. The input geometries of a given vibrational mode were acquired by the pltvib command in ORCA to generate the *xyz* trajectory file. Two geometries with the largest displacements from reference

DOI: 10.1021/acs.inorgchem.9b02039
Inorg. Chem. 2019, 58, 14046−14057

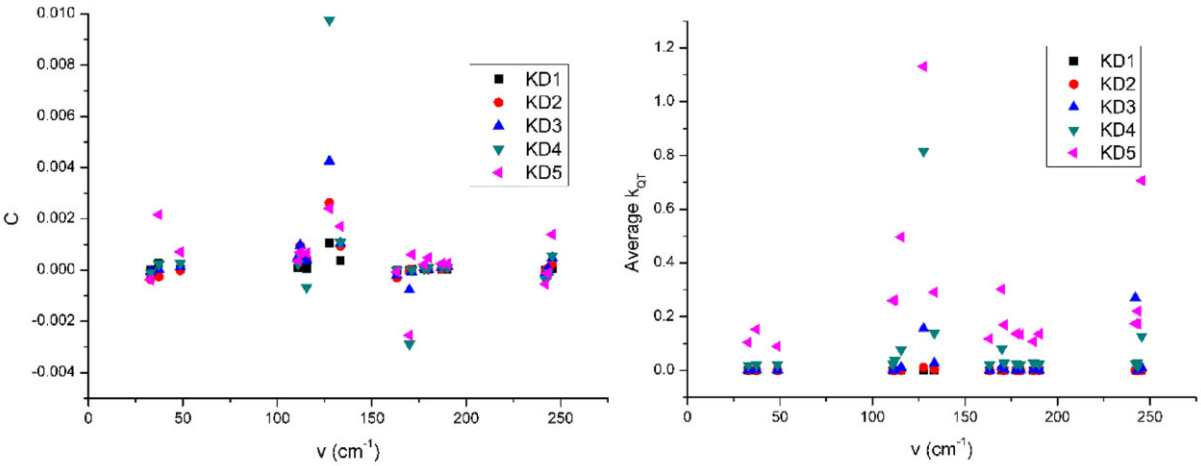

Figure 9. Spin-vibrational coupling coefficient C (left) and average transition magnetic dipole moments k_{QT} (right) for vibrational modes of $[Dy(B_3P_3H_6)_2]^{3+}$.

geometry were then chosen for the spin-vibration coupling analysis. To cope with this task and to be compatible with our estimation of U_{eff} done in the previous section, the subsequent CASSCF calculations were done in MOLCAS with the ANO-RCC basis set and with the help of the SINGLE_ANISO module.

We have used a previously published method of determining the spin-vibration coupling constant C:[14]

$$C = \frac{\hbar}{4\pi}\left(\frac{\partial^2 g_z}{\partial Q_k^2}\right)_e \frac{1}{m_k \nu_k} \tag{5}$$

where g_z is the g-factor for the z-axis, Q_k is the normal vibration coordinate, m_k is the reduced mass, and ν_k is the vibration frequency. To keep the spin-vibration coupling constant dimensionless, we have used those values in SI units.

To gain insight into vibration-induced relaxation, it is assumed that the first vibration with significant g-factor changes would be the most important for the relaxation. In theory, coefficient C should correspond with the transition magnetic dipole moment related to the quantum tunneling. To describe vibrational mode's tunneling, we have made an average of three values of calculated transition magnetic dipole moments from the SINGLE_ANISO module. For that we have used two geometries with maximal displacement, which were used for the spin-vibration coupling analysis described above, with the relaxed reference geometry as the third value. For a list of calculated values corresponding to variations of g_z and the transition magnetic dipole moments, please see Tables S7–S18.

First, the detailed analysis will be discussed for the $[Dy(P_5)_2]^+$ complex. It is obvious that the most important vibrations for magnetic tunneling relaxation are at 296 and 300 cm^{-1} (see SI gif files DyP5_2_296 and DyP5_2_300 for visualization), because they do massive changes to both g-factor and transition magnetic dipole moments (Figure 6). The increase of the tunneling coefficients is significant mainly for third and fourth Kramers doublets with energies of 630 and 829 K, respectively, see Table 2. Although those doublets should not be populated immediately after these vibration states around 300 cm^{-1} become energetically available, we might assume that the relaxation route through those vibrations will lead to the reduction of the estimated U_{eff}.

In the case of $[Dy(N_5)_2]^+$, we can observe relatively strong anisotropy even in the fifth Kramers doublet (Table 2), but higher states are more susceptible to large g-factor and transition magnetic dipole moment changes due to structural changes induced by vibrations (Figure 7). However, in the case of this complex, we can see a relatively larger change of g-factor represented by the coupling factor C than for the $[Dy(P_5)_2]^+$ complex, although those large changes do not correlate with a transition magnetic dipole moments increase in many cases. For the fifth doublet, there is vibration with significantly increased tunneling at 160 cm^{-1} (SI gif file DyN5_2–160). Next, vibrations with increased tunneling are a series above 750 cm^{-1}, which are also affecting the fourth doublet, and then above 880 cm^{-1}, affecting transition magnetic dipole moments even in third doublets. However, those vibrations are energetically quite high and therefore might not affect the relaxation pathway significantly.

For $[Dy(B_3N_3H_6)_2]^{3+}$ (Figure 8), not many vibrations have significantly increased tunneling; we can, however, clearly see one at 294 cm^{-1} (SI gif file DyB3N3H6_2-294) that has both large spin-vibrational coupling and allowed tunneling in the fourth Kramers doublet, therefore allowing relaxation through alternative pathway, when fourth doublet gets populated. This vibration represents Dy–N bond stretching.

For the $[Dy(B_3P_3H_6)_2]^{3+}$ complex (Figure 9), we can see very strong tunneling of magnetization enhanced by the vibration at 128 cm^{-1} (SI gif file DyB3P3H6_2-128), which is also very strongly coupled with g-factor change, surprisingly mainly for the fourth and third doublet, while the fifth doublet is not changed as much. We can assume that this vibration would create one of the main paths for magnetization relaxation.

For $[Dy(B_3S_3H_3)_2]^{3+}$, we have not done this analysis, mainly because of its change of direction of z-axis in the first excited KD, which makes assumptions about its anisotropy in higher KDs pointless.

To summarize, the spin-vibrational analyses suggest that the molecular vibration will not influence the U_{eff} for $[Dy(N_5)_2]^+$; however, we may expect reduction of U_{eff} in the case of

DOI: 10.1021/acs.inorgchem.9b02039
Inorg. Chem. 2019, 58, 14046–14057

$[Dy(P_5)_2]^+$, $[Dy(B_3N_3H_6)_2]^{3+}$, and $[Dy(B_3P_3H_6)_2]^{3+}$ complexes.

CONCLUSIONS

Geometry optimizations and electronic structure analyses have been performed for five inorganic-based Dy^{III} sandwich complexes with N_5^- and P_5^- cyclopentadienyl analogs and with borazine and its derivates $B_3P_3H_6$ and $B_3S_3H_3$. Our goal was to investigate if those compounds could possess similar magnetic properties as organometallic dysprosium double-deckers with cyclopentadienyl ligands. It is suggested that, in terms of the energy barrier height particularly, dysprosocenium analogues $[Dy(N_5)_2]^+$ and $[Dy(P_5)_2]^+$ might reach comparable values to record-breakers $[Dy(Cp^{ttt})_2]^+$ and $[Dy(Cp^{iprS})(Cp^*)]^+$, and therefore, attempts on the preparation of sandwich complexes with inorganic rings might be an interesting feat not only from a synthesist's viewpoint but also from the view of possessing remarkable magnetic properties.

Furthermore, analyses of affecting relaxation mechanisms by molecular vibrations have been performed by calculation of the spin-vibration coupling constants; the results were then compared with the predicted quantum tunneling of magnetization transition magnetic dipole moments. There is a correlation between the high spin vibration coupling constant, based on *g*-factor change, and high transition magnetic dipole moments, which can be helpful for identifying the vibration that is dominant for spin-phonon transitions for compounds, for finding the preferred relaxation mechanism, and possibly for tuning molecular structure to reach the highest possible energetic barriers and hysteresis temperatures.

For complexes $[Dy(P_5)_2]^+$, $[Dy(B_3N_3H_6)_2]^{3+}$, and $[Dy(B_3P_3H_6)_2]^{3+}$, we have found that a small number of vibrations, usually one or two, cause increased transition magnetic dipole moments related to quantum tunneling of the excited states and therefore offering alternative relaxation paths at lower energies than expected from calculations of U_{eff}. Therefore, a possibility for further improvement would be a structural modification of ligands, which would suppress this vibration, or an increase in its energy to prevent it from being populated on lower temperatures.

To conclude, the purely inorganic dysprosocenium sandwich complexes are an interesting alternative to the organometallic species reported so far and certainly deserve further exploration.

ASSOCIATED CONTENT

Supporting Information

The Supporting Information is available free of charge on the ACS Publications website at DOI: 10.1021/acs.inorgchem.9b02039.

Calculated vibration frequencies, both listed in the table (Table S1) and as predicted spectra (Figure S1); aromaticity indexes (Table S2); energy of f-orbitals from CASSCF/DCD-CAS(2) calculations (Table S3); energy of Kramers doublets from CASSCF/DCD-CAS(2) calculations (Table S4); data from CASSCF/DKH calculations with MOLCAS and SINGLE_ANISO module, i.e., *g*-tensor values and the respective Cartesian coordinates (Tables S5 and S6); the variation of g_z-values, coupling coefficient, and transition magnetic dipole moments used for spin-vibrational analysis (Tables S7−S18); additional reversal energy barrier schemes (Figures S2−S5); calculations of U_{eff} based on Boltzmann populations (Figures S5−S8); and Cartesian coordinates of the optimized molecular geometries (PDF)

Gif animations of important molecular vibrations (ZIP)

AUTHOR INFORMATION

Corresponding Author

*E-mail: radovan.herchel@upol.cz.

ORCID

Radovan Herchel: 0000-0001-8262-4666

Notes

The authors declare no competing financial interest.

ACKNOWLEDGMENTS

The authors acknowledge financial support from the Palacký University Olomouc project IGA_PrF_2019_009.

REFERENCES

(1) Caneschi, A.; Gatteschi, D.; Sessoli, R.; Barra, A. L.; Brunel, L. C.; Guillot, M. Alternating Current Susceptibility, High Field Magnetization, and Millimeter Band EPR Evidence for a Ground S = 10 State in [Mn12O12(CH3COO)16(H2O)-4].2CH3COOH.4H2O. *J. Am. Chem. Soc.* **1991**, *113*, 5873−5874.

(2) Ishikawa, N.; Sugita, M.; Ishikawa, T.; Koshihara, S. Y.; Kaizu, Y. Lanthanide Double-Decker Complexes Functioning as Magnets at the Single-Molecular Level. *J. Am. Chem. Soc.* **2003**, *125* (29), 8694−8695.

(3) Rinehart, J. D.; Fang, M.; Evans, W. J.; Long, J. R. A N23-Radical-Bridged Terbium Complex Exhibiting Magnetic Hysteresis at 14 K. *J. Am. Chem. Soc.* **2011**, *133* (36), 14236−14239.

(4) (a) Ding, Y. S.; Chilton, N. F.; Winpenny, R. E. P.; Zheng, Y. Z. On Approaching the Limit of Molecular Magnetic Anisotropy: A Near-Perfect Pentagonal Bipyramidal Dysprosium(III) Single-Molecule Magnet. *Angew. Chem., Int. Ed.* **2016**, *55* (52), 16071−16074. (b) Liu, J.; Chen, Y.-C.; Liu, J.-L.; Vieru, V.; Ungur, L.; Jia, J.-H.; Chibotaru, L. F.; Lan, Y.; Wernsdorfer, W.; Gao, S.; Chen, X.-M.; Tong, M.-L. A Stable Pentagonal Bipyramidal Dy(III) Single-Ion Magnet with a Record Magnetization Reversal Barrier over 1000 K. *J. Am. Chem. Soc.* **2016**, *138*, 5441−5450. (c) Chen, Y. C.; Liu, J. L.; Ungur, L.; Liu, J.; Li, Q. W.; Wang, L. F.; Ni, Z. P.; Chibotaru, L. F.; Chen, X. M.; Tong, M. L. Symmetry-Supported Magnetic Blocking at 20 K in Pentagonal Bipyramidal Dy(III) Single-Ion Magnets. *J. Am. Chem. Soc.* **2016**, *138* (8), 2829−2837.

(5) Goodwin, C. A. P.; Ortu, F.; Reta, D.; Chilton, N. F.; Mills, D. P. Molecular Magnetic Hysteresis at 60 K in Dysprosocenium. *Nature* **2017**, *548* (7668), 439−442.

(6) Guo, F.; Day, B. M.; Chen, Y.; Tong, M.; Mansikkamäki, A.; Layfield, R. A. Magnetic Hysteresis up to 80 K in a Dysprosium Metallocene Single-Molecule Magnet. *Science* **2018**, *362* (6421), 1400−1403.

(7) Randall McClain, K.; Gould, C. A.; Chakarawet, K.; Teat, S. J.; Groshens, T. J.; Long, J. R.; Harvey, B. G. High-Temperature Magnetic Blocking and Magneto-Structural Correlations in a Series of Dysprosium(Iii) Metallocenium Single-Molecule Magnets. *Chem. Sci.* **2018**, *9* (45), 8492−8503.

(8) Aravena, D.; Ruiz, E. Shedding Light on the Single-Molecule Magnet Behavior of Mononuclear DyIII Complexes. *Inorg. Chem.* **2013**, *52* (23), 13770−13778.

(9) (a) Long, J.; Habib, F.; Lin, P.-H.; Korobkov, I.; Enright, G.; Ungur, L.; Wernsdorfer, W.; Chibotaru, L. F.; Murugesu, M. Single-Molecule Magnet Behavior for an Antiferromagnetically Superexchange-Coupled Dinuclear Dysprosium(III) Complex. *J. Am. Chem. Soc.* **2011**, *133* (14), 5319−5328. (b) Tuna, F.; Smith, C. A.; Bodensteiner, M.; Ungur, L.; Chibotaru, L. F.; McInnes, E. J. L.;

DOI: 10.1021/acs.inorgchem.9b02039
Inorg. Chem. 2019, 58, 14046−14057

Winpenny, R. E. P.; Collison, D.; Layfield, R. A. A High Anisotropy Barrier in a Sulfur-Bridged Organodysprosium Single-Molecule Magnet. *Angew. Chem., Int. Ed.* **2012**, *51* (28), 6976−6980. (c) Ungur, L.; Le Roy, J. J.; Korobkov, I.; Murugesu, M.; Chibotaru, L. F. Fine-Tuning the Local Symmetry to Attain Record Blocking Temperature and Magnetic Remanence in a Single-Ion Magnet. *Angew. Chem., Int. Ed.* **2014**, *53* (17), 4413−4417.

(10) Ungur, L.; Chibotaru, L. F. Strategies toward High-Temperature Lanthanide-Based Single-Molecule Magnets. *Inorg. Chem.* **2016**, *55* (20), 10043−10056.

(11) Zhu, Z.; Guo, M.; Li, X. L.; Tang, J. Molecular Magnetism of Lanthanide: Advances and Perspectives. *Coord. Chem. Rev.* **2019**, *378*, 350−364.

(12) Gatteschi, D.; Sessoli, R. Quantum Tunneling of Magnetization and Related Phenomena in Molecular Materials. *Angew. Chem., Int. Ed.* **2003**, *42* (3), 268−297.

(13) Escalera-Moreno, L.; Baldoví, J. J.; Gaita-Ariño, A.; Coronado, E. Spin States, Vibrations and Spin Relaxation in Molecular Nanomagnets and Spin Qubits: A Critical Perspective. *Chem. Sci.* **2018**, *9* (13), 3265−3275.

(14) Escalera-Moreno, L.; Suaud, N.; Gaita-Ariño, A.; Coronado, E. Determining Key Local Vibrations in the Relaxation of Molecular Spin Qubits and Single-Molecule Magnets. *J. Phys. Chem. Lett.* **2017**, *8* (7), 1695−1700.

(15) (a) Nizovtsev, A. S. Search for Aromatic Anions in the P 2 E 3 - (E = N, P, As, Sb, Bi) Series. *Phys. Chem. Chem. Phys.* **2016**, *18* (24), 16084−16087. (b) Gimarc, B. M.; Trinajstic, N. Aromatic Inorganic Rings. *Pure Appl. Chem.* **1980**, *52* (6), 1443−1458. (c) Steudel, R. *The Chemistry of Inorganic Ring Systems*; Elsevier: 1992.

(16) Urnežius, E.; Brennessel, W. W.; Cramer, C. J.; Ellis, J. E.; Schleyer, P.; von, R. A Carbon-Free Sandwich Complex [(P5)2Ti]2-. *Science* **2002**, *295* (5556), 832−834.

(17) (a) Scherer, O. J.; Bruck, T.; Wolmershauser, G. Pentaphosphametallocene. *Chem. Ber.* **1988**, *121* (5), 935−938. (b(1)) Heinl, S.; Balázs, G.; Scheer, M. The Superbulky Pn Ligand Complexes [CpBIGFe(*η*5 -P5)] and [(CpBIGFe)2(*μη* 4:4P4)]—Synthesis and Characterization. *Phosphorus, Sulfur Silicon Relat. Elem.* **2014**, *189* (7−8), 924−932.

(18) Sekar, P.; Umbarkar, S.; Scheer, M.; Voigt, A.; Kirmse, R. Synthesis and Properties of Novel Metal-Linked Pn Ligand Complexes. *Eur. J. Inorg. Chem.* **2000**, *2000* (12), 2585−2589.

(19) Kudinov, A. R.; Loginov, D. A.; Starikova, Z. A.; Petrovskii, P. V.; Corsini, M.; Zanello, P. Iron- and Ruthenium-Containing Triple-Decker Complexes with a Central Pentaphospholyl Ligand - X-Ray Structures of [(*η*-C5H5)Fe(*μ*-*η*:*η*-P5)Ru(*η*-C5Me5)]PF6 and [(*η*-C5Me5)Ru(*μ*-*η*:*η*-P5)Ru(*η*-C5Me5)]PF6. *Eur. J. Inorg. Chem.* **2002**, *2002* (11), 3018−3027.

(20) Gardner, B. M.; Tuna, F.; McInnes, E. J. L.; McMaster, J.; Lewis, W.; Blake, A. J.; Liddle, S. T. An Inverted-Sandwich Diuranium *μ*-H5:H5-Cyclo-P5 Complex Supported by U-P5 *δ*-Bonding. *Angew. Chem., Int. Ed.* **2015**, *54* (24), 7068−7072.

(21) Zhang, C.; Sun, C.; Hu, B.; Yu, C.; Lu, M. Synthesis and Characterization of the Pentazolate Anion Cyclo-N_5^- in $(N_5)_6(H_3O)_3(NH_4)_4Cl$. *Science* **2017**, *355* (6323), 374−376.

(22) (a) Xu, Y.; Wang, Q.; Shen, C.; Lin, Q.; Wang, P.; Lu, M. A Series of Energetic Metal Pentazolate Hydrates. *Nature* **2017**, *549* (7670), 78−81. (b) Xu, Y.; Wang, P.; Lin, Q.; Lu, M. A Carbon-Free Inorganic-Metal Complex Consisting of an All-Nitrogen Pentazole Anion, a Zn(II) Cation and H2O. *Dalt. Trans.* **2017**, *46* (41), 14088−14093. (c) Xu, Y.; Lin, Q.; Wang, P.; Lu, M. Syntheses, Crystal Structures and Properties of a Series of 3D Metal-Inorganic Frameworks Containing Pentazolate Anion. *Chem. - Asian J.* **2018**, *13* (13), 1669−1673.

(23) Tsipis, A. C.; Chaviara, A. T. Structure, Energetics, and Bonding of First Row Transition Metal Pentazolato Complexes: A DFT Study. *Inorg. Chem.* **2004**, *43* (4), 1273−1286.

(24) (a) Carter, T. J.; Wang, J. Y.; Szymczak, N. K. Manganese-Mediated Hydride Delivery to a Borazine by Stepwise Reduction and Protonation. *Organometallics* **2014**, *33* (7), 1540−1543. (b) Huttner, G.; Krieg, B. Übergangsmetallkomplexe Cyclischer *π*-Liganden, VI. Kristall- Und Molekülstruktur von Tricarbonyl(Hexaäthylborazin)-Chrom(0). *Chem. Ber.* **1972**, *105* (10), 3437−3444. (c) Carter, T. J.; Kampf, J. W.; Szymczak, N. K. Reduction of Borazines Mediated by Low-Valent Chromium Species. *Angew. Chem., Int. Ed.* **2012**, *51* (52), 13168−13172.

(25) Braunschweig, H.; Kollann, C.; Müller, M. Synthesis and Structure of the First H1-Borazine Complexes. *Eur. J. Inorg. Chem.* **1998**, *1998* (2), 291−293.

(26) Kaufmann, B.; Metzler, N.; Nöth, H.; Paine, R. T. 1,3,5-Triphenyl-2,4,6-Trimesityl-1,3,5,2,4,6-Triphosphatriborinane: A 6*π*-Electron Heteroaromatic Ligand. *Chem. Ber.* **1994**, *127* (5), 825−827.

(27) (a) Neese, F. The ORCA Program System. *Wiley Interdiscip. Rev. Comput. Mol. Sci.* **2012**, *2* (1), 73−78. (b) Neese, F. Software update: the ORCA program system, version 4.0. *Wiley Interdiscip. Rev. Comput. Mol. Sci.* **2018**, *8* (1), No. e1327.

(28) Tao, J.; Perdew, J. P.; Staroverov, V. N.; Scuseria, G. E. Climbing the Density Functional Ladder: Nonempirical Meta-generalized Gradient Approximation Designed for Molecules and Solids. *Phys. Rev. Lett.* **2003**, *91* (14), 146401.

(29) van Lenthe, E.; Baerends, E. J.; Snijders, J. G. Relativistic Total Energy Using Regular Approximations. *J. Chem. Phys.* **1994**, *101* (11), 9783−9792.

(30) Aravena, D.; Neese, F.; Pantazis, D. A. Improved Segmented All-Electron Relativistically Contracted Basis Sets for the Lanthanides. *J. Chem. Theory Comput.* **2016**, *12* (3), 1148−1156.

(31) Weigend, F.; Ahlrichs, R. Balanced Basis Sets of Split Valence, Triple Zeta Valence and Quadruple Zeta Valence Quality for H to Rn: Design and Assessment of Accuracy. *Phys. Chem. Chem. Phys.* **2005**, *7* (18), 3297−3305.

(32) (a) Neese, F.; Wennmohs, F.; Hansen, A.; Becker, U. Efficient, Approximate and Parallel Hartree-Fock and Hybrid DFT Calculations. A 'Chain-of-Spheres' Algorithm for the Hartree-Fock Exchange. *Chem. Phys.* **2009**, *356* (1−3), 98−109. (b) Izsák, R.; Neese, F. An Overlap Fitted Chain of Spheres Exchange Method. *J. Chem. Phys.* **2011**, *135* (14), 144105.

(33) Weigend, F. A Fully Direct RI-HF Algorithm: Implementation, Optimised Auxiliary Basis Sets, Demonstration of Accuracy and Efficiency. *Phys. Chem. Chem. Phys.* **2002**, *4* (18), 4285−4291.

(34) Roos, B. O. The Complete Active Space Self-Consistent Field Method and its Applications in Electronic Structure Calculations. *Adv. Chem. Phys.* **2007**, *69*, 399−445.

(35) (a) Pathak, S.; Lang, L.; Neese, F. A Dynamic Correlation Dressed Complete Active Space Method: Theory, Implementation, and Preliminary Applications. *J. Chem. Phys.* **2017**, *147* (23), 234109. (b) Lang, L.; Neese, F. Spin-Dependent Properties in the Framework of the Dynamic Correlation Dressed Complete Active Space Method. *J. Chem. Phys.* **2019**, *150* (10), 104104.

(36) (a) Angeli, C.; Cimiraglia, R.; Evangelisti, S.; Leininger, T.; Malrieu, J.-P. Introduction of n-Electron Valence States for Multireference Perturbation Theory. *J. Chem. Phys.* **2001**, *114* (23), 10252−10264. (b) Angeli, C.; Cimiraglia, R.; Malrieu, J.-P. N-Electron Valence State Perturbation Theory: A Fast Implementation of the Strongly Contracted Variant. *Chem. Phys. Lett.* **2001**, *350* (3−4), 297−305.

(37) Neese, F. *J. Chem. Phys.* **2005**, *122*, 034107.

(38) Stoychev, G. L.; Auer, A. A.; Neese, F. Automatic Generation of Auxiliary Basis Sets. *J. Chem. Theory Comput.* **2017**, *13* (2), 554−562.

(39) (a) Aquilante, F.; De Vico, L.; Ferre, N.; Ghigo, G.; Malmqvist, P.-Å.; Neogrady, P.; Pedersen, T. B.; Pitonak, M.; Reiher, M.; Roos, B. O.; et al. MOLCAS 7: The Next Generation. *J. Comput. Chem.* **2010**, *31* (1), 224−247. (b) Duncan, J. A. MOLCAS 7. *J. Am. Chem. Soc.* **2009**, *131* (6), 2416−2416. (c) Karlström, G.; Lindh, R.; Malmqvist, P.-Å.; Roos, B. O.; Ryde, U.; Veryazov, V.; Widmark, P.-O.; Cossi, M.; Schimmelpfennig, B.; Neogrady, P.; et al. MOLCAS: A Program Package for Computational Chemistry. *Comput. Mater. Sci.* **2003**, *28* (2), 222−239. (d) Veryazov, V.; Widmark, P.-O.; Serrano-Andrés, L.; Lindh, R.; Roos, B. O. 2MOLCAS as a Development Platform for Quantum Chemistry Software. *Int. J. Quantum Chem.* **2004**, *100* (4),

DOI: 10.1021/acs.inorgchem.9b02039
Inorg. Chem. 2019, 58, 14046−14057

626−635. (e) Aquilante, F.; Autschbach, J.; Carlson, R. K.; Chibotaru, L. F.; Delcey, M. G.; De Vico, L.; Fdez. Galván, I.; Ferré, N.; Frutos, L. M.; Gagliardi, L.; et al. Molcas 8: New Capabilities for Multiconfigurational Quantum Chemical Calculations across the Periodic Table. *J. Comput. Chem.* **2016**, *37* (5), 506−541.

(40) (a) Heß, B. A.; Marian, C. M.; Wahlgren, U.; Gropen, O. A Mean-Field Spin-Orbit Method Applicable to Correlated Wavefunctions. *Chem. Phys. Lett.* **1996**, *251*, 365. (b) Schimmelpfennig, B. *AMFI, an atomic mean-field spin-orbit integral program*; Stockholm University: 1996.

(41) (a) Douglas, M.; Kroll, N. M. Quantum Electrodynamical Corrections to the Fine Structure of Helium. *Ann. Phys. (Amsterdam, Neth.)* **1974**, *82* (1), 89−155. (b) Hess, B. A. Relativistic Electronic-Structure Calculations Employing a Two-Component No-Pair Formalism with External-Field Projection Operators. *Phys. Rev. A: At., Mol., Opt. Phys.* **1986**, *33* (6), 3742−3748.

(42) (a) Roos, B. O.; Lindh, R.; Malmqvist, P.-Å.; Veryazov, V.; Widmark, P.-O.; Borin, A. C. New Relativistic Atomic Natural Orbital Basis Sets for Lanthanide Atoms with Applications to the Ce Diatom and LuF 3. *J. Phys. Chem. A* **2008**, *112* (45), 11431−11435. (b) Roos, B. O.; Lindh, R.; Malmqvist, P.-Å.; Veryazov, V.; Widmark, P.-O. New Relativistic ANO Basis Sets for Actinide Atoms. *Chem. Phys. Lett.* **2005**, *409* (4−6), 295−299.

(43) (a) Chibotaru, L. F.; Ungur, L.; Soncini, A. The Origin of Nonmagnetic Kramers Doublets in the Ground State of Dysprosium Triangles: Evidence for a Toroidal Magnetic Moment. *Angew. Chem., Int. Ed.* **2008**, *47* (22), 4126−4129. (b) Chibotaru, L. F.; Ungur, L.; Soncini, A. The Origin of Nonmagnetic Kramers Doublets in the Ground State of Dysprosium Triangles: Evidence for a Toroidal Magnetic Moment. *Angew. Chem., Int. Ed.* **2008**, *47* (22), 4126−4129. (c) Chibotaru, L. F.; Ungur, L. Ab Initio Calculation of Anisotropic Magnetic Properties of Complexes. I. Unique Definition of Pseudospin Hamiltonians and Their Derivation. *J. Chem. Phys.* **2012**, *137* (6), 064112. (d) Ungur, L.; Thewissen, M.; Costes, J.-P.; Wernsdorfer, W.; Chibotaru, L. F. Interplay of Strongly Anisotropic Metal Ions in Magnetic Blocking of Complexes. *Inorg. Chem.* **2013**, *52* (11), 6328−6337.

(44) (a) Malar, E. J. P. Study of Aromaticity in Phosphorus Analogues of the Cyclopentadienyl Anion. *J. Org. Chem.* **1992**, *57* (13), 3694−3698. (b) Cui, Y.-H.; Feng, J.-K.; Li, W.-Q.; Sun, C.-C.; Liu, Z.-Z.; Tian, W. Q.; Zhang, G. A Theoretical Study on Structures, Bonding Energies and Aromaticity of Two New Series of Dinuclear Phosphametallocenes: (H5-P5)MM′(H5-P5) and (H5-C5H5)-MM′(H5-P5) (M, M′ = Zn, Cd). *Eur. J. Inorg. Chem.* **2006**, *2006* (14), 2808−2818. (c) Santos, J. C.; Tiznado, W.; Contreras, R.; Fuentealba, P. Sigma-pi Separation of the Electron Localization Function and Aromaticity. *J. Chem. Phys.* **2004**, *120* (4), 1670−1673.

(45) (a) Jemmis, E. D.; Kiran, B. Aromaticity in X3Y3H6(X = B, Al, Ga; Y = N, P, As), X3Z3H3(Z = O, S, Se), and Phosphazenes. Theoretical Study of the Structures, Energetics, and Magnetic Properties. *Inorg. Chem.* **1998**, *37* (9), 2110−2116. (b) Phukan, A. K.; Guha, A. K.; Silvi, B. Is Delocalization a Prerequisite for Stability of Ring Systems? A Case Study of Some Inorganic Rings. *Dalt. Trans.* **2010**, *39* (17), 4126−4137. (c) Ghiasi, R.; Monajjemi, M. Theoretical Study of Borthiin and Its Derivatives: Structure and Aromaticity. *J. Sulfur Chem.* **2007**, *28* (5), 505−511.

(46) Chilton, N. F.; Goodwin, C. A. P.; Mills, D. P.; Winpenny, R. E. P. The First Near-Linear Bis(Amide) f-Block Complex: A Blueprint for a High Temperature Single Molecule Magnet. *Chem. Commun.* **2015**, *51* (1), 101−103.

(47) Lu, T.; Chen, F. Multiwfn: A Multifunctional Wavefunction Analyzer. *J. Comput. Chem.* **2012**, *33* (5), 580−592.

(48) Bader, R. F. *Atoms in molecules: A quantum theory*; Oxford University Press: Oxford, 2003.

(49) Noorizadeh, S.; Shakerzadeh, E. Shannon Entropy as a New Measure of Aromaticity, Shannon Aromaticity. *Phys. Chem. Chem. Phys.* **2010**, *12* (18), 4742−4749.

(50) (a) Atanasov, M.; Ganyushin, D.; Sivalingam, K.; Neese, F. In *Molecular Electronic Structures of Transition Metal Complexes II*; Mingos, D. M. P., Day, P., Dahl, J. P., Eds.; Springer Berlin Heidelberg: Berlin, Heidelberg, 2012; pp 149−220. (b) Singh, S. K.; Eng, J.; Atanasov, M.; Neese, F. Covalency and Chemical Bonding in Transition Metal Complexes: An Ab Initio Based Ligand Field Perspective. *Coord. Chem. Rev.* **2017**, *344*, 2−25.

(51) Gómez-Coca, S.; Aravena, D.; Morales, R.; Ruiz, E. Large Magnetic Anisotropy in Mononuclear Metal Complexes. *Coord. Chem. Rev.* **2015**, *289*−*290*, 379−392.

(52) Aravena, D. Ab Initio Prediction of Tunneling Relaxation Times and Effective Demagnetization Barriers in Kramers Lanthanide Single-Molecule Magnets. *J. Phys. Chem. Lett.* **2018**, *9* (18), 5327−5333.

DOI: 10.1021/acs.inorgchem.9b02039
Inorg. Chem. 2019, 58, 14046−14057

Příloha 2: Kotrle, K.; Atanasov, M.; Neese, F.; Herchel, R. Theoretical Magnetic Relaxation and Spin–Phonon Coupling Study in a Series of Molecular Engineering Designed Bridged Dysprosocenium Analogues. *Inorg. Chem.* 2023, *62* (42), 17499–17509. https://doi.org/10.1021/acs.inorgchem.3c02916.

Inorganic Chemistry

Open Access

pubs.acs.org/IC

Article

Theoretical Magnetic Relaxation and Spin−Phonon Coupling Study in a Series of Molecular Engineering Designed Bridged Dysprosocenium Analogues

Kamil Kotrle, Mihail Atanasov,* Frank Neese, and Radovan Herchel*

Cite This: *Inorg. Chem.* 2023, 62, 17499−17509

Read Online

ACCESS | Metrics & More | Article Recommendations | Supporting Information

ABSTRACT: A detailed computational study of hypothetical sandwich dysprosium double-decker complexes, bridged by various numbers of aliphatic linkers, was performed to evaluate the effect of the structural modifications on their ground-state magnetic sublevels and assess their potential as candidates for single-molecule magnets (SMMs). The molecular structures of seven complexes were optimized using the TPSSh functional, and the electronic structure and magnetic properties were investigated using the complete active space self-consistent field method (CASSCF). Estimates of the magnetic moment blocking barrier (U_{eff}) and blocking temperatures (T_B) are reported. In addition, a new method based on computed derivatives of effective demagnetization barriers U_{eff} with respect to vibrational normal modes was introduced and applied to evaluate the impact of spin−phonon coupling on the SMM properties. On the basis of the computed parameters, we have identified promising candidates with properties superior to those of the existing single-molecule magnets.

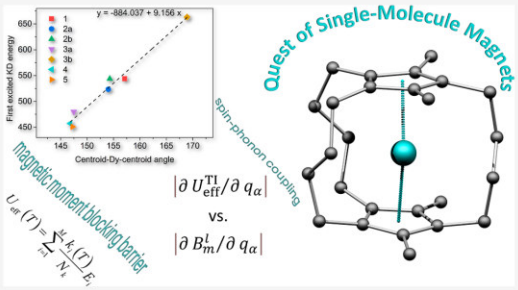

INTRODUCTION

In recent years, research on single-molecule magnets (SMMs) has taken many remarkable steps toward increasing their blocking temperatures (T_B) and relaxation times (τ). Today, the most interesting systems are unquestionably the lanthanide organometallic double-decker complexes. The increase of T_B from 20 K, in the complexes reported early on,[1] to 60 K for $[Dy(Cp^{tBu3})_2][B(C_6F_5)_4]$ (Cp^{tBu3} = 1,2,4 -tris-*t*-butylcyclopentadienyl)[2] and to even higher temperatures, T_B = 80 K for $[Dy(Cp^{iPr5})(Cp^{Me5})][B(C_6F_5)_4]$[3] ($Cp^{iPr5}$ = pentaisopropylcyclopentadienyl Cp^{Me5} = pentamethylcyclopentadienyl), paved the way for systematic increases in the performance of these remarkable SMM systems. In the search for even better compounds, new methods have been foreshadowed, like the replacement of carbon atoms in the cyclopentadienyl ring by heteroatoms[4] or the creation of analogous $[Ln^{II}(Cp^{iPr5})_2]$ type complexes.[5] Although these attempts did not produce a blocking temperature of more than 80 K, the results are nonetheless promising, and additional studies can further push their limits. Sandwich complexes with different numbers of carbon atoms with remarkable magnetic properties and strong anisotropy, such as $C_8H_8^{2-}$ or $C_9H_9^-$ are also worth mentioning. Interestingly, the most promising complexes with these bigger ligands are complexes of erbium rather than dysprosium.[6]

With such progress, one question comes to mind—why is this class of complexes so much better than all the others? Their axial nature gives them the ability to have high energetic barriers, surpassing 1000 or even 2000 K. Although such high barriers have been seen before in pentagonal bipyramidal complexes,[1] their blocking temperatures are much lower; the highest of them $[Dy(Cy_3PO)_2(H_2O)_5]Cl_3$, is "only" 20 K. Nowadays, such behavior is usually explained by the Raman relaxation mechanism. This mechanism allows for a reversal of magnetization before reaching the temperature at which the Orbach relaxation process becomes dominant.[7]

We already know that the magnetic relaxation energy is preferably transferred via vibrations in the surroundings to the thermal bath, e.g., through the low-energy vibrational modes of the molecule or crystal lattice vibrations (phonons). Unfortunately, first-principles calculations of the precise phonon spectrum of a molecular crystal (see ref 45c as an unprecedented model example using a frozen solution) to the required precision are only possible if the crystal structure is available, either experimentally or from periodic DFT methods. However, this method is not feasible for molecular structures that have been calculated ab initio by molecular

Received: August 21, 2023
Published: October 9, 2023

engineering. Hence, the next best approximation is a study of how the spin degrees of freedom couple to the molecular vibrations. This provides at least the initial stage of the mechanism that eventually leads to the dissipation of energy. The hope is that this initial stage, which is specific to a given molecular system, allows a comparison of related molecular systems, because both optical and acoustic phonons at least partially interact with molecules through their vibrational modes, in the part of the spectrum of their respective energies.[8] Thus, a careful study of how the spin degrees of freedom couple to the molecular vibrations is indispensable to provide insight into relaxation mechanisms.

This approach allows vibrational modes to be identified along which the spin-Hamiltonian (SH) parameters of the system significantly change. Such vibrations are labeled as "active" vibrations. Identifying such vibrational modes provides the insight necessary to engineer new systems, in which these modes are affected through the chemical modification of the molecular structure (e.g., the modification, addition, or removal of substituents or functional groups). The goal is to obtain a system in which magnetic energy transfer becomes less efficient, which leads to longer relaxation times and higher blocking temperatures. Similar ideas have been pursued for the $[Dy(Cp^{tBu3})_2][B(C_6F_5)_4]$ complex,[2] where theoretical calculations have provided evidence for the importance of C−H vibrations, when H is directly connected to the cyclopentadienyl cycle. This was demonstrated in a study of a series of similar H-substituted and alkyl-substituted cyclopentadienyl complexes where big differences in relaxation times were observed.[9]

The application of ab initio approaches to explain magnetic anisotropy in dysprosium single-molecule magnets focuses on first-principles calculations of anisotropy barriers, relaxation times, or blocking temperatures at their equilibrium geometry. A way that can predict the effective anisotropy barrier U_{eff} is based on the knowledge of the molecular structure and energetic positions of the thermally accessible Kramers doublets (KDs).[10] The only methods that yield systematically correct results for such systems are based on multireference wave functions, such as the complete active space self-consistent field (CASSCF) method or extensions of the method that introduce dynamic electron correlation, such as the N-electron valence perturbation theory to second order (NEVPT2)[11] or the complete active space perturbation theory to second order (CASPT2).[12]

A very important parameter used in the prediction of U_{eff} is the magnetic dipole matrix elements for transitions between KDs. An alternative method was recently proposed that uses predictions of quantum tunneling rates based on ab initio computed g-factors.[13]

In practice, one can employ the matrix elements of the magnetic dipole operator as a means to estimate the tunneling matrix elements. In fact, we have used such matrix elements from CASSCF wave functions with some success in the past for the in silico design of molecular systems.[14]

Based on such models, various methods have been proposed for the calculation of the blocking temperature, which ultimately is the central macroscopic property of interest. It is important to study the effective barrier rather than the "nominal" barrier that is obtained from the energetic position of the KDs calculated at equilibrium geometry. Incorporating the tunneling dynamics explains why the effective barrier does not always strongly correlate with the nominal barrier. In fact, it has been shown that the majority of the discrepancy arises from different relaxation mechanisms as discussed in the work of Aravena et al.,[7] in which a simple approximation method was proposed for the evaluation of blocking temperatures induced by the Orbach mechanism. The results agreed with the experimental blocking temperatures in some cases of high T_B complexes; other complexes having larger barriers, but low T_B, have been rationalized by the application of the mechanism of Raman relaxation. However, the limitation of this method is that it only examines the static properties, based on electronic energy levels, and applies empirical observations to estimate T_B. It does not provide reliable tools for the study of relaxation times, which require an analysis of phonon dynamics to estimate the attempt time, the τ_0 coefficient in the $\tau = \tau_0 \times \exp(U_{eff}/k_BT)$ expression of the Orbach mechanism of magnetic relaxation.

Recently, a more refined model for magnetic relaxation was proposed; this is based on a consideration of the effect of vibrational normal modes on the magnetic sublevels.[15] These studies have been validated with existing molecules and then applied to the design of dysprosocenium complexes with the desired SMM properties.[16]

Here, we report our theoretical study of seven dysprosium systems with ligand $(Me)_nCp(Lin)_{5-n}Cp(Me)_n$, where Me = methyl and Lin = butylene linker between Cp rings, with various numbers of linkers and geometries. For clarity, they are listed in Table 1, and some examples are shown in Scheme 1.

Table 1. List of Studied Complexes 1−5

name	number of linkers	number of methyls	linker positions	composition
1	1	4	1	$DyC_{22}H_{32}$
2a	2	3	1,2	$DyC_{24}H_{34}$
2b	2	3	1,3	$DyC_{24}H_{34}$
3a	3	2	1,2,3	$DyC_{26}H_{36}$
3b	3	2	1,2,4	$DyC_{26}H_{36}$
4	4	1	1,2,3,4	$DyC_{28}H_{38}$
5	5	0	1,2,3,4,5	$DyC_{30}H_{40}$

Scheme 1. Illustration of the Key Structural Features of the Theoretical Complexes Studied

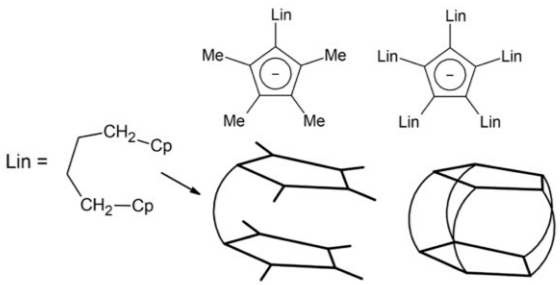

Similar linker bridged sandwich complexes have already been reported upon for transition metals with multiple structural types. Such are nickel complexes with one linker made of alkyl chains of different lengths (three, four, or six atoms) that accounts for the possibility of the inclusion of double bonds.[17] Similar molecular structures have also been prepared with zirconium and may possibly be of use as catalysts for polymerization.[18] Known molecular structures also

https://doi.org/10.1021/acs.inorgchem.3c02916
Inorg. Chem. 2023, 62, 17499−17509

exist for cobalt and rhodium, with doubly linked cyclopentadienylophane-type ligands with linkers that contain 4 carbon atoms.[19]

However, most metallocenophane-type structures are restricted to eighth group elements, especially iron and, to a lesser extent, also ruthenium. Because of this, only molecular structures with four-carbon linkers will be mentioned here, even though many different types have been reported. For iron, such compounds exist for any possible number of linkers, one of which is the so-called superferrocenophane, which is a cage with five linkers,[20] although its synthesis is extremely complicated. An interesting effect has been observed: as the number of linkers increases, the distance between the iron and cyclopentadienyl decreases. In the case of ruthenium, only molecular structures with one[21] or two linkers in the 1,3-positions[22] are known.

This series of iron complexes inspired us to study similar complexes of dysprosium and the effect of molecular vibrations on the SMM parameters—the effective barriers U_{eff} and relaxation time along with the dependence of the number of linkers that are expected to induce rigidity and to have a desirable effect on their SMM properties.

COMPUTATIONAL DETAILS

All of the calculations were carried out using the ORCA software suite. Geometrical optimization and frequency calculations were performed using the ORCA release 4.2.0. The CASSCF calculations were carried out in ORCA release 5.0.2./5.0.3.[23] Geometry optimization with frequency calculations were done using the TPSSh *meta*-GGA functional,[24] with a SARC2 basis set for dysprosium[25] and TZVP bases from the Ahlrichs def2 basis set for all other elements.[26] In these computations, ZORA scalar relativistic corrections were utilized.[27] The RIJCOSX approximation was used to speed up the calculations[28] using SARC/J as an auxiliary basis.[29] With ORCA 4.2.0, large integration grid settings were used (Gridx9, Grid6, ORCA 4.2), with increased precision for dysprosium (SpecialGridIntAcc 10), along with tight SCF convergence criteria.

The TPSSh functional was chosen because it is one of the best methods available to predict the geometries of lanthanide compounds.[30] With this setup, optimized structures (Figures 1 and S1−S5), as well as vibrational frequencies (Table S1), were acquired. The convergence criteria were set to the "TightOpt" settings available in ORCA; if any imaginary frequencies were present, the optimization was rerun using the "VeryTightOpt" setting, and the increment in the numerical frequency calculation was set to 0.001.

State-averaged CASSCF calculations[31] were done using the Sapporo basis set for dysprosium,[32] along with the def2-TZVP basis set for other atoms, using the RIJCOSX approximation with an "AutoAux" automatically generated auxiliary base.[33] The CASSCF used a set of seven active orbitals with nine electrons, CAS(9,7), which enabled the use of the ORCA ab initio ligand field theory (AILFT) module to relate the electronic structure to ligand field concepts.[34] Relativistic effects of the CASSCF calculations were treated by the Douglas−Kroll−Hess (DKH) method.[35] The SINGLE_ANISO program[36] was also utilized through its interface with the ORCA program suite.

Spin−orbit coupling (SOC) within the scalar relativistic CASSCF wave functions was taken into account through the use of quasi-degenerate perturbation theory (QDPT). This produces a relativistic (field free) energy spectrum composed of KDs. Using these relativistic states, the matrix elements of the magnetic dipole operator were evaluated and further used to compute tunneling rates.

The molecular structures and related properties were modeled and viewed through the use of Avogadro,[37] Mercury,[38] and VESTA.[39]

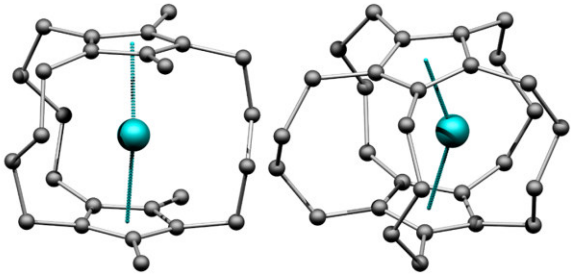

Figure 1. Computed molecular geometries of **3b** (left) and **5** (right). The hydrogen atoms are omitted for clarity. The dotted lines depict the centroid-Dy-centroid interactions.

RESULTS AND DISCUSSION

Optimized Geometries and IR Spectra. The geometrical parameters of the optimized structures are listed in Table 2, and the coordinates of the optimized geometries are attached in a Supporting Information file. Visualizations of the structures are shown in Figures 1 and S1−S5.

Table 2. Comparison of the Selected Geometric Parameters Based on Cyclopentadienyl Ring Centroids between the TPSSh-Optimized Molecular Structures 1−5 and Selected Dysprosocenium Compounds 6−7

complex	Dy-Centr1	Dy-Centr2	Centr1-Dy-Centr2
1	2.297	2.298	157.12
2a	2.293	2.298	154.02
2b	2.289	2.287	154.30
3a	2.264	2.265	147.48
3b	2.253	2.243	168.92
4	2.197	2.203	146.82
5	2.154	2.154	147.24
6 (ref 3)[a]	2.324 [2.296]	2.348 [2.284]	168.9 [162.5]
7 (ref 2)[a]	2.338 [2.318]	2.336 [2.314]	156.5 [152.6]

[a]Entries in square brackets are taken from reported X-ray data subject to disorder in the case of **6**.

It follows from Table 2 that the TPSSh functional provides geometrical parameters similar to those found in the molecular structures, confirmed by experimentation, of the already known dysprosocenium compounds $[Dy(Cp^{tBu3})_2][B(C_6F_5)_4]$ (**7**) and $[Dy(Cp^{iPr5})(Cp^{Me5})][B(C_6F_5)_4]$ (**6**). In addition, we can see a clear trend; as the number of linkers increases, the molecular structure becomes increasingly deformed. If the number of linkers is 3 or higher, the distance between the ring centroids and metal is shortened by about 0.05 Å for each linker added. This might contribute to the increase in instability of the complexes due to sterical deformation; however, we have decided that we will also perform calculations on these types of complexes (**3a**, **4**, and **5**) in

https://doi.org/10.1021/acs.inorgchem.3c02916
Inorg. Chem. 2023, 62, 17499−17509

Table 3. Comparison of Selected Geometric Parameters of Ferrocene Analogues Based on Cyclopentadienyl Ring Centroids

name (CCDC structure ID)	Fe-Centr1	Fe-Centr2	Centr1-Fe-Centr2
1,1′,2,2′-bis(tetramethylene)-ferrocene (COBSAN)[20]	1.625	1.646	173.75
(4)(3)(4)(1,2,3)ferrocenophane (BINMOA)[40]	1.638	1.639	172.19
(4)(4)(4)(4)(3)ferrocenophane (BETRUN)[41]	1.606	1.606	178.88

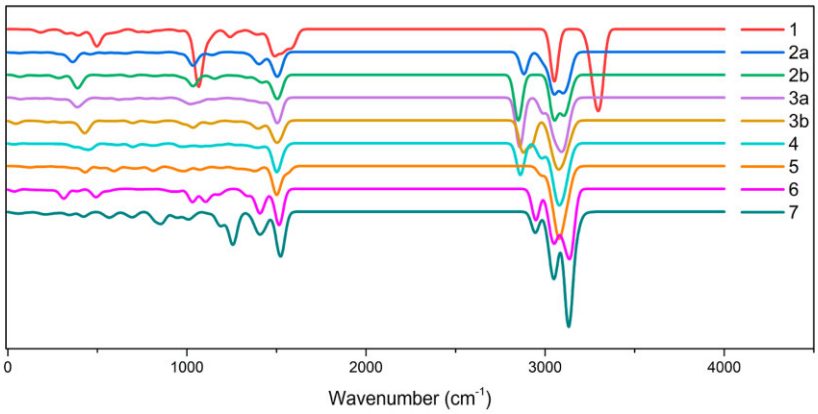

Figure 2. Simulated IR spectra for complexes **1**−**7** with the full width at half maximum (FWHM) set to 50 cm^{-1}.

order to study the effect of a higher number of linkers on the nuclear vibrations and their vibronic activity.

Similar, though less pronounced, effects are also seen for ferrocene derivatives, where the Fe-centroid distances become shorter as the number of linkers increases. It is also noteworthy, that with a smaller number of linkers, the angle between the centroids is slightly deformed from the ideal of 180° (Table 3).

Computed vibrational frequencies show that none of the optimized structures have any negative imaginary frequencies, and thus, they represent true minima on the scalar relativistic ground-state potential energy surface. The vibrational spectra were simulated using the orca_mapspc program in infrared mode with the boundaries set between 0 and 4000 cm^{-1} (Figure 2). A full list of the frequencies can be found in Table S1.

The results show clear trends across the series. In the low-energy part of the spectra for complexes **1** and **2**, there are two areas with prominent vibrations around 500 and 1000 cm^{-1}. As we compare complexes **1**−**5**, we see that these are slightly shifted and their intensity reduces. An inspection showed that these are vibrations from the methyl substituents on the cyclopentadienyl ring.

Similarly, interesting changes are seen around 2800 cm^{-1}, and this was identified as stretching vibrations of the linkers' methyl groups. Vibrations from carbons in the middle of a linker are at lower frequencies around 2800 cm^{-1}, while vibrations from the groups in the neighborhood of the ring are slightly over 3000 cm^{-1}. Complex **1** is an interesting exception; these vibrations are blue-shifted by about 200 cm^{-1}, and the vibrations near to 3100 cm^{-1} correspond to the stretching of the methyl groups. In addition, in complex **5**, vibrational modes, due to the middle atoms in the linker chain, have lost their shift and are almost overlapping, creating only a shoulder at a peak of 3000 cm^{-1}. Curiously, complexes **3a** and **4** have similar shoulders at 3000 cm^{-1}, but in this case, these vibrations emanate from the remaining methyl groups. In complexes **2a** and **2b**, the same vibrations from the methyl groups are seen as a shoulder on the blue side above 3100 cm^{-1}.

To allow comments on the rigidity of the molecular structures, we performed a very simple evaluation. Two different methods based on a comparison between the vibrational displacement vectors of selected atoms were used. The first method used to quantify vibrational displacement was a simple comparison of the sum of the sizes of the displacement vectors for each vibrational mode for the central dysprosium and neighboring carbon. In addition to the studied complexes, $[Dy(Cp^{tBu3})_2]^+$ (**7**)[2] and $[Dy(Cp^{iPr5})(Cp^{Me5})]^+$ (**6**)[3] were also added to the comparison. Their vibrational modes were calculated using the same methods applied to complexes **1**−**5**.

The second method was based on a comparison of the distribution of significant vibrations (those with a Dy atom displacement of more than 0.005 Å were considered to be significant) based on their frequency, as theoretically, shifting these vibrations toward higher frequencies should be beneficial for magnetic behavior.[42]

From this comparison (Figures S6 and S7), considering the results from the first method, it can be concluded that there is a general trend in the series of **1**−**5**. An increase in the number of linkers induces a decrease in vibrational displacement. However, complexes **6** and **7** have even lower values of vibrational displacement than **5**. Therefore, the expectation that a higher number of linkers restricts vibration seems to be at least partially correct; however, it also seems that nonlinked complexes, with substituted Cp rings, can also provide complexes with high rigidity.

An advantageous feature of the proposed linked complexes **1**−**5** is that they lack significant molecular vibrations in the area between 0 and 100 cm^{-1}, especially complexes **4** and **5**, in contrast to the nonlinked complexes **6**−**7**, which have vibrations that are generally shifted toward lower frequencies.

https://doi.org/10.1021/acs.inorgchem.3c02916
Inorg. Chem. 2023, 62, 17499−17509

Thus, this justifies the concept that by adding linkers, it is possible to shift phonons to higher energies.

Electronic Structures. The CASSCF-based scalar relativistic f-orbital orbital energies (obtained from an AILFT analysis) and relativistic many particle spectra (originating from the ground $^6H_{15/2}$ term) are shown in Figure 3 and are documented in Table S2.

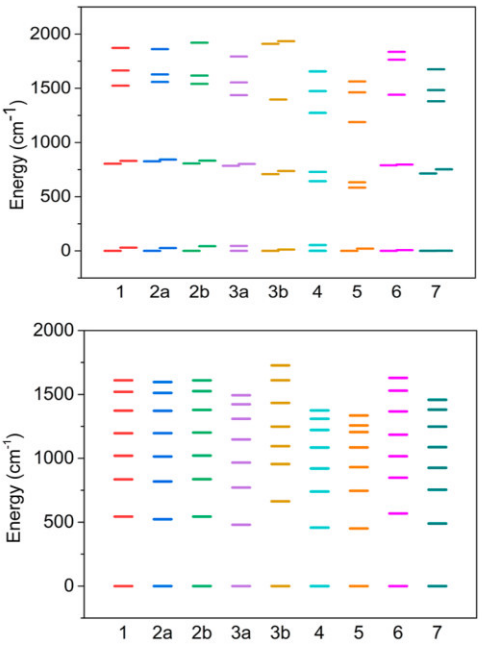

Figure 3. Energy splitting of f-orbitals (top) and Kramers doublets (bottom) of the $^6H_{15/2}$ term for complexes **1**−**7**.

The highest energy splitting of both the f-orbitals and KDs is observed for complex **3b**. However, the general trend across the series is that as the number of linkers increases, the ligand field splitting decreases for both KDs and f-orbitals (which are of course related).

The correlation between the ligand field splitting of the $^6H_{15/2}$ ground state of Dy^{3+} into eight KDs with geometric parameters again confirms the general trend that ligand field splitting increases as axiality increases (Figure 3).[43]

A strong correlation was found between the energy of the lowest excited KD and the angle defined by the ligand centroids and dysprosium atom; this confirms that axiality has the strongest impact on the energetic splitting of KDs. Interestingly, no similar correlation was found between the bond length and ligand field splitting. This correlation is particularly pronounced between **3a** and **3b**, which are both on different ends of the correlation line; this can be traced back to differences in the centroid-Dy-centroid angles, 148° for **3a** in comparison with 170° for **3b** (Table 2, Figure 4).

Next, we calculated the matrix elements for the magnetic transitions between the KDs and quantum tunneling rates; these are listed in Table 4 and depicted in Figure 5 (see also Figures S8−S10). The calculated *g*-factors for each KD are listed in Tables S3−S9.

We have also attempted to estimate the effective barrier for the relaxation of magnetization (Table 5) using a method

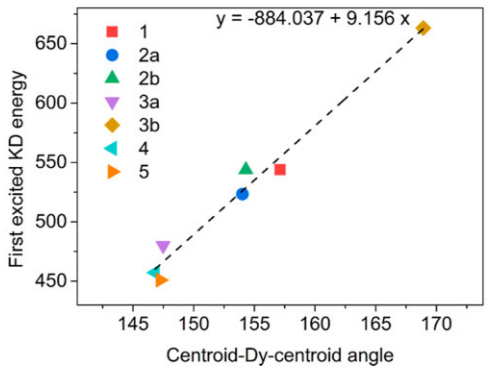

Figure 4. Correlation between the centroid-Dy-centroid angle and Kramers doublets (KD) energy splitting (cm^{-1}) in the studied complexes **1**−**5**.

developed elsewhere[10] with suitable modifications.[14] The effective barrier U_{eff} was calculated using

$$U_{eff}(T) = \sum_{i=1}^{M} \frac{k_i(T)}{N_k} E_i \quad (1)$$

where M is the number of KD states (M = 8 for Dy^{III}), E_i is the energy of the respective state, and N_k is the normalization factor for $k_i(T)$ defined as $N_k = \Sigma_i k_i(T)$. Finally, $k_i(T)$ are the demagnetization rates for the respective states calculated as

$$k_i(T) = \frac{\exp\left(-\frac{E_i}{k_B T}\right)}{Z} k_{QT,i} \quad (2)$$

where $k_{QT,i}$ are the demagnetization magnetic dipole matrix elements listed in Table 4, related to the quantum tunneling within the given KD, Z is the partition function, and k_B is the Boltzmann constant [see the Supporting Information for the MATLAB script that details the calculation of $U_{eff}(T)$].[44] The temperature-dependences of $k_i(T)$ and U_{eff} for complexes **1**−**5** are plotted in Figures S11−S19.

In their article, Aravena et al. have also suggested an approximation method for the prediction of the blocking temperature of the Orbach mechanism by dividing the theoretical energetic barrier by 28. This was derived in a recently published article[7] from the formula of relaxation time, with the assumption, that T_B is temperature, when τ = 100 s, and $\tau_0 \approx 10^{-11}$ to 10^{-12}. This has been shown to agree to an acceptable degree with the experimental values. The computed values of U_{eff} and T_B for complexes **1**−**5** are summarized in Table 5, where complexes **6** and **7** are also added for comparison purposes.

However, $U_{eff}(T)$, given by eqs 1 and 2, is temperature-dependent, while spin−phonon coupling is not. To overcome this controverse, we introduce a temperature-independent effective U_{eff}^{TI} as an auxiliary quantity as per eq 3

$$U_{eff}^{TI} = \sum_{i=1}^{M} \frac{k_{QT,i}}{\sum k_{QT,i}} E_i \quad (3)$$

by simply omitting the Boltzmann factors in eqs 1 and 2. Theoretically, this should serve as a limiting value for U_{eff}, which considers equal occupation of all KDs.

These results show that once again, **3b** is an outlier among the calculated U_{eff} values for the complexes and is predicted to

https://doi.org/10.1021/acs.inorgchem.3c02916
Inorg. Chem. 2023, 62, 17499−17509

Table 4. Energy of Kramers Doublets and Estimated Quantum Tunneling Rates

1	E (cm^{-1})	0	544	836	1020	1197	1373	1520	1611
	QTM	1×10^{-6}	1×10^{-4}	0.003	0.036	0.196	0.378	1.101	3.595
2a	E (cm^{-1})	0	523	819	1014	1197	1371	1512	1597
	QTM	1×10^{-6}	1×10^{-4}	0.002	0.031	0.188	0.279	1.055	3.422
2b	E (cm^{-1})	0	544	837	1022	1201	1379	1526	1610
	QTM	3×10^{-6}	3×10^{-4}	0.009	0.073	0.231	0.599	0.961	3.500
3a	E (cm^{-1})	0	480	771	966	1148	1309	1422	1494
	QTM	1×10^{-5}	4×10^{-4}	0.009	0.082	0.301	0.586	1.624	3.200
3b	E (cm^{-1})	0	663	955	1095	1248	1433	1610	1727
	QTM	5×10^{-7}	4×10^{-5}	0.001	0.004	0.070	0.202	1.012	3.590
4	E (cm^{-1})	0	457	740	921	1085	1222	1309	1375
	QTM	2×10^{-5}	6×10^{-4}	0.013	0.114	0.318	1.252	2.738	3.159
5	E (cm^{-1})	0	451	746	931	1085	1205	1258	1335
	QTM	5×10^{-6}	2×10^{-4}	0.004	0.060	0.256	0.196	2.945	0.779
6	E (cm^{-1})	0	569	848	1016	1185	1367	1530	1629
	QTM	1×10^{-7}	1×10^{-5}	0.001	0.002	0.047	0.097	0.365	3.496
7	E (cm^{-1})	0	490	754	926	1088	1248	1381	1458
	QTM	6×10^{-8}	2×10^{-5}	3×10^{-4}	0.001	0.032	0.238	0.307	3.508

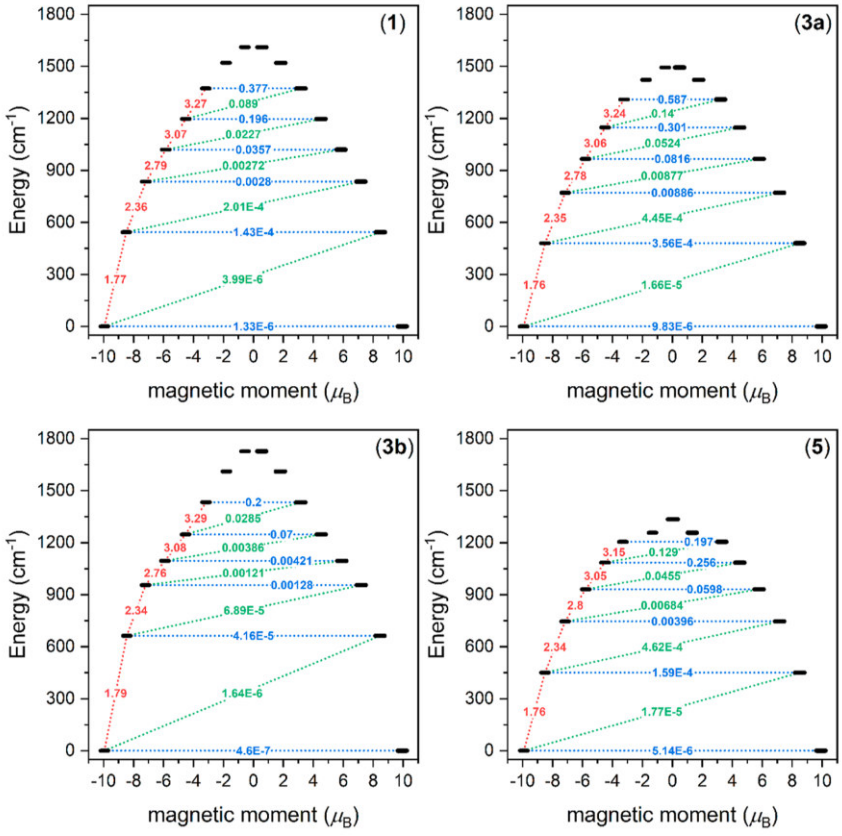

Figure 5. Visualization of the ab initio demagnetization magnetic dipole matrix elements for complexes **1**, **3a**, **3b**, and **5**. The numbers presented for the lowest six doublets represent the corresponding matrix element of the transverse magnetic moment (for values larger than about 0.1, an efficient relaxation mechanism is expected). Dashed blue lines refer to (temperature-assisted) quantum tunneling.

have a barrier that is at least 200 K higher than the rest. This correlates well with the predicted structural correlations discussed above. Computed values of U_{eff}, T_B, and U_{eff}^{TI} for complexes **6** and **7** follow the order of parameters extracted from the interpretation of the experimental a.c. and d.c relaxation data **7**: T_B = 60 K, U_{eff} = 1761 K,[2] and **6**: T_B = 80 K, U_{eff} = 2219 K.[3]

Spin−Phonon Coupling. Phonons are vibrations in the crystal lattices. In the context of SMMs, they function as transmitters of energy to/from the magnetic centers that are in contact with the thermal bath (heat transfer) under the

https://doi.org/10.1021/acs.inorgchem.3c02916
Inorg. Chem. 2023, 62, 17499−17509

Table 5. Estimated Magnetization Blocking Barriers and Blocking Temperatures, Calculated for a Temperature of T = 300 K from eq 1, and Temperature-Independent U_{eff}, Calculated from eq 3

complex	1	2a	2b	3a	3b	4	5	6	7
U_{eff}/K	2069	2072	1991	1888	2306	1777	1749	2233	2023
T_B/K	73.9	74	71.1	67.4	82.3	63.4	62.5	79.8	72.3
U_{eff}^{TI}/K	2239	2228	2221	2057	2423	1880	1805	2315	2069

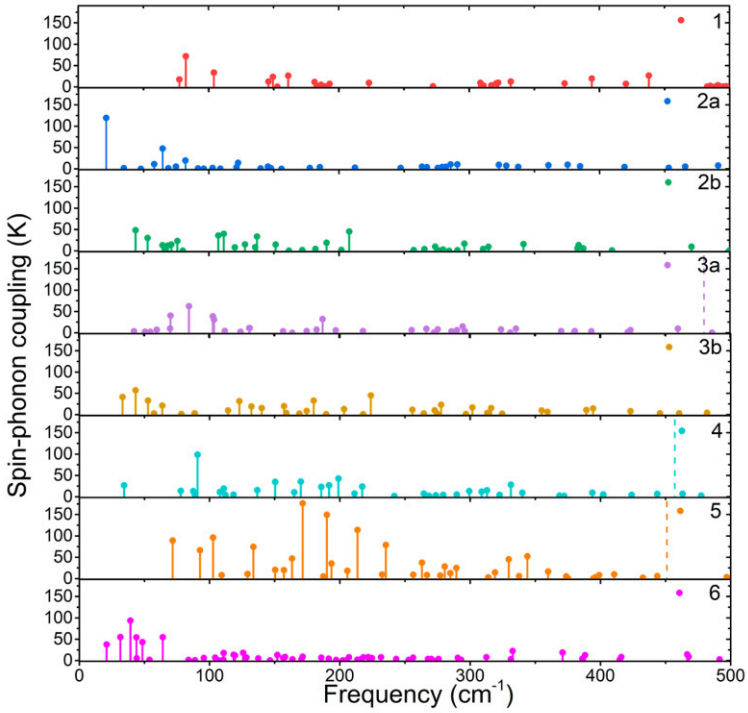

Figure 6. Comparison of the spin−phonon coupling parameters $|\partial U_{eff}^{TI}/\partial q_\alpha|$ for complexes **1**−**6** calculated using eq 4.

condition of thermal equilibrium. Recently, the need to include the effects of phonons to compute magnetic relaxation times has risen, and several methods to quantify their effect have been developed.[45] In a nutshell, these methods rely on a study of the dependence of g-factors,[46] zero-field splitting parameters D and E, crystal field operators,[47] or energy separations between KDs.

Here, we introduce a new approach that takes advantage of an analysis of the impact of molecular vibration on U_{eff} over vibrational modes. We have attempted to use this method as it utilizes information from all KD energies and transition rates, weighted by, what should be, the most preferred relaxation pathway

$$V_\alpha = \left(\frac{\partial U_{eff}^{TI}}{\partial q_\alpha}\right) \tag{4}$$

where U_{eff}^{TI} is calculated using eq 3 and q_α are normal modes.

From a computation point of view, the evaluation was done through the displacement of atomic positions in Cartesian coordinates by 0.05 Å in all directions and recomputing the CASSCF electronic structure with the deformed structure. The resulting values were transferred into dimensionless normal modes (eigenvectors of a Hessian matrix)

$$\left(\frac{\partial U_{eff}^{TI}}{\partial q_\alpha}\right) = \sum_{i=1}^{3N} \sqrt{\frac{\hbar}{\omega_\alpha m_i}} L_{i\alpha} \left(\frac{\partial U_{eff}^{TI}}{\partial X_i}\right) \tag{5}$$

where α corresponds to the respective normal mode, m is the atomic mass, ω_α is the vibration angular frequency, and L is the Hessian eigenvector matrix, and the summation is carried out over $3N$ Cartesian coordinates (X). As the normal modes are dimensionless, the resulting values of $|\partial U_{eff}^{TI}/\partial q_\alpha|$ are given in units of U_{eff}, which are the energy equivalents of K that are usually used for U_{eff}. The outcome of these calculations for **1**−**6** is shown in Figure 6.

Only phonon modes below 500 cm^{-1} are shown as it is important to consider mostly those modes which are achievable by thermal excitations at lower temperatures. It is also noteworthy to mention that this is the energy range where vibrations involving close coordination environment take place. Necessarily, these will induce the largest changes of the magnetic anisotropy with molecular distortions. All of the calculated spin−phonon coupling coefficients are listed in Tables S10−S17.

The effect of spin−phonon coupling on magnetic relaxation will be now discussed in the light of the following points of departure: (i) lowest energy vibrations with maximum values of $|\partial U_{eff}^{TI}/\partial q_\alpha|$ will tend to dominate Raman relaxation times and (ii) vibrations with maximum $|\partial U_{eff}^{TI}/\partial q_\alpha|$ values in the

https://doi.org/10.1021/acs.inorgchem.3c02916
Inorg. Chem. 2023, 62, 17499−17509

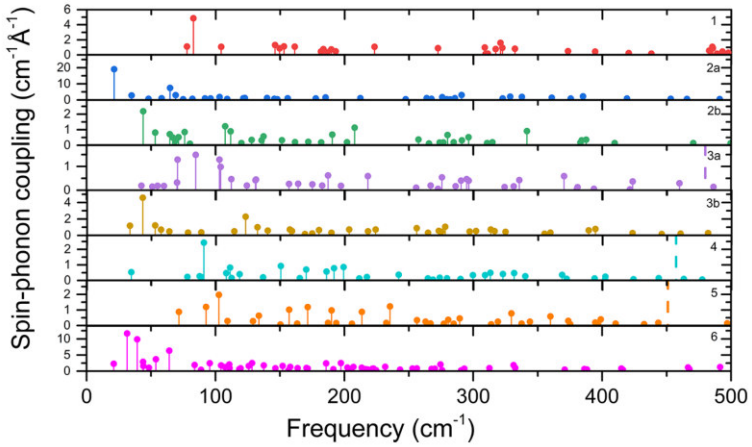

Figure 7. Comparison of the spin−phonon coupling parameters $|\partial B_m^l/\partial q_\alpha|$ for complexes **1**−**6** from eq 6.

vicinity of the lowest excited KD, considering vibrational line broadenings of the order of 10 cm^{-1} (see refs 45c,45d and references cited therein) will mostly affect Orbach relaxation times.

For complex **1**, the vibration with the strongest coupling is the one at 83 cm^{-1}. In this mode, the cyclopentadienyl rings move away from each other and modulate the centriod1-Dy-centroid2 angle, disturbing axiality (see animation comp1-vibr83.gif). Interestingly, this vibration resembles the most active vibrations, which were found in our previous study on inorganic ring systems.[14] However, in comparison to the other members of the series, vibrational modes of **1** are shifted to higher wavenumbers, thus tending to mitigate Raman relaxation terms. Interestingly, the lowest excited KD coincides with a vibration having a vanishingly small $|\partial U_{\mathrm{eff}}^{\mathrm{TI}}/\partial q_\alpha|$ value (Table S10, Figure S22). This is in favor of increasing Orbach relaxation times.

In complex **2a**, the situation is quite similar to that of complex **1**; the first vibration at 22 cm^{-1} is very strongly coupled but shifted to lower energies compared to **1**, thus facilitating Raman relaxation (comp2avibr22.gif). As for **1**, overlap between the lowest KD is very small, which is expected to increase the Orbach relaxation times (Figure S23).

Unlike complexes **1** and **2a**, complex **2b** does not have a vibration that has a $|\partial U_{\mathrm{eff}}^{\mathrm{TI}}/\partial q_\alpha|$ that is significantly larger than the others, with a maximal value of $|\partial U_{\mathrm{eff}}^{\mathrm{TI}}/\partial q_\alpha|$ = 48 cm^{-1}, a value in comparison with $|\partial U_{\mathrm{eff}}^{\mathrm{TI}}/\partial q_\alpha|$ = 94 cm^{-1} for complex **2a**. The largest values are assigned to vibrations at 44 cm^{-1} (twisting of $-CH_3$ groups and shift of the cyclopentadienyl ring, comp2bvibr44.gif) and 208 cm^{-1} (bending on linkers, comp2bvibr208.gif). Other significant vibrations are located at 53, 107, and 112 cm^{-1} (twisting of $-CH_3$ groups on rings, comp2bvibr53.gif, comp2bvibr107.gif, and comp2bvibr112.gif, respectively). There are two weakly coupled vibrations in the vicinity of the lowest excited KD at 544 cm^{-1} (Figure S24).

Complex **3a** has four active vibrations; at 71 cm^{-1}, a deformation of the molecule through twisting of the cyclopentadienyl rings (comp3avibr71.gif) is observed, with three further vibrations at 85, 103, and 104 cm^{-1}, which move cyclopentadienyl ligands, leading to opening of the structure, similar to the active vibrations of previous complexes (animations comp3avibr85.gif, comp3avibr103.gif, and comp3avibr104.gif, respectively). There are no vibrations in the vicinity of the lowest excited KD at 480 cm^{-1}, which is expected to favor increase of Orbach relaxation times (Figure S25).

For complex **3b**, the most important vibrations are at 33 and 43 cm^{-1}, and again these are dominated by twisting of the $-CH_3$ groups (comp3bvibr33.gif and comp3bvibr43.gif, respectively), accompanied by shifts of the cyclopentadienyl rings. Another significant vibration is found at 224 cm^{-1}, with the contribution of the linker atoms (comp3bvibr224.gif). It is interesting that this molecule has a significantly smaller overlap of active vibration with the KD energies than previous complexes, particularly as far as the first excited KD at 663 cm^{-1} is concerned, where no vibrational modes are present nearby (see Figure S26).

In complex **4**, the most significant vibrations are at 34 and 91 cm^{-1}, and both vibrations cause changes in the ligand−metal bonds due to the movement of one linker (comp4vibr34.gif and comp4vibr91.gif, respectively). Other prominent vibrations are at 170 and 199 cm^{-1}, which are vibrations on linkers (comp4vibr170.gif and comp4vibr199.gif, respectively). We note on passing that rigidity induced by the presence of linkers leads to a shift of these vibrations to higher frequencies than in previous complexes. This is expected to suppress pathways for Raman relaxation. Interestingly, also the overlap of low KD energies, particularly the first excited doublet, with vibrations is very small (see Figure S27); as a result, no vibration is in resonance with its excitation energy.

Finally, in complex **5**, there are more significant vibrations than in the previous ones. The first three vibrations at 72, 93, and 103 cm^{-1} are the most important; all of them are vibrations of linkers that cause movement of the central dysprosium atom (comp5vibr72.gif, comp5vibr93.gif, and comp5vibr103.gif, respectively). There are other important vibrations; the highest of them is at 190 cm^{-1}, which is vibration that causes movement in the cyclopentadienyl rings, similar to that described in other complexes (comp5vibr190.gif). There is a weak overlap between the lowest excited KD at 451 cm^{-1} and a neighboring vibration at 444 cm^{-1} (Figure S28).

Phonons have certain levels of anharmonicity, which results in broadening of their spectral line shape. Such effects are beyond all contemporary models of magnetic relaxation based on the Harmonic approximation.[48] Anharmonicity is expected

https://doi.org/10.1021/acs.inorgchem.3c02916
Inorg. Chem. 2023, 62, 17499−17509

to lead to increase of the probability of nonresonant energy transfer, thus contributing to a possible increase in the relaxation rate (see refs 8,45a,47).

When comparing the phonon spectrum with the energies of KDs (Figures S20 and S21), it is visible that especially the first excited doublet in **3b** has the lowest degree of overlap with vibrations (Figure S26). Along with a higher KD splitting of complex **3b**, this is expected to contribute to the superiority of this complex over the other complexes with a smaller number of connections between rings. In particular, **2a** and **2b** have vibrations that overlap their first excited KD with large spin−phonon coupling matrix elements.

For comparison, we have attempted to use another common method for the calculation of spin−phonon coupling, which uses crystal field operators[47]

$$\hat{V}_\alpha = \sum_{lm} \left(\frac{\partial B_m^l}{\partial q_\alpha} \right) \hat{O}_m^l \tag{6}$$

We have used second-order (l = 2) crystal field operators from the SINGLE_ANISO software for $|JM\rangle$. The results suggest that to a certain degree, there is an agreement between the proposed $|\partial U_{\mathrm{eff}}^{\mathrm{TI}}/\partial q_\alpha|$ method for the calculation of spin−phonon coupling coefficients (Figure 7).

In most complexes, the prominent vibrations arise at the same frequencies that were found when using the previous method, although their intensities may differ to a certain degree, and some disagreements might be found, for example, among the lowest-level vibrations of complex **6**, where $|\partial U_{\mathrm{eff}}^{\mathrm{TI}}/\partial q_\alpha|$ shows quite a large number of active vibrations than for $|\partial B_m^l/\partial q_\alpha|$. Despite this, we think that $|\partial U_{\mathrm{eff}}^{\mathrm{TI}}/\partial q_\alpha|$ is an interesting alternative method, as it is tied to U_{eff}, a property that is inherently important for magnetic relaxation, and it also respects the probability of the relaxation pathway due to the use of magnetic moment matrix elements in the calculation.

CONCLUSIONS

In this work, a theoretical study of seven hypothetical double-decker dysprosium complexes was carried out with one to five functional butylene groups connecting the two axial cyclopentadienyl ligands. Complexes of this type have been reported to function as SMMs with record magnetization blocking temperatures.[2,3] The aim of the study was to analyze the effect of the number of linkers and geometry on the vibrational spectra, ligand field splitting of the $^6H_{15/2}$ ground-state multiplet, and SMM properties using correlated CASSCF calculations.

We applied a model put forward by Aravena et al.,[7,10] which was shown to reproduce effective demagnetization barriers and blocking temperatures reasonably well for a series of well-documented Dy^{3+}-based SMMs. In this model, magnetic dipole matrix elements for each KD and its CASSCF energies were employed in the calculation of its contribution to the thermally assisted quantum tunneling rates and effective demagnetization barriers. When applying the model to the series of complexes studied here, with the use of DFT-optimized geometries, we came to the conclusion that complex **3b**, with the highest axiality (as reflected by the angle contended between the centroids of the two ligands and Dy, 170°), outperformed the other complexes in the series. These considerations, based on the assumption of a frozen geometry, have been extended to account for the entire set of molecular vibrations of each complex. More specifically, the linear derivatives of the energies of the eight KDs and the matrix elements of the magnetic dipolar transitions that connect components with magnetizations of the opposite sign were used to compute the $(\partial U_{\mathrm{eff}}^{\mathrm{TI}}/\partial q_\alpha)_o$. This approach is an alternative method for the expression of spin−phonon coupling, which utilizes the influence of molecular vibrations on the energies of KDs and the transition probabilities between magnetic sublevels. We see some advantages to this method, such as the clear relation to perhaps the most important characteristic of SMMs, and also to its ability to weigh the individual contribution of vibrations, through their role in the relaxation pathway. A comparison with the frequently used $|\partial B_m^l/\partial q_\alpha|$ method shows similar vibrations active in magnetic relaxation.

From this approach, one thing we observe is the energetic profile of the vibration, where complexes **1** and **5** are different from the other complexes studied as their vibrations are shifted toward higher frequencies, which should be beneficial due to the lower thermal population of active modes. From the viewpoint of values of spin−phonon coupling, it seems to be quite the opposite. In the middle of the series, complexes **2b**−**4** seem to have better parameters in terms of their lower values of spin−phonon coupling in low-lying vibrational modes. Specifically, complex **3b** is also interesting as it has a low overlap between the vibrational modes and electron transition, and in combination with a predicted high barrier and reasonably low spin−phonon coupling, it is, in our opinion, the most promising complex from the series that was studied.

ASSOCIATED CONTENT

Supporting Information

The Supporting Information is available free of charge at https://pubs.acs.org/doi/10.1021/acs.inorgchem.3c02916.

Molecular geometries of complexes **1**−**5**, visualizations of their molecular structures, additional plots of the magnetization blocking barriers, lists of molecular vibrations and spin−phonon coupling coefficients, and Python and MATLAB scripts for the calculations of the spin−phonon coupling (PDF)

Optimized molecular structures 1−7 (XYZ)

Molecular vibrations (ZIP)

AUTHOR INFORMATION

Corresponding Authors

Mihail Atanasov − *Max-Planck-Institut für Kohlenforschung, Mülheim an der Ruhr D-45470, Germany; Institute of General and Inorganic Chemistry, Bulgarian Academy of Sciences, Sofia 1113, Bulgaria;* orcid.org/0000-0003-4178-2187; Email: mihail.atanasov@kofo.mpg.de

Radovan Herchel − *Department of Inorganic Chemistry, Faculty of Science, Palacký University Olomouc, Olomouc CZ-77146, Czech Republic;* orcid.org/0000-0001-8262-4666; Email: radovan.herchel@upol.cz

Authors

Kamil Kotrle − *Department of Inorganic Chemistry, Faculty of Science, Palacký University Olomouc, Olomouc CZ-77146, Czech Republic*

Frank Neese − *Max-Planck-Institut für Kohlenforschung, Mülheim an der Ruhr D-45470, Germany;* orcid.org/0000-0003-4691-0547

Complete contact information is available at:

https://pubs.acs.org/10.1021/acs.inorgchem.3c02916

Notes

The authors declare no competing financial interest.

■ ACKNOWLEDGMENTS

We gratefully acknowledge the financial support received from Palacký University Olomouc (projects IGA_PrF_2022_006 and IGA_PrF_2021_009).

■ REFERENCES

(1) (a) Liu, J.; Chen, Y.-C.; Liu, J.; Vieru, V.; Ungur, L.; Jia, J.; Chibotaru, L. F.; Lan, Y.; Wernsdorfer, W.; Gao, S.; Chen, X.-M.; Tong, M. A Stable Pentagonal Bipyramidal Dy(III) Single-Ion Magnet with a Record Magnetization Reversal Barrier over 1000 K. *J. Am. Chem. Soc.* **2016**, *138* (16), 5441−5450. (b) Ding, Y.-S.; Chilton, N. F.; Winpenny, R. E. P.; Zheng, Y.-Z. On Approaching the Limit of Molecular Magnetic Anisotropy: A Near-Perfect Pentagonal Bipyramidal Dysprosium(III) Single-Molecule Magnet. *Angew. Chem., Int. Ed.* **2016**, *55* (52), 16071−16074. (c) Chen, Y.-C.; Liu, J.-L.; Ungur, L.; Liu, J.; Li, Q.-W.; Wang, L.-F.; Ni, Z.-P.; Chibotaru, L. F.; Chen, X.-M.; Tong, M.-L. Symmetry-Supported Magnetic Blocking at 20 K in Pentagonal Bipyramidal Dy(III) Single-Ion Magnets. *J. Am. Chem. Soc.* **2016**, *138* (8), 2829−2837.

(2) Goodwin, C. A. P.; Ortu, F.; Reta, D.; Chilton, N. F.; Mills, D. P. Molecular magnetic hysteresis at 60 kelvin in dysprosocenium. *Nature* **2017**, *548* (7668), 439−442.

(3) Guo, F.; Day, B. M.; Chen, Y.; Tong, M.; Mansikkamäki, A.; Layfield, R. A. Magnetic hysteresis up to 80 kelvin in a dysprosium metallocene single-molecule magnet. *Science* **2018**, *362* (6421), 1400−1403.

(4) Evans, P.; Reta, D.; Whitehead, G. F. S.; Chilton, N. F.; Mills, D. P. Bis-Monophospholyl Dysprosium Cation Showing Magnetic Hysteresis at 48 K. *J. Am. Chem. Soc.* **2019**, *141* (50), 19935−19940.

(5) Gould, C. A.; McClain, K. R.; Yu, J. M.; Groshens, T. J.; Furche, F.; Harvey, B. G.; Long, J. R. Synthesis and Magnetism of Neutral, Linear Metallocene Complexes of Terbium(II) and Dysprosium(II). *J. Am. Chem. Soc.* **2019**, *141* (33), 12967−12973.

(6) (a) Münzfeld, L.; Schoo, C.; Bestgen, S.; Moreno-Pineda, E.; Köppe, R.; Ruben, M.; Roesky, P. W. Synthesis, Structures and Magnetic Properties of [(H9-C9H9)Ln(H8-C8H8)] Super Sandwich Complexes. *Nat. Commun.* **2019**, *10* (1), 3135. (b) Ungur, L.; Le Roy, J. J.; Korobkov, I.; Murugesu, M.; Chibotaru, L. F. Fine-Tuning the Local Symmetry to Attain Record Blocking Temperature and Magnetic Remanence in a Single-Ion Magnet. *Angew. Chem., Int. Ed.* **2014**, *53* (17), 4413−4417.

(7) Castro-Alvarez, A.; Gil, Y.; Llanos, L.; Aravena, D. High Performance Single-Molecule Magnets, Orbach or Raman Relaxation Suppression? *Inorg. Chem. Front.* **2020**, *7*, 2478−2486.

(8) Lunghi, A.; Sanvito, S. How Do Phonons Relax Molecular Spins? *Sci. Adv.* **2019**, *5* (9), 1−8.

(9) Randall McClain, K.; Gould, C. A.; Chakarawet, K.; Teat, S. J.; Groshens, T. J.; Long, J. R.; Harvey, B. G. High-Temperature Magnetic Blocking and Magneto-Structural Correlations in a Series of Dysprosium(III) Metallocenium Single-Molecule Magnets. *Chem. Sci.* **2018**, *9* (45), 8492−8503.

(10) Aravena, D. Ab Initio Prediction of Tunneling Relaxation Times and Effective Demagnetization Barriers in Kramers Lanthanide Single-Molecule Magnets. *J. Phys. Chem. Lett.* **2018**, *9* (18), 5327−5333.

(11) (a) Angeli, C.; Evangelisti, S.; Cimiraglia, R.; Maynau, D. A Novel Perturbation-Based Complete Active Space-Self-Consistent-Field Algorithm: Application to the Direct Calculation of Localized Orbitals. *J. Chem. Phys.* **2002**, *117* (23), 10525−10533. (b) Angeli, C.; Cimiraglia, R.; Evangelisti, S.; Leininger, T.; Malrieu, J.-P. Introduction of n-Electron Valence States for Multireference Perturbation Theory. *J. Chem. Phys.* **2001**, *114* (23), 10252−10264. (c) Angeli, C.; Cimiraglia, R.; Malrieu, J.-P. N -Electron Valence State Perturbation Theory: A Spinless Formulation and an Efficient Implementation of the Strongly Contracted and of the Partially Contracted Variants. *J. Chem. Phys.* **2002**, *117* (20), 9138−9153.

(12) Finley, J.; Malmqvist, P.-Å.; Roos, B. O.; Serrano-Andrés, L. The Multi-State CASPT2 Method. *Chem. Phys. Lett.* **1998**, *288* (2−4), 299−306.

(13) Yin, B.; Li, C.-C. A Method to Predict Both the Relaxation Time of Quantum Tunneling of Magnetization and the Effective Barrier of Magnetic Reversal for a Kramers Single-Ion Magnet. *Phys. Chem. Chem. Phys.* **2020**, *22* (18), 9923−9933.

(14) Kotrle, K.; Herchel, R. Are Inorganic Single-Molecule Magnets a Possibility? A Theoretical Insight into Dysprosium Double-Deckers with Inorganic Ring Systems. *Inorg. Chem.* **2019**, *58* (20), 14046−14057.

(15) Ortu, F.; Reta, D.; Ding, Y. S.; Goodwin, C. A. P.; Gregson, M. P.; McInnes, E. J. L.; Winpenny, R. E. P.; Zheng, Y. Z.; Liddle, S. T.; Mills, D. P.; Chilton, N. F. Studies of Hysteresis and Quantum Tunnelling of the Magnetisation in Dysprosium(III) Single Molecule Magnets. *Dalton Trans.* **2019**, *48* (24), 8541−8545.

(16) Ullah, A.; Cerdá, J.; Baldoví, J. J.; Varganov, S. A.; Aragó, J.; Gaita-Ariño, A. In Silico Molecular Engineering of Dysprosocenium-Based Complexes to Decouple Spin Energy Levels from Molecular Vibrations. *J. Phys. Chem. Lett.* **2019**, *10* (24), 7678−7683.

(17) (a) Hailes, R. L. N.; Musgrave, R. A.; Kilpatrick, A. F. R.; Russell, A. D.; Whittell, G. R.; O'Hare, D.; Manners, I. Ring-Opening Polymerisation of Low-Strain Nickelocenophanes: Synthesis and Magnetic Properties of Polynickelocenes with Carbon and Silicon Main Chain Spacers. *Chem. - Eur. J.* **2019**, *25* (4), 1044−1054. (b) Buchowicz, W.; Jerzykiewicz, L. B.; Krasińska, A.; Losi, S.; Pietrzykowski, A.; Zanello, P. Ansa -Nickelocenes by the Ring-Closing Metathesis Route: Syntheses, X-Ray Crystal Structures, and Physical Properties. *Organometallics* **2006**, *25* (21), 5076−5082.

(18) Hüerländer, D.; Kleigrewe, N.; Kehr, G.; Erker, G.; Fröhlich, R. Synthesis, Structural and Chemical Characterization of Unsaturated C4- and C10-Bridged Group-4 Ansa-Metallocenes Obtained through a Ring-Closing Olefin Metathesis Reaction. *Eur. J. Inorg. Chem.* **2002**, 2633−2642.

(19) Schaefer, C.; Scholz, G.; Gleiter, R.; Oeser, T.; Rominger, F. Endohedral Metallocenophanes of Rhodium and Cobalt. *Eur. J. Inorg. Chem.* **2005**, No. 7, 1274−1281.

(20) (a) Bhattacharyya, S. An Expedient, Mild, Reductive Method for the Preparation of Alkylferrocenes. *J. Chem. Soc., Dalton Trans.* **1996**, 4617−4619. (b) Talham, D. R.; Cowan, D. O. Synthesis of New Biferrocene Derivatives Containing Interannular Bridges and Their Mixed-Valence Analogs. *Organometallics* **1987**, *6* (5), 932−937. (c) Hillman, M.; Fujita, E.; Dauplaise, H.; Kvick, A.; Kerber, R. C. Bridged Ferrocenes. 10. Structural Phenomena. *Organometallics* **1984**, *3* (8), 1170−1177. (d) Hisatome, M.; Watanabe, J.; Yamakawa, K.; Iitaka, Y. [45](1,2,3,4,5)Ferrocenophane: Superferrocenophane. *J. Am. Chem. Soc.* **1986**, *108* (6), 1333−1334. (e) Hisatome, M.; Watanabe, J.; Kawajiri, Y.; Yamakawa, K.; Iitaka, Y. Synthesis and Molecular Structure of [45](1,2,3,4,5)Ferrocenophane ([4]-Superferrocenophane). *Organometallics* **1990**, *9* (2), 497−503.

(21) Ohba, S.; Saito, Y.; Kamiyama, S.; Kasahara, A. Structure of 1,3-(1,1'-Ruthenocenediyl)Propane, C13H14Ru, and 1,4-(1,1'-Ruthenocenediyl)Butane, C14H16Ru. *Acta Crystallogr., Sect. C: Cryst. Struct. Commun.* **1984**, *40* (1), 53−55.

(22) Kamiyama, S.; Kasahara, A. Synthesis of [3](1,1′)[3](3,3′)- and [4](1,1′)[4](3,3′)Ruthenocenophanes. *Bull. Chem. Soc. Jpn.* **1984**, *57* (3), 719−724.

(23) (a) Neese, F. The ORCA Program System. *Wiley Interdiscip. Rev.: Comput. Mol. Sci.* **2012**, *2* (1), 73−78. (b) Neese, F. Software Update: The ORCA Program System, Version 4.0. *Wiley Interdiscip. Rev.: Comput. Mol. Sci.* **2018**, *8* (1), No. e1327. (c) Neese, F.; Wennmohs, F.; Becker, U.; Riplinger, C. The ORCA Quantum Chemistry Program Package. *J. Chem. Phys.* **2020**, *152* (22), 224108. (d) Neese, F. Software Update: The ORCA Program System—Version 5.0. *WIREs Comput. Mol. Sci.* **2022**, *12* (5), e1606.

(24) Tao, J.; Perdew, J. P.; Staroverov, V. N.; Scuseria, G. E. Climbing the Density Functional Ladder: Nonempirical Meta-Generalized Gradient Approximation Designed for Molecules and Solids. *Phys. Rev. Lett.* **2003**, *91* (14), 146401.
(25) Aravena, D.; Neese, F.; Pantazis, D. A. Improved Segmented All-Electron Relativistically Contracted Basis Sets for the Lanthanides. *J. Chem. Theory Comput.* **2016**, *12* (3), 1148−1156.
(26) Weigend, F.; Ahlrichs, R. Balanced Basis Sets of Split Valence, Triple Zeta Valence and Quadruple Zeta Valence Quality for H to Rn: Design and Assessment of Accuracy. *Phys. Chem. Chem. Phys.* **2005**, *7* (18), 3297−3305.
(27) van Lenthe, E.; Baerends, E. J.; Snijders, J. G. Relativistic Total Energy Using Regular Approximations. *J. Chem. Phys.* **1994**, *101* (11), 9783−9792.
(28) (a) Neese, F.; Wennmohs, F.; Hansen, A.; Becker, U. Efficient, Approximate and Parallel Hartree-Fock and Hybrid DFT Calculations. A 'Chain-of-Spheres' Algorithm for the Hartree-Fock Exchange. *Chem. Phys.* **2009**, *356* (1−3), 98−109. (b) Izsák, R.; Neese, F. An Overlap Fitted Chain of Spheres Exchange Method. *J. Chem. Phys.* **2011**, *135* (14), 144105. (c) Dutta, A. K.; Neese, F.; Izsak, R. Accelerating the Coupled-Cluster Singles and Doubles Method Using the Chain-of-Sphere Approximation. *Mol. Phys.* **2018**, *116* (11), 1428−1434.
(29) Pantazis, D. A.; Neese, F. All-Electron Scalar Relativistic Basis Sets for the Lanthanides. *J. Chem. Theory Comput.* **2009**, *5* (9), 2229−2238.
(30) (a) Roca-Sabio, A.; Regueiro-Figueroa, M.; Esteban-Gómez, D.; de Blas, A.; Rodríguez-Blas, T.; Platas-Iglesias, C. Density Functional Dependence of Molecular Geometries in Lanthanide(III) Complexes Relevant to Bioanalytical and Biomedical Applications. *Comput. Theor. Chem.* **2012**, *999* (iii), 93−104.
(31) Malmqvist, P.-Å.; Roos, B. O. The CASSCF State Interaction Method. *Chem. Phys. Lett.* **1989**, *155* (2), 189−194.
(32) Noro, T.; Sekiya, M.; Koga, T. Sapporo-(DKH3)-NZP (n = D, T, Q) Sets for the Sixth Period s-d-and p-Block Atoms. *Theor. Chem. Acc.* **2013**, *132* (5), 1363.
(33) Stoychev, G. L.; Auer, A. A.; Neese, F. Automatic Generation of Auxiliary Basis Sets. *J. Chem. Theory Comput.* **2017**, *13* (2), 554−562.
(34) (a) Atanasov, M.; Ganyushin, D.; Sivalingam, K.; Neese, F. A Modern First-Principles View on Ligand Field Theory through the Eyes of Correlated Multireference Wavefunctions. *Struct. Bonding (Berlin)* **2011**, *143*, 149−220. (b) Lang, L.; Atanasov, M.; Neese, F. Improvement of Ab Initio Ligand Field Theory by Means of Multistate Perturbation Theory. *J. Phys. Chem. A* **2020**, *124* (5), 1025−1037.
(35) (a) Hess, B. A. Relativistic Electronic-Structure Calculations Employing a Two-Component No-Pair Formalism with External-Field Projection Operators. *Phys. Rev. A* **1986**, *33* (6), 3742−3748. (b) Douglas, M.; Kroll, N. M. Quantum Electrodynamical Corrections to the Fine Structure of Helium. *Ann. Phys.* **1974**, *82* (1), 89−155.
(36) (a) Chibotaru, L. F.; Ungur, L.; Soncini, A. The origin of nonmagnetic kramers doublets in the ground state of dysprosium triangles: Evidence for a toroidal magnetic moment. *Angew. Chem., Int. Ed.* **2008**, *47*, 4126−4129. (b) Ungur, L.; Van Den Heuvel, W.; Chibotaru, L. F. Ab initio investigation of the non-collinear magnetic structure and the lowest magnetic excitations in dysprosium triangles. *New J. Chem.* **2009**, *33*, 1224−1230. (c) Chibotaru, L. F.; Ungur, L.; Aronica, C.; Elmoll, H.; Pilet, G.; Luneau, D. Structure, magnetism, and theoretical study of a mixed-valence CoII3CoIII4 heptanuclear wheel: Lack of SMM behavior despite negative magnetic anisotropy. *J. Am. Chem. Soc.* **2008**, *130*, 12445−12455.
(37) Hanwell, M. D.; Curtis, D. E.; Lonie, D. C.; Vandermeersch, T.; Zurek, E.; Hutchison, G. R. Avogadro: An Advanced Semantic Chemical Editor, Visualization, and Analysis Platform. *J. Cheminf.* **2012**, *4* (1), 17.
(38) Macrae, C. F.; Edgington, P. R.; McCabe, P.; Pidcock, E.; Shields, G. P.; Taylor, R.; Towler, M.; van de Streek, J. Mercury: Visualization and Analysis of Crystal Structures. *J. Appl. Crystallogr.* **2006**, *39* (3), 453−457.
(39) (a) Momma, K.; Izumi, F. VESTA 3 for Three-Dimensional Visualization of Crystal, Volumetric and Morphology Data. *J. Appl. Crystallogr.* **2011**, *44* (6), 1272−1276. (b) Momma, K.; Izumi, F. VESTA: A Three-Dimensional Visualization System for Electronic and Structural Analysis. *J. Appl. Crystallogr.* **2008**, *41* (3), 653−658.
(40) Hisatome, M.; Kawajiri, Y.; Yamakawa, K.; Kozawa, K.; Uchida, T. Organometallic Compounds. *J. Organomet. Chem.* **1982**, *236* (3), 359−365.
(41) Hisatome, M.; Kawajiri, Y.; Yamakawa, K.; Harada, Y.; Iitaka, Y. A Package Compound of a Metal Atom with a Hydrocarbon [4] [4] [4] [4] [3](1,2,3,4,5)Ferrocenophane. *Tetrahedron Lett.* **1982**, *23* (16), 1713−1716.
(42) Aravena, D.; Ruiz, E. Spin Dynamics in Single-Molecule Magnets and Molecular Qubits. *Dalton Trans.* **2020**, *49* (29), 9916−9928.
(43) Ungur, L.; Chibotaru, L. F. Strategies toward High-Temperature Lanthanide-Based Single-Molecule Magnets. *Inorg. Chem.* **2016**, *55* (20), 10043−10056.
(44) Note: in the original article by Aravena (ref 10), the $k_{QT,i}$ was calculated from *g*-factors.
(45) (a) Lunghi, A.; Totti, F.; Sanvito, S.; Sessoli, R. Intra-Molecular Origin of the Spin-Phonon Coupling in Slow-Relaxing Molecular Magnets. *Chem. Sci.* **2017**, *8* (9), 6051−6059. (b) Escalera-Moreno, L.; Baldoví, J. J.; Gaita-Ariño, A.; Coronado, E. Spin States, Vibrations and Spin Relaxation in Molecular Nanomagnets and Spin Qubits: A Critical Perspective. *Chem. Sci.* **2018**, *9* (13), 3265−3275. (c) Staab, J. K.; Chilton, N. F. Analytic Linear Vibronic Coupling Method for First-Principles Spin-Dynamics Calculations in Single-Molecule Magnets. *J. Chem. Theory Comput.* **2022**, *18*, 6588−6599. (d) Kragskow, J. G. C.; Mattioni, A.; Staab, J. K.; Reta, D.; Skelton, J. M.; Chilton, N. F. Spin-Phonon Coupling and Magnetic Relaxation in Single-Molecule Magnets. *Chem. Soc. Rev.* **2023**, *52*, 4567−4585.
(46) Albino, A.; Benci, S.; Tesi, L.; Atzori, M.; Torre, R.; Sanvito, S.; Sessoli, R.; Lunghi, A. First-Principles Investigation of Spin-Phonon Coupling in Vanadium-Based Molecular Spin Quantum Bits. *Inorg. Chem.* **2019**, *58* (15), 10260−10268.
(47) (a) Briganti, M.; Santanni, F.; Tesi, L.; Totti, F.; Sessoli, R.; Lunghi, A. A Complete Ab Initio View of Orbach and Raman Spin-Lattice Relaxation in a Dysprosium Coordination Compound. *J. Am. Chem. Soc.* **2021**, *143* (34), 13633−13645. (b) Reta, D.; Kragskow, J. G. C.; Chilton, N. F. Ab Initio Prediction of High-Temperature Magnetic Relaxation Rates in Single-Molecule Magnets. *J. Am. Chem. Soc.* **2021**, *143* (15), 5943−5950.
(48) Bunting, P. C.; Atanasov, M.; Damgaard-Møller, E.; Perfetti, M.; Crassee, I.; Orlita, M.; Overgaard, J.; van Slageren, J.; Neese, F.; Long, J. R. A Linear Cobalt(II) Complex with Maximal Orbital Angular Momentum from a Non-Aufbau Ground State. *Science* **2018**, *362* (6421), No. eaat7319.

https://doi.org/10.1021/acs.inorgchem.3c02916
Inorg. Chem. 2023, 62, 17499−17509

Příloha 3: Kotrle, K.; Nemec, I.; Moncol, J.; Čižmár, E.; Herchel, R. 3d–4f Magnetic Exchange Interactions and Anisotropy in a Series of Heterobimetallic Vanadium(IV)–Lanthanide(III) Schiff Base Complexes. *Dalt. Trans.* 2021, *50* (39), 13883–13893. https://doi.org/10.1039/D1DT01944A.

Dalton Transactions

ROYAL SOCIETY OF CHEMISTRY

PAPER

View Article Online
View Journal | View Issue

Cite this: *Dalton Trans.*, 2021, **50**, 13883

3d–4f magnetic exchange interactions and anisotropy in a series of heterobimetallic vanadium(IV)–lanthanide(III) Schiff base complexes†

Kamil Kotrle, [a] Ivan Nemec, [a] Jan Moncol, [b] Erik Čižmár [c] and Radovan Herchel *[a]

Received 14th June 2021,
Accepted 23rd August 2021

DOI: 10.1039/d1dt01944a

rsc.li/dalton

A series of heterobimetallic Ln^{III}–V^{IV} compounds [Ln(VO)L$(NO_3)_3(H_2O)$] (Ln = Gd(**1**), Tb(**2**), Dy(**3**), and Er (**4**)) assembled by a Schiff base ligand (H_2L = *N*,*N*′-bis(1-hydroxy-2-benzylidene-6-methoxy)-1,7-diamino-4-azaheptane) were prepared and studied with experimental and theoretical methods. The single-crystal X-ray analysis revealed the change of the coordination number from 10 found in **1–3** to 9 confirmed in **4**. The DC magnetic data were fit with several Hamiltonians to extract the exchange and anisotropy parameters of complexes **1–4**. This investigation of magnetic properties was carried out using both DFT and CASSCF theoretical calculations. It was found out that exchange interactions in **1**, **3** and **4** are antiferromagnetic, while **2** has ferromagnetic exchange interactions. Moreover, the AC susceptibility measurements revealed the field-induced slow relaxation of magnetization in complexes **2** and **3** which is complicated by the presence of three relaxation channels. Nevertheless, these compounds belong to the first Tb^{III}–V^{IV} and Dy^{III}–V^{IV} single-molecule magnets in this class of compounds.

Introduction

Single-molecule magnets (SMMs) are a class of materials that have sparked a lot of interest since their discovery in the 1990s. Such materials with properties like slow relaxation of magnetization, magnetic hysteresis, and superparamagnetic-like behavior are promising for many areas of practical use, such as memory devices or quantum computing.[1] The story began with Mn12ac, the first single-molecule magnet,[2] a large 12-nuclear cluster composed of Mn^{III} and Mn^{IV} cores with a complicated magnetic exchange interaction structure. The success of this compound led to the preparation of many similar compounds with the aim to reach an even bigger ground spin state than S = 10 for Mn12ac and to further explore this newly discovered phenomenon. Some notable examples of this class of single-molecule magnets are, for example, smaller $\{Fe_8\}$[3] or $\{Mn_4\}$[4] clusters but also extremely large complexes, such as $\{Mn_{84}\}$.[5] Regardless of how interesting those polynuclear systems were, the next breakthrough in this field was not achieved by increasing the ground spin state but rather by increasing the magnetic anisotropy of one central atom. Thus, the proper choice of the central ion is crucial as it turned out to be the case of complex $[TbPc_2]^-$, where Tb has an advantage over any 3rd row element by having a much larger spin–orbit coupling.[6] This also started the era of single-ion magnets, containing only one paramagnetic ion, relying solely on magnetic anisotropy. However, one of the compounds that pushed the limits of blocking temperature was $\{[(Me_3Si)_2N]_2(THF)Tb\}_2(\mu\text{-}\eta^2\text{:}\eta^2\text{-}N_2)^-$, a terbium dimer bridged by the N_2^{3-} radical.[7] This compound is unique also due to its very strong magnetic exchange coupling that contributes strongly to its high blocking temperature (T_B = 14 K). It is worth mentioning that there are also other single-ion magnets with high blocking temperatures, specifically a family of complexes with a pentagonal bipyramidal shape that has blocking temperatures in the range of 14–20 K,[8] and the recently discovered organometallic double-deckers with cyclopentadienyl derivates[9] that were able to reach blocking temperatures up to 80 K.

Although the current best performing compounds, in terms of blocking temperatures and energetic barriers, are mononuclear single-ion magnets, polynuclear systems are still an

[a]*Department of Inorganic Chemistry, Faculty of Science, Palacký University, 17. listopadu 12, CZ-771 46 Olomouc, Czech Republic. E-mail: radovan.herchel@upol.cz; http://www.agch.upol.cz*
[b]*Department of Inorganic Chemistry, Faculty of Chemical and Food Technology, Slovak University of Technology in Bratislava, Bratislava SK-81237, Slovakia*
[c]*Institute of Physics, Faculty of Science, P.J. Šafárik University in Košice, Park Angelinum 9, SK-041 54 Košice, Slovakia*

†Electronic supplementary information (ESI) available. CCDC 2089692–2089695. For ESI and crystallographic data in CIF or other electronic format see DOI: 10.1039/d1dt01944a

interesting topic for advanced studies. Magnetic anisotropy has its origin in the splitting of magnetic energetic levels. Those in the case of single-ion magnets have their origins mainly from the contributions of spin–orbit coupling, crystal field splitting, and electron repulsion.[10] In polynuclear compounds, one additional important parameter is the magnetic exchange interaction. It creates additional splitting of energy levels that can affect magnetic anisotropy in multiple ways as the magnetic exchange has both isotropic and anisotropic contributions. Interestingly, the magnetic exchange interaction was found to suppress quantum tunneling of magnetization in the ground state, which improves the SMM properties.[11] The isotropic exchange interaction between two spins is usually defined by Hamiltonian:

$$\hat{H} = -J(\vec{S}_1 \cdot \vec{S}_2) \quad (1)$$

although other definitions are found in the literature. This approach works well for 3rd row metals because the orbital contribution to the total angular moment in the ground states is usually quenched, which allows us to treat them as spin-only magnetic systems. This is, however, impossible for lanthanide ions (except for Gd^{III}) with much larger spin–orbit coupling, whose total angular moment (**J**) is composed of spin (**S**) and orbital (**L**) contribution.

$$\mathbf{J} = \mathbf{S} + \mathbf{L} \quad (2)$$

Another interesting difference between the 3d and 4f elements is in the strength of a magnetic exchange.[12] Usually, the exchange interactions are a lot stronger in polynuclear complexes comprising d-block metals than f-block metals, especially lanthanides. This different behavior arises from the shielding of the unpaired electrons in (n-2)f-orbitals by the valence ns-orbitals of the lanthanides. For this reason, it is interesting to utilize pairing lanthanides with d-elements to achieve larger magnetic exchange interactions between paramagnetic centers. Because a vast number of 3d–4f complexes have been prepared to this day, only compounds related to the studied compounds will be mentioned here. These complexes belong to a large family of "salen type" Schiff bases, which are known to easily form complexes with 3d elements and lanthanides, with $\{N_2O_2\}$ and usually $\{O_4\}$ coordination modes, respectively, as the latter also depends on other substituents. In addition, this type of compound is most abundant with Cu^{II} and Ni^{II}, and to a lesser extent, which we also mention in our article, with V^{IV}. Considering the magnetism of such compounds, we would like to stress that the Cu^{II} and V^{IV} ions both contribute with $S = 1/2$, which also makes them magnetically isotropic by their nature. The Ni^{II} ions can be either diamagnetic (a square planar shape of the coordination polyhedron) or paramagnetic with $S = 1$ contribution (penta-, hexa-, and heptacoordinations) and non-negligible magnetic anisotropy. Unlike Ln^{III}–Cu^{II} complexes, which have been studied very intensively, there are only a few complexes of Ln^{III}–V^{IV} with ligands and geometry of central atoms as in salen-type complexes (Table 1).

Table 1 Magnetically characterized Ln^{III}–V^{IV} complexes with Schiff base ligands[a]

Formula	J (cm^{-1})	Ref.
$[(VO)Gd(L1)]NO_3{\cdot}n(H_2O)$	−1.6	13
$[(VO)Gd(L2)(NO_3)_3(H_2O)]$	1.5	14
$[(VO)Gd(L3)(NO_3)_3(CH_3COCH_3)]$	−2.6	14
$[(VO)Tb(L3)(NO_3)_3(CH_3COCH_3)]$	0.06(1)	15
$[(VO)Dy(L3)(NO_3)_3(CH_3COCH_3)]$	0.28(1)	15
$[(VO)Ho(L3)(NO_3)_3(CH_3COCH_3)]$	−0.19(1)	15
$[(VO)Er(L3)(NO_3)_3(CH_3COCH_3)]$	−0.02(1)	15

[a] The structures of the ligands are depicted in Fig. S1.†

It has been noted that while in Ln^{III}–Cu^{II} complexes, the magnetic exchange interactions are ferromagnetic in all found cases (Table S1†), the situation is different in Ln^{III}–V^{IV} and both ferromagnetic and antiferromagnetic interactions are possible for those complexes. It is very likely that this is caused by different locations of unpaired electrons in the d-orbitals in the d^1 and d^9 electronic configurations. The Tb^{III}–Cu^{II} and Dy^{III}–Cu^{II} complexes often exhibited properties of SMMs; however, this behavior has not been observed for their vanadium analogs yet.

Therefore, we report here the synthesis and characterization of four Ln^{III}–V^{IV} compounds $[Ln(VO)L(NO_3)_3(H_2O)]$ (Ln = Gd (**1**), Tb(**2**), Dy(**3**), and Er(**4**)) assembled by a Schiff base ligand (H_2L = *N*,*N*′-bis(1-hydroxy-2-benzylidene-6-methoxy)-1,7-diamino-4-azaheptane). The in-depth study of their magnetic properties supported by DC and AC magnetometry and by the theoretical methods performed at the DFT and CASSCF levels of theory is focused on a better understanding of the magnetic exchange coupling between 3d and 4f metals. This can be helpful for designing better performing SMMs based on either 3d–4f dinuclear or polynuclear complexes.

Experimental

General methods

The synthesis of the ligand H_2L, intermediate [VO(L)] (Scheme S1†), and complexes $[Ln(VO)L(NO_3)_3(H_2O)]$ was inspired by previously published methods.[16] The reagents were purchased from commercial sources. The CHN elementary analysis was done using a Thermo Scientific Flash 2000 analyzer. The IR spectra were recorded using a Jasco FT/IR-4700 spectrometer. The XPD patterns were measured using a Rigaku MiniFlex600 diffractometer. The temperature-dependent (T = 1.8–300 K, B = 0.2 T) and field-dependent (B = 0–7 T, T = 2, 5 and 15 K) magnetization and AC susceptibility (in the frequency range 0.1–1000 Hz) measurements were performed using a Quantum Design MPMS3 SQUID magnetometer. Nascent powder samples were firmly pressed in a polypropylene VSM capsule and for such measurements, no subtraction of the sample holder contribution is necessary. The magnetic data were corrected for the diamagnetism of the constituent atoms ($\chi_{dia}/10^{-12}$ m^3 $mol^{-1} = -5 \times M_r$).[17]

The data collection for **3** was made using a Stoe StadiVari diffractometer with a Pilatus3R 300 K hybrid pixel array detector and a microfocused Incoatec HB IμS 2.0 X-ray source (Ag Kα). The data collection for **1**, **2** and **4** was done using an XtaLAB Synergy-I diffractometer with a HyPix3000 hybrid pixel array detector and a microfocused PhotonJet-I X-ray source (Cu Kα). All the crystal structures were solved using the SHELXT program[18] and refined by the full matrix least-squares procedure with Shelxl (ver. 2018/3) in OLEX2 (version 1.3).[19] The multi-scan absorption corrections were applied using the program LANA[20] or CrysAlisPro 1.171.40.82a.[21] The molecular structures and the packing diagram were drawn with MERCURY.[22] The structure shape analysis was done with the help of the SHAPE software.[23] The resulting crystal structures were deposited in the Cambridge Structural Database under the following CSD codes: **1** (2089692), **2** (2089693), **3** (2089694), and **4** (2089695).†

Crystal structure refinement. All non-hydrogen atoms were refined anisotropically. The hydrogen atoms were placed into the calculated positions and they were included in the riding-model approximation with $U_{iso} = 1.2U_{eq}$(C) or $1.5U_{eq}$ (CH_3 and OH) and d(C–H) = 0.95–0.98 Å. The hydrogen atoms of the aqua ligands were located from the difference map and they were further refined and restrained. The crystallographic data are summarized in ESI, Table S2.† The non-routine aspects of the refinement are as follows: in **1–3**, two $-CH_2-$ groups from the aliphatic part of the Schiff base ligand are disordered over two positions (occupation factor ratios, major : minor site = 61 : 39 in **1**, 68 : 32 in **2**, and 54 : 46 in **3**). In **4**, one of the nitrate ligands is disordered over two positions with the major site coordinating the Er atom in a monodentate fashion (occupation factor 0.66). The nitrate ligand of the minor site (occupation factor 0.34) coordinates the Er atom in a bidentate manner.

Synthesis

H_2L ligand. In 10 ml of methanol, *o*-vaniline (6 mmol) and propylenediamine (3 mmol) were added and left at reflux temperature overnight. The resulting yellow solution was evaporated under low pressure and the resulting reddish dense oily liquid was overlayed with 10 ml of diethylether. After treating this mixture with ultrasound, a yellow powder that precipitated was filtered under reduced pressure and washed with diethylether (yield 81%). This product was then used without further purification.

Analytics: calc. for H_2L – $C_{19}H_{22}N_2O_4$, M_{mol} = 342.39 – C 66.65%, H 6.48%, N 8.18%. Found: C 66.65%, H 6.48%, N 8.18%.

[VO(L)]. In 15 ml of methanol, H_2L (1 mmol) and $VO(acac)_2$ (1 mmol) were mixed and left for one hour at reflux temperature. The resulting green precipitate was filtered under reduced pressure and washed with diethylether (yield 77%). This product was used without further purification.

Analytics: calc. for [VO(L)] – $C_{19}H_{20}N_2O_5V$, M_{mol} = 407.31 – C 55.75%, H 5.42%, N 6.84%. Found: C 55.25%, H 4.98%, N 6.59%.

[Ln(VO)L$(NO_3)_3(H_2O)$] (1–4). In 10 ml of acetonitrile, [VO(L)] (0.1 mmol) was suspended and the mixture was slightly heated. Then, 10 ml of acetone with $Ln(NO_3)_3{\cdot}xH_2O$ (0.15 mmol) was added dropwise. During this, the solution changed color from yellow to green. The resulting mixture was stirred for an hour and then filtered and left to stand. Over several days, green crystals appeared in the solution, which were filtered and washed with diethylether.

Analytics: calc. for [Gd(VO)L$(NO_3)_3(H_2O)$] (**1**) – $C_{19}H_{22}N_2O_{15}$VGd, M_{mol} = 768.59 – C 29.69%, H 2.62%, N 9.11%. Found: C 29.21%, H 2.79%, N 8.40%. IR mid in cm^{-1} (ATR): 3568 (w), 3423 (w), 2951 (w), 1625 (s), 1568 (w), 1499 (m), 1465 (s), 1420 (m), 1341 (m), 1274 (s), 1224 (m), 1060 (m), 1027 (m), 988 (m), 939 (m), 855 (m), 735 (m), 635 (w).

Analytics: calc. for [Tb(VO)L$(NO_3)_3(H_2O)$] (**2**) – $C_{19}H_{22}N_2O_{15}$VTb, M_{mol} = 770.27 – C 29.63%, H 2.62%, N 9.09%. Found: C 29.58%, H 2.76%, N 8.76%. IR mid in cm^{-1} (ATR): 3571 (w), 3421 (w), 2950 (w), 1625 (s), 1568 (w), 1500 (m), 1466 (s), 1421 (m), 1341 (m), 1275 (s), 1225 (m), 1060 (m), 1026 (m), 988 (m), 939 (m), 855 (m), 735 (m), 635 (w).

Analytics: calc. for [Dy(VO)L$(NO_3)_3(H_2O)$] (**3**) – $C_{19}H_{22}N_2O_{15}$VDy, M_{mol} = 773.84 – C 29.49%, H 2.61%, N 9.05%, C/N = 3.26. Found: C 29.38%, H 2.78%, N 8.82% C/N = 3.33. IR mid in cm^{-1} (ATR): 3576 (w), 3421 (w), 2951 (w), 1625 (s), 1568 (w), 1503 (m), 1466 (s), 1432 (m), 1341 (m), 1275 (s), 1224 (m), 1060 (m), 1026 (m), 988 (m), 939 (m), 856 (m), 735 (m), 636 (w).

Analytics: calc. for [Er(VO)L$(NO_3)_3(H_2O)$] (**4**) – $C_{19}H_{22}N_2O_{15}$VEr, M_{mol} = 778.62 – C 29.31%, H 2.59%, N 8.99%. Found: C 29.45%, H 2.72%, N 8.79%. IR mid in cm^{-1} (ATR): 3590 (w), 3397 (w), 2952 (w), 1623 (s), 1568 (w), 1505 (m), 1467 (s), 1433 (m), 1320 (m), 1273 (s), 1225 (m), 1059 (m), 1026 (m), 985 (m), 939 (m), 856 (m), 735 (m), 637 (w).

Theoretical calculations

The state average complete active space self-consistent field (SA-CASSCF) wave function calculations were done with OpenMOLCAS 19.11[24] for **2–4** in such a way that only one paramagnetic metal ion was preserved, and all the others were replaced by diamagnetic ions (Tb, Dy, and Er → Lu and V → Ti). The active space was defined by five d-orbitals/seven f-orbitals and the respective number of electrons for vanadium or lanthanide ions (V^{IV}: 1e, Tb^{III}: 8e, Dy^{III}: 9e, and Er^{III}: 11e). The RASSCF method was used for the CASSCF calculations with the following numbers of multiplets: 7 septets, 140 quintets, 113 triplets, and 123 singlets for Tb^{III}, 21 sextets, 224 quartets, and 490 doublets for Dy^{III}, 35 quartets and 112 doublets for Er^{III}, and 5 doublets for V^{IV}. In the cases of Tb^{III}, Er^{III} and V^{IV}, all the multiplets were included in the spin–orbit RASSI-SO procedure, while the number of states for Dy^{III} was limited as follows: 21 sextets, 128 quartets, and 130 doublets. ANO-RCC-VQZP was used for paramagnetic lanthanides, ANO-RCC-VTZP was applied for d-metals, nitrogen atoms and oxygen atoms, ANO-RCC-VDZP for carbon, and ANO-RCC-VDZ for hydrogen atoms.[25]

The hydrogen atom position optimizations, broken symmetry DFT calculations, and CASSCF/NEVPT2 calculations were performed with the help of the ORCA 4.2 software,[26] with

the use of the Libint library.[27] The hydrogen-normalized structure was obtained by optimization using the BP86 DFT functional,[28] with the SARC2-ZORA-QZV basis for dysprosium[29] and ZORA-TZVP bases from Ahlrichs def2 set for all the other elements,[30] except C and H, in which the ZORA-SVP basis was used. All of the bases were utilized for the ZORA relativistic correction.[31] The RIJCOSX approximation was used to speed up the calculation,[32] whereas SARC/J was used as an auxiliary basis. Broken symmetry DFT calculations were performed with similar settings, except with the usage of the TPSSh functional.[33]

The CASSCF/NEVPT2 energy difference between the states with (N) and (N − 2) multiplicity calculations in ORCA was calculated with DKH relativistic correction.[34] The basis used was SARC2-DKH-QZVP for lanthanides and the other bases used were similar to those in DFT, but with DKH utilization. In addition, for CASSCF, the coulombic auxiliary basis def2/SVP-C was used for all atoms except lanthanides, where an automatically generated basis from the AutoAux[35] ORCA function was used. Within these calculations, 8 roots for multiplicities 8 and 6 were calculated for **2**, 7 roots for multiplicities 7 and 5 were calculated for **3**, and 13 roots for multiplicities 5 and 3 were calculated for **4**. Active space was defined by seven 4f-orbitals of lanthanide ion and one 3d-orbital corresponding to a single occupied magnetic orbital (SOMO) of vanadium. The number of electrons was the sum of electrons in the valence shell of Ln^{III} and V^{IV} ions. The Avogadro 1.2.0[36] and VESTA 3[37] software were used for the analysis and visualization of the computational results.

Results and discussion

Synthesis and characterization

In all the complexes that were prepared by the above-described methods, we have observed that adding an excess of lanthanide salt is necessary for dissolving most of the [VO(L)] reactant to prevent contamination of the product. Crystals suitable for X-ray analysis were formed from the solution in a matter of hours.

The composition and purity were verified by CHN analysis, which had sufficiently good results for all complexes of the series. The IR spectra (Fig. S2†) and XPD patterns (Fig. S3–S6†) are almost identical for all compounds, which suggest the isostructurality of the whole series, which was however proven not true, as we further discuss in the structure description part.

Crystal structure description

Compounds **1–3** are isomorphic and crystallize in the monoclinic space group $P2_1/c$. Compound **4** also crystallizes in the monoclinic space group $P2_1/c$ (basic crystallographic data are summarized in ESI Table S2†) but its crystal structure differs and cannot be considered to be formally isostructural with **1–3** (*vide infra*). The crystal structures of **1–4** consist of complex molecules having the general formula $[Ln(VO)L(NO_3)_3(H_2O)]$. The V^{IV} ion is coordinated by two nitrogen and two oxygen atoms of the L^{2-} ligand forming an equatorial plane of the deformed octahedron (continuous shape measures indexes for O_h: 0.996 in **1**, 0.975 in **2**, 0.979 in **3**, and 1.001 in **4**), which has in the axial positions two oxygen atoms from the vanadyl group and the aqua ligand (Fig. 1). The shortest metal–ligand bond length for the V^{IV} ion is observed in the vanadyl group (d(V–O3) = 1.57–1.59 Å), while the longest ones are observed for the bonds with the aqua ligands (d(V–O4) = 2.28–2.32 Å). The Ln central atoms in **1–3** are decacoordinated by ten oxygen donor atoms. Four of them are provided by the outer chelating pocket of the L^{2-} ligands (two phenolate and two methoxy oxygen atoms) and the remaining six originate from three nitrate ligands, which coordinate Ln atoms in a bidentate fashion (Fig. 1a). The coordination polyhedron adopts a very distorted shape close to the tetradecahedron (2 : 6 : 2) (C_{2v}, (continuous shape measures indexes are 2.909 in **1**, 2.673 in **2** and 2.681 in **3**); however, also the distortions calculated for the sphenocorona (C_{2v}) and staggered dodecahedron (2 : 6 : 2, D_2) coordination polyhedra adopt similar values (see ESI, Tables S3 and S4†). In **4**, the structure of the complex molecule is affected by a positional disorder of one of the nitrate ligands. In the major site (66%), the Er atom is nonacoordinated because one of the nitrate ligands coordinates the metal atom in a monodentate manner (Fig. 1b). The coordination polyhedron has a shape closest to the spherical capped square antiprism (C_{4v}, continuous shape measure index is 1.631). In the minor site (34%), the nitrate ligand coordinates the Er atom similarly as in **1–3** in a bidentate manner, thus forming a decacoordinate coordination polyhedron. However, of note here is that the Er–O11 bond is significantly longer (2.89(2) Å) than the similar bonds in **1–3** (Ln–O11 = 2.64–2.69 Å, Table 2).

The shortest Ln–O bond lengths are observed in the bonds involving phenolate oxygen atoms (Ln–O1/2 = 2.31–2.39 Å). Whereas the methoxy oxygen atoms form longer bonds (Ln–O5/6 = 2.45–2.54 Å), the shorter bonds are observed for heavier Ln atoms in agreement with the lanthanide contraction (Table 2). The nitrate ligands form Ln–O bonds with a wide range of bond lengths ranging between 2.26 and 2.69 Å (Table 2). Again, the trend corresponding to the lanthanide contraction can be observed but remarkably with one exception: the Ln–O11 bond lengths are longer for heavier Ln atoms (Table 2). The intradimer Ln···V distances are similar in both crystal structures (3.494(1) in **1**, 3.4823(7) Å in **2**, 3.4741(6) Å in **3**, and 3.4357(9) Å in **4**).

The packing in the crystal structures of **1–3** is the same and the main structural motif can be ascribed to a ladder-like supramolecular substructure of the complex molecules interconnected by strong O–H···O hydrogen bonds (d(O···O) = 2.80–3.25 Å) formed between the hydrogen atoms of the coordinated aqua ligands and the nitrate ligands of the neighboring molecules (Fig. 1e). In **4**, the above-mentioned reorganization of the coordination polyhedron influenced the observed intermolecular interactions. The overall packing is very similar to that in **1–3**, but the change in the denticity of one of the nitrate ligands from two (in **1–3**) to one (**4**) led to a reorientation of the hydrogen atoms of the aqua ligand. One forms contact with the oxygen atom of the monodentately bound nitrate ligand, while the second forms an intra-

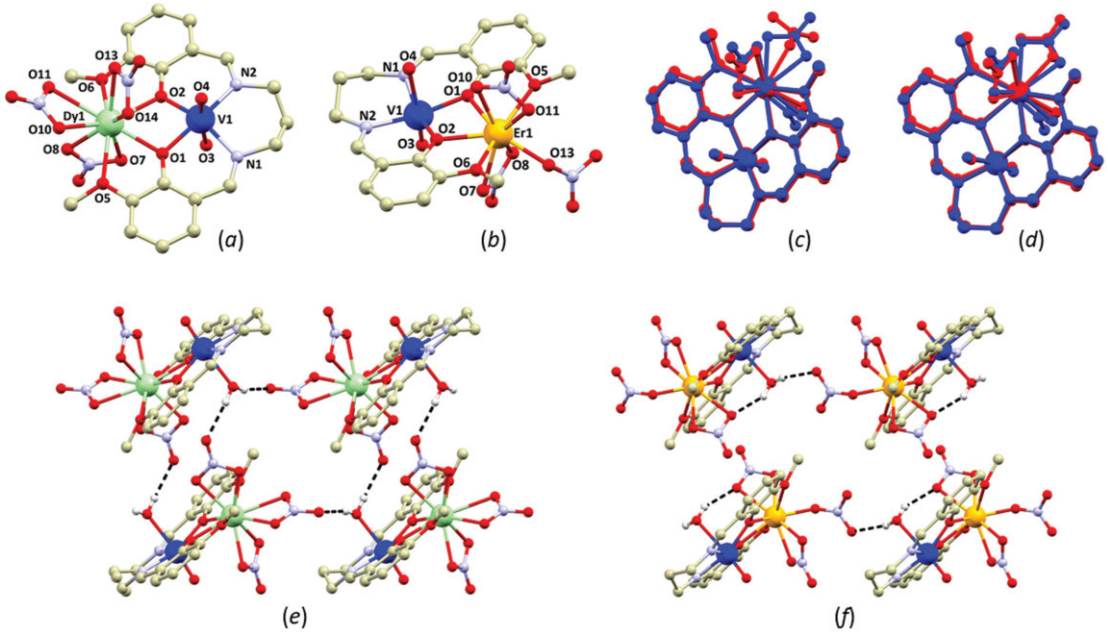

Fig. 1 The molecular structures of **3** (a) and **4** (b) with the major site of the disordered NO_3^- ligand in the structure of **4** shown. An overlay of **3** (blue color) and **4** (red color) showing the major (c) or minor (d) site of the disordered NO_3^- ligand in the structure of **4**. A perspective view down the *b* crystallographic axis of the fragments of the crystal structures of **3** (e) and **4** (major site of disorder shown, f). The hydrogen atoms (except for those involved in hydrogen bonding, hydrogen bonding was depicted by black dashed lines) were omitted for clarity.

Table 2 The metal–ligand bond lengths in **1–4**. All the distances are listed in Å

M–L	**1** (Gd)	**2** (Tb)	**3** (Dy)	**4** (Er)
V1–O1	1.973(5)	1.995(3)	1.991(2)	1.983(3)
V1–O2	1.992(5)	1.978(3)	1.9755(19)	1.974(3)
V1–N1	2.074(7)	2.084(4)	2.078(3)	2.089(4)
V1–N2	2.087(6)	2.080(4)	2.082(2)	2.082(4)
V1–O3	2.321(6)	2.321(3)	2.287(2)	2.308(4)
V1–O4	1.578(6)	1.584(3)	1.592(2)	1.586(4)
Ln–O1	2.394(5)	2.380(3)	2.3716(18)	2.317(3)
Ln–O2	2.386(5)	2.373(3)	2.3541(18)	2.314(3)
Ln–O5	2.531(5)	2.520(3)	2.5051(19)	2.448(4)
Ln–O6	2.536(5)	2.525(3)	2.5206(19)	2.461(4)
Ln–O7	2.504(6)	2.487(3)	2.476(2)	2.441(4)
Ln–O8	2.421(5)	2.411(3)	2.390(2)	2.376(4)
Ln–O10	2.484(6)	2.457(4)	2.430(2)	2.301(14)[a], 2.35(3)[b]
Ln–O11	2.649(8)	2.677(5)	2.692(2)	2.89(2)[b]
Ln–O13	2.453(5)	2.434(3)	2.409(2)	2.395(4)
Ln–O14	2.488(6)	2.477(4)	2.472(2)	2.425(4)

[a] Major disorder site in **4**. [b] Minor disorder site in **4**.

molecular O–H···O hydrogen bond with the coordinated nitrate anion. The overall structural motif is then the one-dimensional chain formed along the *c* crystallographic axis (Fig. 1f). The parameters of the non-covalent interactions in **1–4** are summarized in greater detail in ESI (Table S5 and Fig. S7–S10†).

We would like to dedicate the last paragraph of this section to the discussion of the powder diffraction data as measured for **1–4**. At very first glance, one can see that the experimentally obtained powder diffraction patterns of **1–4** (Fig. S3–S6†) are almost identical, thus confirming the isostructurality of **1–4**. However, as was discussed above, the structures of **1–3** and **4** differ significantly. Therefore, even when the powder diffraction data seemingly confirm the isostructurality of the studied compounds, one should be very careful about drawing the conclusions.

Magnetic measurements

The temperature and field-dependent DC magnetic measurements were performed on complexes **1–4** and the results are shown in Fig. 2.

The values of effective magnetic moments of the prepared compounds **1–4** at 300 K, expressed in the unit of Bohr magneton, are 9.77 (**1**), 9.72 (**2**), 10.60 (**3**), and 9.39 (**4**) and are close to the theoretical values for uncoupled V^{IV}–Ln^{III} systems, which are 8.12 (V-Gd), 9.87 (V-Tb), 10.79 (V-Dy) and 9.74 (V-Er). The magnetic moments stay constant on temperature lowering down to approximately 50 K, where μ_{eff} starts to decrease, which is most likely caused by the zero-field splitting induced by the ligand-field and the spin–orbit interactions, and also due to the magnetic interaction between paramagnetic ions. The only exception is gadolinium, which is slightly rising through almost the whole temperature range, which can

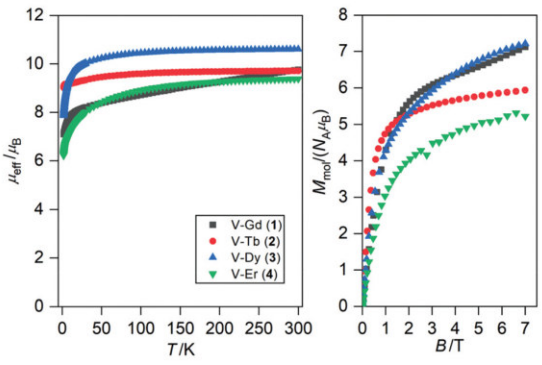

Fig. 2 Magnetic data of **1–4**. Temperature dependence of the effective magnetic moment μ_{eff} calculated from the mean susceptibility measured at B = 0.2 T and the isothermal magnetizations measured at T = 2 K.

be attributed to temperature-independent paramagnetism or unknown impurity. The isothermal magnetizations displayed in Fig. 2 show values between 5.2 and 7.2 at the maximum magnetic field of 7 T and these values are lower than the theoretical field saturation values 8.0 (V-Gd), 10.0 (V-Tb), 11.0 (V-Dy) and 10.0 (V-Er), which confirm the significant magnetic anisotropy of these complexes.

For the interpretation of the magnetic data of complex **1**, containing only Gd^{III} and V^{IV} ions, spin Hamiltonian formalism is an appropriate approach. Therefore, the magnetic data were analyzed using eqn (3)

$$\hat{H} = -J_{Gd-V}(\vec{S}_V\vec{S}_{Gd}) + \mu_B\vec{B}(\overline{\overline{g}}_V\vec{S}_V + \overline{\overline{g}}_{Gd}\vec{S}_{Gd}) \quad (3)$$

where the isotropic exchange and Zeeman terms were introduced. The best fit parameters are J_{Gd-V} = −1.41 cm^{-1} and g_{Gd} = g_V = 2.017, with added temperature-independent magnetism χ_{TIM} = 150 × 10^{-9} m^3 mol^{-1} – Fig. S11.† This high amount of χ_{TIM} might point out the presence of the ferromagnetic impurity in the sample, which can explain the rise of the magnetic moment. However, this behavior was found reproducible for independently prepared batches of **1**. In addition, a very slight sign of nonlinear behavior was found in high-temperature magnetic data (Fig. S12†), which might suggest the presence of a ferromagnetic impurity, possibly Gd_2O_3, in such a small amount, that we were not able to detect by other analytical methods.

For **2**, **3** and **4**, an approach applied for Ln^{III}–Ni^{II} complexes was adopted and implemented.[38] We have used the following Hamiltonian for the fitting of magnetization and magnetic susceptibility:

$$\hat{H} = -J^{JM-S}_{Ln-V}(\vec{S}_V\vec{J}_{Ln}) + D_{Ln}\left(\hat{J}_{z,Ln}{}^2 + \frac{\hat{J}_{Ln}{}^2}{3}\right) + E_{Ln}\left(\hat{J}_{x,Ln}{}^2 - \hat{J}_{y,Ln}{}^2\right) + \mu_B\vec{B}(\overline{\overline{g}}_V\vec{S}_V + \overline{\overline{g}}_{Ln}\vec{J}_{Ln}) \quad (4)$$

where the ground state multiplet of Ln^{III} is described in $|JM\rangle$ basis, its zero-field splitting is defined by D_{Ln} and E_{Ln} (which can be viewed as Stevens operator coefficients for B^0_2 and B^2_2),[39] and the exchange coupling is defined between pseudospin J_{Ln} (J_{Tb} = 6, J_{Dy} = J_{Er} = 15/2) and spin S_V = 1/2. Here we considered the anisotropic values of g_{xy} and g_z of g_{Ln} and the isotropic g_V fixed to a value of 1.95. The magnetic data were fit with the POLYMAGNET program[40] and the best-fits are depicted in Fig. S13–S15,† and the best-fit values of the exchange interactions were J^{JM-S}_{Tb-V} = 0.245 cm^{-1} for **2**, J^{JM-S}_{Dy-V} = −0.254 cm^{-1} for **3**, and J^{JM-S}_{Er-V} = −0.140 cm^{-1} for **4**. The $|D_{Ln}|$ values were found in the range 1.5 to 7.5 cm^{-1} (Table S6†) and generally, the D_{Ln} and E_{Ln} values are comparable to those calculated from CASSCF calculations and SINGLE_ANISO analysis (Table S7,† *vide infra*).

Next, a second method was employed, in which the $|LS\rangle$ basis is used for Ln^{III} with the advantage that in this case, the exchange interaction is defined as an exchange between true spins. Hence, the following Hamiltonian was postulated

$$\hat{H} = -J^{LS-S}_{Ln-V}(\vec{S}_V\vec{S}_{Ln}) + \sum_{j=1}^{2S_{Ln}}\lambda_{j,Ln}(\sigma\vec{L}_{Ln}\vec{S}_{Ln})^j + \sigma D_{Ln}\left(\hat{L}_{z,Ln}{}^2 + \frac{\hat{L}_{Ln}{}^2}{3}\right) + \sigma E_{Ln}(\hat{L}_{x,Ln}{}^2 - \hat{L}_{y,Ln}{}^2) + \mu_B\vec{B}(\overline{\overline{g}}_V\vec{S}_V + \overline{\overline{g}}_{Ln}\vec{S}_{Ln} + \sigma\vec{L}_{Ln}) \quad (5)$$

where λ_{Ln} is the spin–orbit splitting parameter, defined by default in the PHI software,[41] σ is the orbital reduction factor due to covalency, and D_{Ln} and E_{Ln} are parameters that act on the orbital angular momentum. The Zeeman term parameters were set as $g_{L,Ln}$ = 1, $g_{S,Ln}$ = 2, and g_V was again fixed to 1.95. The analyses of the magnetic data of **2–4** were performed in PHI and the best-fits are shown in Fig. S16–S18.† The best-fit values of the magnetic exchange interaction are J^{LS-S}_{Tb-V} = 0.775 cm^{-1} for **2**, J^{LS-S}_{Dy-V} = −0.698 cm^{-1} for **3**, and J^{LS-S}_{Er-V} = −1.56 cm^{-1} for **4**. Note, that the J-values are reported according to the Hamiltonian in eqn (1). The fit D_{Ln}, E_{Ln}, and σ parameters are listed in Table S6,† and it holds that $D_{Ln} = 3B^0_2\theta_2$ and $E_{Ln} = B^0_0\theta_2$, where B^q_k is the Stevens operator parameter and θ is the operator equivalent factor for the corresponding ions (−2/45 for Tb^{III}, −2/135 for Dy^{III}, and 2/495 for Er^{III}).

To summarize, both methods as defined by eqn (4) and (5) and are suitable to describe the static magnetic properties of compounds **2–4**. It seems that the two main parameters, D and E, as analogues of Stevenson operators, are sufficient to capture the effect of ligand-field and spin orbit coupling at the lowest energy levels populated within the experimental temperature window. Furthermore, these approaches enabled us to obtain some insight into the exchange interactions of lanthanides without having to use quantum chemical calculations. Interestingly, the ferromagnetic coupling was established between V^{IV} and Tb^{III} ions in **2**, while antiferromagnetic exchange was found in Ln^{III} Kramers containing ions in compounds **3** and **4**.

Moreover, the AC magnetic susceptibility measurements were also performed for **2–4**. First, the AC susceptibility was measured at the lowest temperature as a function of the magnetic field in order to identify the zero-field or field-induced SMM behavior of these compounds. Compound **4** showed no

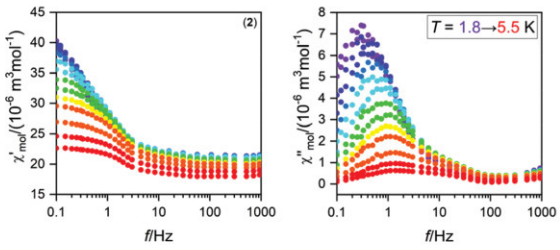

Fig. 3 AC susceptibility data of **2**. The temperature dependence of real and imaginary molar susceptibilities at B = 0.3 T.

out-of-phase susceptibility signal (Fig. S19†) in contrast to compounds **2**–**3** (Fig. 3 and Fig. S20†), for which a larger static magnetic field was necessary to suppress the fast relaxation mechanism. Compounds **2** and **3** show a similar behavior; there are two evident slow relaxation processes located below 1 Hz and below 10 Hz, whereas the third relaxation process emerges above 1000 Hz only for **2**. Despite our effort, it was not possible to find the physically reasonable fits of AC susceptibility data with the Debye model, most probably due to overlapping of the relaxation channels. Nevertheless, these experiments confirmed the presence of the slow relaxation of the magnetization. Hence, the first examples of Tb^{III}–V^{IV} and Dy^{III}–V^{IV} field-induced SMMs are reported.

Theoretical calculations

The aim of the theoretical calculations was to assess various approaches for the evaluation of the magnetic exchange between 3d and 4f metals in the presented series of compounds **1**–**4**. All the discussed calculations were done on molecular geometries obtained from experimental X-ray structures, in which only the positions of hydrogen atoms were optimized by DFT with the BP86 functional (Table S8†). First, we utilized the standard method for molecular magnetism by employing the POLY_ANISO module of the OpenMOLCAS software developed by Chibotaru and Ungur.[42] This approach utilizes the state-averaged complete active-space self-consistent field (SA-CASSCF) calculations separately done for each paramagnetic ion within the complex to properly capture the multireference character of these metal ions. Next, the SINGLE_ANISO module evaluates the zero-field splitting energies and crystal-field parameters. Finally, the POLY_ANISO module calculates the energy levels, zero-field parameters, and magnetic properties for coupled systems by introducing the exchange interaction according to the Linnes model and also the dipolar interactions. Such a workflow is now dominantly used to analyze lanthanide-containing polynuclear compounds. Therefore, the CASSCF calculations were done for V^{IV} and Tb^{III}, Dy^{III}, and Er^{III} ions in **2**–**4**, which provided the information of energy splitting of the respective atomic terms of ^2D and $^7F_6$, $^6H_{15/2}$, and $^4I_{15/2}$ due to the ligand field and the spin–orbit interactions. As expected, the ground state properties of V^{IV} are well defined by the g-tensor with the g-components slightly lower than the free-electron value of 2.0023 and showing small anisotropy (Table S9†). The principal axes of ground-state doublets are shown in Fig. S21.† The calculations for Tb^{III} ions in **2** showed two almost energetically degenerate levels, followed by two other excited states located at ~92 cm^{-1} (Table S10†). As the Tb^{III} ion is a non-Kramers ion, the tunneling gap (Δ_{tun}) within these pairs of states serves as an indicator of the quantum tunneling of the magnetization.[43] The magnetization blocking barrier is depicted in Fig. 4. The Δ_{tun} of the ground pseudo-doublet is relatively large; therefore, the relaxation of the magnetization should be fast.

In the case of the Dy^{III} ion of **3**, the first three Kramers doublets show the significant axial type magnetic anisotropy ($g_z \gg g_{x,y}$) but the values of $g_{x,y}$ are larger than 0.03, which indicates a significant predisposition for the quantum tunneling of the magnetization as evidenced also by the relatively large values of transition magnetic moment matrix elements (Table S11†). The principal axes of ground-state doublets are shown in Fig. S22.† Moreover, the first excited state is rather close (23 cm^{-1}) which certainly contributes to the reduction of the potential for large magnetization reversal barriers. This is also visualized in the plot of the magnetization blocking barrier for **3** (Fig. 5).

Finally, the properties of Er^{III} ion of **4** were calculated resulting in a reasonable energy gap of ~48 cm^{-1} in the first excited state; however, the ground state has significant rhombic parameters ($g_{x,y}$ > 1.6) and the first excited state has the easy-plane type magnetic anisotropy (Table S12† and Fig. 6). The principal axes of the ground-state doublets are shown in Fig. S23.† Such a drastic change in the magnetic properties can be attributed to the changes in the oblate electron densities of Tb^{III} and Dy^{III} ions to the prolate electron density of Er^{III} ions[44] and also to the slight changes in the coordination polyhedron of Er^{III} in contrast to other lanthanides within this series.

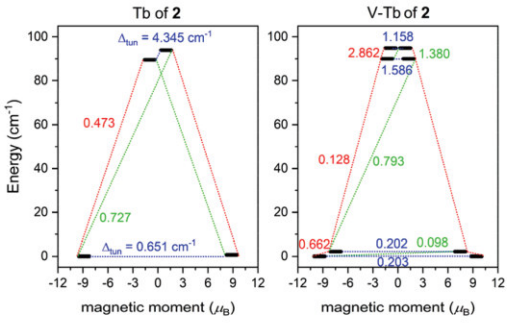

Fig. 4 Magnetization blocking barrier in **2** calculated for Tb^{III} by SINGLE_ANISO (left) and for Tb^{III}–V^{IV} by POLY_ANISO using J^{exch}_{Tb-V} = +0.716 cm^{-1} and J^{dip}_{Tb-V} = −0.0232 cm^{-1} (right) zoomed to the lowest energy levels. The numbers presented in the plot represent the corresponding matrix element of the transversal magnetic moment (for values larger than 0.1, an efficient relaxation mechanism is expected) and Δ_{tun} shows the tunneling gap of the indicated doublets.

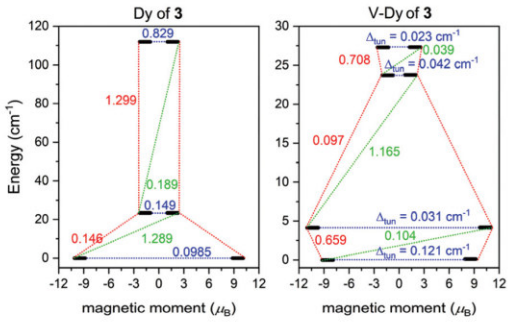

Fig. 5 Magnetization blocking barrier in **3** calculated for Dy^{III} by SINGLE_ANISO (left) and for Dy^{III}–V^{IV} by POLY_ANISO using J^{exch}_{Dy-V} = −1.69 cm^{-1} and J^{dip}_{Dy-V} = −0.0575 cm^{-1} (right) zoomed to the lowest energy levels. The numbers presented in the plot represent the corresponding matrix element of the transversal magnetic moment (for values larger than 0.1, an efficient relaxation mechanism is expected) and Δ_{tun} shows the tunneling gap of the indicated doublets.

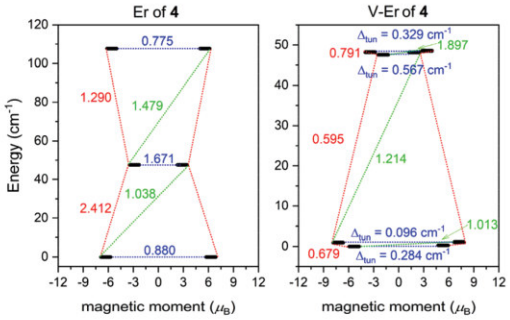

Fig. 6 Magnetization blocking barrier in **4** calculated for Er^{III} by SINGLE_ANISO (left) and for Er^{III}–V^{IV} by POLY_ANISO using J^{exch}_{Er-V} = −0.736 cm^{-1} and J^{dip}_{Er-V} = −0.0552 cm^{-1} (right) zoomed to the lowest energy levels. The numbers presented in the plot represent the corresponding matrix element of the transversal magnetic moment (for values larger than 0.1, an efficient relaxation mechanism is expected) and Δ_{tun} shows the tunneling gap of the indicated doublets.

Afterward, we fitted the experimental magnetic data (temperature and field-dependent magnetization) for **2–4** with the homemade routine in cooperation with the POLY_ANISO module, and thus we were able to estimate the V^{IV}–Ln^{III} magnetic interactions in this series of the compounds. The results of the analysis are depicted in Fig. S24† and the exchange was found to be ferromagnetic for Tb^{III}–V^{IV} with J^{exch}_{Tb-V} = +0.716 cm^{-1} in contrast to Dy^{III}–V^{IV} and Er^{III}–V^{IV} in which antiferromagnetic exchange was determined with J^{exch}_{Dy-V} = −1.69 cm^{-1} and J^{exch}_{Er-V} = −0.736 cm^{-1}. The variation in the magnetic exchange can be assigned to the variation in f-orbitals that are involved in mutual interactions. The POLY_ANISO module also included the dipolar interaction (J^{dip}) between Ln^{III}–V^{IV} ions into the computation and their exact values were subsequently determined as: with J^{dip}_{Tb-V} = −0.0232 cm^{-1}, J^{dip}_{Tb-V} = −0.0575 cm^{-1} and J^{dip}_{Er-V} = −0.0552 cm^{-1}. Thus, the dipolar exchange is much weaker than the magnetic superexchange in this series of 3d–4f compounds. The knowledge about the Ln^{III}–V^{IV} exchange enabled us to construct also the magnetization blocking barrier for compounds **2–4** that are shown in Fig. 4–6. The ferromagnetic Tb^{III}–V^{IV} interactions resulted in the formation of two Kramers doublets separated by ~2 cm^{-1} and the relatively small values of the transversal magnetic moment (~0.2 – Fig. 4), which indicate the possibility of the field-induced slow relaxation of the magnetization. However, the transversal magnetic moment between the first and second Kramers doublets in the opposite direction of the magnetic moment is close to 0.1, which suggests the speeding up of the relaxations. The antiferromagnetic Dy^{III}–V^{IV} led to a decrease in the magnetic moment of the ground state pseudo-doublet and the formation of the next pseudo-doublet at ~4 cm^{-1} – Fig. 5. The Δ_{tun} of both of these two doublets is relatively small and thus we can expect the observation of the slow relaxation of the magnetization at least after applying a non-zero static magnetic field. However, the situation of **4** in the antiferromagnetic Er^{III}–V^{IV} exchange is worse because the value of Δ_{tun} and the transversal magnetic moments among two analogous pseudo-doublets are larger, indicating the predisposition for a much faster relaxation of the magnetization (Fig. 6).

The next theoretical method applied to the presented series is DFT, which is frequently used for evaluating magnetic exchange interaction through the broken-symmetry (BS) approach for metal complexes. For **1**, due to the nature of Gd^{III} and V^{IV} ions, orbital contributions to the ground state can be neglected and a multireferential approach is not necessary anymore. Therefore, the BS approach can be used to obtain the values of the exchange interactions between metals. We have utilized Ruiz's approach:[45]

$$J_{Ruiz} = 2\Delta/[(S_1 + S_2) \times (S_1 + S_2 + 1)]$$

and Yamaguchi's approach:[46]

$$J_{Yam} = 2\Delta/(\langle S^2\rangle_{HS} - \langle S^2\rangle_{BS})$$

where

$$\Delta = E_{BS} - E_{HS}$$

With these approaches, we managed to evaluate J_{Ruiz} = −1.59 cm^{-1} and J_{Yam} = −4.55 cm^{-1}. Thus, the coupling is antiferromagnetic in nature, which is in concordance with the experimental findings.

Although using the BS-DFT approach is not generally advised for other lanthanides, mainly due to their multireferential nature, there have been some attempts to utilize it for lanthanide compounds, whose authors claim to be successful. One such example is the calculation of exchange interactions between lanthanides and N_2^{3-} radicals.[47] Another study was performed at the DFT theory level with the included simulation of the location of β electrons in each of the possible f-orbitals of the Tb(III) ion with the help of orbital location.[48] The authors came to an interesting conclusion, that in every

configuration, the exchange interaction was estimated to be a similar value. If this is universally valid, then the BS approach might be a method that can provide us with approximate values with the advantage of low-cost computation costs. We have used the same computational settings as for the above-mentioned complex **1** and obtained these results: J_{Ruiz} = 0.00635 cm^{-1} and J_{Yam} = 0.0166 cm^{-1} for **2**, J_{Ruiz} = −0.819 cm^{-1} and J_{Yam} = −1.96 cm^{-1} for **3** and J_{Ruiz} = −2.46 cm^{-1} and J_{Yam} = −4.93 cm^{-1} for **4**. These exchange interaction parameters cannot be directly compared with ones calculated with POLY_ANISO, as POLY_ANISO exploits pseudospins for lanthanides within the Lines model, while the BS-DFT approach utilizes real spin values. It is yet another approximation, as the spin–orbit coupling is neglected in this approach. However, we can see that the BS-DFT calculated *J*-values correctly predicted the nature of the magnetic exchange in the Ln^{III}–V^{IV} series. In addition, it must be mentioned that the BS-DFT values are also comparable to values determined by the analysis of the DC magnetic data with eqn (5) (Table S6†). Both methods resulted in a stronger antiferromagnetic exchange of Er^{III}–V^{IV} in **4** than of Dy^{III}–V^{IV} in **2**. In our opinion, great care must be taken when attempting to use the BS-DFT method for such systems, and preferably a large-scale benchmarking would be helpful to see which DFT functional and other computational settings are desirable to acquire qualitative and quantitative agreements with the experiments.

Finally, to address the multireferential nature of lanthanide ions, we have also tried a different approach, where the lowest energy levels are calculated by CASSCF with the help of the ORCA software with the active space comprising all seven 4f-orbitals and one singly occupied magnetic d-orbital (SOMO) from V^{IV}. The multiple low-lying roots (7 for **2**, 8 for **3**, and 13 for **4**) were calculated separately for maximal (M_{max}) and (M_{max} − 2) multiplicities to simulate both the configurations of the unpaired electrons in the d-orbital of V(IV) and therefore the model ferromagnetic and antiferromagnetic coupling between V(IV) and Ln(III). Such a method was already suggested by Costes *et al.*[49] The exchange interaction constant was then obtained from the energy differences between the configurations simulating the electron spins in the ferromagnetic and antiferromagnetic couplings by using the Yamaguchi method. The authors who developed this method have claimed that the interaction constants should be similar through all energetic states. However, we came to a similar conclusion from the results (Table 3). It seems that CASSCF is overestimating the high spin configuration as all interactions in complexes **2–4** came out as ferromagnetic, which contradicts the experiments. With the aim to improve the level of the theory, we have repeated the calculations with CASSCF/NEVPT2 (Table S13†), but unfortunately, this method has not led to results more compatible with the experimental results. However, there is still more space for improvements as there are even more advanced methods for treating MRCI, which can give state energies closer to reality; for example, DDCI3, which was suggested as the most fitting method for exchange interactions in the copper acetate dimer model calculations.[50] However, such methods are very expensive and using them on lanthanide systems can be problematic.

Table 3 CASSCF energy difference between the maximal multiplicity states (modelling ferromagnetic interaction) and the M_{max} − 2 states (modelling antiferromagnetic interaction) in cm^{-1} and the exchange interaction constant obtained by the Yamaguchi approach

State	Δ*E* (2)	Δ*E* (3)	Δ*E* (4)	$J_{(Tb–V)}$ (2)	$J_{(Dy–V)}$ (3)	$J_{(Er–V)}$ (4)
1	5.2	4.7	3.3	1.50	1.57	1.64
2	3.2	3.9	2.8	0.92	1.30	1.39
3	3.3	4.9	4.5	0.95	1.64	2.24
4	3.2	4.2	1.9	0.92	1.40	0.94
5	3.4	3.5	2.2	0.98	1.17	1.09
6	5.4	3.5	2.3	1.55	1.17	1.49
7	2.3	3.5	2.8	0.67	1.17	1.39
8	5.2		4.1		0.57	2.04
9			3.7			1.84
10			4.5			2.24
11			4.0			1.99
12			3.0			1.39
13			3.6			1.79
Avg.				**1.07**	**1.25**	**1.65**

Conclusions

Four new heterobimetallic Ln^{III}–V^{IV} complexes were characterized structurally, and their magnetic properties were scrutinized by various experimental and theoretical methods. It has been shown that complexes **1–3** are isostructural, whereas **4** differs in the coordination mode of one nitrate ligand resulting in a decrease in the coordination number from 10 to 9. The experimental magnetic data were analyzed by various Hamiltonians revealing the antiferromagnetic coupling in **1**, **3** and **4**, while ferromagnetic coupling is present in **2**. Special attention was paid to the 3d–4f exchange with lanthanides having an angular magnetic momentum. Therefore, multiple methods of characterization of magnetic exchange interactions were successfully employed for **2–4**, either based on |JM⟩ or |LS⟩ basis describing the Ln^{III} ion properties. Moreover, three different theoretical methods were employed based on (i) the CASSCF calculation accompanied by the SINGLE_ANISO and POLY_ANISO modules, (ii) the BS-DFT approach, and the (iii) CASSCF and CASSCF/NEVPT2 calculations with active space comprising both f and d orbitals. These results are compared for $J_{Ln–V}$ (cm^{-1}) here:

Method	**2** (Tb^{III}–V^{IV})	**3** (Dy^{III}–V^{IV})	**4** (Er^{III}–V^{IV})
$\|JM\rangle_{Ln} - \|S\rangle_V$	0.245	−0.254	−0.140
$\|LS\rangle_{Ln} - \|S\rangle_V$	0.775	−0.698	−1.56
CASSCF/POLY_ANISO	0.716	−1.69	−0.736
BS-DFT (Ruiz)	0.00635	−0.819	−2.46
BS-DFT (Yamaguchi)	0.0166	−1.96	−4.93
CASSCF/$^{M}\Gamma$ and $^{M-2}\Gamma$ levels	1.07	1.25	1.65
NEVPT2/$^{M}\Gamma$ and $^{M-2}\Gamma$ levels	1.23	0.48	0.03

There is some discrepancy among these methods; on the other hand, for the lanthanides, the exchange interaction con-

stant J_{ex} is usually small compared to that of the d-block elements. Therefore, the requirements of methods to estimate its value correctly are very strict. Therefore, further research must be performed to establish a theoretical method capable of correctly predicting the magnetic exchange in 3d–4f or 4f polynuclear compounds solely based on the structural information. This would enable faster progress in this field of molecular magnetism. To comment on the applied theoretical methods, the most reliable is the utilization of CASSCF together with SINGLE_ANISO and POLY_ANISO modules in combination with the experimental magnetic data.

Furthermore, AC susceptibility confirmed the field-induced slow relaxation of magnetization in **2** and **3**. Thus, these complexes belong to the first Tb^{III}–V^{IV} and Dy^{III}–V^{IV} single-molecule magnets in this class of compounds, which make a new endeavor for similar molecular systems desirable.

Author contributions

Kamil Kotrle: conceptualization, investigation, formal analysis, and writing – original draft. Ivan Nemec: formal analysis, investigation, visualization, and writing – original draft. Jan Moncol: formal analysis, investigation, and writing – review & editing. Erik Čizmár: formal analysis, investigation, and writing – review & editing. Radovan Herchel: conceptualization, investigation, methodology, software, formal analysis, supervision, visualization, and writing – original draft, review & editing.

Conflicts of interest

There are no conflicts of interest to declare.

Acknowledgements

Funding for this project was provided by the research grants IGA_PrF_2020_016 and IGA_PrF_2021_009 (Czech Republic) and APVV-18-0197, APVV-19-0087, and VEGA 1/0639/18 (Slovakia).

Notes and references

1 (*a*) M. Mannini, F. Pineider, P. Sainctavit, C. Danieli, E. Otero, C. Sciancalepore, A. M. Talarico, M.-A. Arrio, A. Cornia, D. Gatteschi and R. Sessoli, *Nat. Mater.*, 2009, **8**, 194–197; (*b*) K. Katoh, H. Isshiki, T. Komeda and M. Yamashita, *Chem. – Asian J.*, 2012, **7**, 1154–1169.

2 A. Caneschi, D. Gatteschi, R. Sessoli, A. L. Barra, L. C. Brunel and M. Guillot, *J. Am. Chem. Soc.*, 1991, **113**, 5873–5874.

3 W. Wernsdorfer, *Science*, 1999, **284**, 133–135.

4 W. Wernsdorfer, N. Aliaga-Alcalde, D. N. Hendrickson and G. Christou, *Nature*, 2002, **416**, 406–409.

5 A. J. Tasiopoulos, A. Vinslava, W. Wernsdorfer, K. A. Abboud and G. Christou, *Angew. Chem., Int. Ed.*, 2004, **43**, 2117–2121.

6 N. Ishikawa, M. Sugita, T. Ishikawa, S. Koshihara and Y. Kaizu, *J. Am. Chem. Soc.*, 2003, **125**, 8694–8695.

7 J. D. Rinehart, M. Fang, W. J. Evans and J. R. Long, *J. Am. Chem. Soc.*, 2011, **133**, 14236–14239.

8 (*a*) Y.-C. Chen, J.-L. Liu, L. Ungur, J. Liu, Q.-W. Li, L.-F. Wang, Z.-P. Ni, L. F. Chibotaru, X.-M. Chen and M.-L. Tong, *J. Am. Chem. Soc.*, 2016, **138**, 2829–2837; (*b*) Y.-S. Ding, N. F. Chilton, R. E. P. Winpenny and Y.-Z. Zheng, *Angew. Chem., Int. Ed.*, 2016, **55**, 16071–16074; (*c*) J. Liu, Y.-C. Chen, J. Liu, V. Vieru, L. Ungur, J. Jia, L. F. Chibotaru, Y. Lan, W. Wernsdorfer, S. Gao, X.-M. Chen and M. Tong, *J. Am. Chem. Soc.*, 2016, **138**, 5441–5450.

9 (*a*) C. A. P. Goodwin, F. Ortu, D. Reta, N. F. Chilton and D. P. Mills, *Nature*, 2017, **548**, 439–442; (*b*) F. Guo, B. M. Day, Y. Chen, M. Tong, A. Mansikkamäki and R. A. Layfield, *Science*, 2018, **362**, 1400–1403; (*c*) K. Randall McClain, C. A. Gould, K. Chakarawet, S. J. Teat, T. J. Groshens, J. R. Long and B. G. Harvey, *Chem. Sci.*, 2018, **9**, 8492–8503.

10 M. Zlatar, M. Gruden, O. Y. Vassilyeva, E. A. Buvaylo, A. N. Ponomarev, S. A. Zvyagin, J. Wosnitza, J. Krzystek, P. Garcia-Fernandez and C. Duboc, *Inorg. Chem.*, 2016, **55**, 1192–1201.

11 S. Demir, I. R. Jeon, J. R. Long and T. D. Harris, *Coord. Chem. Rev.*, 2015, **289-290**, 149–176.

12 (*a*) S. K. Langley, D. P. Wielechowski, V. Vieru, N. F. Chilton, B. Moubaraki, L. F. Chibotaru and K. S. Murray, *Chem. Sci.*, 2014, **5**, 3246–3256; (*b*) R. Sessoli and A. K. Powell, *Coord. Chem. Rev.*, 2009, **253**, 2328–2341; (*c*) V. Chandrasekhar, A. Dey, S. Das, M. Rouzières and R. Clérac, *Inorg. Chem.*, 2013, **52**, 2588–2598; (*d*) E. Colacio, J. E. Ruiz-Sanchez, F. J. White and E. K. Brechin, *Inorg. Chem.*, 2011, **50**, 52.

13 M. Sakamoto, T. Ishikawa, Y. Nishida, Y. Sadaoka, A. Matsumoto, Y. Fukuda, M. Sakai, M. Ohba, H. Sakiyama and H. Ōkawa, *J. Alloys Compd.*, 1996, **238**, 23–27.

14 S. K. Singh and G. Rajaraman, *Dalton Trans.*, 2013, **42**, 3623.

15 T. Ishida, R. Watanabe, K. Fujiwara, A. Okazawa, N. Kojima, G. Tanaka, S. Yoshii and H. Nojiri, *Dalton Trans.*, 2012, **41**, 13609.

16 J.-P. Costes, F. Dahan, B. Donnadieu, J. Garcia-Tojal and J.-P. Laurent, *Eur. J. Inorg. Chem.*, 2001, **2001**, 363–365.

17 R. Boča, *Theoretical Foundations of Molecular Magnetism*, Elsevier, Amsterdam, The Netherlands, 1999.

18 G. M. Sheldrick, *Acta Crystallogr., Sect. A: Found. Adv.*, 2015, **71**, 3.

19 O. Dolomanov, L. J. Bourhis, R. Gildea, J. A. Howard and H. Puschmann, *J. Appl. Crystallogr.*, 2009, **42**, 339.

20 J. Koziskova, F. Hahn, J. Richter and J. Kozisek, *Acta Chim. Slovaca*, 2016, **9**, 136–140.

21 *CrysAlisPro 1.171.40.82a*, Rigaku Oxford Diffraction, 2020.

22 C. F. Macrae, I. Sovago, S. J. Cottrell, P. T. A. Galek, P. McCabe, E. Pidcock, M. Platings, G. P. Shields, J. S. Stevens, M. Towler and P. A. Wood, *J. Appl. Crystallogr.*, 2020, **53**, 226.

23 (*a*) S. Alvarez, *Dalton Trans.*, 2005, 2209–2233; (*b*) S. Alvarez, P. Alemany, D. Casanova, J. Cirera, M. Llunell and D. Avnir, *Coord. Chem. Rev.*, 2005, **249**, 1693–1708; (*c*) D. Casanova, P. Alemany, J. M. Bofill and S. Alvarez, *Chem. – Eur. J.*, 2003, **9**, 1281–1295.

24 I. F. Galván, M. Vacher, A. Alavi, C. Angeli, F. Aquilante, J. Autschbach, J. J. Bao, S. I. Bokarev, N. A. Bogdanov, R. K. Carlson, L. F. Chibotaru, J. Creutzberg, N. Dattani, M. G. Delcey, S. S. Dong, A. Dreuw, L. Freitag, L. M. Frutos, L. Gagliardi, F. Gendron, A. Giussani, L. González, G. Grell, M. Guo, C. E. Hoyer, M. Johansson, S. Keller, S. Knecht, G. Kovačević, E. Källman, G. Li Manni, M. Lundberg, Y. Ma, S. Mai, J. P. Malhado, P. Å. Malmqvist, P. Marquetand, S. A. Mewes, J. Norell, M. Olivucci, M. Oppel, Q. M. Phung, K. Pierloot, F. Plasser, M. Reiher, A. M. Sand, I. Schapiro, P. Sharma, C. J. Stein, L. K. Sørensen, D. G. Truhlar, M. Ugandi, L. Ungur, A. Valentini, S. Vancoillie, V. Veryazov, O. Weser, T. A. Wesołowski, P.-O. Widmark, S. Wouters, A. Zech, J. P. Zobel and R. Lindh, *J. Chem. Theory Comput.*, 2019, **15**, 5925–5964.

25 B. O. Roos, R. Lindh, P.-Å. Malmqvist, V. Veryazov and P.-O. Widmark, *Chem. Phys. Lett.*, 2005, **409**, 295–299.

26 (*a*) F. Neese, *Wiley Interdiscip. Rev.: Comput. Mol. Sci.*, 2018, 8; (*b*) F. Neese, *Wiley Interdiscip. Rev.: Comput. Mol. Sci.*, 2012, **2**, 73–78.

27 E. F. Valeev, *Libint: A library for the evaluation of molecular integrals of many-body operators over Gaussian functions 2.0.7*, http://libint.valeyev.net/.

28 A. D. Becke, *Phys. Rev. A*, 1988, **38**, 3098–3100.

29 D. Aravena, F. Neese and D. A. Pantazis, *J. Chem. Theory Comput.*, 2016, **12**, 1148–1156.

30 F. Weigend and R. Ahlrichs, *Phys. Chem. Chem. Phys.*, 2005, **7**, 3297–3305.

31 E. van Lenthe, E. J. Baerends and J. G. Snijders, *J. Chem. Phys.*, 1994, **101**, 9783–9792.

32 (*a*) F. Neese, F. Wennmohs, A. Hansen and U. Becker, *Chem. Phys.*, 2009, **356**, 98–109; (*b*) A. K. Dutta, F. Neese and R. Izsák, *Mol. Phys.*, 2018, **116**, 1428–1434; (*c*) R. Izsák and F. Neese, *J. Chem. Phys.*, 2011, **135**, 144105.

33 J. Tao, J. P. Perdew, V. N. Staroverov and G. E. Scuseria, *Phys. Rev. Lett.*, 2003, **91**, 146401.

34 (*a*) M. Douglas and N. M. Kroll, *Ann. Phys.*, 1974, **82**, 89–155; (*b*) B. A. Hess, *Phys. Rev. A*, 1986, **33**, 3742–3748.

35 G. L. Stoychev, A. A. Auer and F. Neese, *J. Chem. Theory Comput.*, 2017, **13**, 554–562.

36 M. D. Hanwell, D. E. Curtis, D. C. Lonie, T. Vandermeersch, E. Zurek and G. R. Hutchison, *J. Cheminf.*, 2012, **4**, 17.

37 K. Momma and F. Izumi, *J. Appl. Crystallogr.*, 2011, **44**, 1272–1276.

38 M. Antkowiak, M. C. Majee, M. Maity, D. Mondal, M. Kaj, M. Lesiów, A. Bieńko, L. Kronik, M. Chaudhury and G. Kamieniarz, *J. Phys. Chem. C*, 2021, **125**, 11182–11196.

39 K. W. H. Stevens, *Proc. Phys. Soc., London, Sect. A*, 1952, **65**, 209–215.

40 R. Boča and R. Herchel, *Program POLYMAGNET 2006–2021*.

41 N. F. Chilton, R. P. Anderson, L. D. Turner, A. Soncini and K. S. Murray, *J. Comput. Chem.*, 2013, **34**, 1164–1175.

42 (*a*) L. Ungur, M. Thewissen, J.-P. Costes, W. Wernsdorfer and L. F. Chibotaru, *Inorg. Chem.*, 2013, **52**, 6328–6337; (*b*) L. F. Chibotaru, L. Ungur, C. Aronica, H. Elmoll, G. Pilet and D. Luneau, *J. Am. Chem. Soc.*, 2008, **130**, 12445–12455; (*c*) L. F. Chibotaru, L. Ungur and A. Soncini, *Angew. Chem., Int. Ed.*, 2008, **47**, 4126–4129.

43 J. Wang, J. J. Zakrzewski, M. Zychowicz, V. Vieru, L. F. Chibotaru, K. Nakabayashi, S. Chorazy and S.-I. Ohkoshi, *Chem. Sci.*, 2021, **12**, 730–741.

44 J. D. Rinehart and J. R. Long, *Chem. Sci.*, 2011, **2**, 2078.

45 E. Ruiz, J. Cano, S. Alvarez and P. Alemany, *J. Comput. Chem.*, 1999, **20**, 1391–1400.

46 K. Yamaguchi, S. Yamanaka, M. Nishino, Y. Takano, Y. Kitagawa, H. Nagao and Y. Yoshioka, *Theor. Chem. Acc.*, 1999, **102**, 328–345.

47 V. Vieru, N. Iwahara, L. Ungur and L. F. Chibotaru, *Sci. Rep.*, 2016, **6**, 24046.

48 M. Ferbinteanu, A. Stroppa, M. Scarrozza, I. Humelnicu, D. Maftei, B. Frecus and F. Cimpoesu, *Inorg. Chem.*, 2017, **56**, 9474–9485.

49 F. Cimpoesu, F. Dahan, S. Ladeira, M. Ferbinteanu and J.-P. Costes, *Inorg. Chem.*, 2012, **51**, 11279–11293.

50 R. Emi Maurice, K. Sivalingam, D. Ganyushin, N. Guih, C. De Graaf and F. Neese, *Inorg. Chem.*, 2011, **50**, 6229–6236.

Příloha 4: Kotrle, K.; Nemec, I.; Antal, P.; Petrželová, K.; Čižmár, E.; Herchel, R. 2-Formylphenoxyacetic Acid Schiff Bases: A Promising Ligand Scaffold for Readily Available Trigonal Prismatic Co(II) Single-Ion Magnets. *Inorg. Chem. Front.* 2023, *10* (24), 7319–7332. https://doi.org/10.1039/D3QI01691A.

INORGANIC CHEMISTRY
FRONTIERS

RESEARCH ARTICLE

View Article Online
View Journal

Cite this: DOI: 10.1039/d3qi01691a

2-Formylphenoxyacetic acid Schiff bases: a promising ligand scaffold for readily available trigonal prismatic Co(II) single-ion magnets†

Kamil Kotrle, [a] Ivan Nemec, [a] Peter Antal,[a] Kamila Petrželová, [a] Erik Čižmár [b] and Radovan Herchel *[a]

This article presents a series of six mononuclear Co(II) complexes **1–6** featuring ligands derived from a hexadentate Schiff base family, originating from the condensation of (2-formylphenoxy)acetic acid with various diamines. Notably, these complexes uniquely prefer a trigonal prism geometry, presenting a novel approach to synthesizing complexes with this distinctive shape. The compounds were characterized by elemental analysis, FT-IR spectroscopy, and single-crystal and powder XRD techniques. Furthermore, the magnetism was investigated by DC and AC magnetic measurements and also complemented by X-band EPR spectroscopy. The results reveal that the prepared complexes behave as field-induced single-molecule magnets, characterized by a substantial negative axial zero-field splitting D-parameter and spin reversal energetic barrier U_{eff} reaching values up to 72 K. The theoretical methods based on CASSCF/NEVPT2 calculations were applied to rationalize their magnetic properties. Moreover, these complexes hold promising potential for further functionalization, offering opportunities to enhance their properties, particularly towards developing zero-field single-molecule magnets as evidenced by the slow relaxation of magnetization in zero static magnetic field observed for the zinc-diluted complex **1Zn**.

Received 23rd August 2023,
Accepted 26th October 2023
DOI: 10.1039/d3qi01691a
rsc.li/frontiers-inorganic

Introduction

In recent years, there has been significant development in the field of single-molecule magnets (SMMs), a class of materials that exhibit intriguing magnetic properties, including magnetic hysteresis and slow relaxation of magnetization at the molecular level. This progress began with discovering and studying these effects in large manganese polynuclear clusters, such as the renowned Mn12ac.[1] Subsequent research has explored a wide range of systems, with one notable subclass of SMMs known as single-ion magnets. These magnets consist of only one paramagnetic ion,[2] thereby minimizing the influence of any magnetic exchange interactions. Among this class of compounds, an important group, particularly within the first transition metals row, comprises complexes containing Co(II) as the central ion. Co(II) exhibits interesting magnetic properties due to its spin $S = 3/2$, making it a Kramers ion, and its relatively large spin–orbit coupling resulting from its occupation of the d-orbital.[3]

Although leveraging spin–orbit coupling is key to designing single-molecule magnets with significant magnetic anisotropy, another crucial characteristic of 3d single ion magnets is ligand field splitting, which is usually stronger than spin–orbit coupling.

In six-coordinated Co(II) complexes, the orbital contribution is usually substantial due to the nature of the ground state, which is T_{1g} for an octahedron (O_h), and $^4E'$ for a trigonal prism (D_{3h}). It is common for the (pseudo)octahedral symmetry to result in large and positive values of the axial zero-field splitting parameter D.[4] Positive D-parameter frequently leads to the easy-plane type anisotropy, and only significant rhombicity (E/D ratio) can provide the axial type anisotropy.[5] In the case of trigonal prism symmetry, the D-parameter is typically large and negative.[4] The relationship between the D-parameter and magnetic anisotropy barrier for half-integer spin complexes, such as Co(II), is defined as:[6]

$$U_{eff} = |D|\left(S^2 - \frac{1}{4}\right) \quad (1)$$

It is worth noting that a significant number of complexes with a trigonal prismatic shape exhibit slow relaxation of magnetization even in the absence of an external magnetic field, earning them the designation of zero-field SMMs. Table 1 lists

[a]Department of Inorganic Chemistry, Faculty of Science, Palacký University, 17. listopadu 12, CZ-771 46 Olomouc, Czech Republic. E-mail: radovan.herchel@upol.cz
[b]Institute of Physics, Faculty of Science, P.J. Šafárik University in Košice, Park Angelinum 9, SK-041 54 Košice, Slovakia

†Electronic supplementary information (ESI) available. CCDC 2288033–2288038. For ESI and crystallographic data in CIF or other electronic format see DOI: https://doi.org/10.1039/d3qi01691a

notable examples of trigonal prismatic and trigonally distorted hexacoordinate complexes showing the slow relaxation of magnetization.

It is evident that focusing on the design of Co(II) complexes as potential candidates for SMMs holds intriguing possibilities, including the potential for zero-field single-molecule magnets. However, such magnets are still relatively rare among Co(II) complexes as a whole due to the common occurrence of quantum tunneling of magnetization in the ground state. In the case of six-coordinated Co(II) complexes, the pseudo-octahedral shape is the most commonly observed coordination polyhedron. Therefore, efforts must be made to achieve the trigonal prism shape. Various strategies have already been applied as can be observed in Table 1. An effective approach, seen in most cases,[8–13] involves the use of three heterocyclic binding sites, each with two donor atoms, designed to prevent distortion and maintain the desired shape. In another instance,[14] the trigonal prismatic shape is achieved through bridging oxygen atoms in a tetranuclear core, where Co(II) is surrounded by three diamagnetic Co(III) cores. In the last case,[15] the desired shape is attained through steric hindrance caused by neocuproine methyl groups.

This work presents a series of six complexes (Scheme 1) that employ Schiff base ligands with similar structural motifs. These ligands induce a distorted coordination environment, compelling the Co(II) complexes to adopt shapes that closely resemble trigonal prismatic geometry. The ligands are derived from (2-formylphenoxy)acetic acid, and by incorporating different diamines, we observed a modulation of both the structural and magnetic properties. While analogous structures have been reported previously for Ni(II), Cu(II), Zn(II), and even Co(II), their magnetic properties have not been studied in detail.[16–20]

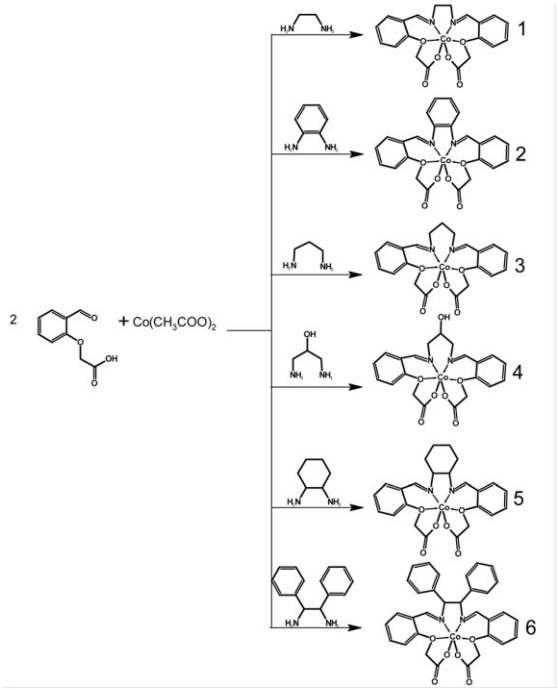

Scheme 1 General scheme for the synthesis of Co(II) complexes [CoL] of **1–6** with respective *in situ* prepared Schiff base ligands H_2L.

Results and discussion

Synthesis and characterisation

The methods employed for the preparation of these complexes are described in the Experimental section below. The Co(II) compounds **1–6** were synthesized by reacting a mixture of cobalt(II) acetate and (2-formylphenoxy)acetic acid with the corresponding amine.

Among these complexes, all except for **2** exhibit good solubility in methanol (MeOH); however, only complex **1** yielded a crystalline product from this solvent. As **3**, **5**, and **6** did not crystallize from methanol due to their high solubility, a mixture of propanol and methanol was chosen as the solvent. For insoluble complex **2**, crystals were obtained from dimethyl-

Table 1 Selected trigonal prismatic and trigonally distorted hexacoordinate Co(II) single-molecule magnets with magnetic parameters and continuous shape measures (CSM) deviations from ideal D_{3h} trigonal prismatic and O_h octahedral geometries *via* SHAPE software[7]

Name	D (cm^{-1})	E (cm^{-1})	U_{eff} (cm^{-1})	τ_0 (s)	B (T)	CSM TP	CSM OH	Ref.
$[Co(tppm)][BPh_4]_2$	−97.2(2)	$9.3(1) \times 10^{-3}$	192	$2.6(2) \times 10^{-12}$	0	0.554	15.893	8
$[Co(hpy)][BPh_4]_2 \cdot 3CH_2Cl_2$	−107.5(4)	3.5(3)	20	$1.2(1) \times 10^{-3}$	0	2.471	8.237	8
$[Co(PzOx)_3(BC_6H_5)]Cl \cdot CHCl_3$	−82	0.246	152	2.07×10^{-9}	0	0.828	16.272	9
$[Co(AcimOx)_3(BC_6H_5)]ClO_4$	−102.5		101	2.56×10^{-6}	0	0.905	13.462	10
$[Co(AcPyOx)_3BC_6H_5]ClO_4$	−86		194.6	3.55×10^{-10}	0	2.006	10.042	11
$\{Na[(Chdc)Co]\}(BPh_4)_3$	−75.8	9.1×10^{-4}	52.6		0.1	1.793	9.293	12
$[Co(tppm)][ClO_4]_2 \cdot 2CH_3CN \cdot H_2O$	−80.7	0.6	39.2	1.7×10^{-4}	0	0.588	14.920	13
$(HNEt_3)[Co^{II}Co^{III}_3(hpmp)_6]$	−115	2.8	76.3	1×10^{-7}	0	2.341	9.284	14
$[Co(neo)(CH_3COO)_2]$			26.3	1.361×10^{-7}	0.1	3.761	11.893	15
$[Co(neo)(piv)_2]$			13.2	6.2×10^{-6}	0.1	9.801	7.650	15
$[Co(neo)(4OH\text{-}benz)_2] \cdot 2CH_3OH$			12.2	1.04×10^{-6}	0.1	10.110	6.352	15

tppm = 6,6′,6″-(methoxymethanetriyl)tris(2-(1*H*-pyrazol-1-yl)pyridine); hpy = tris(2,2′-bipyrid-6-yl)methanol; PzOx = pyrazoloximate, AcimOx = acetylmethylimidazole-oximate, AcPyOx – acetylmethylpyridine-oximate, Chdc – 6,6′-{cyclohexane-1,3,5-diyltris[nitrilo(*E*)methylylidene]} dipyridine-3-carboxamide; H_2hpmp = *R*-4-bromo-2-((2-hydroxy-1-phenylethylimino)methyl)phenol; neo = neocuproine, piv = pivalate, 4OH-benz = 4-hydroxybenzoate.

sulfoxide (DMSO). Complex **3** presented a challenge during its preparation, as it often resulted in the formation of orange powder. Ultimately, this problem was resolved by conducting the reaction without heating the solution to the reflux temperature. Unfortunately, complex **4** could not be obtained in the required quantity and purity for bulk characterization due to the formation of undesired byproducts. However, a small number of single crystals of complex **4** were successfully prepared, and its structure was determined through X-ray analysis. This allowed us to characterize complex **4** at least with theoretical methods. The composition of the prepared complexes was verified through elemental analysis, infrared spectrometry (Fig. S1†), and X-ray powder diffraction (Fig. S2†). For complex **6**, X-ray crystallography indicated the presence of co-crystallized methanol solvent molecules, which displayed notable disorder, likely stemming from solvent loss during the experiment. It was not possible to model the solvent molecules properly and a solvent masking procedure was applied.[21] The resultant masked electron density corresponded to 1.25 methanol molecules per complex molecule. Of note here is that the single crystal measured had been promptly transferred from the solution to high viscosity oil. This action very likely contributed to the reduced rate of solvent loss. Thus, the observed alignment between the outcomes of elemental analysis and the assumption of a solvent-free complex is unsurprising.

Magnetically diluted complex **1Zn** was prepared by using Co(II) and Zn(II) acetate in a 1 : 9 molar ratio. Sample purity was verified by PXRD (Fig. S2†) and CHNS elemental analysis. The composition was studied by the AAS method, which showed a mass fraction of Co of 0.32%, which means that the diluted sample has formula $C_{21}H_{22}N_2O_7Co_{0.026}Zn_{0.974}$.

Crystal structure description

Complexes **1**, **4**, and **5** crystallize in the monoclinic space group $P2_1/n$, while **2** and **3** crystallize in the triclinic space group $P\bar{1}$. Complex **6** crystallizes in the orthorhombic space group *Iba*2. All diffraction experiments were conducted at room temperature. Each compound consists of a [CoL] neutral complex accompanied by co-crystallized solvent molecules of MeOH in the case of **1**, **3**, **4**, and **5**, and DMSO in the case of **2**. In each complex, the cobalt atom is bonded to four oxygen atoms and two nitrogen atoms. Notably, complexes **5** and **6** contain two symmetrically inequivalent molecules of the complex [CoL] in the asymmetric unit, labeled **5a**/**6a** and **5b**/**6b**, respectively (Fig. 1). Additional details about X-ray crystallographic experiments are listed in Table S1.†

The shape of the cobalt coordination polyhedron in all complex molecules is closest to a trigonal prism (D_{3h}), as confirmed by calculations of continuous shape measures (CSMs) using SHAPE software.[7] The minimal distortion pathway between a trigonal prism and an octahedron, as well as the deviation of the prepared complexes' structures from the pathway, is shown in Fig. S3.† It is apparent that all complexes exhibit significant deviations from an octahedron (O_h), except

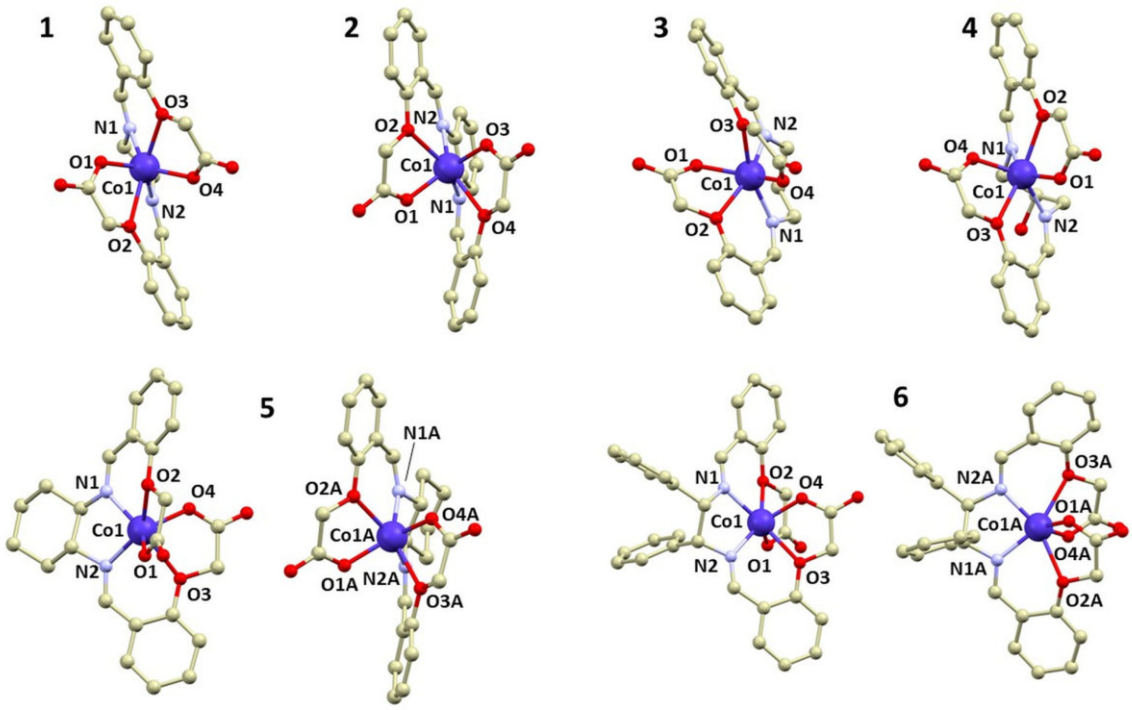

Fig. 1 A perspective view of the crystal structures of **1–6**, with hydrogen atoms omitted for the sake of clarity.

for **3**, which is nearly on the border between an octahedron and a trigonal prism.

In addition to CSM, the shape of the geometry of the coordination environment was also investigated using the newly proposed structural parameter τ_6, a geometry index ranging from 0 (ideal octahedron) to 1 (ideal trigonal prismatic shape).[22] This index is analogous to previously published τ_5 and τ_4 indices for penta- and tetracoordinate complexes, respectively.[23] The parameter τ_6 is defined as

$$\tau_6 = \frac{540 - (\alpha + \beta + \gamma)}{150} \quad (2)$$

with the help of three angles α, β and γ, which are the three greatest valence angles of the coordination center. Index τ_6 shows that all prepared complexes are closer to trigonal prismatic than to octahedral geometry (Table 2). These results seem to correlate well with CSM analysis (Fig. S4†), showing **1** and **5a** as the closest to the trigonal prism, from the studied series.

Furthermore, a previously known similar complex, [Co(fpapn)]·6H_2O (CSD code HOMFOF),[17] was included in the SHAPE analysis, which is a conformational isomer to **3** and exhibits a structure much closer to an ideal octahedron. Interestingly, the use of different solvents (HOMFOF synthesis used a mixture of ethanol and water) for synthesis results in entirely different structures, which are expected to possess distinct properties, especially from a magnetic standpoint.

The distances between the metal and ligand donor atoms, as listed in Table 2, reveal that in most cases, the four bonds between the central atoms and the Schiff base N-atoms or carboxylic group O-atoms have very similar lengths ranging between 2.0 and 2.1 Å. However, the bonds between Co and the etheric group O-atoms (O2 and O3) are longer, ranging between 2.2 and 2.4 Å. Furthermore, structures that differ from others in terms of their shape (CSM), such as **3** and its isomer with the CSD code HOMFOF, do not appear to differ significantly in their bond lengths, except for a shorter distance between the Co atom and the etheric O atom in the HOMFOF structure.

Complexes **1–5** crystallize as crystal solvates, with dimethyl sulfoxide as the solvent in structure **2**, and methanol in all other cases. Methanol is bound to the complex molecule through a hydrogen bond. In structures **1**, **4**, and **5**, it is bound to the carboxylic group oxygen, which is not connected to the central cobalt atom. In structure **3**, methanol is bound to the coordinating carboxylic oxygen atom. Moreover, structure **4** contains a ligand with a hydroxyl group, which forms a hydrogen bond with the carboxyl group oxygen, resulting in a supramolecular structure mediated by hydrogen bridges. Details about observed significant hydrogen bonds are shown in the ESI (Fig. S5†).

Magnetic measurements

DC magnetic measurements were conducted for compounds **1–3** and **5–6**. The measurements consisted of recording the magnetization as a function of temperature under a magnetic field of 0.2 T and as a function of the magnetic field (Fig. 2) at temperatures of 1.8, 5, and 10 K (or 2 and 5 K for compound **1**).

The effective magnetic moments of the prepared compounds at a temperature limit of 300 K are as follows: 4.79μ_B for compound **1**, 5.15μ_B for compound **2**, 4.55μ_B for compound **3**, 5.13μ_B for compound **5**, and 4.83μ_B for compound **6**.

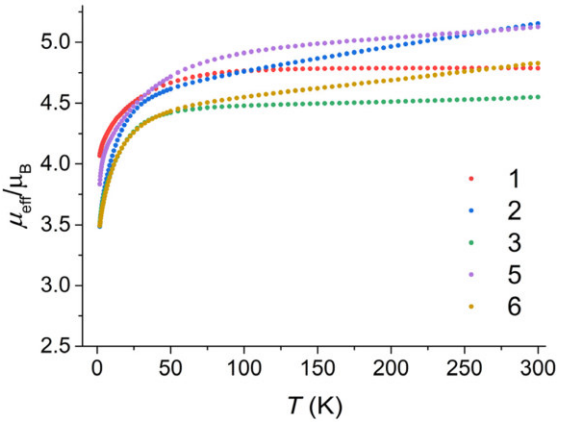

Fig. 2 The effective magnetic moment dependence on temperature for all studied compounds **1–3** and **5–6**.

Table 2 Selected bond distances (Å) and CSM deviations from ideal trigonal prism and octahedron for complexes **1–6**

	Co–N1	Co–N2	Co–O1	Co–O2	Co–O3	Co–O4	CSM TP	CSM OH	τ_6
1	2.0829(19)	2.0736(18)	1.9911(14)	2.3176(14)	2.2822(15)	1.9848(16)	1.631	16.812	0.802
2	2.0883(13)	2.0681(13)	1.9922(12)	2.2846(12)	2.2688(11)	1.9759(12)	1.882	13.748	0.777
3	2.0770(15)	2.0929(15)	2.0370(13)	2.2257(13)	2.2451(13)	2.0110(13)	4.727	5.626	0.525
4	2.130(2)	2.092(2)	1.983(2)	2.335(2)	2.299(2)	1.993(1)	1.481	12.924	0.794
5a	2.0667(19)	2.0739(19)	1.9861(17)	2.2963(15)	2.3525(15)	1.9879(16)	1.911	17.842	0.802
5b[a]	2.083(2)	2.081(2)	1.9946(17)	2.2755(18)	2.2164(16)	2.0099(18)	1.472	12.663	0.785
6a	2.066(6)	2.107(8)	1.951(5)	2.336(5)	2.383(5)	1.970(7)	2.612	18.154	0.760
6b[a]	2.052(6)	2.065(8)	1.998(5)	2.399(6)	2.375(5)	1.978(6)	4.714	15.726	0.694
	Co–N1	Co–N2	Co–O1	Co–O3	Co–O4	Co–O5			
HOMFOF[b]	2.063(2)	2.055(2)	2.042(2)	2.192(2)	2.184(2)	2.032(2)	10.644	1.530	0.320

[a] N1 and N2 for these structures are marked as N3 and N4 in Fig. 1. Same way, O1–O4 are marked as O7–O10. [b] Labeled in a similar way as in Fig. 1, in the HOMFOF cif file, N1 is N1, N2 is N2, O1 is O1, O2 is O3, O3 is O4 and O4 is O5.

The spin-only value for $S = 3/2$ with $g = 2.0$ is $3.87\mu_B$. The observed larger values of the magnetic moment can be attributed to an increased g-factor resulting from orbital contribution and temperature-independent paramagnetism.[24]

DC magnetic data were analyzed using the following spin Hamiltonian:

$$\hat{H} = D(\hat{S}_z^2 - \hat{S}^2/3) + E(\hat{S}_x^2 - \hat{S}_y^2) + \mu_B B g \hat{S} \quad (3)$$

The best-fitted spin Hamiltonian parameters are listed in Table 3 with the standard deviations listed in Table S2,† and calculated magnetic data compared to the experimental ones are depicted in Fig. S6–S10.†

For complexes **5** and **6**, the fits neglected the inclusion of two symmetrically inequivalent molecules in the asymmetric unit. Instead, the fits were performed to obtain the same parameters for both molecules in order to prevent over-parameterization of the fit. In the case of complex **6**, a positive D-parameter was used in the fit, which was suggested by theoretical calculations for one of its symmetrically inequivalent molecules.

AC susceptibility measurements were performed on compounds **1–3** and **5–6** in the presence of a static magnetic field of 0.15 T (0.1 T for **1**), because the tunneling of the magnetization was too fast to observe the out-of-phase signal of AC susceptibility at zero static magnetic field. Under such circumstances, all the measured complexes exhibited out-of-phase signals, indicating the presence of field-induced slow relaxation of magnetization. For the fitting of the AC in-phase and out-of-phase susceptibilities, the Havriliak–Negami model was used[25]

$$\chi(\omega) = \chi_S + \frac{\chi_T - \chi_S}{(1 + (i\omega\tau)^{1-\alpha})^{\beta}} \quad (4)$$

This model is also derived for two relaxation processes:

$$\chi(\omega) = \chi_{S_1} + \frac{\chi_{T_1} - \chi_{S_1}}{(1 + (i\omega\tau_1)^{1-\alpha_1})^{\beta_1}} + \chi_{S_2} + \frac{\chi_{T_2} - \chi_{S_2}}{(1 + (i\omega\tau_2)^{1-\alpha_2})^{\beta_2}} \quad (5)$$

where χ_S and χ_T are adiabatic and isothermic parts of magnetic susceptibility, α and β are parameters describing peak asymmetry and broadness. When two processes are considered, the model is usually simplified with $\chi_{S1} = \chi_{S2}$. However, for certain complexes, simplified variants of this model were employed, such as the Cole–Davidson model ($\alpha = 0$), Cole–Cole model ($\beta = 1$), or Debye model ($\alpha = 0$; $\beta = 1$). Further information regarding the fit parameters can be found in Tables S3–S7.†

For complexes **1**, **2**, and **5**, the inspection of the Argand (Cole–Cole) plot revealed the presence of two relaxation processes. Consequently, the experimental AC data were fitted by considering this observation. Subsequently, the temperature dependence of the relaxation times was analyzed using the following equation:

$$\tau^{-1} = A_{dir} T H^{n_{dir}} + C_{Ram} T^{n_{Ram}} + \tau_0^{-1} e^{\frac{-U_{eff}}{T}} \quad (6)$$

where the direct, Raman, and Orbach relaxation mechanisms are involved. Exponential coefficients were fixed to agree with the theoretical values ($n_{dir} = 4$, $n_{Ram} = 5$).[26] Results are shown in Fig. 3 for **1**, and for the rest of the compounds in Fig. S11–S16.† Complex **6** did not exhibit an observable maximum of out-of-phase susceptibility within the measured frequency range; hence, further analysis was not conducted for this complex. The results for the remaining complexes are provided in Table 4.

In the case of complexes **1** and **2**, only a small range of temperatures (2.2 K–2.6 K for **1** and 2.8 K–3.0 K for **2**) exhibited two clearly distinguishable processes that could be fitted.

Table 3 The best-fitted parameters according to spin Hamiltonian (eqn (1)) for compounds **1–3** and **5–6**

	g^a	D (cm^{-1})	E/D	TIP (cm^3 mol^{-1})
1	2.724; 2.299	−30.3	0.173	0
2	2.344	−13.2	0.281	2.55×10^{-3}
3	2.357; 2.271	−17.0	0.195	3.34×10^{-4}
5	2.641; 2.395	−30.5	0.207	1.33×10^{-3}
6	2.148; 2.326	15.5	0.274	1.67×10^{-3}

[a] Written either as g_{iso}, or g_z; g_{xy}.

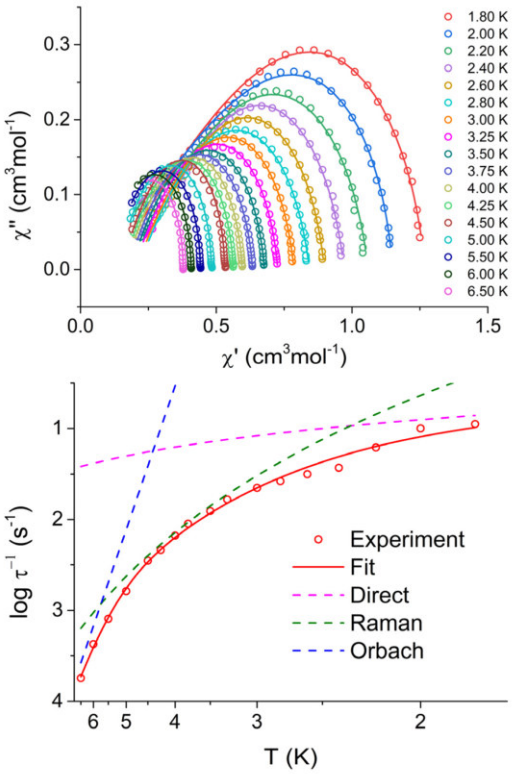

Fig. 3 Argand (Cole–Cole) diagram of in-phase and out-of-phase AC susceptibility (upper panel), and fit of relaxation time for **1** with eqn (6) and parameters listed in Table 4.

Table 4 Fitted parameters from analysis of relaxation processes

Complex	$\log \tau_0^{-1}$ (s^{-1})	U_{eff} (K)	C (s^{-1} K^{-5})	$\log A_{dir}$ (s^{-1} K^{-1} T^{-4})
1	8.45 ± 0.86	72.89 ± 12.59	0.14 ± 0.01	4.60 ± 0.05
2	6.26 ± 0.16	33.63 ± 1.64	0	4.58 ± 0.02
3	9.31 ± 0.17	50.53 ± 1.28	0	3.32 ± 0.03
5s[a]	0	0	0.15 ± 0.01	3.81 ± 0.07
5f	0	0	78.28 ± 12.24	5.89 ± 0.39

Complex	$\log \tau_0^{-1}$ (s^{-1})	U_{eff} (K)	$\log A_{dir}$ (s^{-1} K^{-1} T^{-4})	$\log B_1$ (s^{-1})	$\log B_2$ (s^{-1} T^{-2})
1Zn	5.79 ± 0.10	27.16 ± 0.75	3.52 ± 0.03	3.66 ± 0.06	6.11 ± 0.20

[a] As both processes were analyzed for **5**, they are marked as slower (s) and faster (f).

Consequently, we did not attempt to further analyze this minor process due to insufficient data. For complex **5**, two processes were observable throughout the entire temperature range, allowing us to analyze both of them. However, the data for the faster process was not of sufficient quality to provide a convincing analysis. Two options were tested for its analysis, the combination of Orbach + direct processes, and the combination of Raman + direct processes. The first choice (Raman + direct model) was chosen, because it provided reasonable values of fitted parameters, whereas the second option resulted in unrealistic small values of U_{eff}.

In the case of compounds **1**, **2**, and **3**, values of U_{eff} reasonably correlate with fitted D-parameters from the magnetic data. However, this correlation is not evident in the case of complex **5** for which we assume that the relaxation through the Raman process is too fast to observe Orbach relaxation.

To further study the relaxation of prepared compounds, complex **1** was selected as the most promising one and prepared again as a metal diluted sample with Zn(II), leading to complex **1Zn**. Magnetic measurements (in the range of temperatures 1.8–4.5 K for B = 0.1 T, and range of magnetic fields 0–0.5 T for T = 2 K) show quite a different relaxation profile from non-diluted **1**. We were able to fit the main relaxation process, but there seem to be other minor relaxation processes (some data seem to indicate even three relaxation channels) that we could not analyze in detail due to the insufficient resolution of these additional processes in **1Zn**. Therefore, we have focused only on fitting the most prominent process with clearly visible maxima. The following equation was used for fitting temperature and field-dependent data simultaneously:

$$\tau^{-1} = A_{dir} T H^{n_{dir}} + \frac{B_1}{1 + B_2 H^2} + \tau_0^{-1} e^{\frac{-U_{eff}}{T}} \quad (7)$$

The coefficient for direct relaxation was fixed (n_{dir} = 4) according to the literature as was done in eqn (6) for undiluted samples. However, the fitted U_{eff} for the diluted complex is significantly lower than U_{eff} of **1** (Table 4). The most striking difference between the relaxation in **1** and **1Zn** is the signature of zero-field relaxation observed in AC data suggested by the decrease of the in-phase and increase of the out-of-phase component of AC susceptibility close to the upper measurement frequency limit at 2 K. The relaxation time at zero static magnetic field of **1Zn** is 0.63 ms at 2 K, confirming thus that complex **1** can behave as zero-field SMM.

X-band EPR spectroscopy

The X-band EPR spectra of **1**, **1Zn**, **2**, **3**, **5**, and **6** were measured using powdered samples; the temperature evolution of the EPR spectra (Fig. S17†) shows a decrease of the signal intensity and a significant line broadening with increasing temperature with the lack of spectral details above 30 K. The spin-Hamiltonian and an effective S_{eff} = 1/2 Hamiltonian were used for the analysis of the experimental spectra obtained at 2.3 K. While spin Hamiltonian is often used to describe the two lowest Kramers doublets in Co(II), it is not possible to estimate the value of the D-parameter from X-band EPR for such large values as suggested from the analysis of magnetic data, only the sign of D and E/D ratio. On the other hand, for a large splitting between the ground and first excited Kramers doublet, highly anisotropic effective g-factors obtained from an effective S_{eff} = 1/2 Hamiltonian reflect the influence of higher electronic states and the anisotropy of the crystal field. The spectra were analyzed within the EasySpin Toolbox,[27] including hyperfine interaction (if resolved or necessary for the description) and an anisotropic convolutional broadening ΔB (full-width at half-height, which might reflect the unresolved hyperfine splitting). The splitting due to the hyperfine coupling parameter A was clearly identified only in the experimental EPR spectra of **1Zn** and **2** (see Fig. 4, S17, and S18†).

First, the analysis using spin Hamiltonian formalism was performed, clearly showing $D < 0$ for **2**, **3**, and **5** (see Fig. S17†). For the simulation, the D-parameter was tentatively set to ±10 cm^{-1}, and the obtained parameters are summarised in Table 5. Only one set of parameters was used to simulate the EPR spectra of **5**, but one cannot exclude the presence of a second Co(II) site with similar parameters. Regarding the analysis of **6**, the main component of the spectra at ~200 mT is clearly compatible with $D > 0$. The experiment did not resolve a possible contribution of the predicted Co(II) site with a negative D-parameter (*vide infra*); it might be due to the reduced signal intensity or different line broadening. Interestingly, the E/D ratio for **2**, **5**, and **6** well agrees with the analysis of magnetic data, while for **3** it seems closer to the CASSCF/NEVPT2

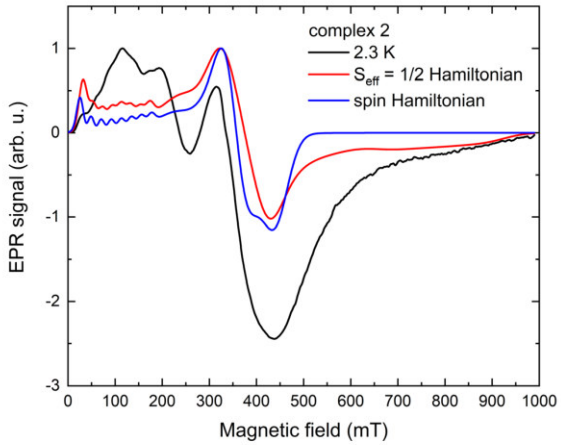

Fig. 4 X-band EPR spectra of **2** obtained at 2.3 K, including simulated spectra, an effective S_{eff} = 1/2 Hamiltonian and spin Hamiltonian models.

Table 5 Spin Hamiltonian parameters for compounds **2**, **3**, **5**, and **6** estimated from X-band EPR; only the sign of a large *D* parameter can be estimated

	D	*E*/*D*	g_x, g_y, g_z	$\Delta B_x, \Delta B_y, \Delta B_z$ (mT)	A_z (MHz)
2	−	0.295	2.12, 2.25, 2.35	50, 45, 55	700
3	−	0.056	2.15, 2.18, 2.38	40, 40, 180	
5	−	0.155	2.11, 2.16, 2.28	140, 130, 250	
6	+	0.180	2.40, 2.20, 2.00	70, 400, 120	

prediction. We could not reasonably reproduce the experimental EPR data of **1** and **1Zn** using the spin Hamiltonian approach, most probably due to a significant influence of hyperfine splitting; therefore, an effective S_{eff} = 1/2 Hamiltonian was used.

The results of the analysis of the EPR spectra using an effective S_{eff} = 1/2 Hamiltonian are summarised in Table 6. They can be understood in the frame of the model that includes spin–orbit coupling and a trigonal crystal field parameter δ to split the $^4T_1$ orbital triplet state originating from the cubic crystal field.[28] The obtained effective *g*-factors in the case of $\delta < 0$ equivalent to easy-axis anisotropy yield highly anisotropic $g'_z \gg g'_x, g'_y$ for $|\delta| > 1000$ cm^{-1}, similar to the ones obtained for **1**, **1Zn**, **2**, **3**, and **5**. Unlike our previous studies, the two lower *g*-factor components do not reach the theoretical

Table 6 Effective S_{eff} = 1/2 Hamiltonian parameters for compounds **1**, **1Zn**, **2**, **3**, **5**, and **6** estimated from X-band EPR

	g'_x, g'_y, g'_z	A'_x, A'_y, A'_z (MHz)	$\Delta B_1, \Delta B_2, \Delta B_3$ (mT)
1	0.68, 2.40, 7.17	110, 580, 650	50, 45, 55
1Zn	0.71, 2.50, 7.17	110, 720, 630	20, 22, 22
2	0.83, 1.77, 6.45	350, 290, 1800	40, 55, 65
3	0.82, 1.79, 6.15	400, 300, 650	20, 80, 100
5	0.74, 1.00, 6.10		120, 160, 180
6	—, 3.39, —		

predictions of the quasi-degenerate perturbation theory.[29] In the case of **6**, a strong central resonance line was assigned to g' = 3.39 characteristic for $\delta > 0$ (easy-plane anisotropy). Interestingly, for **1** and **1Zn**, slightly different *g*-factors and hyperfine interaction parameters were needed to simulate the two datasets (Fig. S17†). The full hyperfine splitting pattern was not resolved even in the diluted sample. Differences in obtained parameters might suggest that the Co(II) dilution also leads to minor changes in its electronic spectra.

Theoretical calculations

Theoretical CASSCF/NEVPT calculations were conducted to provide additional insights into the electronic structure of the prepared complexes and to potentially identify structural correlations and elucidate the magnetic behavior of the studied compounds. The calculations were performed using molecular structures derived from the X-ray data, and only the atomic positions of the hydrogen atoms were optimized using the DFT method.

The energy levels and zero-field splitting (ZFS) parameters of the studied complexes were calculated using the complete active space self-consistent field method (CASSCF) with a 7-electron in 5-orbital active space (CAS(7,5)), which corresponds to the Co(II) $3d^7$ electron configuration. The treatment of dynamic electron correlation was performed using the N-electron valence perturbation theory (NEVPT2) method. The energy of the active metal d-orbitals was calculated using the AILFT (*Ab Initio* Ligand Field Theory) module in ORCA.

In the case of an ideal trigonal prismatic geometry, the d-orbitals are split into three energy levels. The lowest level corresponds to the d_{z^2} orbital, followed by two degenerate orbitals, d_{xy} and $d_{x^2-y^2}$, and the highest level consists of two degenerate orbitals, d_{xz} and d_{yz}. Such ordering of orbitals is clearly visible for all complexes except for **3** and **6b**, suggesting that most of the prepared complexes have crystal field splitting similar to the trigonal prism (Fig. 5).

In a free Co(II) ion, its ground atomic term is ^4F, which is then followed by two excited states ^4P and ^2G. In ideal O_h symmetry, ^4F is split into $^4T_1 + {}^4T_2 + {}^4A_1$ ligand field terms, ^4P into the $^4T_1$ ligand field term, and ^2G into $^2T_1 + {}^2T_2 + {}^2A_1$ ligand field terms. If symmetry is reduced further to D_3, each ^4T term splits into ^4E and ^4A, therefore ground term ^4F is split into $^4E + {}^4E + {}^4A_2 + {}^4A_1$ $^4A_2$, as is observed in the trigonal prism Tanabe Sugano diagram.[30] After further reduction of symmetry by distortion from the ideal shape, ^4E terms are split into 2 levels. Therefore, the ^4F term splits into 7 non-degenerate levels (ligand field terms) in non-ideal symmetry. Thus, if the coordination polyhedron is close to the trigonal prism shape, it should be theoretically possible to see distribution similar to original terms – two close-lying levels from the ground ^4E term, another two levels from the first excited ^4E term, and finally three levels from ^4A terms. It is possible to spot this energy level distribution on prepared complexes, mainly **1** and **4** (Fig. 5). Above ground term levels, 3 quartet levels are visible, which are originating in ^4E and $^4A_2$ from ^4P first excited term,

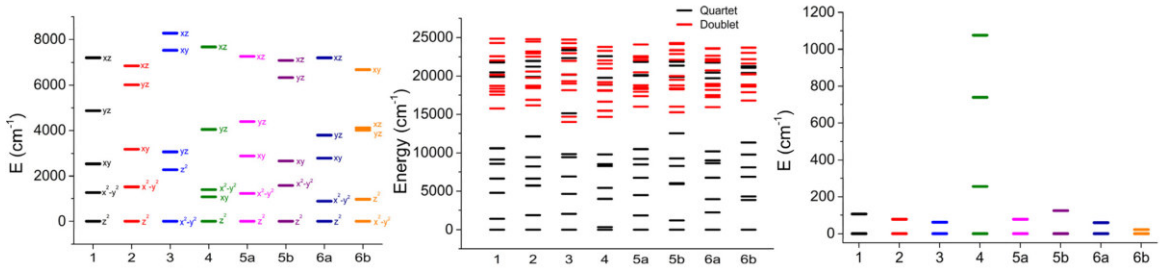

Fig. 5 *Ab initio* energy of d-orbitals (left panel), ligand field terms (center panel), and ligand field multiplets (right panel) for studied complexes.

and also a large number of doublet states, which are from ^{2}G and also higher doublet terms.

The spin–orbit interaction further splits the $^4\Gamma$ ground term into two ligand field multiplets. Theoretically, the D_{3h} symmetry is expected to yield large and negative *D*-parameters. Our calculations have confirmed this assumption, and all the relevant parameters for the studied compounds are listed in Table 7 and Table S8†

Based on the results, it can be observed that among the studied complexes, **5b** and **1** exhibit the most favorable characteristics due to their large negative *D*-parameter. However, it is worth noting that this is a common feature among almost all the complexes, except for the unusual case of **6b**, which appears to have an easy-plane anisotropy with its positive *D*-parameter and significant rhombic components of the *g*-tensor. The ZFS and *g*-factor parameters for complex **4** are approximate because its low-lying excited states (Fig. 5) exclude the application of spin Hamiltonian formalism. Additionally, this is often associated with a larger anisotropy, as evidenced by the significant splitting of the crystal field multiplets (Fig. 5).

Moreover, we analyzed the variation of the calculated *D*-parameter within the series for complexes with a geometry close to the trigonal prism, namely, we took into account complexes **1**, **2**, **4**, **5a**, **5b**, and **6a** that all have the splitting of d-orbitals resembling the expected one for non-ideal D_{3h} symmetry. In such a case, the largest contribution to the *D*-parameter stems from the electron excitation from ground state electronic configuration $d_{z^2}^2 d_{x^2-y^2}^2 d_{xy}^1 d_{yz}^1 d_{xz}^1$ to the first excited state electronic configuration $d_{z^2}^2 d_{x^2-y^2}^1 d_{xy}^1 d_{yz}^2 d_{xz}^1$, which corresponds to the electron transfer between $d_{x^2-y^2}$ and d_{xy} orbitals. Note that in the case of complex **4**, the ordering of these two orbitals is interchanged. Anyway, these two orbitals have the same $|m_l|$ values and thus such excitation ($d_{x^2-y^2} \leftrightarrow d_{xy}$) has a large contribution to the D_{zz} part of the *D*-tensor, which induces a large negative value of the *D*-parameter.[31] The slight energy difference between these orbitals in **4** results in a configuration that closely resembles the orbitally degenerate ^{4}E′ ground state term. Thus, it is not surprising that calculated anisotropy is huge and axial, with limited validity of spin Hamiltonian formalism (Table 7).

Indeed, the respective correlation was established between the *D*-parameter and the energy difference of two d-orbitals $\Delta\varepsilon_d = |\varepsilon(d_{xy}) - \varepsilon(d_{x^2-y^2})|$ as depicted in Fig. 6. Evidently, the magnetic anisotropy parameters are very sensitive to the changes in the shape of the coordination polyhedron reflected in d-orbitals splitting induced by the respective ligand field.

Table 7 Calculated spin Hamiltonian parameters and *g*-factors for studied complexes

	D (cm^{-1})	E/D	g_x	g_y	g_z	Δ^b (cm^{-1})
1	−52.54	0.074	2.216	2.096	2.760	−103.41
2	−38.40	0.050	2.128	2.188	2.602	−77.07
3	−30.70	0.054	2.153	2.177	2.505	−61.67
4[a]	*−127.73*	*0.022*	*1.849*	*2.000*	*3.377*	−255.66
5a	−37.62	0.129	2.113	2.250	2.623	−77.1
5b	−61.87	0.014	2.099	2.147	2.823	−123.78
6a	−27.43	0.232	2.120	2.294	2.532	−59.13
6b	10.83	0.075	2.159	2.290	2.305	21.83

[a] For **4**, spin Hamiltonian parameters are not completely relevant, because it is not possible to fully describe its energy level splitting with spin Hamiltonian formalism. [b] The parameter Δ is defined as the energy difference of the two lowest Kramers doublets.

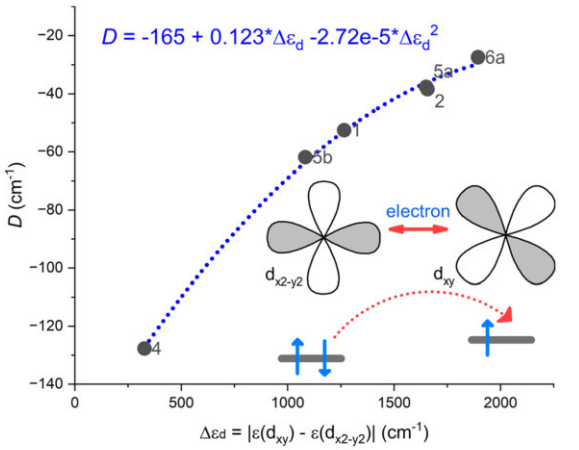

Fig. 6 A correlation established between the *D*-parameter and the energy difference of two d-orbitals $\Delta\varepsilon_d = |\varepsilon(d_{xy}) - \varepsilon(d_{x^2-y^2})|$ using CASSCF/NEVPT2 results for complexes **1**, **2**, **4**, **5a**, **5b**, and **6a**.

To gain a deeper understanding of magnetic behavior, we utilized the computational module SINGLE_ANISO, which enabled us to visualize the anisotropic energy barrier and calculate transition rates as magnetic moment matrix elements. These transition rates provide valuable insights into the probability of relaxation processes and help identify the pathways for magnetization reversal transitions. In the case of a Co(II) system with a spin of 3/2, there are only two Kramers doublets that could potentially be involved in the relaxation. Of particular importance is the transition rate associated with the ground state quantum tunneling of magnetization, as it determines whether the higher Kramers doublet will play a major role in the relaxation mechanism. The output of the SINGLE_ANISO module is depicted in Fig. 7 for **2**, and in Fig. S19† for the rest of the complexes.

Thus, it is evident that complexes **4** and **5b** exhibit the smallest tunneling probabilities in their ground state, which aligns with previous findings describing these complexes as highly anisotropic. These complexes demonstrate tunneling probabilities below 0.1, which render them potential zero-field SMMs. On the other hand, complexes **1**, **2**, and **3** exhibit tunneling probabilities above 0.1, suggesting that quantum tunneling of magnetization (QTM) is likely to play a significant role in their relaxation. However, it is possible to suppress QTM by applying a magnetic field, which transforms these compounds into field-induced single-molecule magnets (SMMs). Finally, complexes **5a** and **6a** show a high probability of QTM, while complex **6b** is predicted to have typical easy-plane spin level splitting, indicating no potential for slow relaxation of magnetization.

To assess the preference of ligand scaffold in complexes **1–6** for trigonal geometry, we chose to perform additional DFT optimizations on their molecular structures in a vacuum with the help of the well-established B3LYP functional. This approach allows us to explore their optimal arrangement while excluding the influence of crystal packing effects. Indeed, the coordination polyhedra in the optimized geometries of all the complexes exhibit a tendency to adopt trigonal symmetry, characterized by relatively modest TP CSM values ranging between 1.6 and 3.7, and τ_6 values found between 0.62 and 0.86 (Table S9†). Remarkably, this inclination persists despite the substantial relaxation observed in the calculated molecular geometries. Evidently, this relaxation is reflected in the elongation of metal–ligand bond lengths, particularly those with the etheric oxygen atoms (O2 and O3), which extend well beyond 2.35 Å (Table S9†). Thus, it seems that the herein utilized ligand motif is rigid enough to provide Co^{II} complexes with a ligand field close to D_3 symmetry and certainly deserves further exploration.

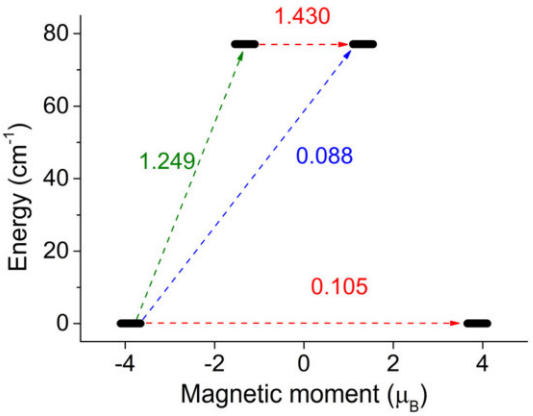

Fig. 7 SINGLE_ANISO description of the magnetic moment matrix elements between Kramers doublets for complex **2**.

We opted to compare our findings also with the data available in CSD. Our search yielded eight crystal structures of complexes containing the Co, Ni and Zn metal centers coordinated with the 2-formylphenoxyacetic acid based Schiff base ligands. Notably, all these complexes incorporate either identical or their methoxy derivatives as those used in the synthesis of **1** and **3**. Specifically, these ligands feature either ethylene (en) or propylene (pr) linkers in their structures.

Upon examining their coordination polyhedra, we observed that these complexes primarily adopt coordination environments that closely resemble either octahedral (Oh) or trigonal prismatic (TP) geometries – Table S10.† Complexes with en linkers tend to favor a trigonal prismatic coordination. Even when the lowest CSM values indicate an octahedral geometry, these values are notably high (>5; CSD codes: RUJNES,[20] SIRMOX[32]), comparable to those calculated for a TP geometry. This suggests significant distortion from an idealized octahedral shape.

Conversely, complexes featuring pr linkers and adopting an Oh geometry (CSD codes: HOMFOF,[17] QEBBIL,[19] SIRMUD[32]) exhibit low CSM values (below 1.56), implying minimal deviation from an ideal octahedral shape. Given that a TP geometry would induce a doubly degenerate ground state for the Co(II) central atom—subject to strong Jahn–Teller distortion—it is reasonable to conclude that ligand rigidity, particularly in ligands with shorter en linkers, plays a key role in stabilizing this geometry.[33]

These observations are consistent with the crystal structures presented in this study. The most significant deviation from a TP geometry was observed in **3** featuring a pr linker (Table 2; CSM TP = 4.727, CSM Oh = 5.626). Interestingly, complex **4** featuring a 2-hydroxypropyl linker closely approximated an ideal TP geometry, even though its linker length is very similar to that of the pr linker. However, this complex also incorporates a hydroxyl group, which influences the overall structure not only through steric hindrance but also by enabling intermolecular hydrogen bonding.

These findings lead to a consideration of the somewhat unpredictable effects of crystal packing and non-covalent interactions. For example, the cobalt coordination environments in solvatomorph **3** and HOMFOF differ markedly. Solvatomorph **3** is a methanol solvate, while HOMFOF contains six co-crystallized water molecules per complex in its structure. Notably,

complexes approximating an Oh geometry frequently feature extensive solvation in their second coordination spheres, as evidenced by the examples of HOMFOF, SIRMOX, and SIRMUD.

In summary, we may conclude that DFT calculations can predict the geometry of these complexes with reasonable accuracy – Fig. S20.† A general guideline could be that rigid linkers in Schiff base ligands based on 2-formylphenoxyacetic acid contribute to the stabilization of a TP geometry in Co(II) complexes. However, this conclusion must be interpreted with caution, as non-covalent interactions, and particularly the co-crystallization of solvent molecules, can significantly influence the geometry of complex molecules in the solid state.

Experimental

General methods

(2-Formylphenoxy)acetic acid was prepared by a previously published method.[34] All the complexes were prepared by *in situ* reactions of (2-formylphenoxy)acetic acid, respective amine, and cobalt(II) acetate. The reagents were purchased from commercial sources. The CHNS elementary analysis was done using a Thermo Scientific Flash 2000 analyzer (Thermo Scientific, Waltham, MA, USA). The IR spectra were recorded using a Jasco FT/IR-4700 spectrometer (Jasco, Easton, MD, USA) using the ATR technique on a diamond plate in the spectral range of 400–4000 cm^{-1}. The powder XRD patterns were measured using a Rigaku MiniFlex600 diffractometer (Rigaku, Austin, TX, USA) equipped with the Bragg–Brentano geometry and using Cu Kα radiation. EPR spectra were measured on powdered samples using a Bruker ELEXSYS II E500 spectrometer.

Synthesis

[Co(fpa-en)]·MeOH (1). In 10 ml of methanol, 72 mg of (2-formylphenoxy)acetic acid (0.4 mmol) was mixed with 50 mg of $Co(CH_3COO)_2{\cdot}4H_2O$ (0.2 mmol). The mixture was stirred for 10 minutes, then 12 mg of 1,2-ethylenediamine (0.2 mmol) was added. The mixture was then refluxed for an hour, during which it changed color to wine red or purple. The mixture was then left to stand for three days, which produced needle-like crystals, which were filtered off and washed with diethylether. Crystals suitable for X-ray diffraction were grown by diffusion of diethyl ether vapors into solution.

Anal. calcd for $C_{21}H_{22}N_2O_7Co$ (**1**): M_{mol} = 473.35 g mol^{-1} – C 53.29; H 4.68; N 5.92%. Found: C 53.08; H 5.08; N 5.88%.

FTIR (ATR, cm^{-1}): 3262 (m), 3053 (w), 2940 (w), 1620 (s), 1494 (s), 1383 (s), 1341 (s), 1244 (s), 1132 (m), 1015 (s), 940 (m), 891 (m), 753 (s), 598 (w), 528 (w).

[Co(fpa-pda)]·DMSO (2). In 10 ml of methanol, 72 mg of (2-formylphenoxy)acetic acid (0.4 mmol) was mixed with 50 mg of $Co(CH_3COO)_2{\cdot}4H_2O$ (0.2 mmol). The mixture was stirred for 10 minutes, then 21.6 mg of *o*-phenylenediamine (0.2 mmol) was added and the mixture was refluxed for an hour, which resulted in the precipitation of red powder. This powder was filtered off, washed with methanol and diethylether and dried. After this, the powder was recrystallized from a mixture of methanol and dimethylsulfoxide (DMSO was added dropwise to the suspension of the powder in methanol until it fully dissolved) by diffusion of diethyl ether vapors, which resulted in red crystals, which were filtered and washed with diethylether.

Anal. calcd for $C_{26}H_{24}N_2O_7SCo$ (**2**): M_{mol} = 567.48 g mol^{-1} – C 55.03; H 3.91; N 4.94; S 5.65%. Found: C 54.51; H 4.15; N 4.94; S 5.07%.

FTIR (ATR, cm^{-1}): 3033 (w), 2991 (w), 2911 (s), 2165 (w), 1981 (w), 1638 (s), 1485 (s), 1380 (s), 1282 (s), 1237 (s), 1161 (m), 939 (m), 822 (m), 751 (s), 614 (w), 518 (w).

[Co(fpa-pn)]·MeOH (3). In 5 ml of propanol and 1 ml of methanol, 72 mg of (2-formylphenoxy)acetic acid (0.4 mmol) was mixed with 50 mg of $Co(CH_3COO)_2{\cdot}4H_2O$ (0.2 mmol). The mixture was stirred for 10 minutes, then 15 mg of 1,3-propylenediamine (0.2 mmol) was added, and the mixture was gently heated for 20 minutes. Then, the product was crystallized by diffusion of diethyl ether vapors, which resulted in purple plate-like crystals, which were filtered off and washed with diethyl ether.

Anal. calcd for $C_{22}H_{24}N_2O_7Co$(**3**): M_{mol} = 487.38 g mol^{-1} – C 54.22; H 4.55; N 5.75%. Found: C 53.45; H 4.87; N 5.70%.

FTIR (ATR, cm^{-1}): 3725 (w), 3630 (w) 3276 (m), 3080(w), 2930 (m), 2820 (w), 2297 (w), 2165 (w), 1618 (s), 1493 (s), 1437 (s), 1247 (m), 1128 (m), 1018 (s), 937 (m), 887 (m), 817 (m), 759 (s), 708 (m), 521 (w), 454 (w), 362 (w).

[Co(fpa-OHpn)]·MeOH (4). In 10 ml methanol, 72 mg of (2-formylphenoxy)acetic acid (0.4 mmol) was mixed with 50 mg of $Co(CH_3COO)_2{\cdot}4H_2O$ (0.2 mmol). The mixture was stirred and slightly heated for 5 minutes, and then 18 mg of 2-hydroxy-1,3-propylenediamine (0.2 mmol) was added; after another 5 minutes, a purple solution was obtained and left to crystallize by diffusion of diethyl ether, which produced a small amount of purple crystals.

[Co(fpa-cn)]·MeOH (5). In 5 ml of propanol and 1 ml of methanol, 72 mg of (2-formylphenoxy)acetic acid (0.4 mmol) was mixed with 50 mg of $Co(CH_3COO)_2{\cdot}4H_2O$ (0.2 mmol). The mixture was stirred for 10 minutes, then 23 mg of cyclohexane-1,2-diamine (0.2 mmol) was added, and the mixture was gently heated for 20 minutes. Then, the product was crystallized by diffusion of diethyl ether vapors, which resulted in purple crystals, which were filtered off and washed with diethyl ether.

Anal. calcd for $C_{25}H_{28}N_2O_7Co$(**5**): M_{mol} = 527.44 g mol^{-1} – C 56.93; H 4.97; N 5.31%. Found: C 56.57; H 4.79; N 5.11%.

FTIR (ATR, cm^{-1}): 3411 (w), 3062 (w), 2929 (m), 2859 (m), 2166 (w), 1628 (s), 1497 (s), 1449 (s), 1381 (s), 1286 (s), 1128 (m), 1004 (s), 939 (m), 894 (m), 821 (m), 759 (s), 614 (w), 515 (w), 453 (w), 400 (w), 353 (w).

[Co(fpa-dpen)] (6). In 5 ml of propanol and 1 ml of methanol, 72 mg of (2-formylphenoxy)acetic acid (0.4 mmol) was mixed with 50 mg of $Co(CH_3COO)_2{\cdot}4H_2O$ (0.2 mmol). The mixture was stirred for 10 minutes, then 42 mg of 1,2-diphenylethylen-1,2-diamine (0.2 mmol) was added, and the mixture was gently heated for 20 minutes. Then, the product

was crystallized by diffusion of diethyl ether vapors, which resulted in purple crystals, which were filtered off and washed with diethyl ether.

Anal. calcd for $C_{32}H_{26}N_2O_7Co$(**6**): M_{mol} = 593.51 g mol^{-1} – C 64.76; H 4.08; N 4.72%. Found: C 64.23; H 4.41; N 4.53%.

FTIR (ATR, cm^{-1}): 3724 (m), 3598 (w), 3398 (m), 3031 (w), 2913 (w), 2360 (w), 2298 (w), 2113 (w), 1982 (w), 1619 (s), 1492 (s), 1376 (s), 1293 (s), 1131 (s), 1027 (s), 937 (m), 827 (m), 754 (s), 702 (s), 596 (m), 519 (w), 458 (w).

[$Co_{0.026}Zn_{0.973}$(fpa-en)]·MeOH (1Zn). In 10 ml of methanol, 72 mg of (2-formylphenoxy)acetic acid (0.4 mmol) was mixed with 5 mg of $Co(CH_3COO)_2{\cdot}4H_2O$ (0.02 mmol) and 39 mg of $Zn(CH_3COO)_2{\cdot}2H_2O$ (0.18 mmol). The mixture was stirred for 10 minutes, then 12 mg of 1,2-ethylenediamine (0.2 mmol) was added. The mixture was then refluxed for an hour, during which it changed color to light purple. The mixture was then left to stand for three days, which produced crystals, which were filtered off and washed with diethylether.

Anal. calcd for $C_{21}H_{22}N_2O_7Co_{0.027}Zn_{0.974}$ (**1Zn**): M_{mol} = 479.66 g mol^{-1} – C 52.59; H 4.20; N 5.84%. Found: C 52.35; H 4.49; N 5.72%.

Theoretical calculations

All theoretical calculations were performed with the use of the ORCA 5.0.2. program package.[35] Initial molecular structures, obtained from X-ray data were treated by DFT hydrogen optimization, with the BP86 functional,[36] with basis sets from Ahlrich def2 basis set,[37] QZVP basis for Co, SVP for C and H atoms, and TZVP for other atoms, and def2/J auxiliary basis. Fully optimized molecular structures reported in Table S9† were obtained with the B3LYP[38] hybrid DFT functional with the help of D4 dispersion correction,[39] and the vibrational analyses confirmed proper convergence for complexes at local energy minimum as there were no imaginary frequencies.

CASSCF calculations were done with the TZVPP basis for Co and the TZVP basis for all other atoms and with def2/J and def2-TZVP/C auxiliary basis sets. The dynamic electron correlation was treated by the RI-NEVPT2 method,[40] and spin–orbit coupling by RI-SOMF(1×) approach.[41] CASSCF was performed for 7 electrons in 5 d-orbitals (selected by ORCA keyword "actorbs dorbs"), which corresponds to the Co(II) valence electron configuration. The number of calculated roots responds to a maximal number of possible roots, 10 states with multiplicity M_S = 4 and 40 roots with M_S = 2. For further analysis of Kramers doublets, the SINGLE_ANISO module[42] was used and set up to calculate with two Kramers doublets. CASSCF calculations were done with the "NoFrozenCore" keyword.

All calculations were performed with the help of the RIJCOSX approximation,[43] with improved integral precision, enabled by "DEFGRID3" ORCA keyword, and strict convergence "TightSCF" settings.

For visualization, the software Avogadro[44] and Mercury[45] were used. Magnetic data were analyzed with the help of software PHI[46] and RELACS.[47] In some parts of the text, ChatGPT 3[48] was used for grammar and stylistic corrections.

Conclusions

A series of six novel complexes were synthesized and characterized using a combination of theoretical and experimental methods, focusing on magnetic properties. These complexes exhibit a notable inclination towards adopting a trigonal prismatic geometry, as confirmed by both experimental observations and theoretical DFT calculations. This inclination is influenced by the building blocks employed in constructing the Schiff base ligand. This observation suggests the potential for further adjustments and fine-tuning of the system to enhance its performance in potential applications. Overall, this system demonstrates remarkable versatility and holds substantial promise for further molecular optimization.

The magnetic properties of the studied complexes were investigated using DC and AC magnetometry, as well as EPR spectroscopy. The obtained results were used to extract the parameters of the spin Hamiltonian. Four of the studied complexes were experimentally confirmed to have large and negative *D*-parameter, indicating axial anisotropy, while complex **6** showed a positive *D*-parameter. These experimental findings were also supported by theoretical calculations.

AC magnetic measurements revealed that the prepared complexes exhibit characteristics of field-induced single-molecule magnets, as evidenced by the significant quantum tunneling of magnetization in the ground state even without the presence of a magnetic field. In the presence of a magnetic field, all of the prepared complexes demonstrate a slow relaxation of magnetization, including also complex **6** which exhibits easy-plane magnetic anisotropy. The observed field induced magnetic relaxation of **6** can be attributed either to the Raman relaxation process or to the presence of complex **6a** within the asymmetric unit which possesses the axial type magnetic anisotropy suitable for the Orbach relaxation process as suggested by theoretical calculations.

The most interesting results were obtained for zinc-diluted sample **1Zn**, for which the slow relaxation of magnetization was observed already at zero static magnetic field. Interestingly, the dilution of the sample resulted in changes in spin Hamiltonian parameters as evidenced by EPR analysis and also in changes in the parameters describing the magnetization relaxation processes. Nevertheless, these results make the utilized ligand scaffold promising for future preparation of zero-field SMMs.

Conflicts of interest

There are no conflicts to declare.

Acknowledgements

We acknowledge financial support from the Palacký University Olomouc project IGA_PrF_2022_006. E. Č. was supported by the Slovak Research and Development Agency, contract no.

APVV-22-0172 and APVV-18-0197. We also thank Mrs. Pavla Richterová for performing elemental analysis.

References

1 A. Caneschi, D. Gatteschi, R. Sessoli, A. L. Barra, L. C. Brunel and M. Guillot, Alternating Current Susceptibility, High Field Magnetization, and Millimeter Band EPR Evidence for a Ground S = 10 State in $[Mn_{12}O_{12}(CH_3COO)_{16}(H_2O)_4]\cdot 2CH_3COOH\cdot 4H_2O$, *J. Am. Chem. Soc.*, 1991, **113**(15), 5873–5874, DOI: **10.1021/ja00015a057**.

2 M. Feng and M. L. Tong, Single Ion Magnets from 3d to 5f: Developments and Strategies, *Chem. – Eur. J.*, 2018, **24**(30), 7574–7594, DOI: **10.1002/chem.201705761**.

3 F. A. Cotton, *Progress in Inorganic Chemistry (Vol.6)*, Interscience Publishers, 1964.

4 A. Sarkar, S. Dey and G. Rajaraman, Role of Coordination Number and Geometry in Controlling the Magnetic Anisotropy in Fe^{II}, Co^{II}, and Ni^{II} Single–Ion Magnets, *Chem. – Eur. J.*, 2020, **26**(62), 14036–14058, DOI: **10.1002/chem.202003211**.

5 (*a*) R. Herchel, L. Váhovská, I. Potočňák and Z. Trávníček, Slow Magnetic Relaxation in Octahedral Cobalt(II) Field-Induced Single-Ion Magnet with Positive Axial and Large Rhombic Anisotropy, *Inorg. Chem.*, 2014, **53**(12), 5896–5898, DOI: **10.1021/IC500916U**; (*b*) I. Nemec, R. Herchel, M. Kern, P. Neugebauer, J. van Slageren and Z. Trávníček, Magnetic Anisotropy and Field–Induced Slow Relaxation of Magnetization in Tetracoordinate Co^{II} Compound $[Co(CH_3{-}im)_2Cl_2]$, *Materials*, 2017, **10**(3), 249, DOI: **10.3390/MA10030249**.

6 G. A. Craig and M. Murrie, 3d Single-Ion Magnets, *Chem. Soc. Rev.*, 2015, **44**(8), 2135–2147, DOI: **10.1039/C4CS00439F**.

7 (*a*) S. Alvarez, Polyhedra in (Inorganic) Chemistry, *Dalton Trans.*, 2005, (13), 2209, DOI: **10.1039/b503582c**; (*b*) S. Alvarez, P. Alemany, D. Casanova, J. Cirera, M. Llunell and D. Avnir, Shape Maps and Polyhedral Interconversion Paths in Transition Metal Chemistry, *Coord. Chem. Rev.*, 2005, **249**(17–18 SPEC. ISS.), 1693–1708, DOI: **10.1016/j.ccr.2005.03.031**; (*c*) D. Casanova, P. Alemany, J. M. Bofill and S. Alvarez, Shape and Symmetry of Heptacoordinate Transition-Metal Complexes: Structural Trends, *Chem. – Eur. J.*, 2003, **9**(6), 1281–1295, DOI: **10.1002/chem.200390145**; (*d*) A. Ruiz-Martínez, D. Casanova and S. Alvarez, Polyhedral Structures with an Odd Number of Vertices: Nine-Atom Clusters and Supramolecular Architectures, *J. Chem. Soc., Dalton Trans.*, 2008, (19), 2583–2591, DOI: **10.1039/b718821h**.

8 B. Yao, M. K. Singh, Y.-F. Deng, Y.-N. Wang, K. R. Dunbar and Y.-Z. Zhang, Trigonal Prismatic Cobalt(II) Single-Ion Magnets: Manipulating the Magnetic Relaxation Through Symmetry Control, *Inorg. Chem.*, 2020, **59**(12), 8505–8513, DOI: **10.1021/acs.inorgchem.0c00950**.

9 V. V. Novikov, A. A. Pavlov, Y. V. Nelyubina, M.-E. Boulon, O. A. Varzatskii, Y. Z. Voloshin and R. E. P. Winpenny, A Trigonal Prismatic Mononuclear Cobalt(II) Complex Showing Single-Molecule Magnet Behavior, *J. Am. Chem. Soc.*, 2015, **137**(31), 9792–9795, DOI: **10.1021/jacs.5b05739**.

10 A. A. Pavlov, D. Y. Aleshin, S. A. Savkina, A. S. Belov, N. N. Efimov, J. Nehrkorn, M. Ozerov, Y. Z. Voloshin, Y. V. Nelyubina and V. V. Novikov, A Trigonal Prismatic Cobalt (II) Complex as a Single Molecule Magnet with a Reduced Contribution from Quantum Tunneling, *ChemPhysChem*, 2019, **20**(8), 1001–1005, DOI: **10.1002/cphc.201900219**.

11 A. A. Pavlov, S. A. Savkina, A. S. Belov, Y. V. Nelyubina, N. N. Efimov, Y. Z. Voloshin and V. V. Novikov, Trigonal Prismatic Tris-Pyridineoximate Transition Metal Complexes: A Cobalt(II) Compound with High Magnetic Anisotropy, *Inorg. Chem.*, 2017, **56**(12), 6943–6951, DOI: **10.1021/acs.inorgchem.7b00447**.

12 T. J. Ozumerzifon, I. Bhowmick, W. C. Spaller, A. K. Rappé and M. P. Shores, Toward Steric Control of Guest Binding Modality: A Cationic Co(II) Complex Exhibiting Cation Binding and Zero-Field Relaxation, *Chem. Commun.*, 2017, **53**(30), 4211–4214, DOI: **10.1039/C7CC01172E**.

13 B. Yao, Y.-F. Deng, T. Li, J. Xiong, B.-W. Wang, Z. Zheng and Y.-Z. Zhang, Construction and Magnetic Study of a Trigonal-Prismatic Cobalt(II) Single-Ion Magnet, *Inorg. Chem.*, 2018, **57**(22), 14047–14051, DOI: **10.1021/acs.inorgchem.8b02692**.

14 Y. Y. Zhu, Y. Q. Zhang, T. T. Yin, C. Gao, B. W. Wang and S. Gao, A Family of $Co^{II}Co^{III}_3$ Single-Ion Magnets with Zero-Field Slow Magnetic Relaxation: Fine Tuning of Energy Barrier by Remote Substituent and Counter Cation, *Inorg. Chem.*, 2015, **54**(11), 5475–5486, DOI: **10.1021/ACS.INORGCHEM.5B00526**.

15 I. Nemec, O. F. Fellner, B. Indruchová and R. Herchel, Trigonally Distorted Hexacoordinate Co(II) Single-Ion Magnets, *Materials*, 2022, **15**(3), 1064, DOI: **10.3390/ma15031064**.

16 J. Wang, D.-S. Zhu, K.-Z. Shao and L. Xu, {2,2′-[Ethane-1,2-Diylbis(Nitrilomethylidyne)]Diphenoxyacetato}zinc(II) Methanol Solvate, *Acta Crystallogr., Sect. E: Struct. Rep. Online*, 2006, **62**(8), m1884–m1886, DOI: **10.1107/S1600536806026791**.

17 Z. L. Wang, D. S. Zhu and R. S. Wang, Crystal Structure of [N,N′-(Bis(2-Phenoxyacetic)Formylidene)Propane- 1,3-Diaminecobalt(II)] Hexahydrate, $[Co(C_{21}H_{20}N_2O_6)]\cdot 6H_2O$, *Z. Kristallogr. – New Cryst. Struct.*, 2008, **223**(3), 217–218, DOI: **10.1524/NCRS.2008.0091**.

18 Z. L. Wang, D. S. Zhu and R. S. Wang, Crystal Structure of [N,N′-(Bis(2-Phenoxyacetic)Formylidene)Propane- 1,3-Diamine-Zinc(II)] - Water - Ethanol (1 : 1 : 0.25), $[Zn(C_{21}H_{20}N_2O_6)]\cdot H_2O\cdot 0.25C_2H_6O$, *Z. Kristallogr. – New Cryst. Struct.*, 2008, **223**(3), 215–216, DOI: **10.1524/NCRS.2008.0090/DOWNLOADASSET/1267-2227.CFF**.

19 L. Yan and C. L. Liu, Synthesis, Structure Characterization, Antibacterial Activity and Fluorescence Studies of a Ni(II) Compound with Schiff-Base Ligand, *Jiegou Huaxue*, 2017, **36**(8), 1315–1320, DOI: **10.14102/J.CNKI.0254-5861.2011-1522**.

20 L. Yan, W. Liu, M. J. Wang, Y. Xu and K. Z. Shi, Synthesis, Characterization, Oxygen Respiratory, Antibacterial Activity, and Photoluminescent Property Studies of One Novel Complex with Schiff-Base Ligand, *Jiegou Huaxue*, 2020, **39**(5), 895–900, DOI: **10.14102/J.CNKI.0254-5861.2011-2585**.

21 P. van der Sluis and A. L. Spek, BYPASS: An Effective Method for the Refinement of Crystal Structures Containing Disordered Solvent Regions, *Acta Crystallogr., Sect. A: Found. Crystallogr.*, 1990, **46**(3), 194–201, DOI: **10.1107/S0108767389011189**.

22 J. Moncol, Geometry index for 6-coordinate compounds, *Czech Chem. Soc. Symp. Ser.*, 2023, **21**, 147.

23 (*a*) A. W. Addison, T. N. Rao, J. Reedijk, J. van Rijn and G. C. Verschoor, Synthesis, Structure, and Spectroscopic Properties of Copper(II) Compounds Containing Nitrogen–sulphur Donor Ligands; the Crystal and Molecular Structure of Aqua[1,7-Bis(N-Methylbenzimidazol-2′-Yl)-2,6-Dithiaheptane] Copper(II) Perchlorate, *J. Chem. Soc., Dalton Trans.*, 1984, 1349–1356, DOI: **10.1039/DT9840001349**; (*b*) L. Yang, D. R. Powell and R. P. Houser, Structural Variation in Copper (I) Complexes with Pyridylmethylamide Ligands: Structural Analysis with a New Four-Coordinate Geometry Index, τ_4, *Dalton Trans.*, 2007, 955–964, DOI: **10.1039/B617136B**.

24 O. Kahn, *Molecular magnetism*, VCH, 1993.

25 S. Havriliak and S. Negami, A Complex Plane Representation of Dielectric and Mechanical Relaxation Processes in Some Polymers, *Polymer*, 1967, **8**(C), 161–210, DOI: **10.1016/0032-3861(67)90021-3**.

26 R. Boča and C. Rajnák, Unexpected Behavior of Single Ion Magnets, *Coord. Chem. Rev.*, 2021, **430**, 213657, DOI: **10.1016/j.ccr.2020.213657**.

27 S. Stoll and A. Schweiger, EasySpin, a Comprehensive Software Package for Spectral Simulation and Analysis in EPR, *J. Magn. Reson.*, 2006, **178**(1), 42–55, DOI: **10.1016/j.jmr.2005.08.013**.

28 M. Suzuki, I. S. Suzuki and J. Walter, Magnetism and superconductivity in $McTa_2S_2C$ (M=Fe, Co, Ni, and Cu), *Phys. Rev. B: Condens. Matter Mater. Phys.*, 2005, **71**(22), 224407, DOI: **10.1103/PhysRevB.71.224407**.

29 (*a*) N. Malinová, J. Juráková, B. Brachňaková, J. D. Midlíková, E. Čižmár, V. T. Santana, R. Herchel, M. Orlita, I. Mohelský, J. Moncol, P. Neugebauer and I. Šalitroš, Magnetization Slow Dynamics in Mononuclear Co(II) Field-Induced Single-Molecule Magnet, *Cryst. Growth Des.*, 2023, **23**(4), 2430–2441, DOI: **10.1021/acs.cgd.2c01388**; (*b*) J. Juráková, J. Dubnická Midlíková, J. Hrubý, A. Kliuikov, V. T. Santana, J. Pavlik, J. Moncoľ, E. Čižmár, M. Orlita, I. Mohelský, P. Neugebauer, D. Gentili, M. Cavallini and I. Šalitroš, Pentacoordinate Cobalt(II) Single Ion Magnets with Pendant Alkyl Chains: Shall We Go for Chloride or Bromide? Inorg, *Chem. Front.*, 2022, **9**(6), 1179–1194, DOI: **10.1039/D1QI01350E**.

30 R. A. D. Wentworth, Trigonal Prismatic vs. Octahedral Stereochemistry in Complexes Derived from Innocent Ligands, *Coord. Chem. Rev.*, 1972, **9**(1–2), 171–187, DOI: **10.1016/S0010-8545(00)80227-1**.

31 D. Dai, H. Xiang and M.-H. Whangbo, Effects of Spin-Orbit Coupling on Magnetic Properties of Discrete and Extended Magnetic Systems, *J. Comput. Chem.*, 2008, **29**(13), 2187–2209, DOI: **10.1002/jcc.21011**.

32 L. Yan and M.-J. Wang, Synthesis, Crystal Structures and Fluorescence of Two Zn(II) Complexes with Schiff Base Ligands, *Chin. J. Inorg. Chem.*, 2013, **29**(11), 2370–2374, DOI: **10.3969/j.issn.1001-4861.2013.00.351**.

33 M. Gruden-Pavlović, M. Perić, M. Zlatar and P. García-Fernández, Theoretical Study of the Magnetic Anisotropy and Magnetic Tunnelling in Mononuclear Ni(Ii) Complexes with Potential Molecular Magnet Behavior, *Chem. Sci.*, 2014, **5**(4), 1453, DOI: **10.1039/c3sc52984c**.

34 H.-S. Lv, S.-Y. Huang, Y. Xu, X. Dai, J.-Y. Miao and B.-X. Zhao, A New Fluorescent PH Probe for Imaging Lysosomes in Living Cells, *Bioorg. Med. Chem. Lett.*, 2014, **24**(2), 535–538, DOI: **10.1016/j.bmcl.2013.12.025**.

35 (*a*) F. Neese, The ORCA Program System, *Wiley Interdiscip. Rev.: Comput. Mol. Sci.*, 2012, **2**(1), 73–78, DOI: **10.1002/wcms.81**; (*b*) F. Neese, Software Update: The ORCA Program System, Version 4.0, *Wiley Interdiscip. Rev.: Comput. Mol. Sci.*, 2018, **8**(1), e1327, DOI: **10.1002/wcms.1327**; (*c*) F. Neese, Software Update: The ORCA Program System—Version 5.0, *Wiley Interdiscip. Rev.: Comput. Mol. Sci.*, 2022, **12**(5), e1606, DOI: **10.1002/wcms.1606**.

36 A. D. Becke, Density-Functional Exchange-Energy Approximation with Correct Asymptotic Behavior, *Phys. Rev. A*, 1988, **38**(6), 3098–3100, DOI: **10.1103/PhysRevA.38.3098**.

37 (*a*) F. Weigend and R. Ahlrichs, Balanced Basis Sets of Split Valence, Triple Zeta Valence and Quadruple Zeta Valence Quality for H to Rn: Design and Assessment of Accuracy, *Phys. Chem. Chem. Phys.*, 2005, **7**(18), 3297–3305, DOI: **10.1039/b508541a**; (*b*) F. Weigend, A Fully Direct RI-HF Algorithm: Implementation, Optimised Auxiliary Basis Sets, Demonstration of Accuracy and Efficiency, *Phys. Chem. Chem. Phys.*, 2002, **4**(18), 4285–4291, DOI: **10.1039/b204199p**.

38 (*a*) P. J. Stephens, F. J. Devlin, C. F. Chabalowski and M. J. Frisch, Ab Initio Calculation of Vibrational Absorption and Circular Dichroism Spectra Using Density Functional Force Fields, *J. Phys. Chem.*, 1994, **98**(45), 11623–11627, DOI: **10.1021/j100096a001**; (*b*) A. D. Becke, Density–functional Thermochemistry. III. The Role of Exact Exchange, *J. Chem. Phys.*, 1993, **98**(7), 5648–5652, DOI: **10.1063/1.464913**; (*c*) C. Lee, W. Yang and R. G. Parr, Development of the Colle-Salvetti Correlation-Energy Formula into a Functional of the Electron Density, *Phys. Rev. B: Condens. Matter Mater. Phys.*, 1988, **37**(2), 785–789, DOI: **10.1103/PhysRevB.37.785**; (*d*) S. H. Vosko, L. Wilk and M. Nusair, Accurate Spin-Dependent Electron Liquid Correlation Energies for Local Spin Density Calculations: A Critical Analysis, *Can. J. Phys.*, 1980, **58**(8), 1200–1211, DOI: **10.1139/p80-159**.

39 E. Caldeweyher, S. Ehlert, A. Hansen, H. Neugebauer, S. Spicher, C. Bannwarth and S. Grimme, A Generally Applicable Atomic-Charge Dependent London Dispersion

Correction, *J. Chem. Phys.*, 2019, **150**(15), 154122, DOI: **10.1063/1.5090222**.

40 Y. Guo, K. Sivalingam, E. F. Valeev and F. Neese, Explicitly Correlated N-Electron Valence State Perturbation Theory (NEVPT2-F12), *J. Chem. Phys.*, 2017, **147**(6), 064110, DOI: **10.1063/1.4996560**.

41 F. Neese, Efficient and Accurate Approximations to the Molecular Spin-Orbit Coupling Operator and Their Use in Molecular g-Tensor Calculations, *J. Chem. Phys.*, 2005, **122**(3), 034107, DOI: **10.1063/1.1829047**.

42 (*a*) L. Ungur, M. Thewissen, J.-P. Costes, W. Wernsdorfer and L. F. Chibotaru, Interplay of Strongly Anisotropic Metal Ions in Magnetic Blocking of Complexes, *Inorg. Chem.*, 2013, **52**(11), 6328–6337, DOI: **10.1021/ic302568x**; (*b*) L. F. Chibotaru and L. Ungur, Ab Initio Calculation of Anisotropic Magnetic Properties of Complexes. I. Unique Definition of Pseudospin Hamiltonians and Their Derivation, *J. Chem. Phys.*, 2012, **137**(6), 064112, DOI: **10.1063/1.4739763**; (*c*) L. Ungur, W. Van Den Heuvel and L. F. Chibotaru, Ab Initio Investigation of the Non-Collinear Magnetic Structure and the Lowest Magnetic Excitations in Dysprosium Triangles, *New J. Chem.*, 2009, **33**(6), 1224–1230, DOI: **10.1039/b903126j**; (*d*) L. F. Chibotaru, L. Ungur and A. Soncini, The Origin of Nonmagnetic Kramers Doublets in the Ground State of Dysprosium Triangles: Evidence for a Toroidal Magnetic Moment, *Angew. Chem., Int. Ed.*, 2008, **47**(22), 4126–4129, DOI: **10.1002/anie.200800283**; (*e*) L. F. Chibotaru, L. Ungur, C. Aronica, H. Elmoll, G. Pilet and D. Luneau, Structure, Magnetism, and Theoretical Study of a Mixed-Valence Co II3CoIII4 Heptanuclear Wheel: Lack of SMM Behavior despite Negative Magnetic Anisotropy, *J. Am. Chem. Soc.*, 2008, **130**(37), 12445–12455, DOI: **10.1021/ja8029416**; (*f*) L. F. Chibotaru, L. Ungur and A. Soncini, The Origin of Nonmagnetic Kramers Doublets in the Ground State of Dysprosium Triangles: Evidence for a Toroidal Magnetic Moment, *Angew. Chem., Int. Ed.*, 2008, **47**(22), 4126–4129, DOI: **10.1002/anie.200800283**.

43 (*a*) A. K. Dutta, F. Neese and R. Izsák, Accelerating the Coupled-Cluster Singles and Doubles Method Using the Chain-of-Sphere Approximation, *Mol. Phys.*, 2018, **116**(11), 1428–1434, DOI: **10.1080/00268976.2017.1416201**; (*b*) R. Izsák and F. Neese, An Overlap Fitted Chain of Spheres Exchange Method, *J. Chem. Phys.*, 2011, **135**(14), 144105, DOI: **10.1063/1.3646921**; (*c*) F. Neese, F. Wennmohs, A. Hansen and U. Becker, Efficient, Approximate and Parallel Hartree–Fock and Hybrid DFT Calculations. A 'Chain-of-Spheres' Algorithm for the Hartree–Fock Exchange, *Chem. Phys.*, 2009, **356**(1–3), 98–109, DOI: **10.1016/j.chemphys.2008.10.036**.

44 M. D. Hanwell, D. E. Curtis, D. C. Lonie, T. Vandermeersch, E. Zurek and G. R. Hutchison, Avogadro: An Advanced Semantic Chemical Editor, Visualization, and Analysis Platform, *J. Cheminf.*, 2012, **4**(1), 17, DOI: **10.1186/1758-2946-4-17**.

45 C. F. Macrae, P. R. Edgington, P. McCabe, E. Pidcock, G. P. Shields, R. Taylor, M. Towler and J. van de Streek, Mercury : Visualization and Analysis of Crystal Structures, *J. Appl. Crystallogr.*, 2006, **39**(3), 453–457, DOI: **10.1107/S002188980600731X**.

46 N. F. Chilton, R. P. Anderson, L. D. Turner, A. Soncini and K. S. Murray, PHI: A Powerful New Program for the Analysis of Anisotropic Monomeric and Exchange-Coupled Polynuclear d - and f -Block Complexes, *J. Comput. Chem.*, 2013, **34**(13), 1164–1175, DOI: **10.1002/jcc.23234**.

47 M. Liberka, M. Zychowicz, W. Zychowicz and S. Chorazy, Neutral Dicyanidoferrate(ii) Metalloligands for the Rational Design of Dysprosium(III) Single-Molecule Magnets, *Chem. Commun.*, 2022, **58**(44), 6381–6384, DOI: **10.1039/D2CC02238A**.

48 OpenAI ChatGPT (2023). **https://chat.openai.com/**. *ChatGPT 12 May version*.

Příloha 5: Bhanja, A.; Smythe, L.; Kotrle, K.; Ortu, F.; Herchel, R.; Murrie, M.; Ray, D. Synthesis of Heptanuclear Ni4Dy3 Coordination Aggregate Using Tridentate Ligand: X-Ray Structure, Magnetism and Theoretical Studies. *Inorganica Chim. Acta* 2021, *526*, 120524. https://doi.org/10.1016/j.ica.2021.120524.

Inorganica Chimica Acta 526 (2021) 120524

Contents lists available at ScienceDirect

Inorganica Chimica Acta

journal homepage: www.elsevier.com/locate/ica

Synthesis of heptanuclear Ni_4Dy_3 coordination aggregate using tridentate ligand: X-ray structure, magnetism and theoretical studies

Avik Bhanja [a], Lucy Smythe [b], Kamil Kotrle [c], Fabrizio Ortu [d], Radovan Herchel [c], Mark Murrie [b], Debashis Ray [a,*]

[a] Department of Chemistry, Indian Institute of Technology, Kharagpur 721302, India
[b] School of Chemistry, University of Glasgow, University Avenue, Glasgow G12 8QQ, UK
[c] Department of Inorganic Chemistry, Faculty of Science, Palacky University, Olomouc CZ-77146, Czech Republic
[d] Department of Chemistry, University of Leicester, Leicester LE1 7RH, UK

ARTICLE INFO

Keywords:
Schiff base
3d-4f complex
Aggregation
Magnetism
CASSCF calculation

ABSTRACT

The Schiff base ligand, 2-(((2-hydroxybenzyl)imino)methyl)phenol (H_2L) having ONO donor centres are utilized to synthesize $\{Ni_4Dy_3\}$ coordination aggregate following the support of six benzoate bridging groups. Sequential addition of $Dy(NO_3)_3{\cdot}6H_2O$ and $NiCl_2{\cdot}6H_2O$ to H_2L followed by $PhCO_2Na$ completes the coordination driven aggregation of heptanuclear $Na[Ni_4Dy_3(L)_4(\mu_3\text{-}OH)_4(\mu_{1,1,3,3}\text{-}PhCO_2)_2(\mu_{1,3}\text{-}PhCO_2)_4(CH_3OH)_4]{\cdot}CH_2Cl_2{\cdot}9H_2O$ (**1**) having 2,3,6M7 − 1 topology. Two adjacent perpendicular inverse Ni_2Dy_2 partial di-cubane units sharing a common vertex through the central Dy^{III} ion resulted a new structural arrangement within the Ni − Dy family of coordination aggregates. The complex shows no slow magnetic relaxation under zero applied fields and only shows a very weak field dependent magnetization. The DFT calculations revealed weak ferromagnetic exchange between benzoato-bridged Ni^{II} ions, whereas the CASSCF calculations were used to identify magnetic anisotropy in Ni^{II} and Dy^{III} ions resulting in low-lying excited states of Dy^{III} ions with significant probability for the quantum tunneling of the magnetization, which rationalize the observed fast dynamics in the magnetic properties.

1. Introduction

Choice and design of multidentate ligand plays a crucial role in coordination driven multinuclear complex formation. Presence of two different types of metal ions with different coordination preferences towards the anionic ligand and co-ligands, lead to a literature unknown coordination pathway for the formation of novel coordination aggregate. Synthetic endeavour to obtain such agglomerate of metal ions lead to the identification of new and aesthetically pleasing structures and properties. The search for such molecules having multiple paramagnetic metal ions of varying types led to the discovery of unique magnetic behaviour; potentially suitable for high density information storage [1,2], spintronics [3] and quantum computing [4]. Such compounds also find application in catalysis [5], unique luminescence behaviour [6,7] and quite often function as single molecule magnet (SMM) below a particular blocking temperature (T_B). [8] Following the first report of Mn_{12} aggregate as SMM [9], several ligand anions bound molecular aggregates have been reported in search of new SMMs which can be effective at higher temperature than the reported ones. [10–12] It is important to note that to behave a molecule as SMM, it must have large ground state spin, high energy barrier and most importantly significant single ion-anisotropy; [13] choice of suitable lanthanide ions thus come into play. The fast advances of Ln^{III} ions involving molecules, especially the Dy^{III} incorporating compounds are of huge interest exhibiting exceptional magnetic properties. [14–19] Use of organic ligand anions, having borderline and hard donor centres, can thus be appropriate for the growth of *3d–4f* aggregates with interesting magnetic behaviour. Amongst the 3d ions, choice of Ni^{II} ion is advantageous because of its appreciable contribution towards magnetic anisotropy [20] and for the interesting exchange interactions with the Dy^{III} ions within molecular aggregates. [21,22]

Synthetic control for such coordination aggregate is itself highly challenging as it depends on several factors like nature of ligand anion, stoichiometric ratio of added metal ions, choice of solvents, pH adjustment from the use of different bases, steric and electronic controls from ancillary ions etc. [23] Alteration of any of these factors is sufficient to change the composition and nature of the product along with its preferred shape and topology. The Lewis acidic nature of the Ln^{III} ions

* Corresponding author.
E-mail address: dray@chem.iitkgp.ernet.in (D. Ray).

https://doi.org/10.1016/j.ica.2021.120524
Received 24 March 2021; Received in revised form 1 July 2021; Accepted 7 July 2021
Available online 12 July 2021

also helps in the hydrolysis of the already coordinated water molecules [24] and in situ generation of hydroxido linkers, which again helps in constructing a multinuclear mineral like magnetic cage. [25] Several multinuclear $Ni^{II}Dy^{III}$ based coordination aggregates has been synthesized in the recent past which includes, Ni_6Dy_4 [26], Ni_8Dy_8 [27], Ni_5Dy_4 [28], Ni_6Dy_6 [29], Ni_6Dy_3 [30], Ni_5Dy_3 [31] having interesting topology such as butterfly, square grid, cube, star etc. Both terminal and central phenol group bearing Schiff bases have potential in synthesizing many Ni-Ln complexes through subtle control of reaction conditions. [32–35] However, fine tuning in the nuclearity of the aggregates and the effect of use of ancillary bridges on the size of the aggregate, still requires extensive synthetic endeavour.

Keeping all these factors in mind, we have focused our attention on synthesizing a flexible phenol-based ligand and its suitability to trap Ni^{II} and Dy^{III} ions with the support of small ancillary bridges (Scheme 1). Thus we have chosen, 2-(((2-hydroxybenzyl)imino)methyl)phenol (H_2L) to synthesize $Na[Ni_4Dy_3(L)_4(\mu_3\text{-}OH)_4(\mu_{1,1,3,3}\text{-}PhCO_2)_2(\mu_{1,3}\text{-}PhCO_2)_4(CH_3OH)_4]\cdot CH_2Cl_2\cdot 9H_2O$ (**1**) from bridging action of hydroxido and benzoate linkers. The present work reports detailed synthetic endeavour, basic spectroscopic characterization, structure determination, magnetic measurements and theoretical validation of the observed properties.

2. Experimental section

2.1. Starting materials

The chemical and reagents required in this work are of reagent grade and used as obtained. Salicylamine is prepared following a modified literature procedure. [36] The following starting materials were used without further purification: $NiCl_2\cdot 6H_2O$ and NEt_3 (S. D. Fine Chemicals, Mumbai, India), $Dy(NO_3)_3\cdot 6H_2O$ (Alfa Aesar, India), salicylaldehyde (Spectrochem Pvt. Ltd. Mumbai).

2.2. Synthesis of 2-((((2-hydroxybenzyl)imino)methyl)phenol (H_2L).

The Schiff base ligand H_2L has been synthesized by following a modified synthetic protocol (Scheme 2). [37] Salicylamine (0.61 g, 0.50 mmol) was dissolve into 20 mL MeOH solution and added dropwise into another MeOH solution (10 mL) of salicylaldehyde (0.61 g, 0.50 mmol). After complete addition, the solution was refluxed for 4 h at 80 °C. A yellow solid product was obtained after complete evaporation of solvent which was next dried under vacuum over fused $CaCl_2$ and P_4O_{10}. Yield: 92.1% (1.13 g). ^1H NMR (400 MHz, $CDCl_3$): 8.4 (s, 1H), 7.3–6.9 (t, 2H), 6.9–6.8 (d, 4H), 4.8 (s, 2H). Selected FT-IR data (KBr) cm^{-1}: 3443 (br), 1654 (s), 1607 (m), 1534 (m), 1477 (s), 1278 (s), 1236 (m), 1175 (w), 1144 (m), 1078 (m), 1037 (w), 723 (m). Anal. Calcd. for (%) $C_{14}H_{13}NO_2$ (226.25): C, 73.99; H, 5.77; N, 6.16. Found: C, 74.29; H, 5.71; N, 6.20.

2.3. Synthesis of $Na[Ni_4Dy_3(L)_4(\mu_3\text{-}OH)_4(\mu_{1,1,3,3}\text{-}PhCO_2)_2(\mu_{1,3}\text{-}PhCO_2)_4(CH_3OH)_4]\cdot CH_2Cl_2\cdot 9H_2O$ (1)

H_2L (0.023 g, 0.10 mmol) was dissolved in 10 mL of MeOH:CH_2Cl_2 (1:1, v/v) solvent mixture. A 5 mL of MeOH solution of $Dy(NO_3)_3\cdot 6H_2O$ (0.033 g, 0.075 mmol) and NEt_3 (0.022 g, 0.20 mmol) was added into the ligand solution. After 1 h of stirring, a 10 mL of MeOH solution of $NiCl_2\cdot 6H_2O$ (0.024 g, 0.10 mmol) was added into that solution and afterwards solid sodium benzoate (0.029 g, 0.20 mmol) was added. The bright green reaction mixture was next stirred for additional 4 h at room temperature, filtered and kept for slow evaporation at low temperature (10–15 °C) for crystallization. Green block shaped single crystals are isolated after a week from the mother liquor, which were characterized by single crystal X-ray structure determination. Yield: 0.024 g, 35% (based on Dy). Anal. Calcd for $C_{103}H_{113}Cl_2N_4NaDy_3Ni_4O_{37}$ (2815.20): C, 43.94; H, 4.05; N, 1.99. Found: C, 44.12; H, 4.10; N, 2.01. Selected FT-IR data (KBr) cm^{-1}: 3363 (br), 1650 (w), 1595 (s), 1556 (s), 1478 (s), 1403 (s), 1290 (m), 1160 (w), 1032 (w), 900 (w), 855 (w), 754 (m), 717 (s), 593 (w).

2.4. Physical measurements

Elemental analysis (C, H, N) of the powder complex were done using the Perkin – Elmer model 240C elemental analyzer. BRUKER D2 PHASER diffractrometer (30 kV/10 mA) were used for the powder X-ray diffraction analysis of the powder sample using Cu – Kα radiation (λ = 1.5418 Å) within 5–50° (2θ) range. For IR spectral measurement, a Perkin – Elmer model RX1 FT – IR spectrometer fitted with KBr disks has been used. Magnetic measurements were carried out on powdered crystalline samples restrained in eicosane using a Quantum Design MPMS 3 SQUID magnetometer. Data were corrected for the diamagnetic contribution of the sample holder and eicosane by measurements, and for the diamagnetism of the compound. [38]

2.5. Theoretical studies

The ORCA 4.2 computational software [39–41] was used for the theoretical calculations, which were based on the experimental X-ray structure complex anion of **1**, $[Ni_4Dy_3(L)_4(\mu_3\text{-}OH)_4(\mu_{1,1,3,3}\text{-}PhCO_2)_2(\mu_{1,3}\text{-}PhCO_2)_4(CH_3OH)_4]^-$, in which only hydrogen atoms positions were normalized in Mercury software. [42] The Douglas-Kroll-Hess Hamiltonian was used to treat relativistic effects [43,44] together with Gaussian finite nucleus model [45] and the increased radial integration accuracy for metal atoms was also set. We used DKH-def2-TZVP for Ni, SARC2-DKH-QZVP for Dy, SARC-DKH-TZVP for Lu and DKH-def2-SVP for all other atoms. [46,47] The auxiliary basis sets were SARC/J and generated by the AutoAux [48] and the chain-of-spheres (RIJCOSX) approximation to exact exchange was also used. [49,50] The state average complete active space self-consistent field (SA-CASSCF) wave functions calculations were done for systems having only one paramagnetic ion, thus Ni atoms were replaced with Zn, and Dy atoms were replaced by Lu. The active space defined by five d-orbitals/seven f-orbitals and respective number of electrons for nickel/dysprosium ions. The number of the involved multiplets was as follows: Ni^{II} – 10 triplets and 15 singlets, Dy^{III} – 21 sextets. The ɒ-tensors and g-tensors were evaluated with the effective Hamiltonian theory.

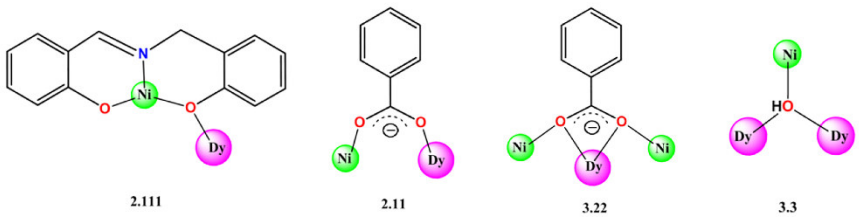

Scheme 1. Different coordination mode of L^{2-}, $PhCO_2^-$ and OH^- in complex 1.

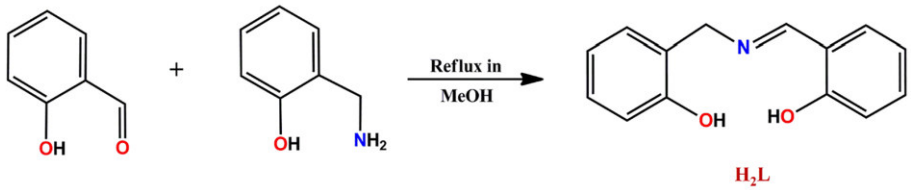

Scheme 2. Synthesis of H_2L.

2.6. X-ray structural studies

Single crystal X-ray structural study of complex **1** is performed in a Bruker SMART APEX-II CCD X-ray diffractometer equipped with a graphite-monochromated Mo-Kα (λ = 0.71073 Å) radiation by the ω scan (width of 0.3° frame^{-1}) at 114 K with a scan rate of 5 s per frame. SAINT, SMART and XPREP software's have been used for indexing, integration and space group determination. [51] Direct method using SHELXT 2014/5 [52] is used to solve crystal structures and refined by full-matrix least squares technique using SHELXL (2014/7) programs. [53] Empirical absorption corrections (multi-scan) were carried out using SADABS program. [54] All non-hydrogen atoms were refined with anisotropic displacement parameters while hydrogen atoms were incorporated at geometrical positions and were refined using the riding model. DIAMOND software was used for presenting the molecular structures. [55] The structure showed a solvent void filled with a number of electron density peaks due to disordered/diffuse solvent and cations; attempts to model this were not possible. Accordingly, the solvent mask routine in OLEX2 [56] was used to account for the contribution of the solvent. The volume and electron density were consistent with the presence of one sodium ion (for charge balance) and 9 water molecules (from the thermogravimetric analysis Fig. S1, ESI) per formula unit. Refinement parameters for complex **1** are summarized in Table 1 and crystallographic data (excluding structure factors) have been deposited with the Cambridge Crystallographic Data Centre as supplementary publications CCDC 2072451 (**1**).

Table 1
Crystallographic data and refinement parameter of complex **1**.

Parameters	Complex 1
Formula	$C_{103}H_{113}Cl_2N_4NaDy_3Ni_4O_{37}$
F.W.(g mol^{-1})	2815.20
crystal system	monoclinic
space group	*C2/c*
Crystal color	Green
a/ Å	22.38(3)
b/ Å	19.13(2)
c/ Å	26.06(3)
α/ deg	90
β/ deg	99.256(18)
γ/ deg	90
V/ Å^3	11012(24)
Z	4
D_c/g cm^{-3}	1.698
μ (mm^{-1})	2.815
F(0 0 0)	5640
Total reflections	66,526
Unique reflections	10,063
Observed reflections	6186
R(int)	0.1461
Parameters	699
R_1; wR_2 (I > 2σ(I))	0.0786, 0.2154
GOF (F^2)	1.042
Largest diff peak and hole (e Å^{-3})	1.391, −2.138
CCDC No.	2,072,451

3. Results and discussion

3.1. Ligand design strategy and synthetic aspects

Simple tridentate Schiff base ligands with ONO donor atoms are known for their potential to synthesize spontaneous self-assembled multinuclear aggregates. Few reports are there for the use of ONO donor Schiff bases with one or two phenolate moiety showing coordination trapping of 3d metal ions. [57–60] This type of ligand system is also useful in producing 4f [61] and *3d-4f* complexes [62]. Usually for coordinating both 3d and 4f ions simultaneously within one frame, –OMe substituted ligands were used severely. But earlier in 2014, Schiff base involving salicylaldehyde and 2-aminophenol, has been utilized to synthesize Ni_4Dy_3 coordination cluster without any MeO − backbone support. [63] Incorporation of extra $-CH_2$ spacer adjacent to imine nitrogen of ONO tridentate span increases the flexibility of the ligand backbone suitable for coordinating 3d ions without accomplishing its coordination demand, helps in synthesizing polynuclear complexes. [64] Previously we have also shown the advantages of the introduction of such flexible arm within ligand scaffold for synthesizing high nuclearity *3d-4f* complexes. [65,66]

Herein, we have synthesized 2-(((2-hydroxybenzyl)imino)methyl) phenol (H_2L) from salicylaldehyde and salicylamine to capture multiple numbers of Ni^{II} and Ln^{III} ions. Reaction of $Dy(NO_3)_3{\cdot}6H_2O$ and $NiCl_2{\cdot}6H_2O$ with H_2L and $PhCO_2Na$ in 1:1(v/v) MeOH:CH_2Cl_2 medium followed by crystallization, resulted $Na[Ni_4Dy_3(L)_4(\mu_3\text{-}OH)_4(\mu_{1,1,3,3}\text{-}PhCO_2)_2(\mu_{1,3}\text{-}PhCO_2)_4(CH_3OH)_4]{\bullet}CH_2Cl_2{\cdot}9H_2O$ (Scheme 3) according to eqn. 1.

$$4H_2L + 3Dy(NO_3)_3{\cdot}6H_2O + 4NiCl_2{\cdot}6H_2O + 6PhCO_2Na + 4CH_3OH + CH_2Cl_2 \rightarrow$$
$$Na[Ni_4Dy_3(L)_4(\mu_3\text{-}OH)_4(\mu_{1,1,3,3}\text{-}PhCO_2)_2(\mu_{1,3}\text{-}PhCO_2)_4(CH_3OH)_4]{\bullet}CH_2Cl_2{\cdot}9H_2O + 8Cl^- + 9NO_3^- + 5Na^+ + 12H^+ + 29H_2O \cdots \text{(eqn. 1)}$$

Infrared spectroscopic analysis was done for complex **1** which displays a broad band around 3363 cm^{-1} for O—H stretching frequencies originating from lattice H_2O, coordinated MeOH and bridging hydroxido groups. Ni^{II} ion bound imine groups show characteristic $-C{=}N-$ stretches at 1650 cm^{-1}, whereas for free ligand H_2L it appears around 1654 cm^{-1} (Fig. S2). Bridging benzoato groups of two categories record sharp asymmetric ($\nu_{a(COO)}$) stretching frequencies at 1595 cm^{-1} and 1556 cm^{-1}. The associated symmetric ($\nu_{a(COO)}$) stretching vibrations are found at 1290 cm^{-1} and 1403 cm^{-1}. The signatory differences (Δ) in $\nu_{a(COO)}$ and $\nu_{s(COO)}$ frequencies of 305 cm^{-1} and 153 cm^{-1} confirms the existence of both $\mu_{1,1,3,3}$ and $\mu_{1,3}$ modes of carboxylato couplers within the resulting coordination aggregates. [67] Bulk sample prepared in different batches are analysed by PXRD method. The experimental diffraction traces for **1** is in good agreement with the simulated pattern obtained by single crystal diffraction in favour of phase purity of the bulk compound (Fig. S3). We have tried to explore the crystallization protocol involving other Ln^{III} ions as well but the reaction pathway found very much metal ion (Dy^{III}) specific.

3.2. Structural depiction of complex *1*

The molecular structure of **1** is identified through single crystal X-ray diffraction studies and the complex crystalizes in monoclinic *C2/c* space

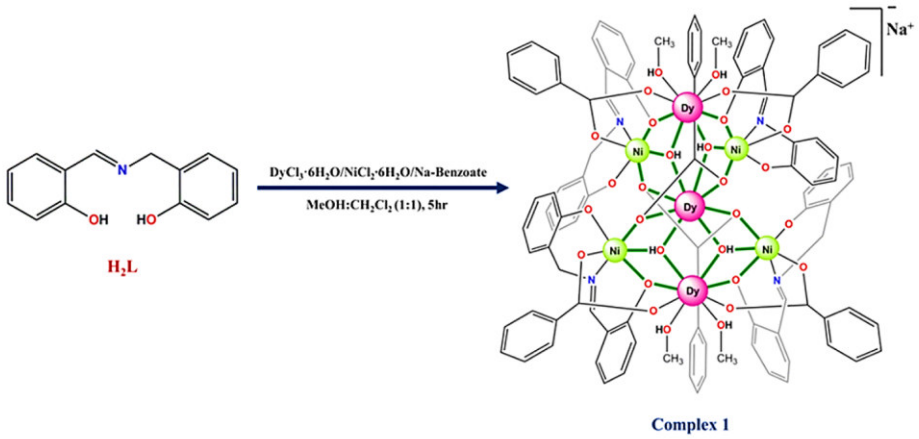

Scheme 3. Synthetic route for complex 1.

group with Z = 4. The overall formula of the molecular structure after the identification of lattice solvent molecules becomes, Na $[Ni_4Dy_3(L)_4(\mu_3\text{-}OH)_4(\mu_{1,1,3,3}\text{-}PhCO_2)_2(\mu_{1,3}\text{-}PhCO_2)_4(CH_3OH)_4]$ $\bullet CH_2Cl_2{\cdot}9H_2O$ (Fig. 1). The asymmetric unit of **1** is identified as $[Ni_2Dy_3(L)_2(\mu_3\text{-}OH)_2(\mu_{1,1,3,3}\text{-}PhCO_2)(\mu_{1,3}\text{-}PhCO_2)_2(CH_3OH)_2]$ (Fig. 2a). The selected bond lengths and bond angles are specified in Table S1-S2 of supporting information.

Detailed structural analysis confirms that the mono-anionic $\{Ni_4Dy_3\}$ aggregate is counterbalanced by a Na^+ ion. The aggregate contains four Ni^{II} and three Dy^{III} centres capped by four L^{2-} supports, each delivering ONO donor atoms. Characteristically each imine nitrogen donor binds each Ni^{II} centre within ONO pocket and bridges one Dy^{III} centre via the phenolato oxygen. Interestingly the phenoxido ends at the rigid imine side of L^{2-}, is utilized for establishing the Ni−O_{Ph}−Dy bridges and the other phenoxido ends remain mono-coordinated to Ni^{II} centres. The molecular core was built upon the peripheral supports from six benzoate linkers and four μ_3-HO^- bridging groups where two partial dicubane cores are remain fused. The $[Ni_4Dy_3O_{12}]^{7+}$ core is generated from the fusion of two Ni_2Dy_2 partial dicubane core on the wings over the central Dy3, having no support from ligand anion and act as connecting point of two perpendicular dicubanes (Fig. 2b). Both the two open dicubane units shows an "*inverse butterfly*" [68] topology where two Dy^{III} centres occupy the body position and two Ni^{II} centres positioned at the tip of the motif with separations of 5.626 and 5.654 Å. Such inverse butterfly topology is rare in Ni-Ln family of complexes.

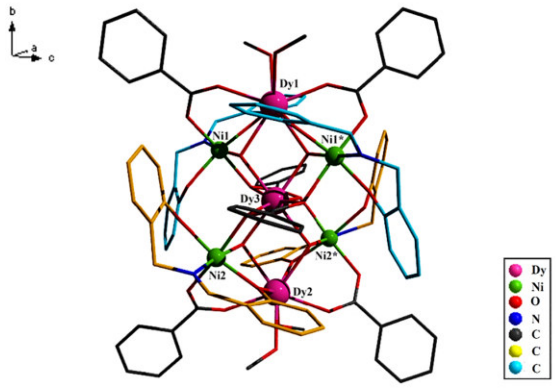

Fig. 1. Molecular structure of complex **1** where the ligand backbone is differently coloured depending upon their metal ion connectivity. Counter-ion, H-atoms and solvent molecules are removed for clarity.

Among the benzoate linkers, four are $\mu_{1,3}$ type connecting one Ni^{II} and one Dy^{III} centres while remaining two are of $\mu_{1,1,3,3}$ type and responsible for linking two Ni^{II} and one Dy^{III} centres (Fig. 2c). Within the two open-dicubane parts of the structure, a total four vertices are occupied by the four oxygen donors from two $\mu_{1,1,3,3}$-benzoato ligand having the longest Ni-O distances of 2.157(7) -2.181(7) Å, while the shortest distances are coming for Ni-$O_{phenoxido}$ bond within 2.010(7) -2.011(7) Å. All four Ni^{II} centres stays in distorted NO_5 octahedral environment (Fig. 3a and 3b) fulfilled from tridentate ONO coordination of each L^{2-} in *meridional* fashion, two O from benzoato site, and one μ_3-hydroxido group. The average Ni-N distances from imine nitrogen donors are lies within the range of 1.966(9) -1.971(9) Å. SHAPE 2.1 analysis also confirms the octahedral coordination geometry around each Ni^{II} centre (Table S3). Within the heptanuclear core structure the mean plane analysis revealed that all the three Dy^{III} centres are nearly co-planar. Within the two butterfly units, all four metal centres of each unit are coplanar, and two such planar units possess an angle of 70.09° to each other (Fig. S4).

Terminal bridging from phenoxido groups of ligand anion and several ancillary oxygen donors provide eight-coordinated environment towards the two terminal Dy^{III} centres Dy1 and Dy2. Both centres are coordinated by eight oxygen donor atoms in a slightly distorted trigonal dodecahedron environment (TDD-8) (Fig. 3c and 3d); CShM analysis, using SHAPE 2.1, gives values of 0.990 for Dy1 and 0.907 for Dy2 (Table S4). Two of the eight oxygen atoms come from two different L^{2-} ligands, two oxygen comes from two $\mu_{1,3}$-benzoato groups, there are two μ_3-OH groups while the seventh and eighth coordination sites come from two terminal MeOH donors. The central Dy3 centre remain in a symmetric environment occupied by four μ_3-hydroxido groups and four oxygen atoms from two $\mu_{1,1,3,3}$-benzoato groups (Fig. 3e). The SHAPE 2.1 calculation suggests a distorted cubic geometry (CU-8 = 2.164, Table S4). For Dy1 and Dy2, the Dy-O bonds lie within 2.308(8) - 2.457 (8) Å range where the shortest one is from benzoate oxygen (O5) and longest one is from MeOH oxygen (O14). Similarly Dy-O bond lengths around Dy3 remain within 2.298(7) -2.438(7) Å where the $\mu_{1,1,3,3}$-benzoate oxygen (O10) register the longest bond.

Within the molecular core, both the Dy1···Dy3 and Dy2···Dy3 distances are close by 3.862(5) and 3.836(5) Å respectively and the Ni···Dy separations are in shorter range within 3.402(4) -3.432(4) Å. The core structure gives ∠Dy1-O12-Dy3 and ∠Dy2-O11-Dy3 angles registering 109.3(3)° and 108.1(3)° respectively. Three different types of oxygen atoms record three different ∠Ni-O-Dy angles. The ∠Ni-O-Dy angles from

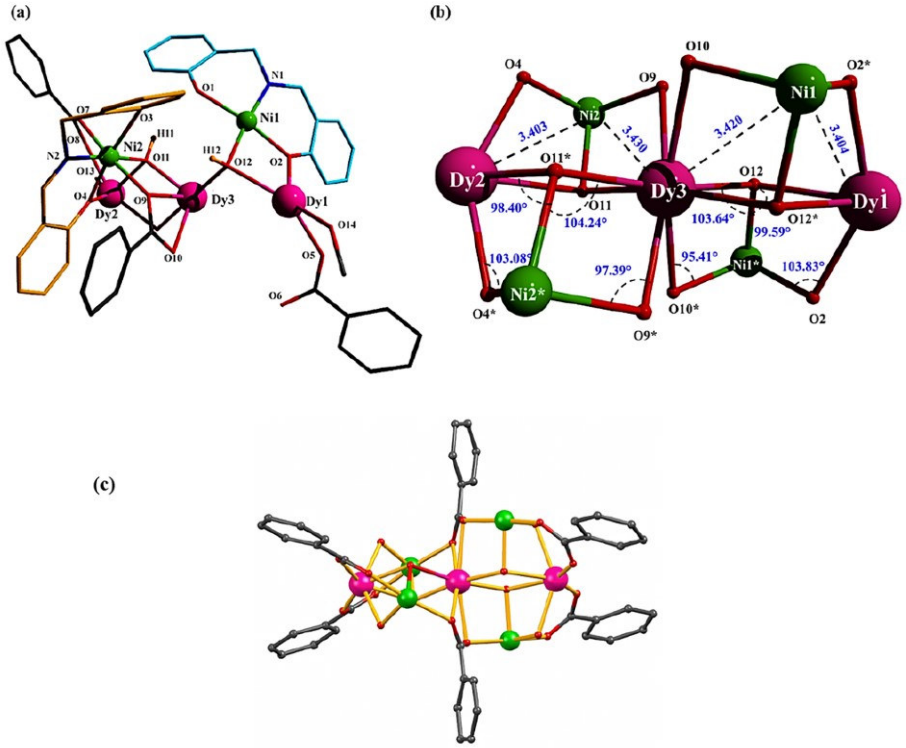

Fig. 2. (a) Asymmetric unit of complex **1**; (b) intermetallic distances (Å) and angles within $[Ni_4Dy_3O_{12}]$ core consisting of fused double partial dicubane units; (c) Ni_4Dy_3 aggregate holding by six benzoate linkers of two different types.

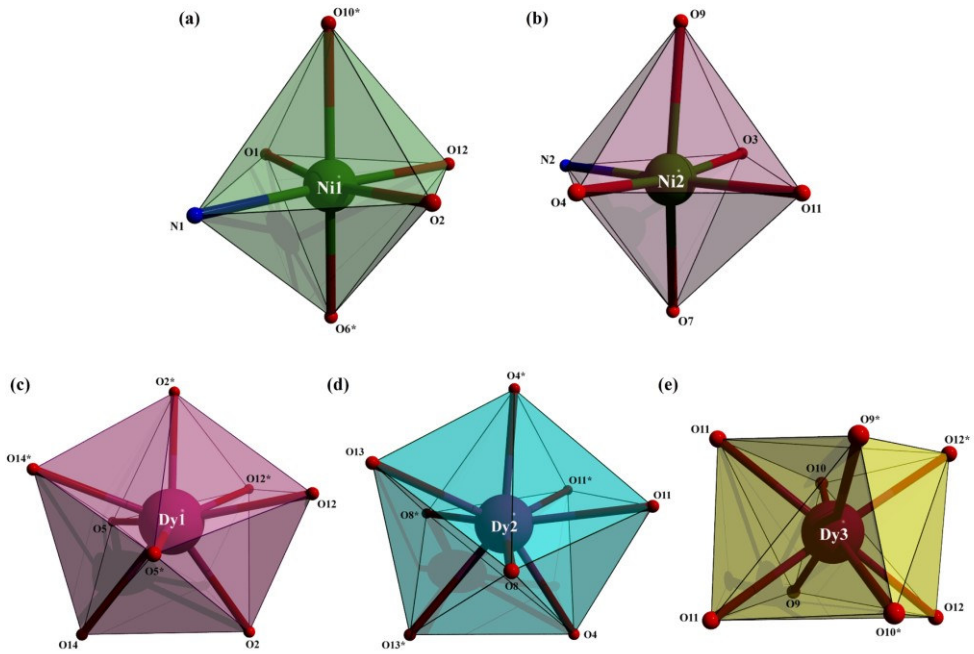

Fig. 3. (a and b) Distorted octahedral geometry around Ni1 and Ni2 centres; (c and d) Distorted trigonal dodecahedron geometry around Dy1 and Dy2 centres; and (e) Distorted cubic geometry around Dy3 centre.

bridging benzoato groups are the smallest at 95.4(3) -98.2(3)° range. The ∠Ni-O-Dy angles for phenoxido bridges and for hydroxido bridges remain within the range of 103.1(3) -103.6(4)° and 98.2(3) -104.2(3)° respectively. The Ni_4Dy_3 aggregate is assembled without any secondary H-bonding interactions. Only a weak hydrogen bonding contacts are present between the coordinated MeOH and lattice water molecules (Fig. S5).

3.3. Topological depiction

The topological description for the key structural features of **1** is identified using methods of Kostakis et al. [69–71] The analysis shown that the Ni_4Dy_3 aggregate can be described by the symbol 2,3,6M7 − 1. The 2,3,6M7 − 1 motif is comprised of four fused triangles; where each triangle consists of two Dy^{III} and one Ni^{II} node (Fig. 4). With respect to the central Dy^{III} node, the four Ni^{II} nodes forms a tetrahedral arrangement. The survey of the database [72] revealed that 2,3,6M7 − 1 motif is reported for Cu_5Gd_2 [73], Zn_6Na [74], Zn_7 [74] complexes, where the Zn_7 coordination polymer matches well with our topology.

3.4. Magnetic properties

The temperature dependent magnetic susceptibility data of complex **1**, plotted as χT vs. T, is shown in Fig. 5. The data were collected over a temperature range of 290–2 K in a magnetic field of 0.1 T. The experimental value of χT at 290 K is 47.9 $cm^3\ mol^{-1}$ K, consistent with the expected χT value for uncoupled spins (4 Ni^{II} ions and 3 Dy^{III} ions (g_{Dy} = 1.333 and g_{Ni} = 2.3) = 47.8 $cm^3\ mol^{-1}$ K). The χT value slowly decreases to 47.0 $cm^3\ mol^{-1}$ K at 90 K and then more sharply to a plateau of 44.1 $cm^3\ mol^{-1}$ K at 20 K, before decreasing further to a minimum of 41.3 $cm^3\ mol^{-1}$ K. For complex **1**, $M/N\beta$ = 23.5 at 2 K and 7 T (Fig. 5) and is not saturated due to the inherent magnetic anisotropy of the Dy^{III} and Ni^{II} ions.

The AC susceptibility values are measured over a temperature range of 40-2 K under zero dc field and under a field of 2000 Oe to probe whether the complex displayed slow relaxation of the magnetisation. No slow magnetic relaxation is observed under zero dc field (Fig. S7) and only a very small response below 3 K is seen under the applied dc field (Fig. S8), and therefore no further ac measurements were carried out. A {Ni_4Dy_3} complex with a different topology and containing one diamagnetic Ni(II) centre giving an effective {Ni_3Dy_3} unit shows intramolecular ferromagnetic interactions and the onset (no maxima in χ'') of slow relaxation of the magnetisation at low temperature. For this reported complex, no supporting theoretical studies were carried out so the origin of the slow relaxation and hence the difference in properties to **1** is not clear. [63]

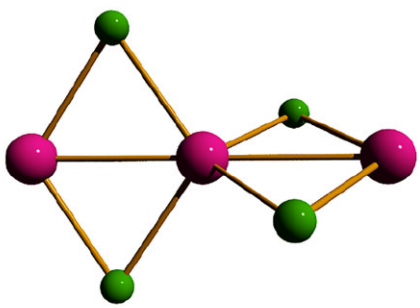

Fig. 4. 2,3,6M7 − 1 topological network for the present work. Green node; Ni^{II} and magenta node; Dy^{III} ions. (For interpretation of the references to color in this figure legend, the reader is referred to the web version of this article.)

3.5. Theoretical CASSCF calculations

The theoretical calculations are performed employing the ORCA 4.2 computational package for the complex anion $[Ni_4Dy_3(L)_4(\mu_3\text{-}OH)_4(\mu_{1,1,3,3}\text{-}PhCO_2)_2(\mu_{1,3}\text{-}PhCO_2)_4(CH_3OH)_4]^-$ of **1**. Herein, we focused on the study of the magnetic anisotropy of paramagnetic Ni^{II} and Dy^{III} ions. Due to multireference character of such metal complexes, the state-averaged complete active space self-consistent field (SA-CASSCF) method was employed. In these calculations, the active space was defined by eight electrons in five d-orbitals for Ni^{II}, which results in ten triplets and fifteen singlets. There are two crystallographically independent nickel atoms for which these CASSCF calculations were performed. First, ab initio ligand field theory (AILFT) [75,76] was used to analyze the energies of d-orbitals as showed in Fig. 6. The pattern is typical for octahedral complexes (set of t_{2g} and e_g orbitals), however, the degeneracy of e_g orbitals is removed due to lower symmetry of the ligand field.

The respective ligand field terms and multiplets are showed also in Fig. 6 confirming well separated ground state S = 1 with the zero-field splitting parameters: D = -13.9 cm^{-1} and E/D = 0.265 for Ni1 and D = -12.9 cm^{-1} and E/D = 0.205 for Ni2. Such values are in reasonable agreement with other O_h Ni^{II} complexes. [77] Next, the CASSCF calculations were done for all three crystallographically independent dysprosium atoms focusing on the ligand field induced splitting of $^6H_{15/2}$ state. The Fig. 7 is showing the splitting of f-orbitals and energies of ligand field multiplets. Dy1 and Dy2 ions have similar geometry of the coordination polyhedra, therefore, the calculated patterns of f-orbitals and multiplet energy levels are similar. The energies of the eight Kramers doublets are also listed in Table 2, together with g-tensor values of each doublet for S_{eff} = 1/2. The positive information deduced from these calculation is that lowest Kramers possess large axial symmetry ($g_{x,y}$ less than 0.5, $g_z \approx$ 18–19), however, $g_{x,y}$ components are quite large, thus the quantum tunneling of the magnetization is expected. Moreover, lowest excited states are rather close and have larger $g_{x,y}$ components too, which increases also probability of thermally-assisted quantum tunneling.

The analysis of the coordination polyhedra with the help of SHAPE resulted in the best match for TDD-8 and CU-8 shapes and therefore we have performed also CASSCF calculations for simple model complex $[DyF_8]^{5-}$ having these symmetries of the ligand field - Fig. 8. In case of TDD-8 symmetry, the ground state and first excited states are well energetically separated have significant axial anisotropy: g_x = 0.023, g_y = 0.023, g_z = 19.858 for the first Kramers doublet and g_x = 0.055, g_y = 0.055, g_z = 17.262 for the second Kramers doublet. On contrary, CU-8 symmetry provides three very close lying Kramers doublets separated by less than 3 cm^{-1} having also insufficient axial anisotropy: g_x = 7.555, g_y = 7.611, g_z = 7.659 for the first Kramers doublet, g_x = 3.333, g_y = 5.015, g_z = 11.306 for the second Kramers doublet and g_x = 1.200, g_y = 4.267, g_z = 12.028 for the third Kramers doublet. Thus, it can be concluded that TDD-8 is superior to CU-8, and the larger deviation from CU-8 symmetry for Dy3 atom than deviations of Dy1 and Dy2 atoms from TDD-8 (see section 3.2) is beneficial.

The magnetic properties of **1** is impossible to treat with incorporating interactions among paramagnetic ions due to very large number of spin states, $3^4 16^3$ = 5308416 and therefore only some aspects of the intra-cluster interactions can be evaluated. First, we discuss the dipole–dipole interactions between Dy^{III} ions. The respective orientations of g_z axes of ground Kramers doublets are displayed in Fig. 9. The dipole–dipole interactions are evaluated between Dy^{III} ions using well-known formula,

$$E_{ij}^{dipolar} = \frac{\mu_0}{4\pi r^3}\left[\vec{\mu}_i \cdot \vec{\mu}_j - 3\frac{\left(\vec{\mu}_i \cdot \vec{r}\right)\left(\vec{\mu}_j \cdot \vec{r}\right)}{r^2}\right] \quad (2)$$

where magnetic moments were calculated based on the orientation of g_z-

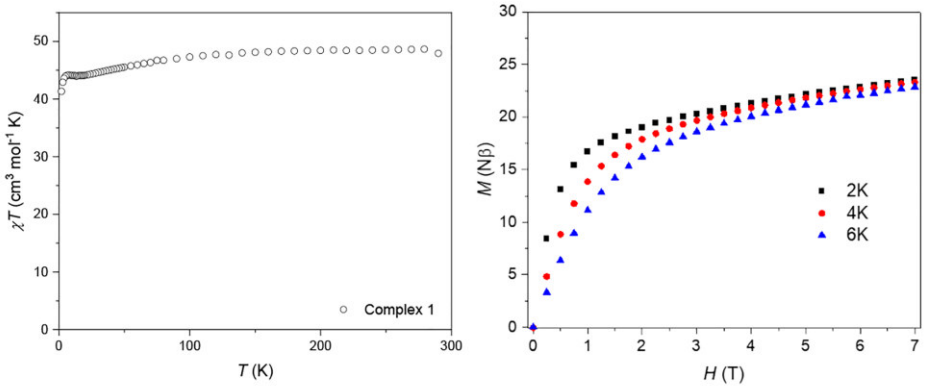

Fig. 5. Left: Temperature dependence of χT for complex **1**. Right: Magnetization vs. field data for complex **1** at 2, 4 and 6 K.

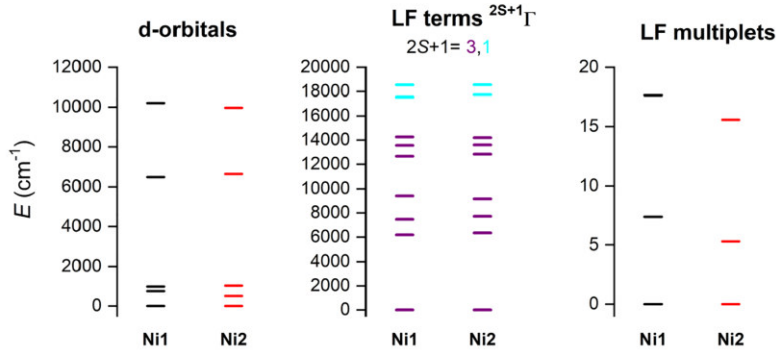

Fig. 6. The results of the CASSCF calculations with CAS(8,5) for Ni ions in complex anion of **1**. The plot of the d-orbitals splitting calculated by ab initio ligand field theory (AILFT) (left), low-lying ligand-field terms (middle), and ligand-field multiplets showing splitting of ground triplet state (right).

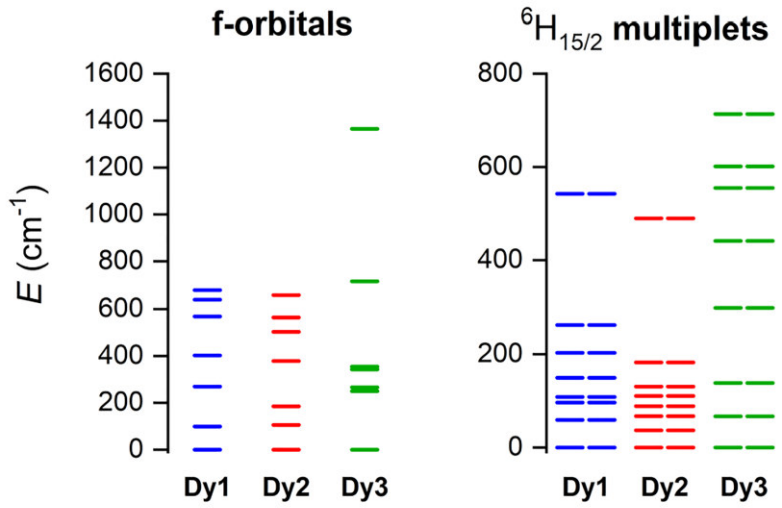

Fig. 7. The results of the CASSCF calculations with CAS(9,7) for Dy ions in complex anion of **1**. The plot of the f-orbitals splitting calculated by ab initio ligand field theory (AILFT) (left), and ligand-field multiplets showing splitting of $^{6}H_{15/2}$ state (right).

Table 2
The CASSCF calculated energies and parameters for Dy^{III} centres of **1.**

–	Dy1			Dy2			Dy3		
	ε(cm^{-1})	g_x, g_y, g_z	α (°)	ε(cm^{-1})	g_x, g_y, g_z	α (°)	ε (cm^{-1})	g_x, g_y, g_z	α (°)
1	0	0.088 0.096 19.440	0	0	0.238 0.329 19.133	0	0	0.039 0.332 18.216	0
2	59	0.348 0.400 15.513	39.5	37	0.156 0.366 16.406	117.0	67	2.362 4.328 12.664	180.0
3	96	0.009 0.088 19.719	131.8	67	2.519 8.810 9.215	155.6	138	0.945 5.994 9.672	180.0
4	108	1.131 3.128 11.484	24.1	89	0.112 3.344 8.248	47.4	300	0.411 6.915 7.513	180.0
5	150	5.110 6.406 7.542	90.0	111	0.146 0.832 15.579	126.2	441	2.081 5.684 7.133	90.0
6	203	0.456 0.811 10.349	101.1	131	0.307 1.675 10.802	95.7	555	0.692 5.155 13.577	90.0
7	262	0.125 0.506 14.575	110.6	182	0.081 0.158 15.350	64.7	601	1.879 2.066 14.589	90.0
8	542	0.000 0.001 19.668	122.9	490	0.002 0.002 19.792	127.3	714	0.094 0.904 16.368	90.0

[a]angle α is the angle between the g_z component of the lowest and the n^{th} Kramers pairs.

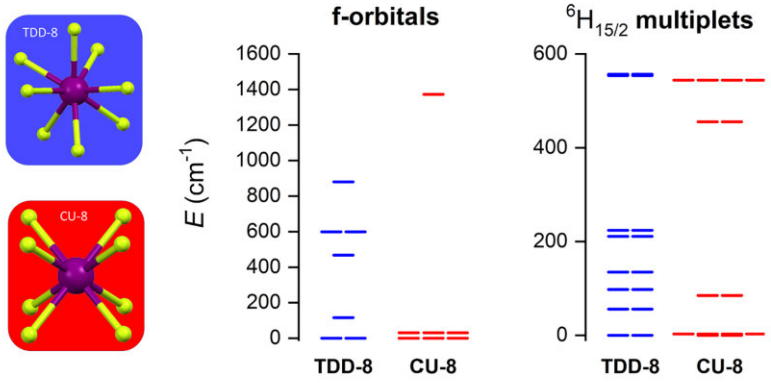

Fig. 8. The results of the CASSCF calculations with CAS(9,7) for model complex $[DyF_8]^{5-}$ with the ideal symmetry of the coordination polyhedron: triangular dodecahedron (TDD-8) and cube (CU-8). The plot of the f-orbitals splitting calculated by ab initio ligand field theory (AILFT) (left), and ligand-field multiplets showing splitting of $^6H_{15/2}$ state (right).

component of respective ground state Kramers doublets and r is the distance between two magnetic moments. The analysis provided us with these values: E_{13} = -1.96 × 10^{-5} cm^{-1}, E_{23} = 2.45 × 10^{-5} cm^{-1} and E_{12} = 0.35 cm^{-1}, suggesting a relatively strong ferromagnetic dipole interaction between Dy1 and Dy2, mostly due to very similar orientation of their magnetic moments, and negligible dipole interactions between adjacent ions.

Next, the isotropic exchange between Ni^{II} ions bridged by benzoate groups (Ni1-Ni2* and Ni1*-Ni2) were calculated by the broken-symmetry Density Functional Theory (DFT) using PBE0 hybrid functional [79] and the same basis sets as for previous CASSCF calculations. In this calculation, all other metals were replaced by their diamagnetic analogues. The the energy difference between high-spin (HS) and broken-symmetry (BS) spin states was calculated as $\triangle = E_{BS} - E_{HS}$ = 3.667 cm^{-1}, thus proposing ferromagnetic coupling. The exchange coupling J-parameter was calculated by Yamaguchi's approach, [80,81] which resulted in $J = 1.84$ cm^{-1} for the spin Hamiltonian formulated as $\hat{H} = -J(\vec{S}_1 \cdot \vec{S}_2)$ and the respective broken-symmetry spin density is depicted in Fig. 10. Thus, the last unknow interactions in **1** are the exchange interactions of the types Dy-Dy and Dy-Ni. They cannot be theoretically evaluated due to the lack of suitable theoretical approach for 4f-4f and 4f-3d coupling, in which the lanthanide can not be described by the spin Hamiltonian model. Moreover, the literature survey of smaller and therefore theoretically tractable Ni-Dy system with similar bridging ligands, for which Ni-Dy interactions were determined, was unsuccessful. This points to the fact that the investigation of 3d-4f coupling deserves more scientific exploration.

To summarize, the predispositions of **1** to behave as SMM are more likely enhanced by the ferromagnetic dipolar coupling between Dy1 and Dy2 ions and also by the ferromagnetic exchange coupling between Ni ions, but on other hand they are compromised by low lying excited states of Dy^{III} ions and significant non-zero values of $g_{x,y}$ of the respective Kramers doublets, and quite large rhombicity of Ni^{II} ions, which all speeds up the QTM process.

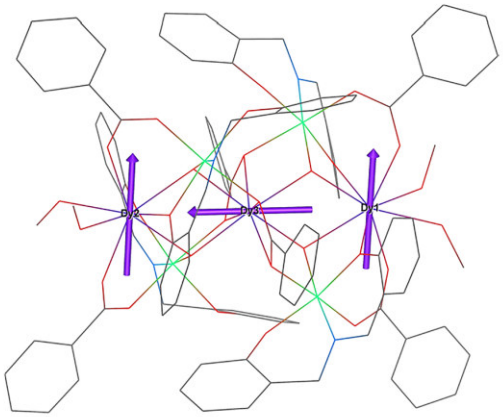

Fig. 9. The molecular structure of complex anion of **1** overlaid with violet arrows representing the g_z-axis of ground state Kramer doublet of respective Dy atoms determined by CASSCF calculations visualized with VESTA 3 program. [78]

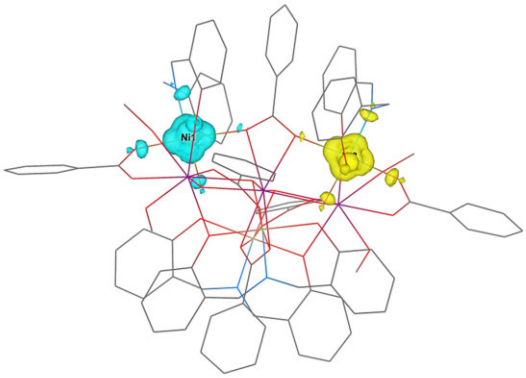

Fig. 10. The calculated spin density distribution using PBE0 functional for anionic complex of **1** for the broken-symmetry state. Positive and negative spin density is represented by yellow and cyan surfaces, respectively. The isodensity surfaces are plotted with the cut-off value of 0.01 ea_0^{-3}. Hydrogen atoms are omitted for clarity.

4. Conclusion

The tridentate ONO donor ligand 2-(((2-hydroxybenzyl)imino) methyl)phenol, in the presence of ancillary bridging upon progressive reaction with $Dy(NO_3)_3{\cdot}6H_2O$ and $NiCl_2{\cdot}6H_2O$ unfolded the aggregation path to synthesize $\{Ni_4Dy_3\}$ complex. Hydrolytic reaction condition favoured the most readily self-assembling heptanuclear conglomerate **1** bearing four ligand anions, four Ni^{II} and three Dy^{III} ions. Benzoate and hydroxido linkers supported the molecular core which has a unique topology where two nearly perpendicular inverse butterfly subunits, fused at the central Dy^{III} centre. Complex shows an overall weak ferromagnetic exchange coupling in the low temperature regime. No slow magnetic relaxation observed under zero dc field and only a slight response below 3 K realised under the applied dc field. Theoretical calculations exclude large U_{eff} for the system due to the presence of low-lying excited states with insufficient axial magnetic anisotropy.

Declaration of Competing Interest

The authors declare that they have no known competing financial interests or personal relationships that could have appeared to influence the work reported in this paper.

Acknowledgements

A.B. is thankful to DST-INSPIRE for the research fellowship. R.H. and K.K. acknowledge the financial support from the institutional sources of the Department of Inorganic Chemistry, Palacký University Olomouc, Czech Republic. M.M. thanks the University of Glasgow for financial support. We acknowledge FIST program of DST, New Delhi for the SC-XRD facility at the Department of Chemistry, IIT Kharagpur.

Appendix A. Supplementary data

CCDC 2072451 contains the crystallographic data for **1**. The electronic supplementary information (ESI) file contains TGA, FTIR, PXRD curve, packing diagram, selected bond lengths and angles, SHAPE 2.1 analysis and AC susceptibility plots described in Figure S1−S7 and Tables S1−S4 in the text. Supplementary data to this article can be found online at https://doi.org/10.1016/j.ica.2021.120524.

References

[1] D. Gatteschi, R. Sessoli, J. Villain, Molecular Nanomagnets, Oxford University Press, Oxford, U. K., 2006.
[2] D. Gatteschi, Adv. Mater. 6 (1994) 635–645, https://doi.org/10.1002/adma.19940060903.
[3] L. Bogani, W. Wernsdorfer, Nat. Mater. 7 (2008) 179–186, https://doi.org/10.1038/nmat2133.
[4] M.N. Leuenberger, D. Loss, Nature 410 (2001) 789–793, https://doi.org/10.1038/35071024.
[5] G. Gao, L. Wang, R. Zhang, C. Xu, H. Yang, W. Liu, Dalton Trans. 48 (2019) 3941–3945, https://doi.org/10.1039/C8DT05048A.
[6] W.-K. Wong, H. Liang, W.-Y. Wong, Z. Cai, K.-F. Li, K.-W. Cheah, New J. Chem. 26 (2002) 275–278, https://doi.org/10.1039/B104175B.
[7] T. Gao, P.-F. Yan, G.-M. Li, G.-F. Hou, J.-S. Gao, Inorg. Chim. Acta 361 (2008) 2051–2058, https://doi.org/10.1016/j.ica.2007.10.021.
[8] Y. Li, Q. Shang, Y.-Q. Zhang, E.–C. Yang, X.–J. Zhao,, Chem. Eur. J. 22 (2016) 18840–18849, https://doi.org/10.1002/chem.201603800.
[9] R. Sessoli, H.-L. Tsai, A.R. Schake, S. Wang, J.B. Vincent, K. Folting, D. Gatteschi, G. Christou, D.N. Hendrickson, J. Am. Chem. Soc. 115 (1993) 1804–1816, https://doi.org/10.1021/ja00058a027.
[10] C.J. Milios, A. Vinslava, A.G. Whittaker, S. Parsons, W. Wernsdorfer, G. Christou, S. P. Perlepes, E.K. Brechin, Inorg. Chem. 45 (2006) 5272–5274, https://doi.org/10.1021/ic0606678.
[11] M. Hołyńska, D. Premužić, I.-R. Jeon, W. Wernsdorfer, R. Clérac, S. Dehnen, Chem.-Eur. J. 17 (2011) 9605–9610, https://doi.org/10.1002/chem.201101807.
[12] K.C. Mondal, A. Sundt, Y. Lan, G.E. Kostakis, O. Waldmann, L. Ungur, L. F. Chibotaru, C.E. Anson, A.K. Powell, Angew. Chem., Int. Ed. 51 (2012) 7550–7554, https://doi.org/10.1002/anie.201201478.
[13] J.D. Rinehart, J.R. Long, Chem. Sci. 2 (2011) 2078–2085, https://doi.org/10.1039/C1SC00513H.
[14] V. Chandrasekhar, S. Das, A. Dey, S. Hossain, J.-P. Sutter, Inorg. Chem. 52 (2013) (1965) 11956–11961, https://doi.org/10.1021/ic401652f.
[15] W.-M. Wang, X.-M. Kang, H.-Y. Shen, Z.-L. Wu, H.-L. Gao, J.-Z. Cui, Inorg. Chem. Front. 5 (2018) 1876–1885, https://doi.org/10.1039/C8QI00214B.
[16] W.-M. Wang, X.-Z. Li, L. Zhang, J.-L. Chen, J.-H. Wang, Z.-L. Wu, J.-Z. Cui, New J. Chem. 43 (2019) 7419–7426, https://doi.org/10.1039/C8NJ04454F.
[17] W.-M. Wang, L.-Y. He, X.-X. Wang, Y. Shi, Z.-L. Wu, J.-Z. Cui, Dalton Trans. 48 (2019) 16744–16755, https://doi.org/10.1039/C9DT03478A.
[18] W.-M. Wang, C.-L. Xue, R.-Y. Jing, X. Ma, L.-N. Yang, S.-C. Luo, Z.-L. Wu, New J. Chem. 44 (2020) 18025–18030, https://doi.org/10.1039/D0NJ03442H.
[19] S. Zhang, J. Tang, J. Zhang, F. Xu, S. Chen, D. Hu, B. Yin, J. Zhang, Inorg. Chem. 60 (2021) 816–830, https://doi.org/10.1021/acs.inorgchem.0c02863.
[20] S.K. Singh, T. Gupta, P. Badkur, G. Rajaraman, Chem. Eur. J. 20 (2014) 10305–10313, https://doi.org/10.1002/chem.201402694.
[21] A. Bhanja, M. Schulze, R. Herchel, E. Moreno-Pineda, W. Wernsdorfer, D. Ray, Inorg. Chem. 59 (2020) 17929–17944, https://doi.org/10.1021/acs.inorgchem.9b01517.
[22] K.C. Mondal, G.E. Kostakis, Y. Lan, W. Wernsdorfer, C.E. Anson, A.K. Powell, Inorg. Chem. 50 (2011) 11604–11611, https://doi.org/10.1021/ic2015397.
[23] R.E.P. Winpenny, J. Chem. Soc. Dalton Trans. (2002) 1–10, https://doi.org/10.1039/B107118C.
[24] Z. Zhang, Y. Zhang, Z. Zheng, Lanthanide Hydroxide Cluster Complexes via Ligand Controlled Hydrolysis of the lanthanide Ions, Struct. Bond. 173 (2017) 1–49.
[25] R. Wang, H. Liu, M.D. Carducci, T. Jin, C. Zheng, Z. Zheng, Inorg. Chem. 40 (2001) 2743–2750, https://doi.org/10.1021/ic001469y.
[26] H.-M. Dong, Y. Li, Z.-Y. Liu, E.-C. Yang, X.-J. Zhao, Dalton Trans. 45 (2016) 11876–11882, https://doi.org/10.1039/C6DT02003H.

[27] C. Papatriantafyllopoulou, T.C. Stamatatos, C.G. Efthymiou, L. Cunha-Silva, F.A. A. Paz, S.P. Perlepes, G. Christou, Inorg. Chem. 49 (2010) 9743–9745, https://doi.org/10.1021/ic101581g.
[28] F. Shao, J.-J. Zhuang, M.-G. Chen, N. Wang, H.-Y. Shi, J.-P. Tong, G. Luo, J. Tao, L.-S. Zheng, Dalton Trans. 47 (2018) 16850–16854, https://doi.org/10.1039/C8DT04153A.
[29] D.I. Alexandropoulos, L.C.- Silva, G. Lorusso, M. Evangelisti, J. Tang, T. C. Stamatatos, Chem. Commun. 52 (2016) 1693–1696, https://doi.org/10.1039/C5CC09385F.
[30] A.B. Canaj, D.I. Tzimopoulos, M. Siczek, T. Lis, R. Inglis, C.J. Milios, Inorg. Chem. 54 (2015) 7089–7095, https://doi.org/10.1021/acs.inorgchem.5b01149.
[31] H. Wang, H. Ke, S.Y. Lin, Y. Guo, L. Zhao, J. Tang, Y.-H. Li, Dalton Trans. 42 (2013) 5298–5303, https://doi.org/10.1039/C3DT32572E.
[32] S. Biswas, J. Goura, S. Das, C.V. Topping, J. Brambleby, P.A. Goddard, V. Chandrasekhar, Inorg. Chem. 55 (2016) 8422–8436, https://doi.org/10.1021/acs.inorgchem.6b01019.
[33] A. Bhanja, R. Herchel, Z. Travnícek, D. Ray, Inorg. Chem. 58 (2019) 12184–12198, https://doi.org/10.1021/acs.inorgchem.9b01517.
[34] Z.-S. Meng, F.-S. Guo, J.-L. Liu, J.-D. Leng, M.-L. Tong, Dalton Trans. 41 (2012) 2320–2329, https://doi.org/10.1039/C1DT10869G.
[35] A. Vráblová, M. Tomás, L.R. Falvello, L. Dlháň, J. Titiš, J. Černák, R. Boča, Dalton Trans. 48 (2019) 13943–13952, https://doi.org/10.1039/C9DT02122A.
[36] I. Zagol-Ikapitte, V. Amarnath, M. Bala, L.J. Roberts, J.A. Oates, O. Boutaud, Chem. Res. Toxicol. 23 (2010) 240–250, https://doi.org/10.1021/tx900407a.
[37] M.E. Moustafa, Synth. React. Inorg. Met.-Org. Chem. 33 (2003) 453, https://doi.org/10.1081/SIM-120019998.
[38] K. Lahn, Molecular Magnetism, VCH Publishers, New York, 1993.
[39] F. Neese, Wiley Interdiscip. Rev. Comput. Mol. Sci. 2 (2012) 73–78, https://doi.org/10.1002/wcms.81.
[40] F. Neese, Wiley Interdiscip. Rev. Comput. Mol. Sci. 8 (2018), e1327, https://doi.org/10.1002/wcms.1327.
[41] F. Neese, F. Wennmohs, U. Becker, C. Riplinger, J. Chem. Phys. 152 (2020), 224108, https://doi.org/10.1063/5.0004608.
[42] C.F. Macrae, I. Sovago, S.J. Cottrell, P.T.A. Galek, P. McCabe, E. Pidcock, M. Platings, G.P. Shields, J.S. Stevens, M. Towler, P.A. Wood, J. Appl. Cryst. 53 (2020) 226–235, https://doi.org/10.1107/S1600576719014092.
[43] M. Douglas, N.M. Kroll, Ann. Phys. (N. Y). 82 (1974) 89–155, https://doi.org/10.1016/0003-4916(74)90333-9.
[44] B.A. Hess, Phys. Rev. A 33 (1986) 3742–3748, https://doi.org/10.1103/PhysRevA.33.3742.
[45] L. Visscher, K.G. Dyall, Atom. Data Nucl. Data Tables 67 (1997) 207–224, https://doi.org/10.1006/adnd.1997.0751.
[46] F. Weigend, R. Ahlrichs, Phys. Chem. Chem. Phys. 7 (2005) 3297–3305, https://doi.org/10.1039/B508541A.
[47] D. Aravena, F. Neese, D.A. Pantazis, J. Chem. Theory Comput. 12 (2016) 1148–1156, https://doi.org/10.1021/acs.jctc.5b01048.
[48] G.L. Stoychev, A.A. Auer, F. Neese, J. Chem. Theory Comput. 13 (2017) 554–562, https://doi.org/10.1021/acs.jctc.6b01041.
[49] F. Neese, F. Wennmohs, A. Hansen, U. Becker, Chem. Phys. 356 (2009) 98–109.
[50] R. Izsák, F. Neese, J. Chem. Phys. 135 (2011), 144105, https://doi.org/10.1063/1.3646921.
[51] SAINT, SMART and XPREP, Siemens Analytical X-ray Instruments Inc., Madison, WI, 1995.
[52] G.M. Sheldrick, SHELXT - Integrated space-group and crystal-structure determination, Acta Cryst. A71 (2015) 3–8, https://doi.org/10.1107/S2053273314026370.
[53] G.M. Sheldrick, Crystal structure refinement with SHELXL, Acta Cryst. C71 (2015) 3–8, https://doi.org/10.1107/S2053229614024218.
[54] G.M. Sheldrick, SADABS Software for Empirical Absorption Correction; Institute fur Anorganische Chemieder Universitat, University of Göttingen, Göttingen, Germany, 1999–2003..
[55] DIAMOND, Visual Crystal Structure Information System, version 3.1; Crystal Impact: Bonn, Germany, 2004.
[56] O.V. Dolomanov, L.J. Bourhis, R.J. Gildea, J.A.K. Howard, H. Puschmann, J. Appl. Cryst. 42 (2009) 339–341, https://doi.org/10.1107/S0021889808042726.
[57] K.I. Alexopoulou, A. Terzis, C.P. Raptopoulou, V. Psycharis, A. Escuer, S. P. Perlepes, Inorg. Chem. 54 (2015) 5615–5617, https://doi.org/10.1021/acs.inorgchem.5b00521.
[58] A.K. Dutta, S. Biswas, S. Dutta, L.N. Dawe, C.R. Lucas, B. Adhikary, Inorg. Chim. Acta 444 (2016) 141–149, https://doi.org/10.1016/j.ica.2016.01.036.
[59] M. Nihei, N. Hoshino, T. Ito, H. Oshio, Polyhedron 22 (2003) 2359–2362, https://doi.org/10.1016/S0277-5387(03)00159-1.
[60] A. Sieber, C. Boskovic, R. Bircher, O. Waldmann, S.T. Ochsenbein, G. Chaboussant, H.U. Gudel, N. Kirchner, J.v. Slageren, W. Wernsdorfer, A. Neels, H. Stoeckli-Evans, S. Janssen, F. Juranyi, H. Mutka, Inorg. Chem. 44 (2005) 4315–4325, https://doi.org/10.1021/ic050134j.
[61] S. Mukherjee, J. Lu, G. Velmurugan, S. Singh, G. Rajaraman, J. Tang, S.K. Ghosh, Inorg. Chem. 55 (2016) 11283–11298, https://doi.org/10.1021/acs.inorgchem.6b01863.
[62] D.I. Alexandropoulos, T.N. Nguyen, L. Cunha-Silva, T.F. Zafiropoulos, A. Escuer, G. Christou, T.C. Stamatatos, Inorg. Chem. 52 (2013) 1179–1181, https://doi.org/10.1021/ic302505p.
[63] S. Mukherjee, B. Joarder, S. Xue, J. Tang, S.K. Ghosh, Proc. Natl. Acad. Sci. India, Sect. A Phys. Sci. 84 (2014) 151–156, https://doi.org/10.1007/s40010-013-0116-2.
[64] C. Yang, Q.-L. Wang, G.-T. Tang, C. Wang, S.-P. Yan, D.-Z. Liao, J. Coord. Chem. 63 (2010) 505–514, https://doi.org/10.1080/00958970903509277.
[65] A. Bhanja, E. Moreno-Pineda, R. Herchel, W. Wernsdorfer, D. Ray, Dalton Trans. 49 (2020) 7968–7976, https://doi.org/10.1039/D0DT01675F.
[66] A. Bhanja, L. Smythe, R. Herchel, I. Nemec, M. Murri, D. Ray, Dalton Trans. (2021) in press, https://doi.org/10.1039/D0DT04168H.
[67] K. Nakamoto, in Infrared Spectra of Inorganic and Coordination Compounds, 4th edn, Wiley Interscience, New York, 1986.
[68] G. Abbas, M. Ibrahim, S.F.M. Schmidt, E. Moreno-Pineda, C.E. Anson, A.K. Powell, Polyhedron 158 (2019) 255–261, https://doi.org/10.1016/j.poly.2018.06.051.
[69] G.E. Kostakis, V.A. Blatov, D.M. Proserpio, Dalton Trans. 41 (2012) 4634–4640, https://doi.org/10.1039/C2DT12263D.
[70] G.E. Kostakis, I.J. Hewitt, A.M. Ako, V. Mereacre, A.K. Powell, Phil. Trans. R. Soc. A 368 (2010) 1509–1536, https://doi.org/10.1098/rsta.2009.0279.
[71] G.E. Kostakis, A.K. Powell, Coord. Chem. Rev. 253 (2009) 2686–2697, https://doi.org/10.1016/j.ccr.2009.05.002.
[72] http://www.sussex.ac.uk/lifesci/k ostakislab/picd/ (retrieved April 28, 2015).
[73] G. Wu, I.J. Hewitt, S. Mameri, Y. Lan, R. Clerac, C.E. Anson, S. Qiu, A.K. Powell, Inorg. Chem. 46 (2007) 7229–7231, https://doi.org/10.1021/ic070296a.
[74] L. Hou, J.-P. Zhang, X.-M. Chen, S.W. Ng, Chem. Commun. (2008) 4019–4021, https://doi.org/10.1039/B809069F.
[75] M. Atanasov, D. Ganyushin, K. Sivalingam, F. Neese, in: Molecular Electronic Structures of Transition Metal Complexes II, Springer, Berlin Heidelberg, Berlin, Heidelberg, 2012, pp. 149–220.
[76] S.K. Singh, J. Eng, M. Atanasov, F. Neese, Coord. Chem. Rev. 344 (2017) 2–25, https://doi.org/10.1016/j.ccr.2017.03.018.
[77] J. Titiš, R. Boča, Inorg. Chem. 49 (2010) 3971–3973, https://doi.org/10.1021/ic902569z.
[78] K. Momma, F. Izumi, J. Appl. Crystallogr. 44 (2011) 1272–1276, https://doi.org/10.1107/S0021889811038970.
[79] C. Adamo, V. Barone, J. Chem. Phys. 110 (1999) 6158–6170, https://doi.org/10.1063/1.478522.
[80] K. Yamaguchi, Y. Takahara, T. Fueno in: V.H. Smith (Ed.) Applied Quantum Chemistry. Reidel, Dordrecht, 1986, pp 155−184. https://doi.org/10.1007/978-94-009-4746-7_11.
[81] T. Soda, Y. Kitagawa, T. Onishi, Y. Takano, Y. Shigeta, H. Nagao, Y. Yoshioka, K. Yamaguchi, Chem. Phys. Lett. 319 (2000) 223–230, https://doi.org/10.1016/S0009-2614(00)00166-4.

Příloha 6: Dutta, B.; Guizouarn, T.; Pointillart, F.; Kotrle, K.; Herchel, R.; Ray, D. Lanthanoid Coordination Prompts Unusually Distorted Pseudo-Octahedral Ni^{II} Coordination in Heterodinuclear Ni–Ln Complexes: Synthesis, Structure and Understanding of Magnetic Behaviour through Experiment and Computation. *Dalt. Trans.* 2023, *52* (30), 10402–10414. https://doi.org/10.1039/D3DT01387A.

Dalton Transactions

ROYAL SOCIETY OF CHEMISTRY

PAPER

View Article Online
View Journal | View Issue

Cite this: *Dalton Trans.*, 2023, **52**, 10402

Lanthanoid coordination prompts unusually distorted pseudo-octahedral Ni^{II} coordination in heterodinuclear Ni–Ln complexes: synthesis, structure and understanding of magnetic behaviour through experiment and computation†

Biswarup Dutta,[a] Thierry Guizouarn,[b] Fabrice Pointillart, [b] Kamil Kotrle, [c] Radovan Herchel [c] and Debashis Ray *[a]

In this work, a new family of binuclear Ni^{II}–Ln^{III} complexes with the formula $[NiLn(L)_2(NO_3)_3]\cdot 0.5H_2O$ (Ln = Gd, **1**; Tb, **2**; Dy, **3**; Ho, **4**; Er, **5**; Yb, **6**; Y, **7**) was synthesized using a thioether group-bearing Schiff base. Due to the strict hard/soft dichotomy between the 4f and 3d metal ions, selective coordination of Ni^{II} and 4f metal ions was achieved with the adjacent soft ONS and hard OO binding pockets of the ligand. All the complexes **1–7** exhibit a Ni^{II} centre in a distorted pseudo-octahedral geometry with the Ln^{III} centres in distorted bicapped square-antiprism geometry. The huge distortion around the Ni^{II} centres is triggered for the accommodation of larger lanthanoids to the adjacent OO coordination site, and this forces the Ni^{II} centres to have a tridentate coordination from the ONS, as intermediate between *meridional* and *facial* binding. Field-induced single-molecule magnetic behaviour was observed for heterodinuclear complexes involving Kramers lanthanide ions (Ln^{III} = Dy, Er and Yb), with magnetic relaxation occurring through an Orbach process only for **5**. DFT calculations using various functionals (BP86, B3LYP, PBE0, TPSSh, PWPB95, R^2SCAN) were applied to calculate the isotropic exchange, showing good agreement with the experiment (J_{Gd-Ni} = +1.78 cm^{-1}). CASSCF calculations for Ni^{II} and Ln^{III} ions were also performed to reveal detailed information about their electronic structure and magnetic anisotropy, supporting the experimental observations. This study accentuates the mutual distortion of coordination geometry induced by flexibility of the ligand backbone with the simultaneous binding of two different metal ions.

Received 10th May 2023,
Accepted 30th June 2023

DOI: 10.1039/d3dt01387a

rsc.li/dalton

Introduction

The experimental coordination chemists have seen rekindled interest in synthesizing new molecules combining two different metal-ion (3d and 4f) centres for their potential use as single-molecule magnets (SMMs).[1–3] This class of discrete coordination complexes display slow relaxation of magnetization and/or magnetic hysteresis below their blocking temperatures (T_B).[4] They have potential applications in ultrahigh-density data storage, molecular spintronics, quantum computations, and magnetocaloric materials.[5–8] From the era of Mn_{12}Ac showing slow relaxation of magnetization, several synthetic methodologies have been explored to obtain newer SMMs based on only 3d and/or 4f ions.[9,10] It has now been identified that the 3d–4f magnetic interaction can be utilized to slow the rate of magnetic relaxation processes in bimetallic or higher order complexes.[11] Another approach for manipulating single-molecule magnetism is tuning the quantum tunnelling of magnetization through such 3d–4f interactions.[12] A heterometallic Fe^{II}–Dy^{III} complex showing single-molecule magnetic behaviour with a huge anisotropy barrier of 319 cm^{-1} has been reported by Tong and co-workers.[13] The magnetic properties of the 4f ions is dependent on their coordination geometry, surrounding ligand field, and magnetic interactions with adjacent metal ions (3d or 4f).[14] The coordination environments and their deviation from regular ones have a substantial influence on the behaviour of the newer group of single-molecule magnets.[15] Axially symmetric crystal-field

[a]*Department of Chemistry, Indian Institute of Technology, Kharagpur 721302, India. E-mail: dray@chem.iitkgp.ac.in*
[b]*Univ. Rennes, CNRS, ISCR (Institut des Sciences Chimiques de Rennes) – UMR 6226, F-35000 Rennes, France*
[c]*Department of Inorganic Chemistry, Faculty of Science, Palacký University, 17. listopadu 12, 77146 Olomouc, Czech Republic*

†Electronic supplementary information (ESI) available. CCDC 2163624–2163630. For ESI and crystallographic data in CIF or other electronic format see DOI: https://doi.org/10.1039/d3dt01387a

environments around the 4f ions and strong exchange coupling between the metal ions could lead to a significant SMM behaviour.[16,17]

A pivotal condition for acquiring high-performance SMMs is the efficacious involvement of the individual magnetic anisotropy of the metal sites[18] and a large ground spin state (S).[19] When the large magnetic moment and strong magneto-anisotropy of 4f ions are combined with adjacent 3d ions, it leads to stronger magnetic exchange than the 4f–4f interactions.[20,21] For the last three decades, planned synthesis to obtain fascinating but simple magnetic molecules has resulted in unique structures with more 3d and 4f ions, and such arrangements gifted newer insights into molecular magnetism from the viewpoints of simple experiments and supported by magnetic measurements and theoretical justifications.[22] The 3d–4f magnetic exchange interactions are known to be weak because of the quite efficient shielding of the 4f orbitals of the Ln^{III} ion by the fully occupied 5s and 5p orbitals.[23]

In recent years, several examples of Cu–Ln complexes were examined for their varying magnetic behaviours, and the exchange coupling constants are dependent on the geometrical factors.[24–27] Such studies for Ni–Ln complexes are limited because of the presence of the diamagnetic and square-planar Ni centres having isotropic $^3A_{2g}$ ground state.[28,29] However, it was found that even in a weak O_h crystal field, mixing of the excited states could lead to enhanced magnetic anisotropy and hence induce zero-field splitting (ZFS).[30,31] Apart from that, the Ni^{II} centre often exhibits ferromagnetic exchange coupling with 4f metal ions.[32–37] Hence, the new family of SMMs possessing large effective energy barriers for the reversal of magnetization (U_{eff}), and hence higher blocking temperatures (T_B), can be constructed by putting highly anisotropic trivalent 4f and bivalent Ni ions in close proximity. The higher coordination requirement around the Ln^{III} ions following ligand chelation is achieved by inorganic anions like NO_3^-, RCO_2^- *etc*.[38,39]

Toward this goal, we made use of the ligand 3-methoxy-*N*-[2-(methylsulfanyl)phenyl]salicylaldimine (HL) with fused and adjacent ONS and OO coordination pockets for the synthesis of a series of dinuclear complexes $[NiLn(L)_2(NO_3)_3]\cdot0.5H_2O$ (Ln = Gd, Tb, Dy, Ho, Er and Yb) and $[NiY(L)_2(NO_3)_3]\cdot0.5H_2O$. While accommodating the two OO pockets around the 4f ions, two ligand anion scaffolds suffer critical distortion of the octahedral geometry, wrapping the Ni^{II} center, which is further amplified due to the coordination –SMe groups having the larger S donor capable of accepting deviations from regular bond angles and distances for ideal octahedral geometry. The level of distortion was established from single-crystal X-ray structural characterization of the synthesized series of complexes. DC and AC magnetic susceptibility studies were performed on polycrystalline powder samples to examine the contributions from the highly distorted octahedral Ni^{II} centre frozen in intermediate coordination geometry, which is away from the *fac* and *mer* isomers. To understand the electronic structure and magnetic exchange coupling, *ab initio* calculations were performed for the correlation between experiment and theory.

Experimental section

Reagents and starting materials

Chemicals used were obtained from the following sources: dichloromethane and triethylamine (SRL, Mumbai, India); $Gd(NO_3)_3\cdot6H_2O$, $Tb(NO_3)_3\cdot5H_2O$, $Dy(NO_3)_3\cdot5H_2O$, and $Ho(NO_3)_3\cdot5H_2O$, $Yb(NO_3)_3\cdot5H_2O$ and 2-(methylthio)aniline (Alfa Aesar, UK); $Er(NO_3)_3\cdot5H_2O$, and $Y(NO_3)_3\cdot6H_2O$ (Sigma Aldrich); *o*-vanillin (Spectrochem Pvt. Ltd, Mumbai, India); $Ni(NO_3)_2\cdot6H_2O$ and acetonitrile (E. Merck, India). All the chemicals and solvents used in this work were reagent-grade materials and used as received without further purification.

Synthesis of ligand

3-Methoxy-*N*-[2-(methylsulfanyl)phenyl]salicylaldimine (HL). The Schiff base (HL) ligand was synthesized *via* a direct single-step imine condensation reaction of 3-methoxysalicylaldehyde (*o*-vanillin) and 2-(methylthio)aniline with a yield of 86%, as reported earlier.[40] ATR-FTIR and NMR spectral measurements were performed for the characterization of HL, and the solid ligand was used directly for reactions with two different types of metal ion salts. Yield = 86%. Selected IR peaks: (KBr, cm^{-1}, vs = very strong, br = broad, s = strong, m = medium, w = weak): 1610 (s, $\tilde{\nu}_{C.N}$); anal. calcd (%) for $C_{15}H_{15}NO_2S$: C, 65.91; H, 5.53; N, 5.12. Found (%): C, 65.76; H, 5.46; N, 5.17.

Synthesis of complexes

$[Ln^{III}Ni^{II}(L)_2(NO_3)_3]\cdot0.5H_2O$ and $[Y^{III}Ni^{II}(L)_2(NO_3)_3]\cdot0.5H_2O$. A common method of synthesis was adopted to obtain all seven compounds of the series. HL (0.2 mmol, 0.0546 g) was dissolved in 10 mL of acetonitrile–dichloromethane (2 : 1) solvent mixture. Solid $Ni(NO_3)_2\cdot6H_2O$ (0.1 mmol, 0.0290 g) was added, it followed by magnetic stirring for 1 h. After that, solid $M(NO_3)_3\cdot nH_2O$ (0.1 mmol; n = 6 for M^{3+} = Gd (**1**); Y (**7**) and n = 5 for M^{3+} = Tb (**2**), Dy (**3**), Ho (**4**), Er (**5**) and Yb (**6**)) was added to the pale-yellow solution and stirred further for 15 min. Then, NEt_3 (0.2 mmol, 28 μl) was further added to the solution, and the reaction mixture was stirred for a further 7 h at room temperature. A turbid yellowish-green solution was obtained, which was filtered, and the clear greenish-yellow filtrate was left undisturbed for slow evaporation. Green block-shaped air-stable crystals were acquired after a week, suitable for single-crystal analysis. The characterization data of the complexes are given below.

$[NiGd(L)_2(NO_3)_3]\cdot0.5H_2O$ (1). HL (0.0546 g, 0.2 mmol), $Ni(NO_3)_2\cdot6H_2O$ (0.0290 g, 0.1 mmol), Et_3N (28 μl, 0.2 mmol), and $Gd(NO_3)_3\cdot6H_2O$ (0.0451 g, 0.1 mmol). Yield: 0.040 g (41.8%). Anal. calcd (%) for $C_{30}H_{29}NiN_5O_{13.5}S_2Gd$: C, 37.70; H, 3.06; N, 7.33. Found (%): C, 37.40; H, 3.01; N, 7.50. Selected IR peaks: (KBr, cm^{-1}): 1619 (s, $\tilde{\nu}_{C.N}$), 1383 (s, $\tilde{\nu}_{NO_3}$).

$[NiTb(L)_2(NO_3)_3]\cdot0.5H_2O$ (2). HL (0.0546 g, 0.2 mmol), $Ni(NO_3)_2\cdot6H_2O$ (0.0290 g, 0.1 mmol), Et_3N (28 μl, 0.2 mmol),

and $Tb(NO_3)_3{\cdot}5H_2O$ (0.0453 g, 0.1 mmol). Yield: 0.034 g (35.6%). Anal. calcd (%) for $C_{30}H_{29}NiN_5O_{13.5}S_2Tb$: C, 37.64; H, 3.05; N, 7.32. Found (%): C, 37.52; H, 3.06; N, 7.39. Selected IR peaks: (KBr, cm^{-1}): 1618 (s, $\bar{\nu}_{C.N}$), 1388 (s, $\bar{\nu}_{NO_3}$).

$[NiDy(L)_2(NO_3)_3]{\cdot}0.5H_2O$ (3). HL (0.0546 g, 0.2 mmol), $Ni(NO_3)_2{\cdot}6H_2O$ (0.0290 g, 0.1 mmol), Et_3N (28 μl, 0.2 mmol), and $Dy(NO_3)_3{\cdot}5H_2O$ (0.0438 g, 0.1 mmol). Yield: 0.052 g (54.1%). Anal. calcd (%) for $C_{30}H_{29}NiN_5O_{13.5}S_2Dy$: C, 37.50; H, 3.04; N, 7.29. Found (%): C, 37.43; H, 3.08; N, 7.26. Selected IR peaks: (KBr, cm^{-1}): 1621 (s, $\bar{\nu}_{C.N}$), 1380 (s, $\bar{\nu}_{NO_3}$).

$[NiHo(L)_2(NO_3)_3]{\cdot}0.5H_2O$ (4). HL (0.0546 g, 0.2 mmol), $Ni(NO_3)_2{\cdot}6H_2O$ (0.0290 g, 0.1 mmol), Et_3N (28 μl, 0.2 mmol), and $Ho(NO_3)_3{\cdot}5H_2O$ (0.0459 g, 0.1 mmol). Yield: 0.040 g (41.5%). Anal. calcd (%) for $C_{30}H_{29}NiN_5O_{13.5}S_2Ho$: C, 37.40; H, 3.03; N, 7.27. Found (%): C, 37.51; H, 3.06; N, 7.22. Selected IR peaks: (KBr, cm^{-1}): 1622 (s, $\bar{\nu}_{C.N}$), 1388 (s, $\bar{\nu}_{NO_3}$).

$[NiEr(L)_2(NO_3)_3]{\cdot}0.5H_2O$ (5). HL (0.0546 g, 0.2 mmol), $Ni(NO_3)_2{\cdot}6H_2O$ (0.0290 g, 0.1 mmol), Et_3N (28 μl, 0.2 mmol), and $Er(NO_3)_3{\cdot}5H_2O$ (0.0443 g, 0.1 mmol). Yield: 0.049 g (50.8%). Anal. calcd (%) for $C_{30}H_{29}NiN_5O_{13.5}S_2Er$: C, 37.31; H, 3.03; N, 7.25. Found (%): C, 37.39; H, 3.04; N, 7.28. Selected IR peaks: (KBr, cm^{-1}): 1621 (s, $\bar{\nu}_{C.N}$), 1383 (s, $\bar{\nu}_{NO_3}$).

$[NiYb(L)_2(NO_3)_3]{\cdot}0.5H_2O$ (6). HL (0.0546 g, 0.2 mmol), $Ni(NO_3)_2{\cdot}6H_2O$ (0.0290 g, 0.1 mmol), Et_3N (28 μl, 0.2 mmol), and $Yb(NO_3)_3{\cdot}5H_2O$ (0.0443 g, 0.1 mmol). Yield: 0.044 g (45.3%). Anal. calcd (%) for $C_{30}H_{29}NiN_5O_{13.5}S_2Yb$: C, 37.09; H, 3.01; N, 7.21. Found (%): C, 37.16; H, 3.03; N, 7.27. Selected IR peaks: (KBr, cm^{-1}): 1618 (s, $\bar{\nu}_{C.N}$), 1383 (s, $\bar{\nu}_{NO_3}$).

$[NiY(L)_2(NO_3)_3]{\cdot}0.5H_2O$ (7). HL (0.0546 g, 0.2 mmol), $Ni(NO_3)_2{\cdot}6H_2O$ (0.0290 g, 0.1 mmol), Et_3N (28 μl, 0.2 mmol), and $Y(NO_3)_3{\cdot}6H_2O$ (0.0383 g, 0.1 mmol). Yield: 0.050 g (56.4%). Anal. calcd (%) for $C_{30}H_{29}NiN_5O_{13.5}S_2Y$: C, 40.60; H, 3.29; N, 7.89. Found (%): C, 40.30; H, 3.05; N, 7.70. Selected IR peaks: (KBr, cm^{-1}): 1623 (s, $\bar{\nu}_{C.N}$), 1382 (s, $\bar{\nu}_{NO_3}$).

Physical measurements

ATR-FTIR spectra were measured on a PerkinElmer Spectrum two spectrometer by placing the samples over the ATR crystal of the instrument. A PerkinElmer model 240C elemental analyzer was used for elemental analysis (C, H, and N) of the powder samples. The phase purity of the bulk samples was checked from powder XRD patterns on a Bruker D2 PHASER X-ray diffractometer (30 kV, 10 mA) with Cu-Kα radiation (λ = 1.5418 Å) within the 5–50° (2θ) range and fixed-time counting of 4 s at 25 °C.

Magnetic measurements

DC magnetic susceptibility measurements were performed on a solid-immobilized polycrystalline sample with a Quantum Design PPMS magnetometer between 2 and 300 K under an applied magnetic field of 0.02 T for the temperature range of 2–20 K, 0.2 T for 20–80 K, and 1 T for 80–300 K. AC magnetic susceptibility measurements were performed on Quantum Design PPMS magnetometers over the 10–10 000 Hz frequency range. These measurements were all corrected for diamagnetic contribution, as calculated with Pascal's constants.

X-ray crystallographic measurements

A Bruker SMART APEX-II CCD X-ray diffractometer equipped with graphite-monochromated Mo Kα (λ = 0.71073 Å) radiation and an ω scan (width of 0.3° per frame) was used for single-crystal XRD structural studies of all of the complexes, performed at 296 K for complexes **1–7** and with a scan rate of 6 s per frame. The SAINT, SMART, and XPREP software packages[41] were used for the index, integration, and space-group determination of each frame. The SHELXS-2014[42] direct method was used to solve the crystal structure, which was again refined by the full-matrix least-squares technique of the SHELXL (2014/7)[43] programs within WINGX, version 1.80.05.[44] The multi-scan method of the SADABS[45] program was used for empirical absorption corrections. Heavier atoms such as Ni and Ln were determined easily, whereas all other non-H atoms were refined with anisotropic displacement, and the riding model was used to incorporate the H atoms in idealized positions. DIAMOND software[46] was utilized for presentation of the crystal structures. The crystal data and refinement parameters for complexes **1–7** are summarized in Table S1.† The crystallographic data (excluding structural factors) have been deposited with the Cambridge Crystallographic Data Centre as supplementary publications CCDC 2163624–2163630.†

Theoretical calculations

The theoretical calculations were performed with the ORCA 5.0 software.[47–49] The state average complete active space self-consistent field (SA-CASSCF)[50] wave function method was applied for all studied complexes. The active space was defined by seven f-orbitals, and numbers of multiplets were determined from the respective electronic configuration of the lanthanide ions: Gd^{III} ion with 1 octet, 48 sextets, 392 quartets, and 784 doublets; Tb^{III} ion with 7 septets, 140 quintets, 588 triplets, and 490 singlets; Dy^{III} ion with 21 sextets, 224 quartets, and 490 doublets; Ho^{III} ion with 35 quintets, 210 triplets, and 196 singlets; Er^{III} ion with 35 quartets and 112 doublets; Yb^{III} ion with 7 doublets. In the case of Ni^{II} ions, the active space was defined by five d-orbitals and eight electrons, which resulted in 10 triplets and 15 singlets, and calculations were complemented by *N*-electron valence second-order perturbation theory (NEVPT2).[51–55] The Douglas–Kroll–Hess (DKH) Hamiltonian was used to treat relativistic effects.[56,57] The relativistic basis sets were utilized as follows: SARC2-DKH-QZV for lanthanides and DKH-def2-TZVP for non-metal atoms except for C and H atoms, for which the DKH-def2-SVP basis set was used.[58,59] The auxiliary basis set SARC/J[60] and the AutoAux generation procedure,[61] together with the chain-of-spheres (RIJCOSX) approximation to exact exchange,[62,63] were used to speed up the calculations. The three-dimensional plots of molar magnetization (Fig. S13–S18†) were made using a home-made script and the SINGLE_ANISO module, which enables the calculation of molar magnetization for any direction of the magnetic field. The calculations of magnetic exchanges between Gd(III) and Ni(II), along with Er(III) and Ni(II), were carried out using the DFT method with the same basis as the

above-described calculations. More strict convergence criteria and integral precision were achieved by using "VeryTightSCF" and "DefGrid3" keywords. Several DFT functionals were applied, namely BP86,[64] B3LYP,[65–68] PBE0,[69,70] TPSSh,[71] PWPB95 [72] and R^{2}SCAN.[73] The experimental X-ray structures were used for all calculations, in which hydrogen atom positions were normalized in Mercury software.[74] The calculated data were visualized with the VESTA 3 program[75] and the Chemcraft software.

Results and discussion

The coordination reactivity of HL for preferential trapping of 3d and 4f ions was explored with $Ni(NO_3)_3{\cdot}6H_2O$ and $Ln(NO_3)_3{\cdot}xH_2O$ (Ln = Gd, Tb, Dy, Ho, Er, Tb, Y) in the presence of NEt_3, as summarized in Scheme 1.

The reaction of HL and NEt_3 with $Ni(NO_3)_3{\cdot}6H_2O$ and $Ln(NO_3)_3{\cdot}xH_2O$ in a 2 : 2 : 1 : 1 molar ratio, in acetonitrile–dichloromethane medium under room temperature and with magnetic stirring, provided yellowish-green solutions from which green block-shaped crystals of **1–7** were obtained in 41.8%, 35.6%, 54.1%, 41.5%, 50.8%, 45.3%, and 56.4% yields, respectively (Scheme 1).

Single-crystal X-ray structure analysis revealed the formation of severely distorted bimetallic neutral $\{Ni^{II}Ln^{III}\}$ cores in **1–7**. Trapping of Ln^{III}/Y^{III} ions from the used nitrate salts is facilitated by the bridging coordination of two phenoxido and two adjacent –OMe groups. Metal ion salt-derived nitrate anions occupy the remaining six coordination sites around the Ln^{III}/Y^{III} ion, resulting in a bicapped square-antiprism coordination environment. The existence of a larger 4f ion triggers a huge alteration of the O_h geometry around the adjacent Ni^{II} ion. The choice of –SMe group in the ligand anion backbone, with the larger atomic radius of the sulphur atom, is accountable for sustaining longer bond distances and bond angles at the Ni^{II} ion. After standardizing the synthetic procedure and optimizing the initial trials, the isolated products were characterized using CHN analysis and through ATR-FTIR spectroscopic signatures. The characteristic bond stretch for the Ni^{II} ion-bound imine group, $\nu_{C=N}$, appeared at around 1618–1623 cm^{-1} for the entire family. These values are blue shifted compared to the value of 1610 cm^{-1} for the free ligand (Fig. S1 in ESI†). The bulk powder samples, synthesized in different batches, were also analysed using PXRD technique. The experimental diffraction traces for all seven compounds are in good agreement with the simulated patterns obtained using single-crystal diffraction data, which also confirm the phase purity of the bulk compound (Fig. S2 and S3 in ESI†).

Description of the crystal structures

$[Ln^{III}Ni^{II}(L)_2(NO_3)_3]{\cdot}0.5H_2O$ and $[Y^{III}Ni^{II}(L)_2(NO_3)_3]{\cdot}0.5H_2O$ (Ln = Gd, 1; Tb, 2; Dy, 3; Ho, 4; Er, 5; Yb, 6; and Y, 7). Suitable single crystals of **1–7** were obtained from a MeCN–DCM (2 : 1, v/v) solvent mixture. All the seven complexes are found to be isostructural and crystallize in the monoclinic $P2_1/n$ space group with $Z = 4$, and in all cases, the asymmetric unit contains the whole molecule. Selected metric parameters pertaining to the structures are listed in Tables S2–S15 in the ESI.† Since the complexes are isostructural, the structural description is given mainly with respect to the Dy derivative (**3**) as a representative example from the entire series. Each charge-neutral bimetallic complex consists of a severely distorted $\{Ni^{II}Ln^{III}\}$ core (Fig. 1) shaped with the use of two bent L^- anions. Each L^- anion provides a twisted ONS coordination for the Ni^{II} centre. This twisting is forced due to the accommodation of the Ln^{III} ion side by having defined bidentate OO coordination sites, ultimately arresting in bicapped square-antiprism geometry. This twist in the ligand anion backbone allows the very unusual deviation from planar *meridional* coordination around the Ni^{II} centre. The planar structure is normally expected in free ligand HL due to the maximum amount of π conjugation.

The complex **3** consists of a $\{Dy^{III}Ni^{II}O_2\}$ type diamond core (Fig. 2) developed from the connectivity of two phenoxido oxygen donors (O1 and O3) from two ligands. The binding of 4f ions enforces a huge strain on the otherwise planar ligand backbone, resulting in severe distortion of the octahedral geometry around the Ni^{II} centre within the $N_2S_2O_2$ coordination sphere.

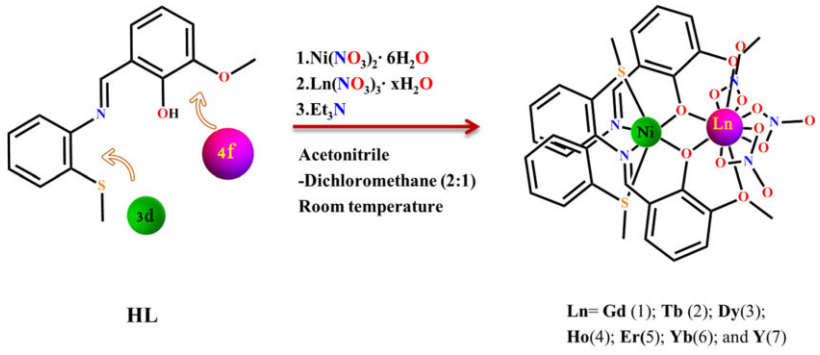

HL

Ln= Gd (1); **Tb** (2); **Dy**(3); **Ho**(4); **Er**(5); **Yb**(6); and **Y**(7)

Scheme 1 Synthetic routes for complexes **1–7**.

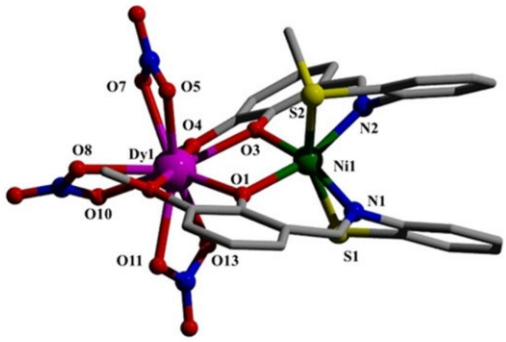

Fig. 1 Molecular structure of **3** with the atom numbering scheme. Hydrogen atoms are omitted for clarity. Color code: Ni^{II} green, Dy^{III} magenta, N blue, O red, S yellow, C grey.

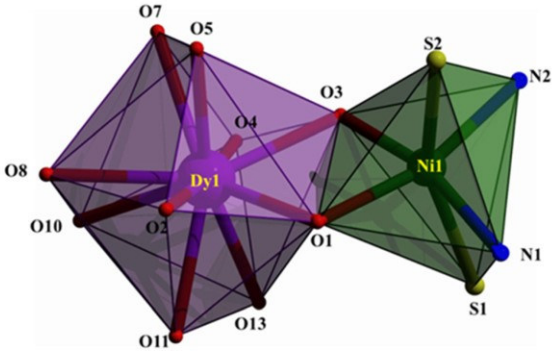

Fig. 2 Severely distorted octahedral coordination geometry around Ni^{II} and bicapped square-antiprismatic coordination geometry around Dy^{III} in **3**.

For ONS tridentate chelation around the Ni ion, the Ni^{II}–N distances are slightly longer at 2.013 and 2.029 Å, compared to Ni^{II}–O distances at 1.997 and 1.995 Å, while bulkier S donors show comparatively longer Ni^{II}–S separations at 2.556 and 2.545 Å. The ligand bites form six- and five-membered chelate rings, with the O_{Ph}–Ni–N_{im} angles of 89.77° and 90.56° and N_{im}–Ni–S angles of 76.46° and 73.96°, respectively. In this intermediate mode in **3**, all the *cis* angles vary in a wide range 82.42–101.13°, and the S–Ni–S angle is 158.76°, which deviates largely from ideal *fac* geometry. Thus, the final binding mode can be assumed to be distorted *facial* type (Fig. 3).

The ligand bites form six- and five-membered chelate rings, with the O_{Ph}–Ni–N_{im} angles of 89.77° and 90.56° and N_{im}–Ni–S angles of 76.46° and 73.96°, respectively. In this intermediate mode in **3**, all the *cis* angles vary in a wide range, 82.42–101.13°, and the S–Ni–S angle is 158.76°, which deviates largely from ideal *fac* geometry. The N_2O_2 basal plane is 26% distorted toward T_d (τ_4 value is 0.26).[76] Thus, the final binding mode can be assumed to be distorted *facial* type[77] (Fig. 3).

During coordination of the Ln^{III}/Y^{III} ion, the geometry around the Ni^{II} ion experiences huge distortion and thus can significantly deviate from a perfect octahedron. The magnitude of distortion from an ideal octahedral geometry can be obtained by calculating the angular distortion parameter Σ. Accordingly, we calculated the octahedral distortion parameter Σ,[78] which can be defined as the sum of the deviations from 90° for the 12 *cis* angles of the Ni^{II} octahedron. Σ is zero for a perfect octahedral system. The distortion parameter $\sum$Ni for **3** at 298 K is 76.43°, demonstrating huge distortion from the regular O_h system. The coordination geometry around each Ni^{II} centre was analysed with a continuous shape measure using the SHAPE program, and the CShM value obtained is 3.897, which also reflects a huge distortion from the perfect octahedral geometry (the trigonal prism arrangement has a CShM of 9.566, Table S16 in ESI†).[79]

The ten-coordinated environments around the Dy^{III} ion are accomplished by two bidentate O, OMe parts from two L^- and three O,O donor-based bidentate nitrate ions. The arrangement of ten O donors around the Dy^{III} centres resulted in a shape close to bicapped square-antiprismatic (Fig. 2; D_{4d}, continuous shape measure index is 3.105 by SHAPE 2.1, Table S17 in the ESI†). Amongst them, the nature of three different types of O donors gave Dy–O separations in the 2.332–2.751 Å range, where the shortest ones are from phenolate donors (2.332 and 2.310 Å) and the longest ones (2.712 and 2.751 Å) were for –OMe donors (Fig. 4). Within this bicapped structure, the longest axis is defined by O2–Dy1–O4, subtending an angle of 175.08° at the Dy1 centre. The three chelating NO_3^- anions recorded intermediate Dy–O separations in the 2.419–2.475 Å range.

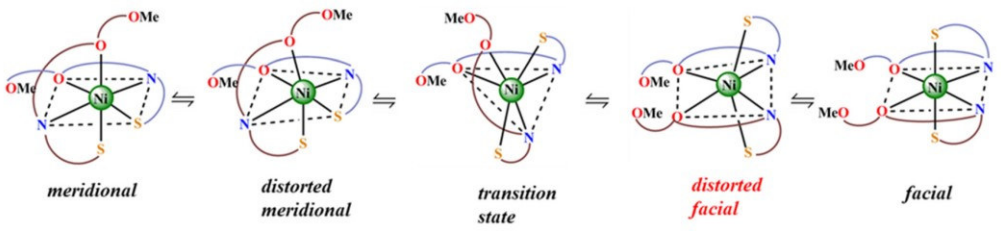

Fig. 3 Transition between ideal *mer* and *fac* octahedral geometries around the Ni^{II} center. In the absence of Ln^{III}, the geometry around Ni^{II} is closer to *mer*, while upon coordination of Ln^{III}, the geometry is best described as distorted *fac*, which is passed through distorted *mer* and TS.

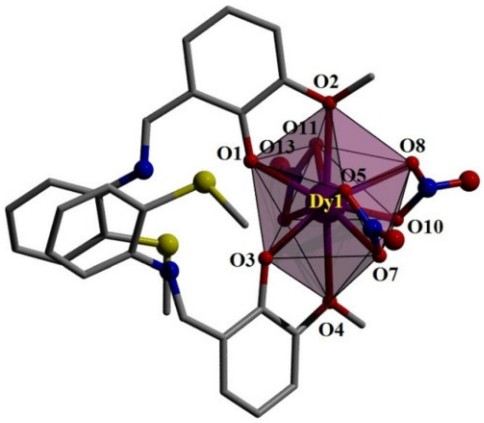

Fig. 4 Arrangement of different O-donors in bicapped square-antiprismatic polyhedron around Dy1. Ni1 is omitted for clarity.

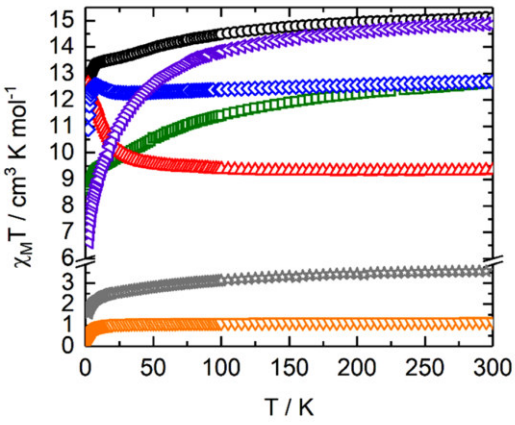

Fig. 5 Thermal variation of the magnetic susceptibility $\chi_M T$ in the 2–300 K temperature range for **1** (red up triangles), **2** (blue lozenges), **3** (black circles), **4** (purple triangles), **5** (green squares), **6** (grey stars) and **7** (down orange triangles).

The bridging phenolate donors (O1 and O3) register Dy1–O(1/3)–Ni1 angles of 103.93° and 104.64°, respectively. This connectivity brought Dy1 and Ni1 at a distance of 3.415 Å. Such bridging arrangement provided the $\{Ni^{II}Ln^{III}O_2\}$ core with substantial variation in the O1–Dy^{III}–O3 and O1–Ni^{II}–O3 angles of 68.92° and 82.29°, due to the size and coordination number differences between the two types of metal ions. The Ni–$(\mu\text{-}O)_2$–Dy diamond core is almost planar, with a small hinge angle of 4.38°.

The $Ln^{III}\cdots Ni^{II}$ separations decrease in the order **1** > **2** > **3** > **4** > **5** > **6** (Gd1···Ni1, 3.454 Å; Tb1···$Ni1^{II}$, 3.418 Å; Dy1···Ni1, 3.415 Å; Ho1···Ni1, 3.412 Å; Er1···Ni1, 3.403 Å; Yb1···Ni1, 3.385 Å), in agreement with the lanthanide contraction (Fig. S20†).

Magnetic properties

The static magnetic properties were studied by measuring the thermal dependence of the $\chi_M T$ product (χ_M is the molar magnetic susceptibility and T is the temperature in Kelvin) for compounds **1**–**7** (Fig. 5). First of all, the $\chi_M T(T)$ plot for **7** takes a room-temperature value of 1.16 cm^3 K mol^{-1}, in agreement with a single paramagnetic Ni(II) centre in an octahedral environment where the orbital moment is largely quenched with $S = 1$ and $g = 2.15$.[80] The $\chi_M T$ product remains constant down to 15 K, and then slightly decreases due to weak zero-field splitting and/or intermolecular interaction. For **1**, the room-temperature $\chi_M T$ value is 9.35 cm^3 K mol^{-1}, in good agreement with the expected value of 9.035 cm^3 K mol^{-1} for two uncoupled Ni(II) ($S = 1$, $g = 2.15$) and Gd(III) ($S = 7/2$, $g = 2.00$) ions. The $\chi_M T$ product remains almost constant, up to 50 K, and then increases at low temperature up to 12.63 cm^3 K mol^{-1} at 2 K, which is close to the expected value for two ferromagnetically coupled Ni(II) and Gd(III) ions. The room-temperature $\chi_M T$ values are 12.70 cm^3 K mol^{-1}, 15.11 cm^3 K mol^{-1}, 14.84 cm^3 K mol^{-1}, 12.69 cm^3 K mol^{-1} and 3.56 cm^3 K mol^{-1}, in agreement with the expected values of 12.98 cm^3 K mol^{-1}, 15.33 cm^3 K mol^{-1}, 15.23 cm^3 K mol^{-1}, 12.64 cm^3 K mol^{-1} and 3.73 cm^3 K mol^{-1} for compounds **2**–**6**, respectively. The ferromagnetic coupling is clearly observable in **2** between the Ni(II) and Tb(III) ions, with an increase of $\chi_M T$ at low temperature, while for **3** and **5**, only a change of $\chi_M T(T)$ slope is observed. For **4** and **6**, such magnetic interaction cannot be identified from the $\chi_M T(T)$ curve. For all the compounds, the decrease of $\chi_M T(T)$ at low temperature is mainly attributed to thermal depopulation of the M_J doublet states of the lanthanide center.

The field variation of the magnetization for **1**–**7** is depicted in Fig. S4.† The $M(H)$ values are $8.48N\beta$, $6.39N\beta$, $6.58N\beta$, $6.32N\beta$, $5.69N\beta$, $2.97N\beta$ and $1.28N\beta$ at 50 kOe for **1**–**7**, far from the expected saturated value (except for **1** and **7**) due to significant magnetic anisotropy of the lanthanide ion.

The DC magnetic data analysis for compound **7**, in which the only paramagnetic ion is Ni^{II} with $S = 1$, was based on the spin Hamiltonian comprising the zero-field splitting term (ZFS) and Zeeman term as follows:

$$\hat{H} = D_{Ni}(\hat{S}_z{}^2 + \hat{S}^2/3) + E_{Ni}(\hat{S}_x{}^2 - \hat{S}_y{}^2) + \mu_B B g \hat{S}. \quad (1)$$

The magnetic data were fitted with the program POLYMAGNET.[81] The best fit was achieved for the positive value of the axial ZFS parameter $D = +8.1$ cm^{-1} with $g = 2.09$ and $\chi_{TIP} = 2.38 \times 10^{-4}$ emu mol^{-1} (TIP is temperature independent paramagnetism), see Fig. S5.† It was found that the rhombic parameter E does not improve the fit of the experimental data; therefore, it was set to zero. The positive value of D is in concordance with the magneto-structural correlation published by Titiš *et al.*,[82] because Ni^{II} ions in **1**–**7** possess distorted pseudo-octahedral arrangement.

Next, the compound **1** was analysed with following spin Hamiltonian:

$$\hat{H} = -J_{Gd\text{-}Ni}(\vec{S}_{Gd}\vec{S}_{Ni}) + D_{Ni}(\hat{S}_z{}^2 + \hat{S}^2/3) + \mu_B B(g_{Gd}\hat{S}_{Gd} + g_{Ni}\hat{S}_{Ni}), \quad (2)$$

in which the isotropic exchange was also introduced. The ZFS of Gd^{III} was neglected, as usually, the magnetic anisotropy of this ion having $^8S_{7/2}$ ground multiplet is diminishing. The best fit was found for J_{Gd-Ni} = +1.78 cm^{-1}, D_{Ni} = +8.4 cm^{-1} with g_{Gd} = 2.0 (fixed), and g_{Ni} = 2.20, see Fig. S6.† Thus, the ferromagnetic exchange was quantified. Also, we observed small variations of the ZFS parameter of Ni^{II} in **1** and **7**, which is also supported by small variations of these parameters as deduced from the theoretical calculations (*vide infra*, Table S25†).

The dynamic magnetic properties of the heterobimetallic NiLn complexes were investigated. Only complex **5** displayed an out-of-phase (χ''_M) component of the magnetic susceptibility in zero applied DC field at 2 K, but with a maximum at a higher frequency than 10 kHz (Fig. 6a). Such lack of slow magnetic relaxation behaviour could be due to an efficient relaxation through quantum tunnelling of the magnetization (QTM). Nevertheless, it is well known that the latter can be cancelled by applying an external DC field. Thus, the field dependence of magnetic susceptibility was measured for all the compounds. None of the compounds involving non-Kramers lanthanide ions (integer spin) showed slow magnetic relaxation in the 0–3000 Oe field range at 2 K due to spin parity. Contrariwise, the three compounds involving anisotropic Kramers, Dy(III) (**3**, Fig. S7†), Er(III) (**5**, Fig. 6a and Fig. S8†) and Yb(III) (**6**, Fig. S9†) displayed slow magnetic relaxation. The χ''_M maxima for **3** and **6** remain at higher frequency than 10 kHz, while clear maxima are observed for **5** in the experimental frequency range of 10–10 000 Hz under an applied field range of 0–3000 Oe at 2 K (Fig. 6a). The extended Debye model (eqn (S1)†) allowed the extraction of the relaxation times at any DC field (see plot in Fig. 6b and Table S18†).[83,84] When increasing the applied DC field, the magnetization relaxation rate initially decreased until it reached a minimum value, and then increased at higher DC field values. Such behavior is coherent with relaxation *via* QTM at low static magnetic field followed by the activation of a direct mechanism for stronger fields. The τ *vs.* H plot was fitted with (eqn 3):

$$\tau^{-1}(T,H) = AH^4T + \frac{B_1}{1+B_2H^2} + \underbrace{\tau_0{}^{-1}\,e\left(\frac{U_{eff}}{k_BT}\right) + CT^n}_{k(T)}. \quad (3)$$

From left to right, the terms are the expressions of direct (A is a constant for the direct process, H the magnetic field, and T the temperature), QTM (with B_1 and B_2 as constants for the QTM process) and thermally activated (Orbach and Raman)

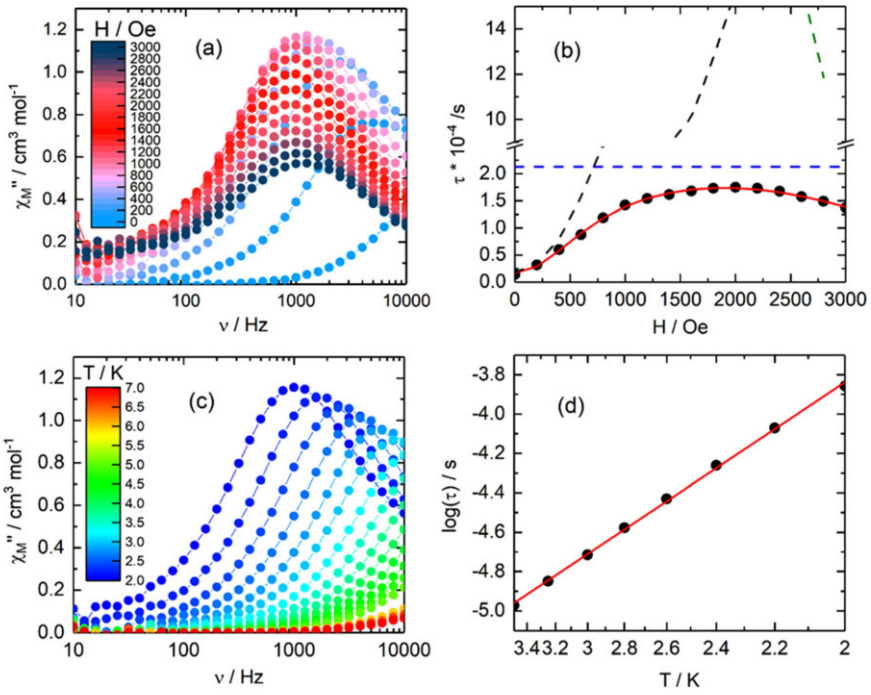

Fig. 6 (a) Field dependence of the out-of-phase component of magnetic susceptibility (χ''_M) at 2 K in the field range of 0–3000 Oe for **5**. (b) Field variation of the relaxation time (τ, black dots) for **5** with the best fitted curve in red. Each relaxation process is represented as follows: QTM (black dashed line), direct (green dashed line), and thermally activated $k(T)$ contribution (Orbach + Raman, blue dashed line). Parameters are given in the text. (c) Frequency dependence of χ''_M at 1000 Oe in the temperature range of 2–7 K for **5**. (d) Temperature variations of the relaxation times in the range of 2 K to 3.5 K under 1000 Oe (full black circles). The red lines depict the best fits with parameters given in the text.

(with U_{eff} = effective energy barrier, k_B the Boltzmann constant, C and n are respectively the constant and exponent for Raman process) contributions. $k(T)$ means that both Raman and Orbach processes are thermally dependent.

The best fit was obtained with the following parameters: $B_1 = 5.6(6) \times 10^5$ s^{-1}, $B_2 = 2.2(3) \times 10^{-5}$ Oe^{-2}, $A = 1.37(7) \times 10^{-11}$ s^{-1} K^{-1} Oe^{-4} and $k(T) = 2.13(7) \times 10^{-4}$ s^{-1} (Fig. 6b). While the optimal field value is about 2000 Oe, the value of 1000 Oe was selected as a good compromise between the χ''_M amplitude and the relaxation time (τ) to study the temperature-dependent behaviour of magnetic susceptibility for **5** (Fig. 6c and Fig. S10†). In such applied magnetic field, a frequency dependence of the magnetic susceptibility is observed in the 2–7 K temperature range (Fig. 6c and Fig. S10†), and τ is extracted using the extended Debye model (eqn (S1) and Table S19†).

The thermal variation of τ is depicted as $\log(\tau)$ *vs.* T in Fig. 6d, and it can be fitted using the same eqn (3). The best fit was found using an Orbach process only, with parameters $\Delta = 12.1(2)$ K and $\tau_0 = 3.49(2) \times 10^{-7}$ s, in agreement with the field dependence of magnetic susceptibility (Fig. 6b). The normalized Argand attested that 80% of the sample is involved in slow magnetic relaxation under an applied DC field of 1000 Oe (Fig. S11†).

Theoretical calculations

The magnetic properties of compounds **1–7** were investigated by theoretical methods, namely, with the state average complete active space self-consistent field (SA-CASSCF) wave function method, as described in detail in the Experimental section. The calculations were performed for each dinuclear unit by substituting the paramagnetic Ni^{II} with Zn^{II} ion, and similarly, by substituting paramagnetic Ln^{III} with diamagnetic Y^{III} ion. With the help of *ab initio* ligand field theory (AILFT),[85,86] the energies of d- and f-orbitals were calculated, respectively. Moreover, the computational results were analysed with the SINGLE_ANISO module,[87] which provided the *ab initio* magnetization blocking barriers, zero-field splitting parameters, as well as *g*-factors, as summarized in Tables S20–S24† for Ln^{III} ions and in Table S25† for Ni^{II} ion.

First, the properties of Ni^{II} will be discussed. The splitting of d-orbitals, ligand-field terms, and ligand-field multiplets is depicted in Fig. 7. The d-orbitals splitted in the distorted octahedral ligand field in the following order: $d_{xz} \approx d_{yz}$, d_{xy}, d_{z^2}, $d_{x^2-y^2}$, with the spanning interval of ~14 000 cm^{-1}, where the *xy*-plane is defined by $\{NiO_2N_2\}$ atoms and *z*-axis by {SNiS} atoms. The respective orbitals are shown in Fig. S12.† The ground atomic term ^{3}F of Ni^{II} is split to $^3A_{2g}$, $^3T_{2g}$ and $^3T_{1g}$ ligand-field terms in the ideal O_h symmetry, but in the case of complexes **1–7** studied herein, the symmetry is lower, and thus further splitting of these ^{3}T-terms is observed (see Fig. 7, middle). As a consequence of the spin–orbit coupling and ligand field, the zero-field splitting of the $(2S + 1)$ ground state is evident in Fig. 7 (right). It was found that the axial ZFS parameter D for Ni^{II} ion is in the narrow range of 13–14 cm^{-1} with a relatively small rhombic parameter $|E|$ around 2.4–2.6 cm^{-1}, resulting in easy plane magnetic anisotropy (Fig. S13 and Table S25†).

Due to the inner character of f-orbitals, the effect of the ligand field is weaker; the f-orbitals are split in the range from 500 to 700 cm^{-1}, and the splitting of the respective ligand-field multiplets spans the interval up to ~400 cm^{-1} for **2–6**, as depicted in Fig. 8. The ZFS parameter $D = -0.021$ cm^{-1} for Gd^{III} ion in **1** is negative and minute as expected, and the rhombic parameter $E = -0.007$ cm^{-1} is negligible. Next, the Kramers ions are the Dy^{III} of **3**, Er^{III} of **5** and Yb^{III} of **6**, for which the analysis of the lowest Kramers doublet revealed an axial type of magnetic anisotropy (Tables S21, S23, and S24†); the largest energy gap to the first excited state is found for Er^{III} of **5** with energy at 98 cm^{-1}, and the lowest gap is found for Dy^{III} of **3** with energy at 25 cm^{-1}.

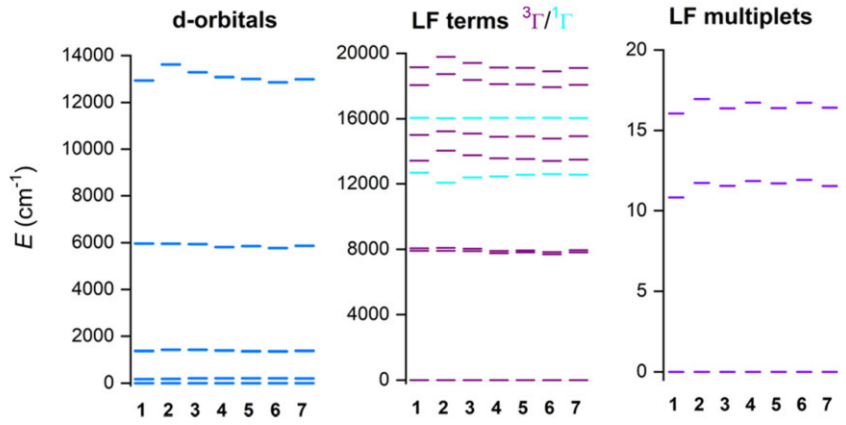

Fig. 7 The output of the ORCA CASSCF/NEVPT2 calculations with CAS(8,5) for Ni^{II} ions in complexes **1–7**. The plot of the d-orbital splitting calculated using *ab initio* ligand field theory (AILFT) (left), low-lying ligand-field terms (middle), and ligand-field multiplets showing splitting of the ground triplet state (right).

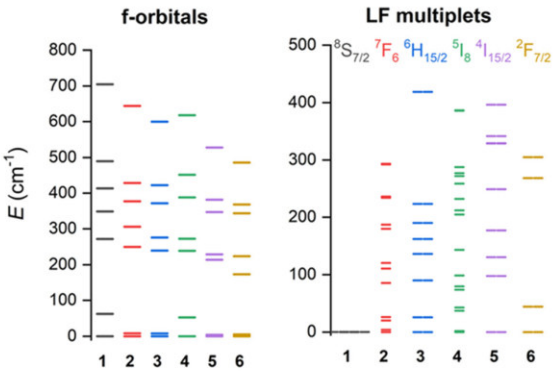

Fig. 8 The output of the ORCA CASSCF calculations for Ln^{III} ions in complexes **1–6**. Left: The plot of the f-orbital splitting calculated using *ab initio* ligand field theory (AILFT). Right: Ligand-field multiplets showing splitting of the ground atomic multiplet.

The calculated matrix element of the transversal magnetic moment within the ground Kramers doublet is lowest for the Er^{III} of **5**; thus, this compound should have the best properties to suppress the quantum tunnelling mechanism, as experimentally observed (Fig. 9).

The non-Kramers ions, Tb^{III} of **2** and Ho^{III} of **4**, possess the two lowest levels, which can be considered as pseudo-doublets; however their energy gap Δ_{tun} is relatively large (Δ_{tun} = 4.0 cm^{-1} for Tb^{III} and Δ_{tun} = 1.8 cm^{-1} for Ho^{III}, Tables S20 and S22†), which supports the lack of slow relaxation of the magnetization in these compounds (Fig. S19†). Nevertheless, all Ln^{III} ions in **2–6** produce the axial type of magnetic anisotropy, as is visible from the three-dimensional plots of the molar magnetization shown in Fig. S13–S18 in ESI.†

Finally, the strength of the magnetic exchange interaction in the Gd^{III}–Ni^{II} complex **1** and Er^{III}–Ni^{II} complex **5** was calculated using DFT method *via* the broken symmetry (BS) approach. This method is usually used for 3d metal ions and for gadolinium ions due to the lower contribution of spin–orbit coupling to the respective ground terms. BS-DFT is thus only sporadically used for other lanthanides, and herein, we present results not only for **1** but also for **5**. In this work, two methods of calculating the magnetic exchange interaction were used (with spin Hamiltonian defined as $H = -J(S_1S_2)$), namely the approach by Ruiz:[88]

$$J^{Ruiz} = 2\Delta/[(S_1 + S_2) \cdot (S_1 + S_2 + 1)]$$

and the approach by Yamaguchi:[89]

$$J^{Yam} = \frac{2\Delta}{\langle S_{HS}\rangle^2 - \langle S_{LS}\rangle^2},$$

where in both equations,

$$\Delta = E_{BS} - E_{HS}.$$

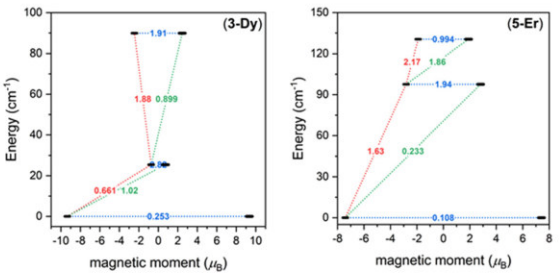

Fig. 9 Magnetization blocking barrier of Kramers ions: Dy^{III} of **3**, Er^{III} of **5** and Yb^{III} of **6** calculated using SINGLE_ANISO from the respective CASSCF calculations, zoomed to the lowest energy levels. The numbers presented in the plot represent the corresponding matrix element of the transversal magnetic moment (for values larger than 0.1, an efficient relaxation mechanism is expected).

In combination with several DFT functionals (BP86, B3LYP, PBE0, TPSSh, PWPB95, R^2SCAN), both methods were employed to calculate the magnetic exchange interactions, and the resulting values are compared in Table 1.

The results indicate that all of the methods used in this study have produced similar outcomes, which confirm the ferromagnetic nature of the magnetic exchange coupling between Gd(III) and Ni(II), which is in accordance with experimental data (J_{Gd-Ni} = +1.78 cm^{-1}). The best agreement is found for J^{Ruiz} calculated by BP86 and for J^{Yam} calculated by R^2SCAN. The scale of the magnetic exchange interaction is relatively small, although this is common among lanthanide-containing systems, due to the shielding of their unpaired electrons in f-orbitals. Similarly, the ferromagnetic exchange was calculated by all functionals also for the Er(III) and Ni(II) complex **5**, which is in concordance with the experiment. Interestingly, R^2SCAN and PWPB95 functionals suggest that ferromagnetic exchange is stronger in **1**; however, other functionals predicted stronger exchange in **5**.

As the Er^{III}–Ni^{II} compound **5** showed the best SMM properties examined by AC susceptibility measurements, an attempt was made to reveal detailed information about this complex. Thus, a homemade routine was used to fit experimental DC magnetic data of **5**, both temperature and field dependent, in cooperation with the POLY_ANISO module.[90,91] Herein, the eight lowest states of the Er^{III} ion and the three lowest states of the Ni^{II} ion were included in the exchange

Table 1 Comparison of several DFT functionals employed in the DFT broken-symmetry approach of magnetic exchange interaction calculation

	Gd^{III}–Ni^{II} complex **1**			Er^{III}–Ni^{II} complex **5**		
Method	Δ (cm^{-1})	J^{Ruiz} (cm^{-1})	J^{Yam} (cm^{-1})	Δ (cm^{-1})	J^{Ruiz} (cm^{-1})	J^{Yam} (cm^{-1})
BP86	21.619	1.74	3.08	23.524	5.38	7.84
B3LYP	16.741	1.36	2.40	9.785	2.24	3.26
PBE0	16.559	1.34	2.36	8.609	1.96	2.86
TPSSh	21.188	1.72	3.02	12.146	2.78	4.04
PWPB95	14.835	1.20	2.12	5.326	1.22	1.78
R^2SCAN	12.571	1.02	1.80	3.584	0.82	1.20

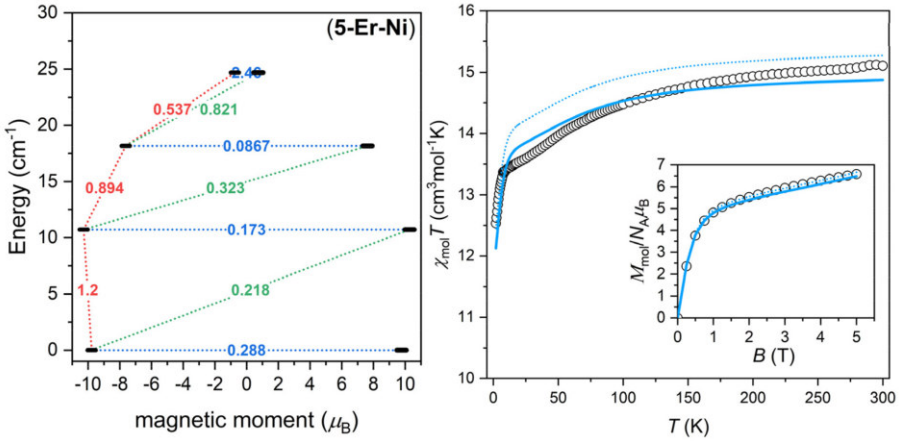

Fig. 10 The POLY_ANISO calculations for complex **5** with J_{Er-Ni} = 1.65 cm^{-1}. Left: Magnetization blocking barrier zoomed to the lowest energy levels. The numbers presented in the plot represent the corresponding matrix element of the transversal magnetic moment (for values larger than 0.1, an efficient relaxation mechanism is expected). Right: Temperature dependence of the χT product and (inset) the isothermal magnetization measured at T = 2 K. Experimental data – full symbols, calculated data – dotted line, calculated data scaled by 0.974 – full line.

interaction calculations. The best agreement was obtained with J_{Er-Ni} = 1.65 cm^{-1} with the scaling factor 0.974 (Fig. 10). The lowest energy gap is 10.7 cm^{-1} (15.3 K), which is in reasonable agreement with the experimental value of Δ = 12.1 K.

Conclusions

In summary, a –SMe donor group-bearing Schiff base HL was utilized to isolate a new family of dinuclear Ni–Ln complexes (**1–6**) and the corresponding yttrium analogue (**7**). The entrapment of the larger Ln^{III} ion in the OO pocket adjacent to the ONS part of L$^-$ bound to the Ni^{II} ion forces twisting of the backbone while fixing the OO part around the Ln^{III} ions. The comparatively larger –SMe donor group from one end of L$^-$ absorbs the unusual distortion in octahedral geometry around the Ni^{II} ion. Such distortions lead to a distorted *facial* arrangement of the ONS part of L$^-$ for a family of binuclear Ni–Ln complexes. The paramagnetic behaviour of the distorted octahedral Ni(II) was demonstrated by the magnetic behaviour of **7**, while **1** led to the conclusion that Ni(II) and Gd(III) are ferromagnetically coupled (J_{Gd-Ni} = +1.78 cm^{-1}). Such ferromagnetic coupling could be also observed for **2**, **3** and **5**, while it was not experimentally observed for the other heterobimetallic complexes. The compounds involving Kramers lanthanide ions such as Dy(III) (**3**), Er(III) (**5**) and Yb(III) (**6**) behave as field-induced single-molecule magnets, while those involving non-Kramers ions did not, due to spin parity. The slow magnetic relaxation occurred through an Orbach process only for **5**, with an effective energy barrier of 12 K. Several DFT functionals were applied to evaluate the isotropic exchange in **1**, revealing the good performance of the R^{2}SCAN functional. Moreover, CASSCF/NEVPT2 calculations for Ni^{II} in **1–7** supported easy plane magnetic anisotropy induced by the distorted octahedral coordination polyhedra in these complexes. The CASSCF/SINGLE_ANISO calculations provided the explanation for fast magnetic relaxation in **2–6** and identified Er^{III} complex **5** as the best candidate for SMM behaviour.

Conflicts of interest

There are no conflicts to declare.

Acknowledgements

BD would like to thank IIT Kharagpur for the research facility and his fellowship. TG and FP like to acknowledge the CNRS, University of Rennes and the European Research Council through the ERCCoG 725184 MULTIPROSMM (project no. 725184) for financial support. KK and RH acknowledge the financial support from project IGA_PrF_2023_007.

References

1 R. Sessoli, H. L. Tsai, A. R. Schake, S. Wang, J. B. Vincent, K. Folting, D. Gatteschi, G. Christou and D. N. Hendrickson, *J. Am. Chem. Soc.*, 1993, **115**, 1804–1816.
2 K. Liu, W. Shi and P. Cheng, Toward heterometallic single-molecule magnets: Synthetic strategy, structures and properties of 3d-4f discrete complexes, *Coord. Chem. Rev.*, 2015, **289–290**, 74–122.
3 L. Rosado Piquer and E. C. Sañudo, Heterometallic 3d-4f single-molecule magnets, *Dalton Trans.*, 2015, **44**, 8771–8780.

4 G. Christou, D. Gatteschi, D. N. Hendrickson and R. Sessoli, High-spin molecules: a novel cyano-bridged $Mn_9^{II}Mo_6^{V}$ molecular cluster with a S = 51/2 ground state and ferromagnetic intercluster ordering at low temperatures, *MRS Bull.*, 2000, **25**, 66–71.

5 M. Affronte, Molecular nanomagnets for information technologies, *Mater. Chem.*, 2009, **19**, 1731–1737.

6 G. Aromí and O. Roubeau, in *Lanthanide Molecules for Spin-Based Quantum Technologies*, ed. J.-C. G. Bünzli and V. K. Pecharsky, Elsevier, 2019, vol. 56, pp. 1–54.

7 L. Bogani and W. Wernsdorfer, *Nat. Mater.*, 2008, **7**, 179.

8 H. J. Lun, L. Xu, X. J. Kong, L. S. Long and L. S. Zheng, A high-symmetry double-shell $Gd_{30}Co_{12}$ cluster exhibiting a large magnetocaloric effect, *Inorg. Chem.*, 2021, **60**, 10079–10083.

9 R. Sessoli and A. K. Powell, Strategies towards single molecule magnets based on lanthanide ions, *Coord. Chem. Rev.*, 2009, **253**, 2328–2341.

10 M. Andruh, J.-P. Costes, C. Diaz and S. Gao, 3d–4f Combined Chemistry: Synthetic Strategies and Magnetic Properties, *Inorg. Chem.*, 2009, **48**, 3342–3359.

11 X.-L. Li, F.-Y. Min, C. Wang, S.-Y. Lin, Z. Liu and J. Tang, Utilizing 3d–4f magnetic interaction to slow the magnetic relaxation of heterometallic complexes, *Inorg. Chem.*, 2015, **54**, 4337–4344.

12 J. Li, R.-M. Wei, T.-C. Pu, F. Cao, L. Yang, Y. Han, Y.-Q. Zhang, J.-L. Zuo and Y. Song, Tuning Quantum Tunneling of Magnetization through 3d-4f Magnetic Interactions: An Alternative Approach for Manipulating Single-Molecule Magnetism, *Inorg. Chem. Front.*, 2017, **4**, 114–112.

13 J.-L. Liu, J.-Y. Wu, Y.-C. Chen, V. Mereacre, A. K. Powell, L. Ungur, L. F. Chibotaru, X.-M. Chen and M.-L. Tong, A Heterometallic Fe^{II}–Dy^{III} Single-Molecule Magnet with a Record Anisotropy Barrier, *Angew. Chem., Int. Ed.*, 2014, **53**, 12966–12970.

14 K. Bar, C. Pichon and J. P. Sutter, Magnetic anisotropy in two- to eight-coordinated transition–metal complexes: Recent developments in molecular magnetism, *Coord. Chem. Rev.*, 2016, **308**, 346–380.

15 K. Katoh, B. K. Breedlove and M. Yamashita, Symmetry of octa-coordination environment has a substantial influence on dinuclear Tb^{III} triple-decker single-molecule magnets, *Chem. Sci.*, 2016, **7**, 4329–4340.

16 W. Wernsdorfer, N. Aliaga-Alcalde, D. N. Hendrickson and G. Christou, Exchange-Biased Quantum Tunnelling in a Supramolecular Dimer of Single-Molecule Magnets, *Nature*, 2002, **416**, 406–409.

17 J. Liu, Y. C. Chen, J. L. Liu, V. Vieru, L. Ungur, J. H. Jia, L. F. Chibotaru, Y. Lan, W. Wernsdorfer, S. Gao, X. M. Chen and M. L. Tong, A stable pentagonal bipyramidal Dy(III) single-ion magnet with a record magnetization reversal barrier over 1000 K, *J. Am. Chem. Soc.*, 2016, **138**, 5441–5450.

18 A. M. Ako, I. J. Hewitt, V. Mereacre, R. Clérac, W. Wernsdorfer, C. E. Anson and A. K. Powell, A ferromagnetically coupled Mn19 aggregate with a record S = 83/2 ground spin state, *Angew. Chem., Int. Ed.*, 2006, **45**, 4926–4929.

19 D. N. Woodruff, R. E. P. Winpenny and R. A. Layfield, A. Lanthanide single-molecule magnets, *Chem. Rev.*, 2013, **113**, 5110–5148.

20 S. K. Langley, D. P. Wielechowski, B. Moubaraki and K. S. Murray, Enhancing the magnetic blocking temperature and magnetic coercivity of $\{Cr^{III}{}_2Ln^{III}{}_2\}$ single-molecule magnets via bridging ligand modification, *Chem. Commun.*, 2016, **52**, 10976–10979.

21 H. L. C. Feltham and S. Brooker, Review of purely 4f and mixed-metal nd-4f single-molecule magnets containing only one lanthanide ion, *Coord. Chem. Rev.*, 2014, **276**, 1–33.

22 C. Benelli and D. Gatteschi, Magnetism of Lanthanides in Molecular Materials with Transition-Metal Ions and Organic Radicals, *Chem. Rev.*, 2002, **102**, 2369–2388.

23 N. Ahmed, T. Sharma, L. Spillecke, C. Koo, K. Uddin Ansari, S. Tripathi, A. Caneschi, R. Klingeler, G. Rajaraman and M. Shanmugam, Probing the Origin of Ferro-/Antiferromagnetic Exchange Interactions in Cu(II)–4f Complexes, *Inorg. Chem.*, 2022, **61**, 5572–5587.

24 J. P. Costes, C. Duhayon, S. Mallet-Ladeira, S. Shova and L. Vendier, Does the Sign of the Cu–Gd Magnetic Interaction Depend on the Number of Atoms in the Bridge, *Chem. – Eur. J.*, 2016, **22**, 2171–2180.

25 M. Ferbinteanu, A. Stroppa, M. Scarrozza, I. Humelnicu, D. Maftei, B. Frecus and F. Cimpoesu, On the Density Functional Theory Treatment of Lanthanide Coordination Compounds: A Comparative Study in a Series of Cu–Ln (Ln = Gd, Tb, Lu) Binuclear Complexes, *Inorg. Chem.*, 2017, **56**, 9474–9485.

26 A. Dey, P. Bag, P. Kalita and V. Chandrasekhar, Heterometallic Cu^{II}-Ln^{III} complexes: Single molecule magnets and magnetic refrigerants, *Coord. Chem. Rev.*, 2021, **432**, 213707.

27 A. Worrell, D. Sun, J. Mayans, C. Lampropoulos, A. Escuer and T. C. Stamatatos, Oximato-Based Ligands in 3d/4f-Metal Cluster Chemistry: A Family of $\{Cu_3Ln\}$ Complexes with a "Propeller"-like Topology and Single-Molecule Magnetic Behavior, *Inorg. Chem.*, 2018, **57**, 13944–13952.

28 J. Lisowski and P. Starynowicz, Heterodinuclear Macrocyclic Complexes Containing Both Nickel(II) and Lanthanide(III) Ions, *Inorg. Chem.*, 1999, **38**, 1351–1355.

29 T. Sanada, T. Suzuki and S. Kaizaki, Heterotrinuclear complexes containing d- and f-block elements: synthesis and structural characterisation of novel lanthanide(III)–nickel(II)–lanthanide(III) compounds bridged by oxamidate, *J. Chem. Soc., Dalton Trans.*, 1998, 959–956.

30 M. Frost, K. L. M. Harriman and M. Murugesu, The rise of 3-d single-ion magnets in molecular magnetism: towards materials from molecules?, *Chem. Sci.*, 2016, **7**, 2470–2491.

31 G. A. Craig and M. Murrie, 3d single-ion magnets, *Chem. Soc. Rev.*, 2015, **44**, 2135–2147.

32 C. Meseguer, S. Titos-Padilla, M. M. Hänninen, R. Navarrete, A. J. Mota, M. Evangelisti, J. Ruiz and

E. Colacio, Single-Molecule Magnet Behavior and Magnetocaloric Effect in Ferromagnetically Coupled Ln^{III}-Ni^{II}-Ni^{II}-Ln^{III} (Ln^{III} = Dy^{III} and Gd^{III}) Linear Complexes, *Inorg. Chem.*, 2014, **53**, 12092–12099.

33 M. Towatari, K. Nishi, T. Fujinami, N. Matsumoto, Y. Sunatsuki, M. Kojima, N. Mochida, T. Ishida, N. Re and J. Mrozinski, Syntheses, Structures, and Magnetic Properties of Acetato- and Diphenolato-Bridged 3d–4f Binuclear Complexes $[M(3\text{-MeOsaltn})(MeOH)_x(ac)Ln(hfac)_2]$ (M = Zn^{II}, Cu^{II}, Ni^{II}, Co^{II}; Ln = La^{III}, Gd^{III}, Tb^{III}, Dy^{III}; 3-MeOsaltn = N,N′-Bis(3-methoxy-2-oxybenzylidene)-1,3-propanediaminato; ac = Acetato; hfac = Hexafluoroacetylacetonato; x = 0 or 1), *Inorg. Chem.*, 2013, **52**, 6160–6178.

34 A. Bhanja, E. Moreno-Pineda, R. Herchel, W. Wernsdorfer and D. Ray, Self-Assembled Octanuclear $[Ni_5Ln_3]$ (Ln = Dy, Tb and Ho) Complexes: Synthesis, Coordination Induced Ligand Hydrolysis, Structure and Magnetism, *Dalton Trans.*, 2020, **49**, 7968–7976.

35 A. Bhanja, R. Herchel, Z. Travnícek and D. Ray, Two types of hexanuclear partial tetracubane $[Ni_4Ln_2]$ (Ln = Dy, Tb, Ho) complexes of thioether-based Schiff base ligands: synthesis, structure, and comparison of magnetic properties, *Inorg. Chem.*, 2019, **58**, 12184–12198.

36 A. Chakraborty, N. Ahmed, J. Ali, S. Moorthy, J. Goura, S. K. Singh, G. Rogez and V. Chandrasekhar, Exchange-driven slow relaxation of magnetization in $Ni^{II}{}_2Ln^{III}{}_2$ (Ln^{III} = Y, Gd, Tb and Dy) butterfly complexes: experimental and theoretical studies, *Dalton Trans.*, 2022, **51**, 14721–14733.

37 T. D. Pasatoiu, J.-P. Sutter, A. M. Madalan, F. Z. C. Fellah, C. Duhayon and M. Andruh, Preparation, Crystal Structures, and Magnetic Features for a Series of Dinuclear $[Ni^{II}Ln^{III}]$ Schiff-Base Complexes: Evidence for Slow Relaxation of the Magnetization for the Dy^{III} Derivative, *Inorg. Chem.*, 2011, **50**, 5890–5898.

38 L. Jiang, Y. Liu, X. Liu, J. Tian and S. Yan, Three series of heterometallic Ni^{II}–Ln^{III} Schiff base complexes: synthesis, crystal structures and magnetic characterization, *Dalton Trans.*, 2017, **46**, 12558–12573.

39 M. X. Yao, X. Y. Lu, Z. X. Zhu, X. W. Deng and S. Jing, Synthesis, structures and magnetism of a series of dinuclear and one-dimensional Ni–Ln complexes: single-molecule magnetic behavior in one-dimensional nitrate-bridged Dy analogue, *New J. Chem.*, 2015, **39**, 8356–8363.

40 C. G. Hamaker and D. M. Corgliano, 3-Methoxy-*N*-[2-(methylsulfanyl)phenyl] salicylaldimine, *Acta Crystallogr., Sect. E: Struct. Rep. Online*, 2006, **62**, 68–69.

41 *SAINT, SMART and XPREP*, Siemens Analytical X-ray Instruments Inc., Madison, WI, 1995.

42 G. M. Sheldrick, *Acta Crystallogr., Sect. A: Found. Adv.*, 2015, **71**, 3–8.

43 G. M. Sheldrick, *Acta Crystallogr., Sect. C: Struct. Chem.*, 2015, **71**, 3–8.

44 G. M. Sheldrick, *SADABS Software for Empirical Absorption Correction*, University of Göttingen, Institute fur Anorganische Chemieder Universitat, Göttingen, Germany, 1999–2003.

45 L. J. Farrugia, WinGX and ORTEP for Windows: an Update, *J. Appl. Crystallogr.*, 2012, **45**, 849–8540.

46 *DIAMOND, Visual Crystal Structure Information System, version 3.1*, Crystal Impact, Bonn, Germany, 2004.

47 F. Neese, *Wiley Interdiscip. Rev.: Comput. Mol. Sci.*, 2012, **2**, 73–78.

48 F. Neese, Software update: the ORCA program system, version 4.0, *Wiley Interdiscip. Rev.: Comput. Mol. Sci.*, 2018, **8**, e1327.

49 F. Neese, F. Wennmohs, U. Becker and C. Riplinger, The ORCA Quantum Chemistry Program Package, *J. Chem. Phys.*, 2020, **152**, 224108–224125.

50 P. Å. Malmqvist and B. O. Roos, The CASSCF state interaction method, *Chem. Phys. Lett.*, 1989, **155**, 189–194.

51 C. Angeli, R. Cimiraglia, S. Evangelisti, T. Leininger and J. P. Malrieu, Introduction of n-Electron Valence States for Multireference Perturbation Theory, *J. Chem. Phys.*, 2001, **114**, 10252–10264.

52 C. Angeli, R. Cimiraglia and J. P. Malrieu, n-Electron Valence State Perturbation Theory: A Fast Implementation of the Strongly Contracted Variant, *Chem. Phys. Lett.*, 2001, **350**, 297–305.

53 C. Angeli, R. Cimiraglia and J. P. Malrieu, n-Electron Valence State Perturbation Theory. A Spinless Formulation and an Efficient Implementation of the Strongly Contracted and of the Partially Contracted Variants, *J. Chem. Phys.*, 2002, **117**, 9138–9153.

54 C. Angeli, S. Borini, M. Cestari and R. Cimiraglia, *J. Chem. Phys.*, 2004, **121**, 4043–4049.

55 C. Angeli, B. Bories, A. Cavallini and R. Cimiraglia, *J. Chem. Phys.*, 2006, **124**, 054108.

56 M. Douglas and N. M. Kroll, Quantum Electrodynamical Corrections to the Fine Structure of Helium, *Ann. Phys.*, 1974, **82**, 89–155.

57 B. A. Hess, Relativistic Electronic-Structure Calculations Employing a Two-Component No-Pair Formalism with External-Field Projection Operators, *Phys. Rev. A*, 1986, **33**, 3742–3748.

58 F. Weigend and R. Ahlrichs, Balanced Basis Sets of Split Valence, Triple Zeta Valence and Quadruple Zeta Valence Quality for H to Rn: Design and Assessment of Accuracy, *Phys. Chem. Chem. Phys.*, 2005, **7**, 3297–3305.

59 D. Aravena, F. Neese and D. A. Pantazis, Improved Segmented All-Electron Relativistically Contracted Basis Sets for the Lanthanides, *J. Chem. Theory Comput.*, 2016, **12**, 1148–1156.

60 D. A. Pantazis and F. Neese, All-Electron Scalar Relativistic Basis Sets for the Lanthanides, *J. Chem. Theory Comput.*, 2009, **5**, 2229–2238.

61 G. L. Stoychev, A. A. Auer and F. Neese, Automatic Generation of Auxiliary Basis Sets, *J. Chem. Theory Comput.*, 2017, **13**, 554–562.

62 F. Neese, F. Wennmohs, A. Hansen and U. Becker, Efficient, Approximate and Parallel Hartree-Fock and Hybrid DFT Calculations. A "Chain-of-Spheres" Algorithm for the Hartree-Fock Exchange, *Chem. Phys.*, 2009, **356**, 98–109.

63 R. Izsák and F. Neese, An overlap fitted chain of spheres exchange method, *J. Chem. Phys.*, 2011, **135**, 144105.

64 A. D. J. Becke, Density-Functional Exchange-Energy Approximation with Correct Asymptotic Behavior, *Phys. Rev. A*, 1988, **38**, 3098–3100.

65 A. D. J. Becke, Density-functional Thermochemistry. III. The Role of Exact Exchange, *Chem. Phys.*, 1993, **98**, 5648–5652.

66 C. Lee, W. Yang and R. G. Parr, Development of the Colle-Salvetti Correlation-Energy Formula into a Functional of the Electron Density, *Phys. Rev. B: Condens. Matter Mater. Phys.*, 1988, **37**, 785–789.

67 S. H. Vosko, L. Wilk and M. Nusair, Accurate Spin-Dependent Electron Liquid Correlation Energies for Local Spin Density Calculations: A Critical Analysis, *Can. J. Phys.*, 1980, **58**, 1200–1211.

68 P. J. Stephens, F. J. Devlin, C. F. Chabalowski and M. J. Frisch, Ab Initio Calculation of Vibrational Absorption and Circular Dichroism Spectra Using Density Functional Force Fields, *J. Phys. Chem.*, 1994, **98**, 11623–11627.

69 C. Adamo and V. Barone, Toward Reliable Density Functional Methods without Adjustable Parameters: The PBE0 Model, *J. Chem. Phys.*, 1999, **110**, 6158–6170.

70 J. P. Perdew, M. Ernzerhof and K. Burke, Rationale for Mixing Exact Exchange with Density Functional Approximations, *J. Chem. Phys.*, 1996, **105**, 9982–9985.

71 J. Tao, J. P. Perdew, V. N. Staroverov and G. E. Scuseria, Climbing the Density Functional Ladder: Nonempirical Meta-Generalized Gradient Approximation Designed for Molecules and Solids, *Phys. Rev. Lett.*, 2003, **91**, 146401.

72 L. Goerigk and S. Grimme, Efficient and Accurate Double-Hybrid-Meta-GGA Density Functionals—Evaluation with the Extended GMTKN30 Database for General Main Group Thermochemistry, Kinetics, and Noncovalent Interactions, *J. Chem. Theory Comput.*, 2011, **7**, 291–309.

73 J. W. Furness, A. D. Kaplan, J. Ning, J. P. Perdew and J. Sun, Accurate and Numerically Efficient r^2SCAN Meta-Generalized Gradient Approximation, *J. Phys. Chem. Lett.*, 2020, **11**, 8208–8215.

74 C. F. Macrae, I. Sovago, S. J. Cottrell, P. T. A. Galek, P. McCabe, E. Pidcock, M. Platings, G. P. Shields, J. S. Stevens, M. Towler and P. A. Wood, Mercury 4.0: from visualization to analysis, design and prediction, *J. Appl. Crystallogr.*, 2020, **53**, 226–235.

75 K. Momma and F. Izumi, VESTA 3 for Three-Dimensional Visualization of Crystal, Volumetric and Morphology Data, *J. Appl. Crystallogr.*, 2011, **44**, 1272–1276.

76 L. Yang, D. R. Powell and R. P. Houser, Structural variation in copper(I) complexes with pyridylmethylamide ligands: structural analysis with a new four-coordinate geometry index, τ_4, *Dalton Trans.*, 2007, **9**, 955–964.

77 D. Basak, J. van Leusen, T. Gupta, P. Kögerler, V. Bertolasi and D. Ray, Unusually Distorted Pseudo-Octahedral Coordination Environment around Co^{II} from Thioether Schiff Base Ligands in Dinuclear [CoLn] (Ln = La, Gd, Tb, Dy, Ho) Complexes: Synthesis, Structure, and Understanding of Magnetic Behavior, *Inorg. Chem.*, 2020, **59**, 2387–2405.

78 R. Ketkaew, Y. Tantirungrotechai, P. Harding, G. Chastanet, P. Guionneau, M. Marchivie and D. J. Harding, OctaDist: a tool for calculating distortion parameters in spin crossover and coordination complexes, *Dalton Trans.*, 2021, **50**, 1086–1096.

79 *SHAPE, version 2.0*, Electronic Structure Group, Universiat de Barcelona, Barcelona, Spain, 2010.

80 K. E. R. Marriott, L. Bhaskaran, C. Wilson, M. Medarde, S. T. Ochsenbein, S. Hill and M. Murrie, Pushing the limits of magnetic anisotropy in trigonal bipyramidal Ni(II), *Chem. Sci.*, 2015, **6**, 6823–6828.

81 R. Boča and R. Herchel, *Program POLYMAGNET*, 2006–2021.

82 J. Titiš and R. Boča, Magnetostructural *D* Correlation in Nickel(II) Complexes: Reinvestigation of the Zero-Field Splitting, *Inorg. Chem.*, 2010, **49**, 3971–3973.

83 C. Dekker, A. F. M. Arts, H. W. de Wijn, A. J. van Duyneveldt and J. A. Mydosh, Activated dynamics in a two-dimensional Ising spin glass: $Rb_2Cu_{1-x}Co_xF_4$, *Phys. Rev. B: Condens. Matter Mater. Phys.*, 1989, **40**, 11243–11251.

84 K. S. Cole and R. H. Cole, Dispersion and Absorption in Dielectrics I. Alternating Current Characteristics, *J. Chem. Phys.*, 1941, **9**, 341–351.

85 M. Atanasov, D. Ganyushin, K. Sivalingam and F. Neese, *Molecular Electronic Structures of Transition Metal Complexes II*, ed. D. M. P. Mingos, P. Day and J. P. Dahl, Springer Berlin Heidelberg, Berlin, Heidelberg, 2012, pp. 149–220.

86 S. K. Singh, J. Eng, M. Atanasov and F. Neese, Covalency and chemical bonding in transition metal complexes: An ab initio based ligand field perspective, *Coord. Chem. Rev.*, 2017, **344**, 2–25.

87 L. F. Chibotaru and L. Ungur, *Ab initio* calculation of anisotropic magnetic properties of complexes. I. Unique definition of pseudospin Hamiltonians and their derivation, *J. Chem. Phys.*, 2012, **137**, 064112–064133.

88 E. Ruiz, J. Cano, S. Alvarez and P. Alemany, Broken symmetry approach to calculation of exchange coupling constants for homobinuclear and heterobinuclear transition metal complexes, *J. Comput. Chem.*, 1999, **20**, 1391–1400.

89 K. Yamaguchi, S. Yamanaka, M. Nishino, Y. Takano, Y. Kitagawa, H. Nagao and Y. Yoshioka, Symmetry and Broken Symmetries in Molecular Orbital Descriptions of Unstable Molecules II. Alignment, Flustration and Tunneling of Spins in Mesoscopic Molecular Magnets, *Theor. Chem. Acc.*, 1999, **102**, 328–345.

90 L. F. Chibotaru, L. Ungur and A. Soncini, The Origin of Nonmagnetic Kramers Doublets in the Ground State of Dysprosium Triangles: Evidence for a Toroidal Magnetic Moment, *Angew. Chem., Int. Ed.*, 2008, **47**, 4126–4129.

91 L. Ungur, M. Thewissen, J.-P. Costes, W. Wernsdorfer and L. F. Chibotaru, Interplay of Strongly Anisotropic Metal Ions in Magnetic Blocking of Complexes, *Inorg. Chem.*, 2013, **52**, 6328–6337.